Heart Failure and Associated Structural and Functional Remodeling: Assessment Employing Various Magnetic Resonance Imaging Methodologies

A DISSERTATION
SUBMITTED TO THE FACULTY OF THE GRADUATE SCHOOL
OF THE UNIVERSITY OF MINNESOTA
BY

Michael D. Eggen

IN PARTIAL FULFILLMENT OF THE REQUIREMENTS
FOR THE DEGREE OF
DOCTOR OF PHILOSOPHY

Advisor: Paul A. Iaizzo, PhD

December 2009

Acknowledgements

I'd like to thank God, my family, Dr. Paul Iaizzo, Dr. Cory Swingen, Dr. Mike Loushin, the Visible Heart Lab staff and graduate students, my exam committee, and everyone who supported and/or contributed to this research.

Thesis Abstract

Cardiovascular magnetic resonance imaging (MRI), or cardiac MR, is currently considered the "gold" standard for noninvasively characterizing cardiac function and viability, having 3D capabilities and a high spatial and temporal resolution. More recently, the capabilities of MRI have been extended to study tissue microstrucure and fiber orientation in both the brain and the heart through specially designed pulse sequences which are sensitive to diffusion. In this specialized imaging method, known as diffusion tensor magnetic resonance imaging (DTMRI), myofiber orientation can be probed in high resolution and this technique has been successfully utilized to study the helical arrangement of muscle fibers within the myocardium. As such, the counter-wound helical structure of the myocardium is considered to be responsible for the torsional or wringing motion of the left ventricle and serves three main mechanical functions: (1) equalizing myofiber strain and workload; (2) optimizing the volume of blood ejected during systole (stroke volume); and/or (3) storing torsional energy in the intracellular and extracellular matrices and, when released, increasing ventricular filling during diastole. Therefore, cardiac fiber orientation can also be considered as a primary determinant of ventricular pump function, and is of great clinical interest in the study of structure and function within either the normal or diseased heart.

To date, the primary focus of cardiac DTMRI has been to characterize myofiber orientation in healthy animal hearts, with little progress in the study of myofiber arrangement in the diseased heart. As such, due to the long scan times required for in vivo DTMRI, and the limited availability of freshly excised human hearts for ex vivo

imaging, data are limited in the characterization of fiber orientation in both healthy and diseased human hearts. Therefore, in my thesis research, the primary objective was to investigate myofiber orientation in both healthy and diseased hearts using DTMRI. Specifically, changes in myofiber orientation were investigated in a high rate pacing model of dilated cardiomyopathy in swine, and also in excised healthy and diseased human hearts obtained from the Bequest Anatomy program at the University of Minnesota, and LifeSource (the Upper Midwest, a non-profit organ procurement organization). In addition, the mechanical activation due to cardiac pacing from the right ventricular apex was uniquely characterized in a case study of an isolated human heart using MRI, as cardiac pacing from the right ventricular apex is known to chronically result in deleterious changes in fiber orientation and cardiac function.

My thesis was divided into several chapters, in the first it was considered paramount to gain a thorough understanding of cardiac MRI. As such, a review of cardiovascular MRI is provided in Chapter 1. The goal of this chapter was to familiarize the reader with cardiac MR and nomenclature, review current techniques to quantify cardiac function with MRI, and to introduce the reader to cardiac diffusion tensor magnetic resonance imaging (DTMRI), which is used in the present work to quantify fiber orientation in the heart.

In Chapter 2, a literature review of cardiac fiber orientation and relevant changes resulting from disease is presented, and the measurement of fiber orientation using DTMRI is further discussed. The intent of this chapter is to familiarize the reader with

diffusion imaging and the associated parameters used to characterize fiber orientation and tissue integrity. In addition, the methodologies and computational tools developed to measure fiber orientation using a 3 tesla Siemens MRI clinical scanner are described.

Chapters 3-5 describe novel investigations in the assessment of fiber orientation using DTMRI. In chapter 3, the effects of decomposition on the diffusion properties of the myocardium were studied in freshly excised human hearts recovered at varying post mortem intervals. From this study, the time frame for the recovery of a human heart was determined to be 3 days, such that the tissue still remains viable for the measurement of fiber orientation using DTMRI. In Chapter 4, a swine model of dilated cardiomyaphy was used to assess in vivo functional and anatomical changes resulting from severe dilation of both the right and left ventricle. Following in vivo functional imaging, ex vivo DTMRI was used to investigate the resultant fiber orientation. Chapter 5 provides a preliminary comparison of fiber orientation in healthy and diseased human hearts, collected within a post-mortem interval of 3 days.

Furthermore, in Chapter 6, the mechanical activation during pacing from the right ventricular apex was studied in an isolated human heart. Since pacing from the right ventricular apex is known to cause deleterious changes in fiber orientation, it was of great interest to characterize myocardial strain and motion during RVA pacing as part of my thesis work.

In general, this research project has advanced our overall knowledge as to our understanding of ex vivo DTMRI, and the remodeling of the myocardial architecture in heart failure. This described work is not an exhaustive list of the changes in fiber orientation that occur in every type of cardiomyopathy, but provides novel insights into fiber reorganization which occurs in swine due congestive heart failure, and in human hearts excised from patients with a history of heart failure. Additionally, with the development of methodologies and computational tools presented here, and the study of post mortem intervals on the diffusion properties of the myocardium, the framework has been laid for the future analysis of fiber orientation in other cardiomyopathies presented in human cadaveric hearts.

Table of Contents

List of Tables

List of Figures

List of Abbreviations

MR: magnetic resonance

MRI: magnetic resonance imaging

DTMRI: diffusion tensor magnetic resonance imaging

FA: fractional anisotropy

ADC: apparent diffusion coefficient

PMI: post mortem interval

BW: body weight

ED LVP: end-diastolic left ventricular pressure

ES LVP: end-systolic left ventricular pressure

HW: heart weight

LV EDV: left ventricular end-diastolic volume

LV EF: left ventricular ejection fraction

LV ESV: left ventricular end-systolic volume

LVP: left ventricular pressure

LV SI: left ventricular sphericity index

LV SV: left ventricular stroke volume

TAD: total activation duration

DCM: dilated cardiomyopathy

EDV: end-diastolic volume

EF: ejection fraction

ESV: end-systolic volume

HF: heart failure

HRP: high-rate pacing

LV: left ventricle/left ventricular

LVP: left ventricular pressure

RVA: right ventricular apex

RVP: right ventricular pressure

TAD: total activation duration

Chapter 1: Cardiovascular Magnetic Resonance Imaging[†]

[†] Authors: Michael D. Eggen, MS[1,2], Cory M. Swingen, PhD[3]

Department of Biomedical Engineering[1], Department of Surgery[2], Department of Medicine[3], University of Minnesota, Minneapolis, Minnesota, 55455

This review was published in Handbook of Cardiac Anatomy, Physiology and Devices. 2nd edition, edited by Paul Iaizzo, New York: Springer; 2009.

Preface

Cardiovascular magnetic resonance imaging (MRI), or simply cardiac MR, is considered the ‘‘gold’’ standard for noninvasively characterizing cardiac function and viability, having 3Dcapabilities and a high spatial, and temporal, resolution. This imaging modality has proven to be an invaluable tool in diagnosing complex cardiomyopathies. Several clinical uses of cardiac MR include: (1) measuring myocardial blood flow; (2) the ability to differentiate between viable and nonviable myocardial tissue; (3) depicting the structure of peripheral and coronary vessels (magnetic resonance angiography); (4) measuring blood flow velocities (MR velocity mapping); (5) examining metabolic energetics (MR spectroscopy); (6) assessing myocardial contractile properties (multislice, multiphase cine imaging, MR tagging); and/or (7) guiding interventional procedures with real-time imaging (interventional MRI). Considering the expansive capabilities of cardiac MR, a condensed review of the concepts and applications of cardiac MR are provided in this chapter.

This review of cardiovascular magnetic resonance imaging is a chapter in the 2nd edition of the Handbook of Cardiac Anatomy, Physiology, and Devices, edited by Paul Iaizzo. It was my privilege to work with Dr. Cory Swingen in expanding and revising this chapter. My efforts for this chapter were focused on regional myocardial function, fiber structure and DTMRI, MRI and biomedical devices, and quantitative analysis of cardiac MR. Interestingly, I was the human volunteer for some the images analyzed in this review, specifically Figure 1.6 and Figure 1.15. Also, I ran the Siemens 1.5 tesla and 3.0 tesla MRI scanners located at the Fairview University Medical Center to obtain some of

the other images that appear in this chapter. In addition, for the section on biomedical device performance, I lead a chronic pacing study in swine to assess regional myocardial function during pacing, where I was responsible for programming the pacemaker, MR imaging, and data analysis (Figure 1.11).

Introduction

‘‘Magnetic resonance imaging’’ (MRI) of the heart has rapidly become very popular worldwide for its clinical versatility and flexibility, since it allows one to acquire Information on anatomical structure and function simultaneously. An additional benefit of MRI is that patients are not subjected to any ionizing radiation or invasive procedures (e.g., catheterization). Recently, many specialized MR techniques have become available for cardiovascular imaging and thus may potentially replace other types of imaging modalities. As such, cardiac MR may become the ‘‘one-stop shop’’ for imaging, as it is able to (1) measure myocardial blood flow; (2) differentiate viable from nonviable myocardial tissue; (3) depict the structure of peripheral and coronary vessels (magnetic resonance angiography); (4) measure blood flow velocities (MR velocity mapping); (5) examine metabolic energetics (MR spectroscopy); (6) assess myocardial contractile properties (multislice, multiphase cine imaging, MR tagging); and/or (7) guide interventional procedures with realtime imaging (interventional MRI). The capabilities of MRI as a tomographic imaging modality to capture, with high spatial resolution, the anatomy of 3D structures was already well appreciated before the first attempts were made to apply MRI to the heart. Cardiac motion, compounded by respiratory motion and turbulent blood flow in the ventricular cavities and large vessels, initially imposed formidable barriers to the acquisition of artifact free images that could depict the cardiac anatomy with sufficient detail. It has taken well over a decade for cardiac MRI to mature to the point where it is currently being applied in routine fashion in the clinical setting. Therefore, in the future, other cardiac imaging modalities such as ultrasound imaging and nuclear imaging may be partially eclipsed by MRI for selected

applications. This chapter provides a condensed review of the basic principles of MRI and introduces the reader to some of the concepts and terminology necessary to understand the application of MRI to the heart. We then proceed to describe a wide range of cardiac applications of MRI, both in vivo and ex vivo, which should interest the biomedical engineer. While the capabilities of cardiac MRI are quite extensive, our choice of topics for this chapter is rather judicious, as cardiac MRI has evolved to the point where entire books are published on the subject.

Overview of MRI

Magnetic resonance imaging works using the principle of nuclear magnetic resonance. That is, in the presence of a strong magnetic field (typically 1.5–3 tesla range for clinical systems), protons in the body are stimulated to emit radio waves. These radio waves are detected by an antenna, or coil, placed around the body region of interest and the signals are decomposed to reconstruct an image. We present a short summary of the basic concepts here and refer the reader to the overall literature for an in-depth examination.

Resonance

Inside the MRI scanner protons in the body align with the magnetic fields, similar to what happens to a compass needle placed in a magnetic field. These magnetic dipoles, if tipped away from the direction of the magnetic field, will precess about the direction of the static magnetic field (Figure 1.1). This precession has a rotation frequency, ν_L, that is directly proportional to the magnetic field strength, B_o. For hydrogen nuclei, the precession frequency varies with field strength as

$$\nu_L = 42.6[MHz/Tesla] \cdot B_o[Tesla].$$

The precession frequency is also known as the ‘‘Larmor frequency.’’ Tipping a nuclear magnetic moment away from the direction of the z-axis (B_o direction) can be accomplished by applying an oscillating magnetic field, denoted by B_1, in a direction perpendicular to B_o. The radio frequency transmitter should be tuned to a frequency close to the Larmor frequency to elicit a resonant excitation. After a radio frequency excitation pulse, the static magnetic field, B_o, causes precession of the transverse magnetization component, which can be detected with an external coil as shown in Figure 1.2. It is customary to refer to the magnetic fields that are oscillating at radio frequencies and turned on for brief durations as ‘‘radio frequency pulses.’’ A pulse that tips the magnetic moment from the z-axis into the x–y plane is referred to as a ‘‘90° radio frequency pulse’’; a pulse that inverts the orientation of the magnetic moment is called a ‘‘180° or inversion pulse.’’ In general, the degree to which the spins are tipped into the transverse (x–y) plane is referred to as the ‘‘flip angle.’’

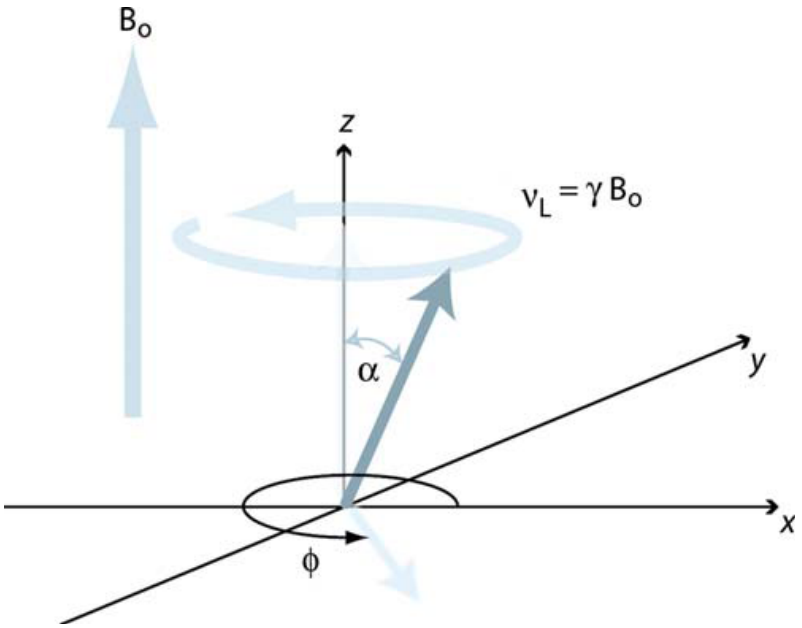

Figure 1.1 A single magnetic dipole moment in a static magnetic field of strength, B_o. It is customary to align the z-axis of a rectangular coordinate system with the direction of the externally applied static magnetic field, B_o. In this example, the magnetic moment, initially aligned with the applied magnetic field, was tipped away from the z direction by an angle α through application of an oscillating magnetic field (not shown). The oscillating magnetic field is kept on only for the time necessary to tip the magnetic dipole moment by a certain angle, α in this example. After turning the oscillating magnetic field off, the magnetic dipole moment precesses about the B_o direction at a frequency, $\nu_L=\gamma \cdot B_0$, where γ is a constant, the gyromagnetic ratio, and represents a property of the nucleus. For ^{1}H nuclei, γ equals 42.6 MHz/tesla. The angle φ denotes the phase angle of the magnetization component in the x–y plane, orthogonal to the direction of B_o.

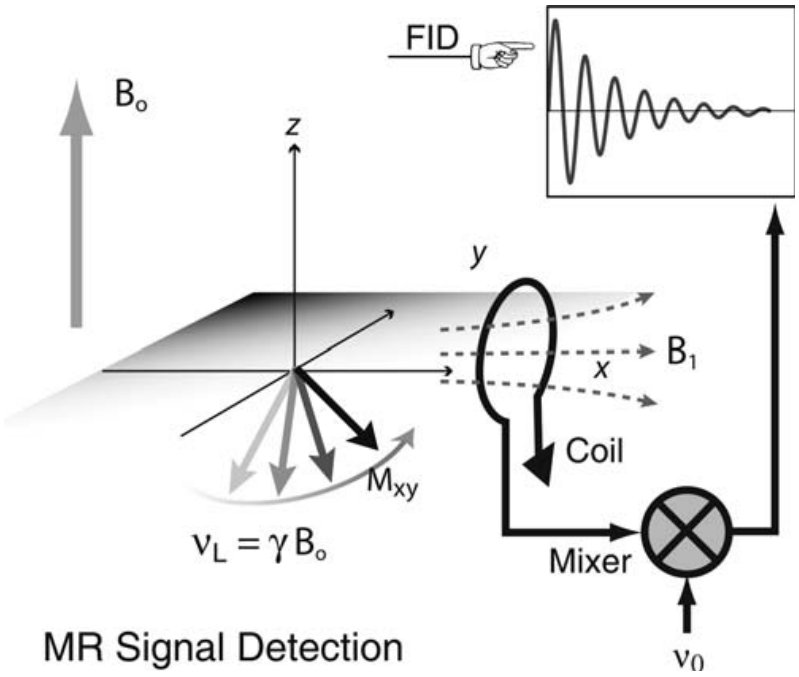

Figure 1.2 The transverse magnetization component of a nuclear dipole precesses at the Larmor frequency and produces an oscillating magnetic flux density that can be detected with a wire loop that is part of a resonant circuit. The induced voltage is amplified and mixed with the signal of an oscillator. The low-frequency component from the mixer is a free induction decay with frequency ν_L-ν_o. Often two coils, oriented perpendicular to each other, are used to detect the signal from the M_x and M_y components of the transverse magnetization, which are in quadrature, i.e., they have a relative phase difference of 90°. By detection of the quadrature components, it is possible to determine the sign of the difference ν_L-ν_o, and by combination of the two signals, after phase shifting one by 90°, one improves the signal to noise by a factor of $\sqrt{2}$. FID = free induction decay; MR = magnetic resonance.

Immediately after a radio frequency excitation, individual magnetic moments that were tipped into the transverse plane become in phase, i.e., they have the same phase angle. If all magnetic moments were to precess at exactly the same Larmor frequency, this phase coherence would persist. Residual magnetic field inhomogeneities, magnetic dipole interactions between neighboring nuclei, molecule-specific shifts of the precession frequency, and other factors produce a distribution of Larmor frequencies. The frequency shifts relative to a reference frequency can be tissue specific, as in the case of

^{1}H nuclei in fatty tissue. The spread of Larmor frequencies results in a slow loss of phase coherence of the transverse magnetization, i.e., the sum of all transverse magnetization components decays with time. The decay following a radio frequency excitation is called ‘‘free induction decay,’’ and often has the shape of an exponential function with an exponential time constant denoted as T2, roughly on the order of ~0.1 to ~10^2 ms for ^{1}H nuclei in biological systems. In the presence of field inhomogeneities and other factors that cause a spread of Larmor frequencies, the transverse magnetization decay is further shortened. To distinguish the latter situation, one introduces a time constant, T2*, that is characteristic of the exponential decay of the transverse magnetization in ‘‘heterogeneous’’ environments. It follows that T2* is always shorter than T2.

After any radio frequency excitation that tips the magnetization vectors away from the direction of the applied static magnetic field, B_o, the nuclear spins will, over time, realign themselves with the magnetic field to reach the same alignment as before the radio frequency excitation. This time constant is denoted as T1.

The Echo

A loss of phase coherence due to any spread in Larmor frequencies, for example, due to magnetic field inhomogeneities, can be (at least partially) reversed by applying a 180° pulse that flips the magnetization in the x–y plane such that the faster precessing spins now lag behind and the more slowly precessing spins are ahead, compared to spins precessing at the mean Larmor frequency. Once the echo amplitude peaks, the spread of

Larmor frequencies again causes a loss of phase coherence. Multiple 180° pulses can be applied to repeatedly reverse the loss of phase coherence and thereby produce a train of spin echoes, referred to as ‘‘fast spin echo imaging.’’ The decay of the spin echo amplitudes is governed by the decay constant T2, while a free induction decays with a characteristic time constant T2*, with T2* < T2. Importantly, for cardiac imaging applications, it is useful to note that the spin echo (and spin echo trains in particular) provides a method to attenuate the signal from flowing blood, while obtaining ‘‘normal’’ spin echoes from stationary or slow-moving tissue.

Spin echoes provide an effective means of refocusing the transverse magnetization for optimal MR signal detection. A similar, but nevertheless different, type of echo-like effect can be achieved by applying two magnetic field gradient pulses of opposite polarity instead of a 180° radio frequency pulse. The first gradient pulse causes a rapid dephasing of the transverse magnetization; the second gradient pulse, of opposite polarity, can reverse this effect. An echo-type signal is observed and peaks at the point where the phase wrap produced by the first pulse is cancelled. This type of echo is called a ‘‘gradient echo.’’

A train of gradient echoes can be created by consecutive pairs of dephasing and rephasing gradient waveforms. The acquisition of multiple-phase-encoded gradient echoes after a single radio frequency excitation is useful for very rapid image acquisition, but is limited by the T2* decay of the signal.

A variation of the gradient echo technique that reestablishes phase coherence to the best possible degree before application of the next radio frequency excitation (i.e., the next phase-encoding step) can be used to produce a steady state. This allows the application of radio frequency pulses with fairly large flip angles. Instead of relying on T1 relaxation to return the magnetization from the transverse plane to the B_o direction, the magnetization is toggled back and forth by the radio frequency pulses between the z-axis and the transverse plane. The attainable signal-to-noise ratio with this approach is significantly higher than with ‘‘conventional’’ gradient echo imaging. This type of gradient echo imaging is referred to in the literature by various acronyms—‘‘steady-state free precession imaging,’’ ‘‘TrueFISP,’’ or ‘‘balanced fast field echo imaging.’’ In particular, for cardiac cine studies, this technique has led to a marked improvement of image quality. Steady-state free precession (SSFP) works best with very short repetition times that, in turn, impose high demands on the gradient system of the MR scanner in terms of ramping gradients up and down.

Image Contrast

Biological tissues and blood have approximately the same density of ^{1}H nuclei, and spin-density images show poor contrast to differentiate, e.g., tissue from blood or fat from muscle. One of the most appealing aspects of MRI is the ability to manipulate the image contrast based on differences in the T1 or T2 relaxation times. For a gradient echo sequence, the T1 weighting is determined by the combination of flip angle and repetition time. Reducing repetition time or increasing the flip angle increases the T1 weighting in the image.

The T2* weighting of a gradient echo image is controlled by the time delay between the radio frequency pulse and the center of the readout window, i.e., the echo time TE. The T2 weighting of the spin echo signal is similarly determined by the echo time. In a fast spin echo sequence, one can use multiple echoes to read out the signal with different phase encodings for each echo. Controlling the T1 weighting through adjustment of repetition time and the flip angle imposes some limits that can be circumvented by applying an inversion pulse before the image acquisition and performing the image acquisition as rapidly as possible. The time between the inversion pulse and the start of the image acquisition controls the T1 contrast in this case. The image acquisition after the magnetization inversion is typically performed with a gradient echo sequence that uses small flip angles, i.e., the T1 contrast is controlled by the prepulse and the delay after the prepulse, instead of the repetition time and the flip angle, α, of the gradient echo image acquisition. Gradient echo imaging with a magnetization preparation in the form of a 180° or 90° radio frequency pulse is often the method of choice to acquire rapid T1- weighted images of the heart. MR contrast agents, such as gadolinium, provide a further means for controlling the image contrast by injecting a compound with paramagnetic ions that reduce the T1 of blood and tissue permeated by the agent. The local T1 reduction depends on (1) delivery of contrast agent to the tissue region through the blood vessels; (2) the degree to which the contrast agent molecules can cross barriers such as the capillary barrier; and (3) the distribution volume of the contrast agent within the tissue. The contrast seen after injection of such an agent can be used to determine pathology, such as the breakdown of the cardiac cell membranes and/or an above-normal concentration of contrast agent in infarcted myocardium.

Cardiac MR Techniques and Applications

Cardiac Morphology

The accurate depiction of cardiac morphology is important in most imaging applications. Numerous MR techniques have been developed and they are generally categorized based on the appearance of the intracardiac blood in the image, as either ‘‘black-blood’’ or ‘‘bright-blood’’ techniques.

‘‘Spin echo’’ (SE) was the first sequence used for the evaluation of cardiac morphology; however, it was not until the advent of ECG gating that SE imaging became substantially more important by reducing motion artifacts associated with the beating heart. SE images are called ‘‘black-blood’’ images due to the signal void created by flowing blood, which provides very good contrast between the myocardium and the blood. Slower moving blood, particularly adjacent to the ventricular walls, however, can cause the blood signal to appear brighter, effectively reducing the quality of the image. So, presaturating with a radio frequency pulse and reducing the echo time (TE) is used to minimize the blood signal and increase the contrast in the image [1]. Although widely available, SE imaging is limited due to its poor temporal resolution and susceptibility to respiratory and other motion artifacts. Nevertheless, these problems have been overcome through the development of sequences with shorter acquisition times, so-called fast (or turbo) SE pulse sequences. Although soft tissue contrast is not as optimal, these sequences have become the frontline sequence for depiction of cardiac morphology (Figure 1.3).

Figure 1.3 Cardiac anatomy of a canine heart imaged with a T2-weighted fast spin echo sequence and in-plane resolution of 1.2 mm. Cardiac structures such as the left ventricle (LV), right ventricle (RV), and aorta are labeled. The signal from blood in the ventricular cavities was nulled by a magnetization preparation consisting of radio frequency inversion pulses. Furthermore, the use of an echo train (with seven spin echoes in this case) and a long effective echo time also causes attenuation of the signal from moving blood. These so-called black-blood imaging techniques are very useful for anatomical imaging to avoid image artifacts from flowing blood.

Global Cardiac Function

Global and regional assessments of ventricular function with MRI are very well established and have been shown to be accurate and reproducible compared with other imaging modalities for the calculation of volumes, masses, and derived parameters such as stroke volume and ejection fraction [2, 3]. Thus, it is now considered the gold standard for the evaluation of cardiac function and mass in numerous studies comparing different imaging modalities [4].

Cine loops are acquired to follow the changes in ventricular dimensions over the entire cardiac cycle and thus to assess cardiac function. The acquisition of each image in the cine loop is broken up into several ‘‘segments,’’ and the image segments are acquired over consecutive heartbeats, as shown in Figure1.4. The acquisition of such image segments for each cardiac phase is subsequently synchronized with the heart cycle by

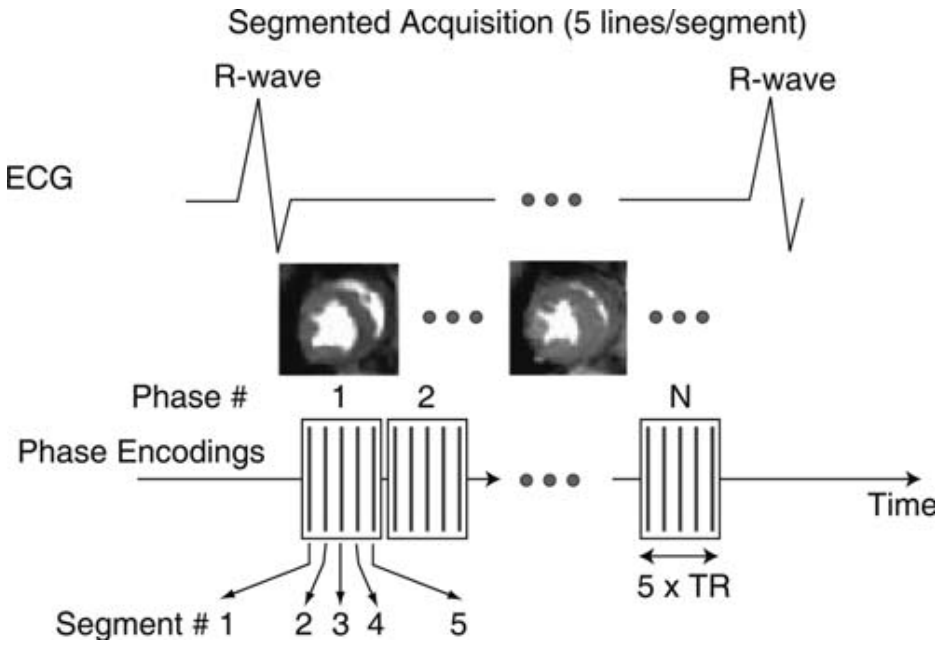

Figure 1.4 Illustration of the principle of segmented acquisitions of data, as used for imaging multiple phases of the cardiac cycle in ventricular function studies. The image acquisition is synchronized to the cardiac cycle by triggering of the pulse sequence with the R-wave on the ECG. The total number of phase encodings is split into five groups or segments in this example. The same five phase encodings are performed during each phase of one cardiac cycle. During the next R-to-R interval, five other phase encodings are performed for each cardiac phase. The R-wave-triggered acquisition of phase encodings is repeated *k* number of times to obtain a total of *k*5 phase encodings. The temporal extent of each cardiac phase is shown in the diagram by the boxes that contain the symbolic representations of the phase-encoded lines as vertical lines. The temporal resolution (TR) of the resulting cine loop is determined by the number of lines per segment (five in this example) and the repetition time for each phase-encoding step. Typical resolutions are on the order of 40–50 ms for resting heart rates and higher during inotropic stimulation of the patient's heart. The image acquisition is performed while the patient holds his/her breath. In this example the required duration of the breath-hold would be *k* heartbeats, with *k* typically on the order of 10–20, depending on the heart rate.

gating of the encoding steps with the patient's electrocardiogram. This technique works well as long as the subject has a regular heartbeat. The final result of the segmented acquisition is a series of images, one for each phase of the cardiac cycle. These images can be played as a cine loop, e.g., to assess ventricular function. To increase the

sharpness of the quality of images, clinicians ask patients to hold their breath during image acquisition. The segmented data acquisition approach always involves a tradeoff between temporal resolution (i.e., number of frames covering one R-to-R interval) and spatial resolution, as the image acquisition needs to be performed within a time short enough to allow for suspended breathing.

Typically, for the measurement of global cardiac function, ‘‘bright-blood cine MRI’’ is performed in multiple short-axis views, covering the heart from base to apex, using a multiphase, segmented k-space, ‘‘gradient echo’’ (GRE) sequence [5–7]. Yet, to date, GRE studies have suffered due to saturation effects in areas of low blood velocity, causing reduced contrast between blood and myocardium within the ventricular cavity [8]. In general, this problem causes difficulties in detection of the endocardial border, most dramatically in long-axis views of the heart where there is very minimal motion of blood through the imaging plane, as the majority of blood is moving within the image plane in these views as shown in Figure 1.5A. Such problems associated with GRE cine imaging have recently been minimized with the advent of SSFP sequences (Figure 1.5).

Although the concept of SSFP imaging has been described in the literature for many years, only recently has MR hardware developed to the point that these techniques have become practical and available on clinical scanners (e.g., those from multiple vendors) [9, 10]. Steady-state free precession sequences have dramatically improved contrast to noise, shortened acquisition times, and increased both spatial and temporal resolutions in comparison with previous GRE techniques [2, 11, 12]. These improvements have

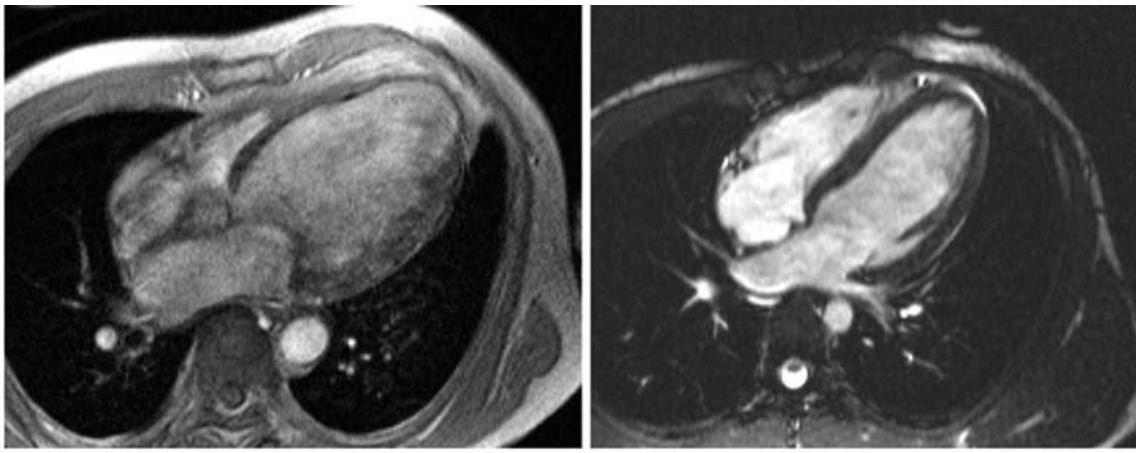

Figure 1.5 Comparison of end-diastolic long-axis views acquired with a segmented gradient echo sequence (A) and a steady-state free precession (SSFP) sequence (B). The SSFP technique provides significantly higher contrast to noise between intraventricular blood and myocardium, resulting in improved endocardial border definition throughout the cardiac cycle, as compared with the older gradient echo sequence.

enhanced the detection of the epicardial and endocardial surfaces (delineation of trabeculation and papillary muscle), both manually and with automated detection schemes, resulting in improved accuracy and reproducibility for the quantification of cardiac mass and volumes [13, 14]. Scan times have been reduced as well, such that SSFP sequences for an entire 3D data set covering the heart can be acquired within a single breath-hold.

Steady-state free precession techniques are also employed in the emerging area of real-time MR imaging. Recently, real-time imaging techniques have been developed and improved such that they will be employed in future cardiac function studies, as well as in the emerging field of interventional imaging with MRI. These real-time sequences continuously acquire images of the heart with sufficiently high temporal resolution

similar to fluoroscopy [15] without the need for ECG triggering or breathholding, therefore making it possible to image patients with severe arrhythmias or heart disease. In the past, these were difficult requirements to fulfill with segmented k-space GRE or SSFP sequences. Furthermore, newly developed sequences implementing image reconstruction techniques with sensitivity encoding (SENSE) and simultaneous acquisition of spatial harmonics (SMASH) have reported imaging temporal resolutions down to 13 ms with a spatial resolution of 4.1 mm [16].

Regional Myocardial Function

Ventricular volumes and derived parameters such as stroke volume and ejection fraction are the most commonly used variables for the assessment of systolic function in the clinical setting; however, they have associated limitations related to the measurement of contractile properties of the heart. Furthermore, these descriptors of cardiac performance do not take into consideration the importance of regional contractile dysfunction, the degree and extent of which are important prognostic factors with ischemic heart disease, and/or following myocardial infarction [17–19]. It is generally accepted that quantitative estimates of wall motion and relative changes in wall thickening (expressed as percentage (%) of end-diastolic wall thickness) are useful for measuring regional function and are also more precise than the subjective visual wall motion scoring system which is commonly used in the clinic today [20, 21]. Wall motion changes and thickening are usually measured along the length of a centerline between the segmented endocardial and epicardial borders of the heart. They are further divided into myocardial segments of equal circumferential extent that are positioned

relative to the location of an anatomical landmark such as the anterior–septal junction of the left ventricle and right ventricle. Dynamic changes in wall thickening can be considered as the radial component of myocardial strain, defined as the percent change in dimension from a resting state. Such strain analyses have proven very useful for the assessment of regional contractile function in both animals and human patients [22–24].

Circumferential shortening and radial thickening are two components of myocardial strain typically assessed by MRI tagging [25–29]. This approach has a higher sensitivity to the identification of noncontracting regions of the myocardium compared to ‘‘conventional’’ cine MRI. As such, cine imaging of the heart can be combined with a series of magnetization preparation pulses that null the longitudinal magnetization along thin parallel stripes in the slice plane. The stripes or tags appear as black lines on the MR images and can be applied in two directions in a single slice, forming a grid pattern. This grid pattern is created immediately after the R-wave of the EKG and before acquisition of the segmented phase encodings (Figure 1.4). The grid tags visible in the resulting images are ‘‘imbedded’’ in the tissue and are therefore distorted if any myocardial motion occurs. Thus, intramyocardial displacements and myocardial strain can be tracked through monitoring visible motion and deformation of the tag lines, respectively. Figure 1.6 shows an example of a myocardial grid pattern laid down at end-diastole and, in a second frame, the same pattern is recorded at end-systole with evident distortion of the tag lines due to myocardial contraction. The tag lines, created right after the R-wave, tend to fade during the cardiac cycle due to T1 relaxation, but for normal resting heart rates (e.g., 60–70 beats/min) the tag lines can persist long enough

to allow visualization of cardiac motion over nearly the entire R-to-R interval. Importantly, tag lines in the ventricular blood pool disappear very quickly because of the rapid motion and mixing of blood in the ventricle; this effect is then useful for clearly defining the endocardial borders.

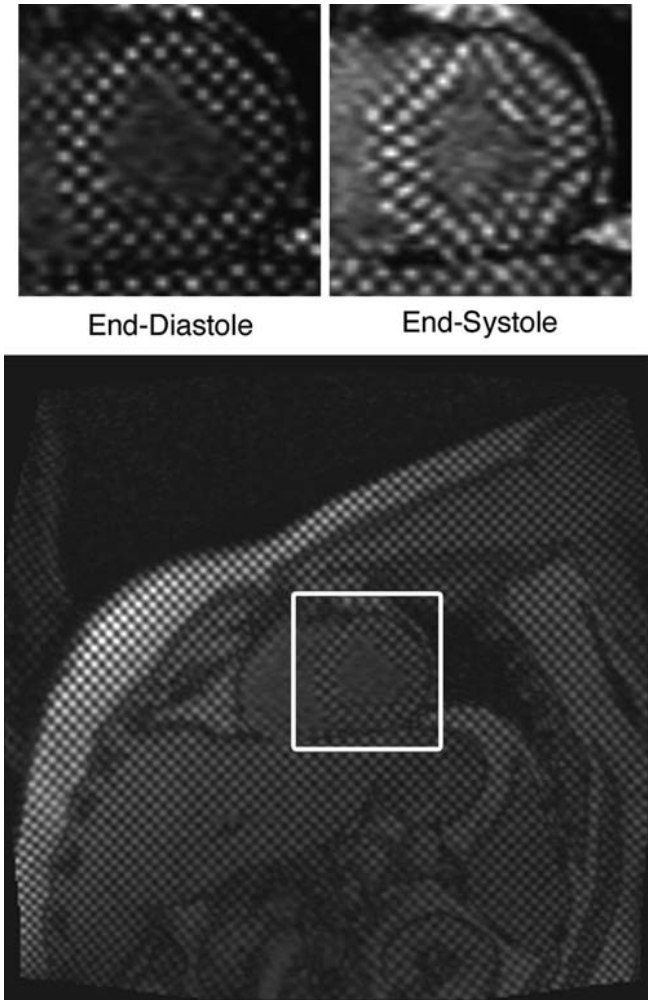

Figure 1.6 Images with spatial modulation of magnetization in the form of vertical and horizontal stripes in a human volunteer. The grid-tag lines spaced 6 mm apart were created immediately after the R-wave of the ECG. The *upper left* panel shows a magnified view of the heart during this initial phase. A second image is shown on the *upper right* for an end-systolic phase, with the distortion of the tag lines due to cardiac contraction clearly apparent. The tagging technique is equivalent to the implantation of intramyocardial markers. Tracking of the tag lines over the cardiac cycle allows determination of myocardial strains and has been shown to provide a sensitive method for assessing regional wall motion abnormalities.

Myocardial Perfusion

Myocardial blood flow is assessed using very rapid MR imaging of the heart during the first passage of an administered contrast agent through the heart. T1 changes in the myocardium are directly proportional to the contrast agent concentration in the blood or tissue [30, 31], so that through the use of T1-weighted imaging techniques, myocardial territories affected by a coronary artery lesion can be both qualitatively and quantitatively evaluated. Furthermore, the myocardial territory affected by a coronary artery lesion may or may not show a perfusion deficit under resting conditions; however, during an imposed pharmacological stress, a stenotic vessel cannot respond (dilate) like a healthy vessel resulting in ‘‘vascular steal,’’ a phenomenon in which increased blood flow to the myocardium is supplied by nonstenotic vessels [32]. Consequently, the relative blood flow is reduced through stenotic vessels resulting in a detectable perfusion deficit in the images; as such, both areas of reversible and nonreversible (scar) defects can be represented [33].

First pass perfusion imaging is typically performed using multislice fast gradient echo imaging, with saturation-recovery magnetization preparation obtained during the rapid administration (7 ml/s) of a small contrast agent dose (approximately 0.04 mmol/kg for the extracellular gadolinium agent Gd-DTPA). A saturation-recovery magnetization preparation consists of a nonslice selective 90° radio frequency pulse, followed by a gradient crusher pulse designed to dephase the transverse component of the magnetization [34]. This preparation drives the magnetization into a well-defined state, permitting the acquisition of a T1-weighted GRE signal that is independent of the

properties of any previous relaxation delay, thus preventing fluctuations in the image signal intensities due to variations in the heart rate or ECG trace. Nevertheless, imaging is typically performed throughout the duration of 40–50 heartbeats to adequately capture the first pass of the injected contrast agent through the heart. With currently employed clinical 1.5 tesla MRI scanners (with state-of-the-art gradient coils and amplifiers producing gradient field amplitudes of 20–40 mtesla/m with slew rates up to 150 mtesla/m/s), this imaging can be done in approximately three to four slices for every heartbeat, with an in-plane image resolution of 2 mm or better.

Qualitative analyses of perfusion studies can be made by viewing the sequence of images as a movie loop and visually grading the rate of contrast enhancement in myocardial segments. However, qualitative assessments are highly observer dependent and thus are also subjective to misinterpretation based on image artifacts or variations in the image brightness due to the inhomogeneous detection of theMRsignal by the surface coils. Therefore, in the future, a more quantitative technique based on the time course of signal intensity in the different myocardial segments of interest can provide an objective and robust method of analysis (Figure 1.7).

Myocardial Viability

The ability to distinguish nonviable myocardium is of critical importance in the management of patients with both acute and chronic coronary artery disease syndromes; yet, this is complicated by the presence of both reversibly damaged and infarcted myocardium. Until very recently, thallium single proton emission computed

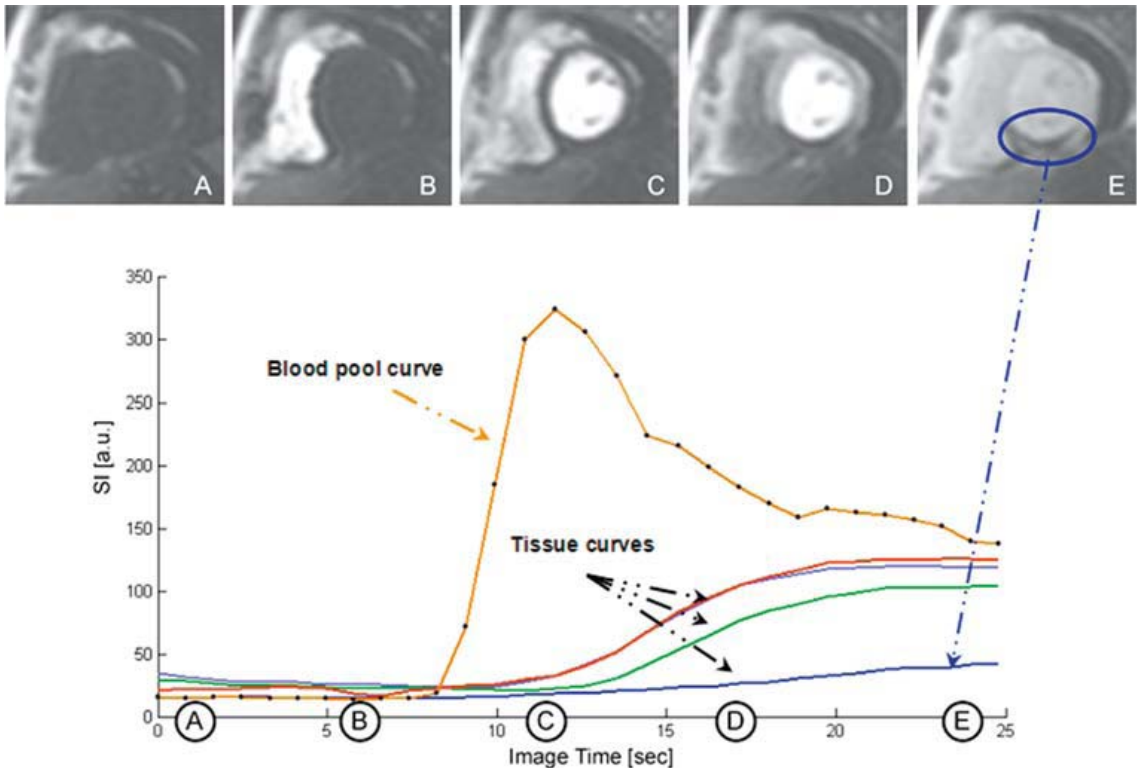

Figure 1.7 A sample of images acquired using a fast T1-weighted gradient echo sequence during a bolus injection of 0.04 mmol/kg of the extracellular contrast agent Gd-DTPA is shown, with the resulting signal intensity curves for the left ventricular blood pool and several myocardial segments below. The first image in the series (A) shows a short-axis image of the heart prior to injection of the contrast agent. Following injection, the contrast agent quickly enters the right ventricle (B) and left ventricle (C) and then passes through the coronary and microcirculation (D, E) causing signal enhancement throughout the myocardium. This example shows a clear perfusion defect in the inferior wall of the left ventricle which can be seen in images D and E (circled) and also the corresponding tissue curve immediately following the first pass of the contrast through the left ventricle.

tomography (SPECT) and positron emission tomography (PET) were the primary tools for evaluation of myocardial viability. However, with the development of delayed contrast-enhanced MRI (ce-MRI), the cardiac MRI method has quite dramatically and rapidly ascended into the forefront of viability imaging [35, 36]. In general, this technique has been shown to identify irreversibly damaged myocardium in both acute and chronic settings following a myocardial infarction and, in tandem with cine

imaging, can be used to consistently predict reversibly damaged tissue that may benefit from revascularization and/or other therapies [37, 38]. Furthermore, with the availability of substantially higher spatial resolution than nuclear techniques, ce-MRI can detail the transmural extent of irreversibly damaged tissue and detect both small and large subendocardial defects not identified by either SPECT or PET [39, 40].

So-called delayed ce-MRI is performed following the intravenous administration of a gadolinium-chelate contrast agent; typical dosages for imaging viability are on the order of 0.1–0.2 mmol/kg. The contrast agents more readily cross the cell membrane due to the severe myocardial injury and loss of viability [33, 35, 41, 42]. After an appropriate delay (approximately 10–15 min), the contrast agent achieves approximate distribution equilibrium, and loss of functional viability and subsequent leakage of contrast agent result in T1-weighted signal enhancement because the distribution volume of the contrast agent is larger in the injured tissue compared to normal. Such imaging is typically performed under resting conditions using a breath-hold ‘‘inversion recovery’’ prepared and T1-weighted segmented GRE sequence. The appropriate inversion delay time following the inversion pulse (approximately 250 ms or less) results in signal nulling of viable myocardium. Note that, for the best results, appropriate inversion delay times are iteratively chosen for each patient. This results in images where the normal viable myocardium is dark, and nonviable, fibrotic, or scarred tissue has dramatically increased (hyperenhanced) signal intensity (Figure 1.8). Typically, one or two signal averages are used with an in-plane image resolution of approximately 1.5 mm; this approach as a 2Dsequence requires multiple breath-holds to encompass the left

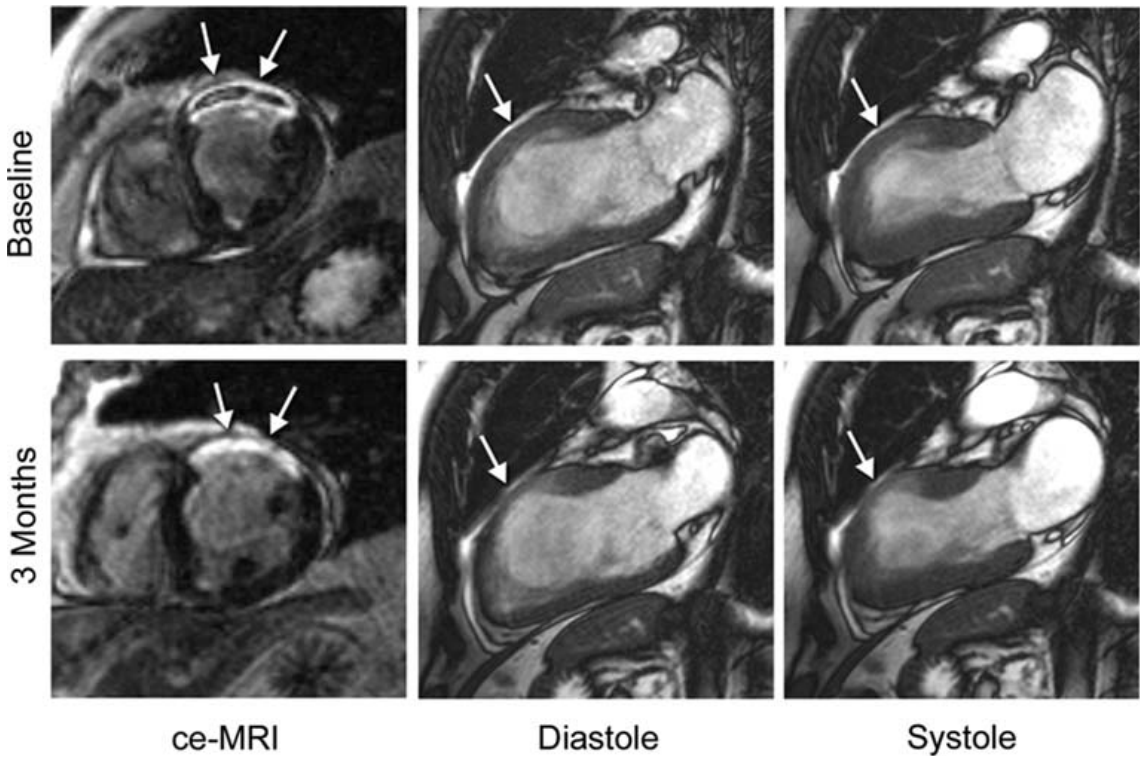

Figure 1.8 Example of an initial and follow-up MRI exam comparing the region of infarction (arrows) with wall thickness and contractility. The acute study at 2 days (top) shows evidence of microvascular obstruction within the infarct and reduced wall thickening in the anterior region, shown here by long-axis cine images. During the 3-month study (bottom), there is no longer a sign of microvascular obstruction within the infarct territory, diastolic wall thickness has decreased, and contractility has improved in regions adjacent to the infracted territory.

ventricle and can be typically accomplished in less than 10 min. In addition, 3D approaches can also be used that cover the entire ventricle in a single, yet longer, breathhold with comparable, but not as good, image quality.

While the delayed ce-MRI sequence is the most widely accepted approach for viability imaging with MRI, there are other less popular techniques that should be mentioned (e.g., imaging with the use of a manganese-based contrast agent). Manganese is a Ca^{2+} analog that is actively taken up by viable cells, thus in obtaining T1-weighted images,

viable tissue is enhanced (bright) while nonviable tissue remains dark [43]. Manganese contrast agents are not currently being used in clinical cardiac imaging; however, this may provide an effective alternative method in the near future. MRI imaging of sodium or potassium are also effective methods with potential for imaging viability, but their use remains strictly a research tool due to the very limited availability of multifrequency MRI scanners for clinical use [44].

Blood Flow Velocity

A recorded MR signal can be represented in terms of a magnitude and a phase component. As such, MRI images can be analyzed to elicit the spatial variations of the signal magnitudes, but it is also possible to create maps showing the spatial variations of the signal phases. Furthermore, it has been shown that the phase of the signal is sensitive to the velocity of tissue or blood. The so-called phase contrast MRI technique uses the phases of the signals to measure relative velocities. For an in-depth discussion of these methodologies, we refer the reader to the literature. Yet, an example of a phase contrast flow velocity measurement in an aorta is shown in Figure 1.9, which has been used to calculate pulse wave velocities for measuring vessel stiffness [45].

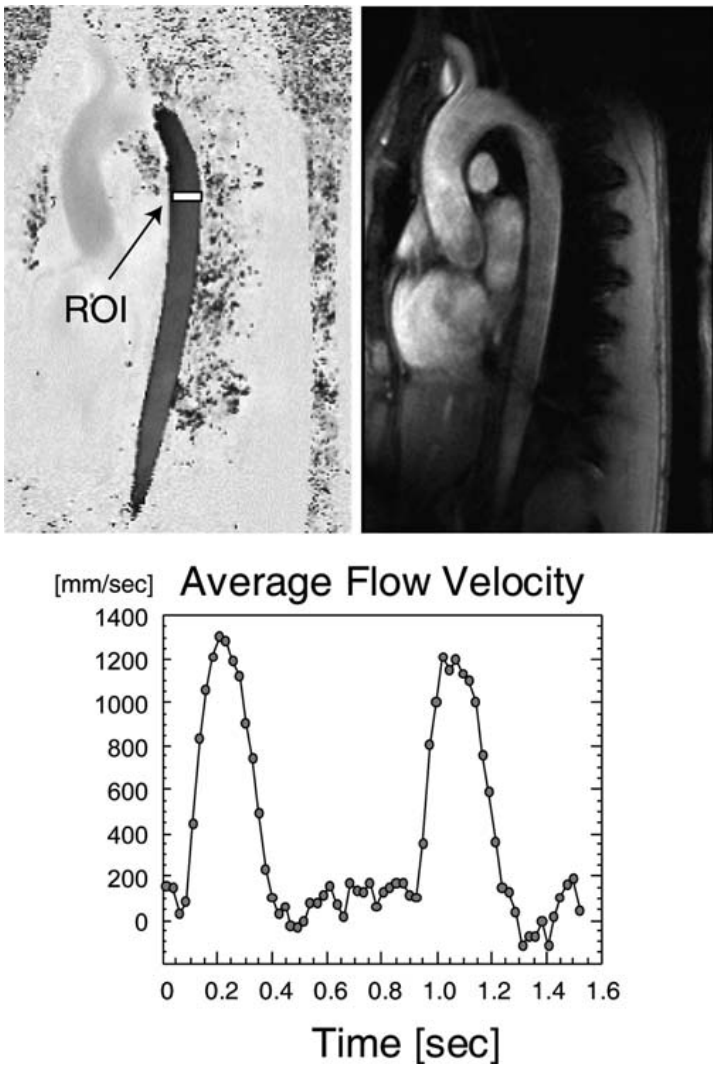

Figure 1.9 Phase contrast imaging of the aorta in a human volunteer. Both the magnitude and phase images are shown. Images were acquired for 70 cardiac phases, covering approximately 2.5 heartbeats. A region of interest (white box) was placed on the phase images in the thoracic aorta to determine the variation of flow velocity in the vertical direction of the image plane. The variation of the velocity is shown in the graph. ROI = region of interest.

Fiber Structure

Importance of Myofiber Orientation

The analysis of myocardial microstructure continues to be considered an important factor in better understanding underlying pathologies and/or associated arrhythmias.

This is due to the fact that structural fiber arrangement is modified over the time course of various cardiomyopathies. In the healthy heart, it is generally accepted that cardiac muscle fibers or myofibers are arranged as counter-wound helices encircling the ventricular cavities and where fiber orientation is a function of their transmural location [46–48]. Furthermore, myofibers are predominantly organized in the base-apex direction at the epicardial and endocardial surfaces and rotate to a circumferential direction in the midwall. This counter-wound helical structure is considered to be responsible for the torsional or wringing motion of the left ventricle that serves three main mechanical functions: (1) equalizing myofiber strain and workload; (2) optimizing the volume of blood ejected during systole (stroke volume); and (3) storing torsional energy in the intracellular and extracellular matrices and, when released, increasing ventricular filling during diastole [49–56]. Therefore, cardiac fiber orientation can also be considered as a primary determinant of ventricular pump function.

Quantifying Fiber Structure with Diffusion Tensor MRI

More recently, ‘‘diffusion tensor’’ MRI (DTMRI) has been developed and employed as a nondestructive means to quantify 3D ventricular fiber orientation [46, 57–60]. The underlying principle in determining cardiac fiber orientation by DTMRI is that the fastest direction of water diffusion corresponds to the local myofiber orientation. Therefore, by obtaining a series of diffusion-weighted images, the effective diffusion tensor of water in the myocardium can be estimated using a relationship between the measured echo attenuation in each imaging voxel and the applied diffusion-sensitizing gradient [61]. As such, diffusion-weighted pulse sequences are designed such that

molecular displacements in the direction of the applied diffusion-sensitizing gradients will attenuate the echo signal, thus enabling the estimation of water diffusivity in a given direction. The strength of the diffusion weighting or *b*-value usually ranges from 500 to 1500 s/mm^2 in cardiac DTMRI. The diffusion tensor, which is typically a symmetric 3 × 3 second rank tensor, is determined for each imaging voxel and represents the net 3D diffusion in the tissue. In order to determine the required six independent parameters of the diffusion tensor, at least seven images must be obtained for a given slice—six diffusion-weighted images applied in six noncolinear directions and one diffusion-independent image. However, it is also common today to estimate the diffusion tensor by applying multiple diffusion weightings in 12–16 directions. Nevertheless, ventricular fiber orientation can be obtained with DTMRI due to the anisotropic nature of water diffusion in the myocardium [62]. The fastest direction of diffusion or primary eigenvector of diffusion has been validated to coincide with the local longitudinal myofiber orientation, as water diffusion in the cross fiber directions is restricted by the cellular borders and laminar sheets in the myocardium [63, 64]. Note that the secondary and tertiary eigenvectors of diffusion correlate with the laminar sheet direction and sheet normal, respectively [58, 65, 66].

From a research perspective, it is also interesting to note that DTMRI can be used to obtain fiber orientation both in vivo and ex vivo [67, 68]. Currently, cardiac DTMRI is not a clinically employed cardiac MR protocol, as this imaging technique does not contribute to the diagnosis of cardiomyopathies. However, in concert with myocardial tagging, in vivo DTMRI does provide valuable insights into the myofiber structure–

function relationship in the ventricles in both normal and diseased states. In general, the spatial resolution of diffusion imaging is dependent on the diffusion-sensitizing pulse sequence and magnetic strength of the scanner. For example, for in vivo diffusion imaging of large mammalian hearts in a 1.5 tesla magnetic field, a spatial resolution of approximately $3 \times 3 \times 3$ mm^3 can be expected [69]. For ex vivo diffusion imaging with high-field MRI scanners (3–9.4 tesla), a spatial resolution less than $1 \times 1 \times 1$ mm3 can easily be obtained. An example of ex vivo DTMRI of a freshly cardiopleged and isolated human heart is shown in Figure 1.10. The raw diffusion images are shown along with the fiber orientation projected into the imaging plane as determined by the primary eigenvector of diffusion for a midventricular slice.

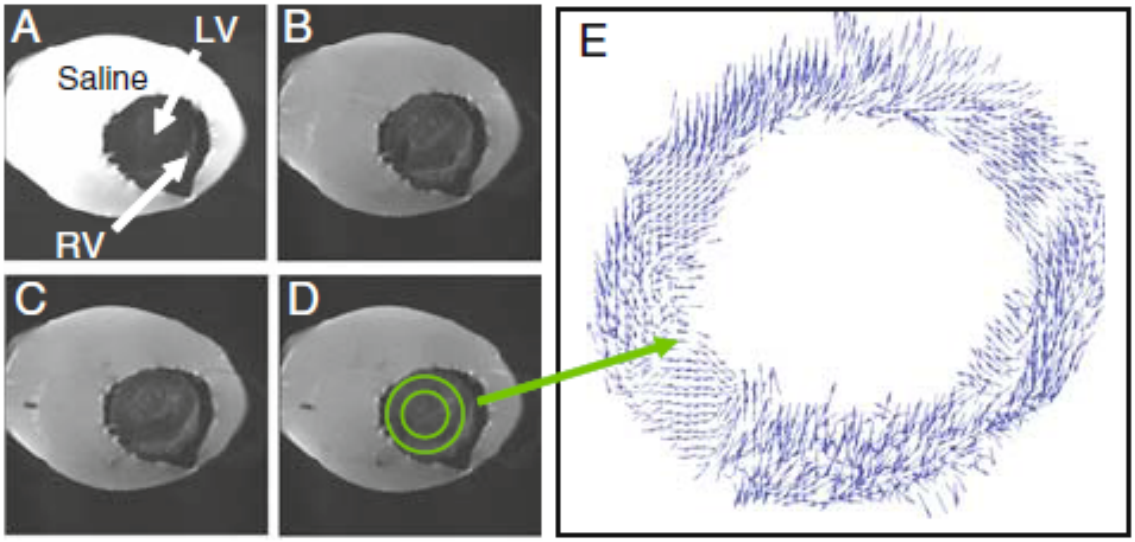

Figure 1.10 Diffusion tensor MRI of a freshly excised normal human heart. The unfixed heart was submerged in saline and all air was removed prior to imaging. For the determination of cardiac fiber orientation, six diffusion-weighted images were acquired with one nondiffusion-weighted image (A) at the midventricular level. Three diffusion-weighted images are shown (B, C, D) acquired with diffusion gradients applied in three orthogonal directions. The left ventricular fiber orientation is projected onto the imaging plane (E) as determined by the primary eigenvector of diffusion or direction of fastest diffusion. Imaging parameters were as follows: field of view = 180×180 mm^2, matrix = 196×196, in-plane spatial resolution = 0.9×0.9 mm2, *b*-value = 1000 s/mm^2; the slice thickness was 3 mm. LV= left ventricle; RV= right ventricle.

Pathological Changes in Fiber Structure

It was recently reported that by using cardiac DTMRI in conjunction with phase contrast strain-rate imaging, Tseng et al. were able to determine that a state of fiber disarray exists in hypertrophic cardiomyopathy, which results in a disordered pattern of principle myocardial shortening. In the same study, these investigators observed that a positive correlation exists between fiber disarray and myocardial hypokinesis [69]. Additionally, several studies have attempted to quantify cardiac fiber architectural remodeling after the occurrence of myocardial infarction [70, 71]. In these reports, fiber disarrays and increases in diffusivity were evident in the infarcted regions; this was considered to be consistent with abnormal wall motion and/or cell death.

MRI and Biomedical Devices

Real-Time Imaging and Cardiovascular Interventions

To date, x-ray-based fluoroscopic techniques have been the gold standard for most invasive diagnostic and/or therapeutic applications relative to the heart. However, with the advent of ultrafast MRI and the development of MRI-compatible catheters and guidewires, the goal of achieving real-time guidance by MRI for cardiovascular interventions is emerging as a new alternative [72]. More specifically, the use of MRI for guided interventions would minimize or even eliminate reliance on ionizing radiation and iodinated contrast agents, an advantage particularly for pediatric patients. To date, continuous improvements of MRI techniques and MRI scanner hardware have rendered it feasible to achieve the relative clinical fluoroscopic image rates of 5–15 images/s [73]. Thus, it is considered highly probable to use MRI for guiding

interventional cardiovascular procedures, such as coronary catheterization [74] and cell or gene therapy delivery [15], with close to real-time image refresh rates. Initial interventional studies with MRI guidance have demonstrated the advantages of MRI, including (1) the ability to image arbitrarily oriented cross-sections; (2) interactive steering of the image plane; and (3) excellent soft tissue contrast for the detection and visualization of lesions [75].

Several other technical advances have also been considered as crucial for advancing the possibility of performing interventional procedures under MRI guidance, including (1) development of 1.5 tesla magnets with short bores that allow access to the groin area for catheter based procedures; (2) LCD monitors that can be exposed to high magnetic fields to allow the operator to perform an intervention and control MRI scan parameters from a position right next to the magnet; and (3) development of catheter-based MRI antennae for localized intravascular signal reception and high-resolution imaging [76].

For MRI-guided cardiac interventions, one of the basic requirements is to visualize and track the catheters and devices used in the therapies while they are manipulated through the heart and vascular spaces [77]. In general, catheter-tracking techniques can be divided into two categories—active and passive. Active tracking of catheters and devices requires the instrument to receive or send a signal in order to identify its relative location. For example, a receiving coil can be incorporated into the device and thus connected to the scanner such that the position can be located based on the frequency of the received signal from the body coil. Passive tracking of catheters involves creating a

signal void without interfering with the image quality of the tissue being imaged. This latter method can be achieved through the choices of materials incorporated into the catheter or device. For example, small amounts of titanium, gold, or copper can be deposited into the catheter tip in order to introduce a susceptibility artifact such that the tip of the catheter can be continuously tracked.

A recent development in the emerging field of MRI guided cardiac interventions is the real-time delivery of transcatheter valves. Recently, McVeigh et al. demonstrated that a transcatheter bioprosthetic aortic valve could be delivered via a direct approach through the left ventricular apex in approximately 90 s with real-time interactive MRI guidance [78]. Importantly, immediately after the procedure, myocardial perfusion, blood flow through the valve, and ventricular function were assessed with MRI in order to verify proper placement of the valve. It is considered that this minimally invasive MRI-guided aortic valve replacement technique may prove to be a less morbid approach than conventional valve replacement surgeries, and thus may have added benefits for the very ill and/or elderly patient population.

To date, other reported MRI-guided cardiac interventions and applications include (1) diagnostic cardiac catheterization; (2) electrophysiological recording/radio frequency ablation; (3) balloon dilation and stent placement; and (4) atrial septal defect closure [77]. For an in-depth discussion of the advantages and difficulties associated with these MRI-guided cardiac interventions, we refer the reader to the growing body of related literature.

MRI Safety and Compatibility

Most currently used implantable devices contain metallic parts that would likely both seriously interfere with MR cardiac imaging and/or pose potential safety risks for the patient. More specifically, implanted devices with ferromagnetic parts are considered a strict contraindication for cardiac MRI because of the potential associated hazards due to magnetic-induced movement, dislodgement, and/or heating effects. Although cardiac pacemakers are implanted in large numbers of patients, to date, there is no consensus whether or not pacemakers are MRI compatible or MRI safe. For example, the considered risks involved in scanning a patient with an implanted pacemaker include lead tip heating, which may damage the tissue resulting in a failure of the pacing pulse to capture the targeted tissue, and/or damage to the electrical circuitry inside the pacemaker. These risks, in turn, are also dependent on many variables including (1) relative lead position; (2) pacemaker position; (3) manufacturer of the pacemaker; and/or (4) area of the body scanned. Despite these risks, it should be noted that case studies have been published in which patients with a cardiac pacemaker were scanned and no complications were observed [79]. In another example, Roka et al. used a 1.5 tesla MRI system to assist in finding the optimal left ventricular pacing site in a patient, based on myocardial viability during an upgrade to a biventricular pacing system [80]; they reported no malfunction in the pacemaker or changes in the relative pacing thresholds.

‘‘MRI compatibility’’ can be quite simply defined as the property of a device not to interfere with imaging, e.g., by causing distortions of the magnetic field that cause

signal loss. Note that a device may be MR compatible, but that does not necessarily mean it is ‘‘MR safe.’’ The latter requires that the exposure to a strong static magnetic field, pulsing of the magnetic field gradients, and applications of radio frequency pulses do not cause any adverse effects to the patient. For example, the pulsing of the magnetic field gradients produces a changing magnetic flux that can induce current flow in lead wires which, in turn, may lead to tissue heating, and thus cell damage or death. Furthermore, the presence of metallic parts can also cause an inhomogeneous deposition of radio frequency power in the vicinity of the device, which could lead to broader radio frequency heating of tissue or blood. Therefore, to date, implanted cardiac pacemakers are a contraindication not only for MRI cardiac exams, but for MRI exams in general. It is noteworthy that one group of investigators reported that MRI imaging caused temperature elevations at pacing lead tips as high as 23.5°C at 0.5 tesla and 63.1°C at 1.5 tesla [81, 82]. As such, there has been some progress in the development of MRI safe cardiac pacemakers. Recently, one medical device manufacturer released an MRI safe pacing system for sale in Europe, and is seeking FDA approval for release in the United States (EnRhythm® MRI SureScan™ pacemaker and CapSureFix® MRI SureScan™ pacing leads, Medtronic, Inc., Minneapolis,MN). We can expect other medical device manufacturers to follow suit in the development of such devices in the future.

It is foreseen that a new set of MRI safety concerns may arise when such imaging is performed using intravascular coils [83, 84]. Such intravascular coils may, for example, be used to examine vulnerable plaque on vessel walls; localized heating in the vicinity

of the coil could disrupt the plaque, thus causing catastrophic consequences. Note that heating strongly depends on the wavelength (MRI frequency), geometry of the body and the device, and placement of the body and device with respect to each other and within the MR system. On the other hand, one could also foresee potentially using this heating phenomenon to induce therapy itself (e.g., tumor ablation to lesion formation). For further information on MRI compatible and MRI-safe biomedical devices and additional contraindications for cardiac MRI exams, we refer the reader to the growing body of literature on this topic.

Assessment of Biomedical Device Performance

Cardiac MRI also provides a unique opportunity to test, in vivo, the performance of implanted devices such as prosthetic heart valves and heart pacing devices (those that would be considered both MRI compatible and safe). For example, in patients with artificial aortic valves, the flow downstream from the implanted valve may be severely altered. These changes have been associated with an increased risk of thrombus formation and mechanical hemolysis. Therefore, the capabilities of MRI velocity mapping would be considered very useful for the noninvasive evaluation of the flow profiles in such patients with a mechanical valve prosthesis [85, 86]. For example, in one report, Botnar et al. found that peak flow velocity in the aorta was significantly higher in patients with valvular prosthesis than in normal patients [87]. In that same study, the investigators also reported that diastolic mean flow was negative in patients after valve replacement, but not in controls. Furthermore, in instances where real-time MRI is used to guide the placement of a stented artificial valve, an assessment of the

flow profile can be obtained immediately to determine the relative success of the implant procedure.

Interestingly, the usefulness of MRI for assessing the function of cardiac pacing devices has already been proven in experimental animal studies [88], although currently there exist hurdles for performing cardiac MRI on patients with such devices. For example, in our laboratory, we have quantified pacing-induced left ventricular dyssynchrony in swine paced from the right ventricular apex, a standard pacing lead implant site, using MR tissue tagging. Figure 1.11 demonstrates that right ventricular apex pacing alters the mechanical activation pattern of the left ventricle, resulting in circumferential stretch in the lateral and posterior walls and regional variations in circumferential shortening in end-systole.

Quantitative Analysis of Cardiac MR

It is important to note that post-processing of cardiac MRI studies represents the stage at which the full potential of the cardiac MRI examination may be best realized. Post-processing is comprised of two major steps: image post-processing and data post processing. The first step largely involves segmentation algorithms to delineate and extract features and structures of interest from the collected images. The second step consists mainly of applying mathematical and statistical methods to aid in a given diagnosis.

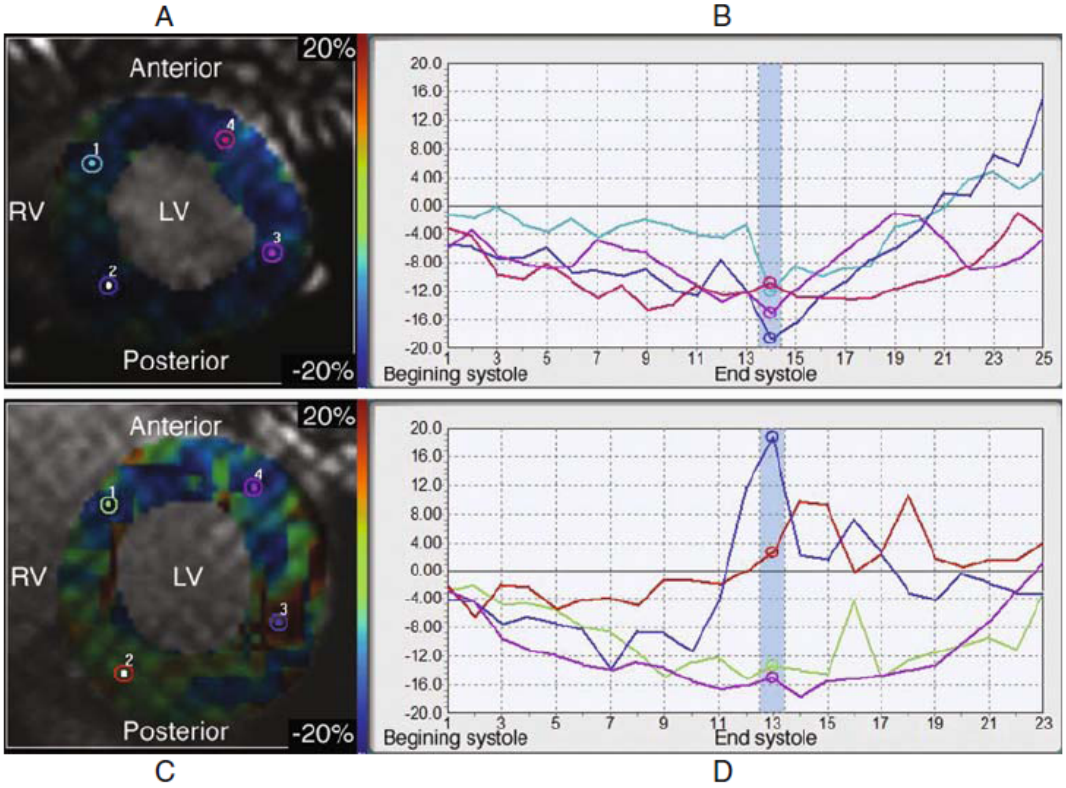

Figure 1.11 Circumferential strain quantified by MR tissue tagging in a normal porcine heart (A, B) and after 6 weeks of cardiac pacing from the right ventricular apex in the same heart (C, D). Graphs (B) and (D) plot the circumferential strain values throughout the cardiac cycle prior to pacing and after 6 weeks of pacing at the specified probe locations in (A) and (C), respectively. Pacing from the right ventricular apex caused regional disarray in cardiac strain in the left ventricle at end-systole (C) and throughout the cardiac cycle (D), in comparison to the same heart 6 weeks prior to the onset of pacing (A, B). Right ventricular apex pacing induces left ventricular dyssynchrony and results in poor left ventricular pump function. LV=left ventricle; RV = right ventricle.

For many cardiac investigative protocols, the myocardium is the area of interest for analysis, so one needs to segment the myocardium from the rest of the image to extract further information, e.g., utilize contrast enhancement in a perfusion study or monitor systolic thickening of the wall for a MR cine study.

Ventricular Function

Quantitative analyses of relative ventricular function are also based on the segmentation of the myocardium. In general, this is achieved by drawing contours on the endocardial and epicardial borders of the myocardium (Figure 1.12). In general, the ventricular volumes of interest are the end-diastolic and end-systolic volumes, as well as derived parameters such as the stroke volume and ejection fraction. Although ventricular volumes have been computed from differently orientated views of the heart, analyses of the short-axis views are most widely used in cardiac MRI due to their proven accuracy [89–92]. In the simplest case, myocardial segmentation is performed only for the images corresponding to the end-diastolic and end-systolic phases. The end-diastolic phase is defined as the phase containing the largest blood pool area in the left ventricle, whereas the end-systolic phase is identified as the image containing the smallest blood pool area (Figure 1.13).

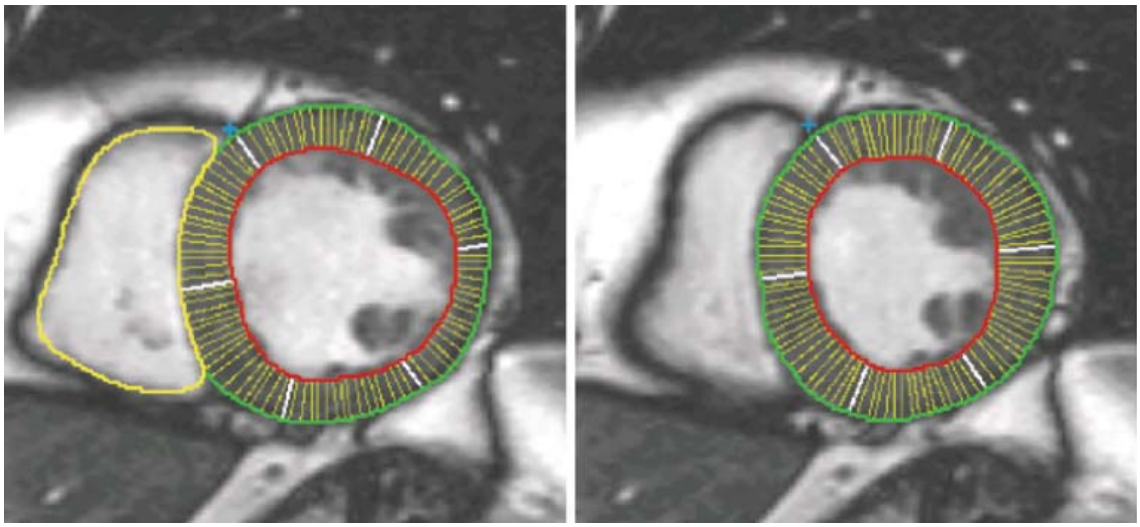

Figure 1.12 Example of myocardial segmentation for two images corresponding to the end-diastolic (*left*) and end-systolic (*right*) phases in a patient with poor cardiac function. Contours are drawn around the blood pool demarking the endocardium and the epicardium. A contour is also drawn around the right ventricular blood pool. For this particular patient, the cross-section of ventricular cavity with the short-axis view changed significantly less than in a healthy normal. Also shown are chords connecting the endocardial and epicardial borders. The chords are orthogonal to a centerline between the two contours. The chords measure the true thickness of the myocardium as opposed to radial chords that emanate from the center of the left ventricle.

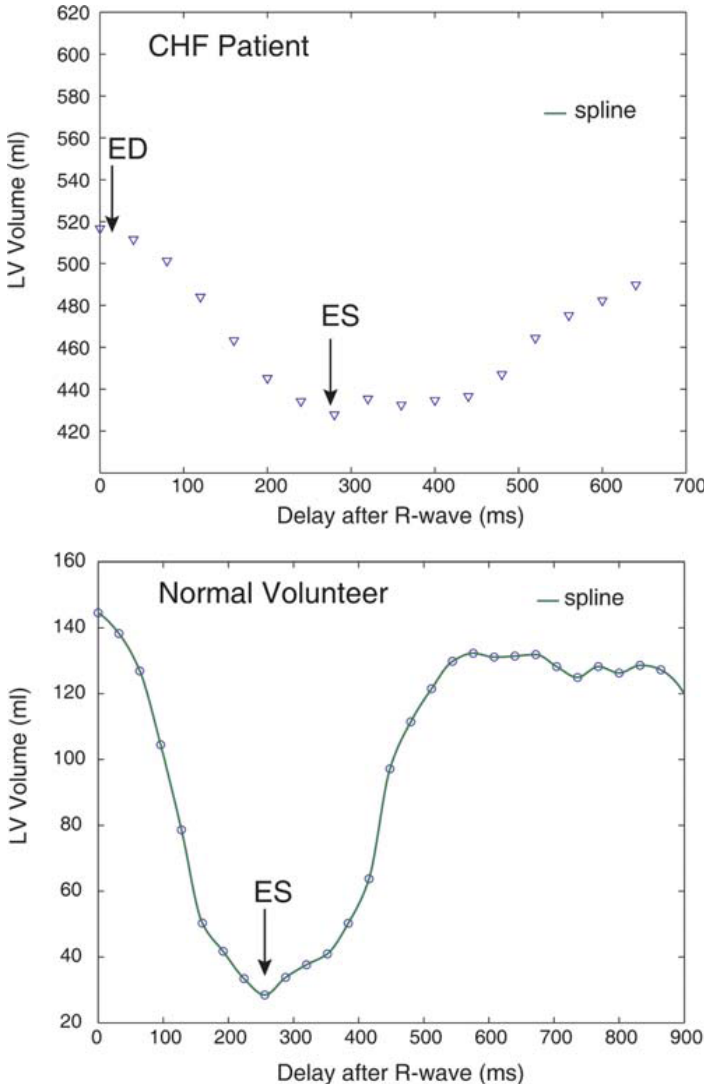

Figure 1.13 Volume–time graph with the end-diastolic (ED) and end-systolic (ES) phases. The upper graph shows the variation of left ventricular (LV) volume over the cardiac cycle for a patient with congestive heart failure (CHF), and the lower graph is the same type of graph for a healthy volunteer. The CHF patient had an enlarged ventricle (i.e., large volume) and a very low ejection fraction. Because of the low ejection fraction, the curve in the CHF patient is relatively flat. Ventricular volumes were calculated by Simpson's rule from a set of short-axis images. The endocardial border had been traced on each cine frame to obtain a complete left ventricular volume versus time curve.

Once the end-diastolic and end-systolic phases are fixed, the contours are drawn in the images for the end-diastolic and end-systolic phases for all slices containing left ventricle. In images for a basal slice of the left ventricle, parts of the aorta and aortic valve may be visible. It should be noted that inclusion of contours above the mitral valve plane will significantly overestimate the values for myocardial mass and ventricular volume. Thus, the careful inclusion or exclusion of slices near the base of the heart for determination of the volumes at end-diastole and end-systole is of considerable importance for an accurate determination of the relative ventricular volumes. Once all contours are drawn and verified, the ventricular volume can be computed by simple slice summation using Simpson's rule with the slice thickness as the increment.

Recently, Young and colleagues [92] proposed an optimization method for speeding up the process of contour drawing by placing guide points on the endocardial and epicardial borders, instead of drawing continuous contours for both borders. The algorithm then automatically detects the myocardial borders by interpolation between the guide points. This user-friendly method reduces the burden of generating contours compared to the conventional tracing of the contours. Subsequently, Swingen et al. [93] modified the guide point technique by including feedback from continuously updated 3D models of the heart, to evaluate both the placement of guide points and the accuracy of the computed volumes. They showed that the combined use of short- and long-axis views results in more accurate estimates of the ventricular volumes and myocardial mass, compared to exclusive reliance on short-axis views [94] (Figure 1.14).

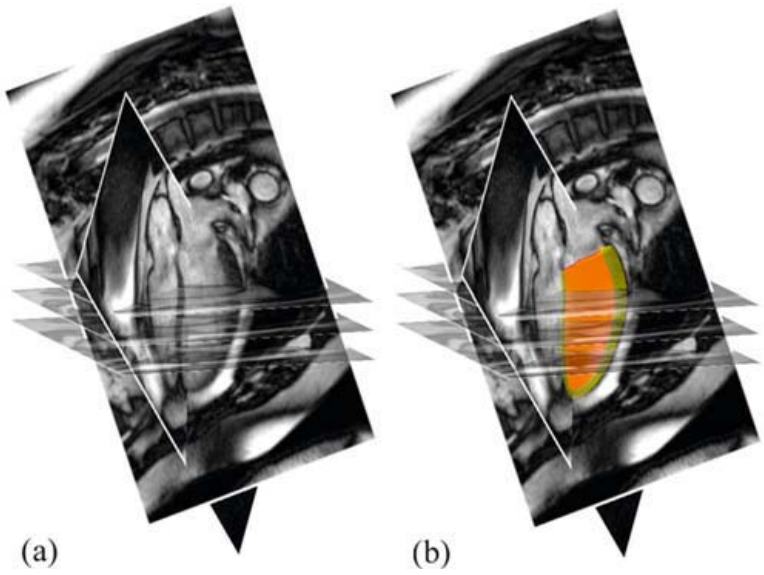

Figure 1.14 A typical set of TrueFISP slices using a 3D analysis protocol (a) with co-registered long- and short-axis images (three of six short-axis images shown for clarity). Image set with 3D model of the left ventricle (b).

Common parameters of interest for volumetric analyses are as follows:

- Left ventricular mass: The myocardial mass is obtained by multiplying the myocardial volume by the myocardial specific gravity (1.05). Myocardial volume is calculated as the difference between the epicardial and endocardial volumes. The normal mean for left ventricular mass is 92±16 g/m^2 of body surface area.
- Stroke volume: The stroke volume is calculated as the difference between end-diastolic and end-systolic blood or chamber volumes, and it represents the volume of blood ejected by a ventricle per heartbeat (in the absence of aortic regurgitation). Unless shunts and valvular regurgitation are present, the calculated stroke volumes of the two ventricles should be nearly equal. This is a rule of thumb for verification of the volume computation.

- Ejection fraction: This is the ratio of the ventricular stroke volume to the end-diastolic volume. The normal range is between 55 and 65%. An ejection fraction of less than 40% is considered to indicate impaired ventricular function.
- Cardiac output: This is the product of stroke volume and heart rate. It is a measure of the volume of blood ejected by the heart per beat. For an average adult, cardiac output is 4–8 l/min. Cardiac output is often corrected by normalization with respect to the body surface area.

Analysis of Wall Motion and Regional Myocardial Strain

Analysis of Relative Wall Motion

MRI wall motion analyses are typically performed to measure the changes in thickness of the left ventricular wall, from diastole to systole [95–100]. Wall motion abnormalities are commonly associated with many cardiac diseases, including dilated cardiomyopathy, end-stage valvular disease, and ischemic heart disease.

The assessment of relative myocardial wall thickness, thickening, and wall motion abnormalities proceeds from the MRI segmentation along the endocardial and epicardial borders. For example, a centerline can be drawn between the myocardial contours [101]; approximately 100 chords are then drawn orthogonal to the centerline at equal intervals to intersect the two myocardial contours (Figure 1.12). With the centerline technique, the chords are optimally placed to measure the exact thickness of the transmural myocardium [101].

Parameters of interest for wall motion analyses include the following:

- Myocardial thickness: The lengths of the orthogonal chords, from the endocardial to the epicardial borders, measuring myocardial thicknesses.
- Myocardial thickening: Differences in end-diastolic and end-systolic thicknesses, as a percentage of end-diastolic thickness; these are measures of relative wall thickening and can be considered as the radial component of myocardial strain.

Analysis of Regional Myocardial Strain with Tagged MR Images

Although the time-consuming analyses of tagged MR images have been limiting factors for the widespread quantitative analyses of myocardial strains, a recently developed ‘‘harmonic phase’’ (HARP) MR technique permits fast and accurate analyses of strains from MRI tagging protocols [102–104]. The resultant analyses based on this technique are very fast, accurate, and observer independent since the myocardial strains are computed from information contained in the images, not the manual operator task of tracking the tagline intersections [105]. Figure 1.15 demonstrates a typical analysis of cardiac circumferential strain in three phases of the cardiac cycle using the HARP technique from data obtained from a human volunteer (HARP, Diagnosoft, Inc., Palo Alto, CA). The circumferential strain values peak at _20% in the midwall where myofibers are predominately oriented in the plane of the cardiac short axis, consistent with the maximal amount of shortening permissible in a cardiac myocyte.

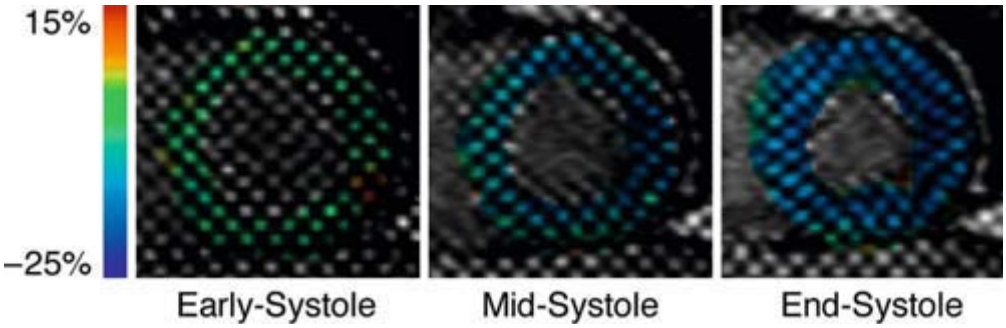

Figure 1.15 Analysis of cardiac circumferential strain in a human volunteer for three phases of the cardiac cycle using the HARP technique for MR tissue tagging analysis (HARP, Diagnosoft, Inc., Palo Alto, CA). Circumferential strain in the images is indicated by the color palette. The grid-tag spacing used in this analysis was 6 mm.

Perfusion Analysis

‘‘Myocardial perfusion’’ is a measure of blood flow (e.g., ml/min) per unit mass of myocardial tissue. Myocardial perfusion should ideally match the demand for oxygen in the myocardium. Commonly, perfusion is assessed at both rest and during stress to evaluate the capacity of the coronary circulation to increase blood flow above its baseline level, and thus match increases in oxygen demand. A ratio of the perfusion parameters, measured at stress and divided by the value for rest, will give a so-called perfusion reserve. In healthy individuals, myocardial blood flow increases approximately three- to fourfold above its baseline level with maximal vasodilation; with disease, the perfusion reserve decreases, and a flow reserve on the order of 2.5:1 is often used as the cutoff for deciding whether or not cardiovascular disease is present.

The analysis of myocardial perfusion can be carried to different levels of study, depending on the diagnostic needs and clinical resources available. One type of qualitative analysis associated with nuclear imaging is performed by visual comparison

of the peak contrast enhancement in different myocardial segments during the first pass of the contrast medium through the left ventricle. The images are often viewed for this purpose in cine mode; delays in contrast enhancement and/or a reduced peak contrast enhancement relative to other myocardial sectors are then interpreted as signatures of locally reduced myocardial blood flow. However, to do so accurately, the absence of image artifacts is important if the analysis is purely qualitative and visual; if so, then no image post-processing is necessary. Nevertheless, a qualitative analysis does have limited capability to detect global reductions of myocardial perfusion, especially in patients with multiple vessel coronary artery disease.

A quantitative analysis of MRI perfusion studies commonly starts with image segmentation, similar to the procedure used for the analysis of cine studies. First, a technician typically segments one image with good contrast enhancement along the endocardial and epicardial borders of the left ventricle. These contours are then either copied to the remaining images in the data set or an automated algorithm is employed to identify the borders of the myocardium and this self-adjusts the contour positions. The latter approach is extremely useful (or even essential), as the number of images in a perfusion data set can be very large compared to a cine data set. In other words, the task of simply copying the contours to all other images would require extensive manual editing of the contour by the user. Unlike cine images, the myocardial boundaries can be slightly blurred in perfusion images due to the reduced spatial resolution and cardiac motion. Segmentation of myocardial perfusion images is therefore considered typically more challenging than for cine MR studies.

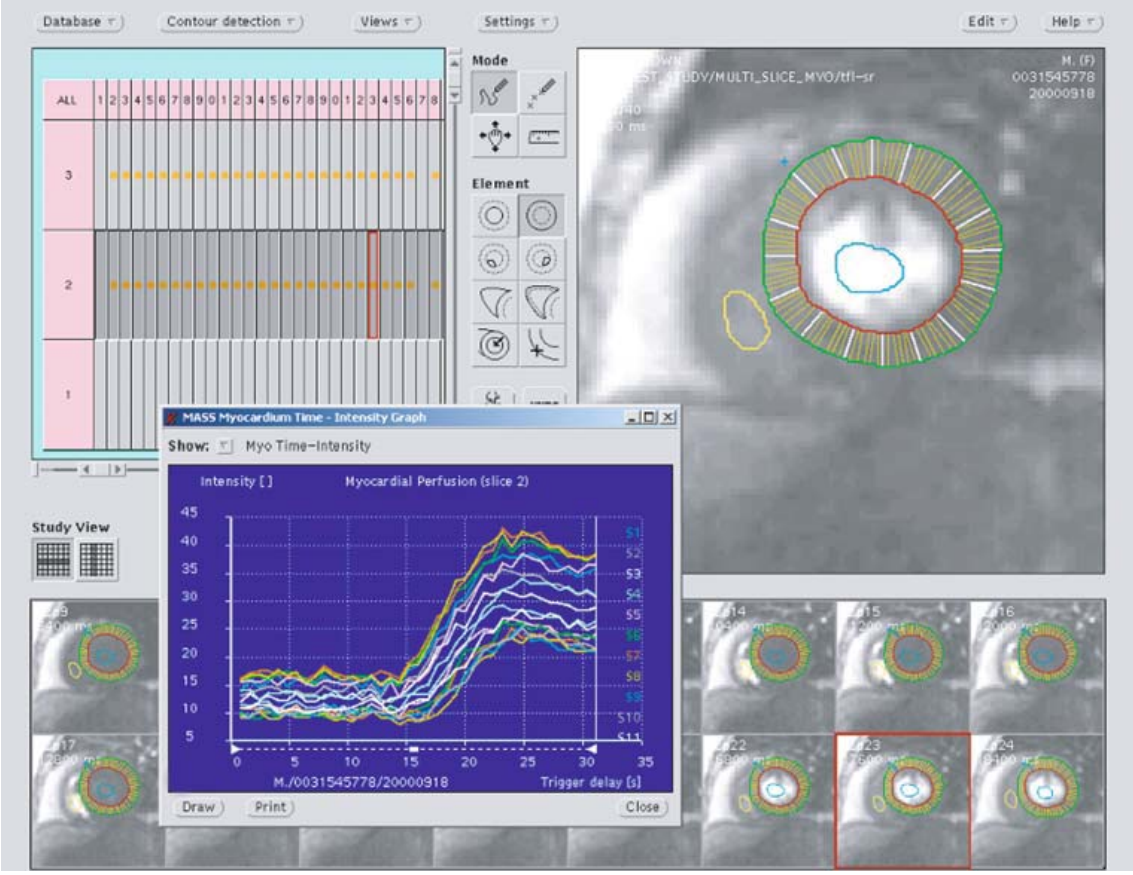

Figure 1.16 Example of a typical graphical user interface software for analysis of perfusion studies. Segmentation contours are drawn by the user to define the endocardial and epicardial borders. Similar to the approach used for cine analysis, the analysis is carried out on a sector basis; in this case, 16 sectors have been defined. The drawn contours can be copied to other images for the same slice position in the perfusion study. After adjustment of the contours in each image, the software calculated the mean signal intensity in each myocardial sector. As a result, one can obtain graphs depicting the change in signal intensity in each myocardial sector as a function of image number or time (see inset panel).

Once the myocardium is extracted by image segmentation, it is divided into smaller segments or sectors similar to those defined in cine wall motion analyses and corresponding to the individual coronary supplied territories [106]. The signal intensity averages can be plotted versus the image number, or versus the time from the beginning of the perfusion scan. Various parameters that will characterize the contrast enhancement kinetics are computed from these signal intensity curves for assessing

perfusion (see below). A typical interface with the software tool that can be used for analysis of MR perfusion studies is shown in Figure 1.16.

As the perfusion images are acquired quite rapidly (<250 ms per image), there is often significant noise in the embedded images. Thus, to extract perfusion parameters, it is useful to perform some curve fitting to smooth out these signal intensity curves. One widely used method for this purpose is the gamma variate function [107], which approximates the first pass portion of the measured curves quite well. A gamma variate curve fitted to a signal intensity curve obtained from an MR perfusion study in a patient study is shown in Figure 1.17. Nevertheless, there are certain constraints for the gamma variate analyses, e.g., it is best optimized only when the first pass portion of the curve is used (from the foot to the peak of the curve). To date, a number of parameters have been proposed for a semi-quantitative assessment of perfusion. Commonly used parameters are as follows:

- Percent peak enhancement: The peak signal normalized by the derived average baseline signal, i.e., signal before arrival of contrast agent expressed as a percentage.
- Upslope: The slope of the first pass segment primarily from the start of appearance of the contrast (foot) in the myocardium to the peak.
- Time to peak: The time from the foot to the peak of the curve.
- Mean transit time: The average time required for a unit volume of blood to transit through the region of interest. It can be determined as the ratio of blood

volume in the region of interest to the blood flow through the region of interest. This value can be estimated from the gamma variate fit to the tissue curve.

- Dynamic distribution volume: The area under the signal intensity curve, often normalized by the area under the corresponding curve for the left ventricle.

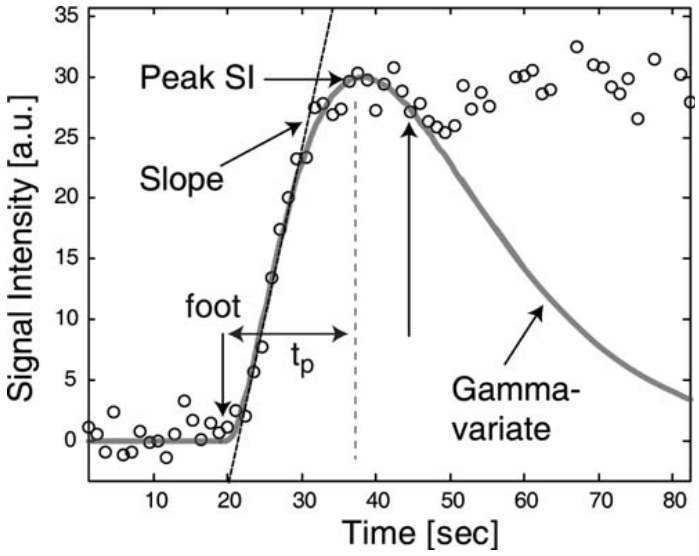

Figure 1.17 Signal intensity curve for a myocardial sector in the lateral wall. Each of the data points (round circles) represents the mean signal intensity measured in the images for the user-defined myocardial sector. The images were acquired with a fast T1 weighted gradient echo sequence during injection of a 0.075 mmol/kg bolus of Gd DTPA, an extracellular MR contrast agent. The gamma variate function can only be used to fit the portion of the tissue curve corresponding to the first pass of the contrast agent. The gray curve represents the best fit of gamma variate function to be part of the experimental data, covering the range indicated by the vertical arrows. The gamma variate fit was extrapolated to the end of the measurement range. In many cases, the end of the first pass and the appearance of the recirculation component can be best ascertained from the signal intensity changes observed in the left ventricular blood pool. Also shown are semi-quantitative perfusion parameters such as the slope, peak signal intensity, and the time from the foot to the peak (t_p).

More recently, the upslope parameter is increasingly becoming the most widely used parameter for a semi-quantitative evaluation of myocardial perfusion. The up-slopes of the tissue curves are generally normalized by the upslope of the signal intensity curves for a region of interest in the center of the left ventricle, with the latter being considered

as an arterial input in such analyses. The ratio defined as the normalized up-slopes of the tissue curve measured for maximal vasodilation divided by the corresponding upslope value at rest has been proposed as a perfusion reserve index [108–111]. Yet, the perfusion reserve derived from the up-slopes generally underestimates the actual ratio of blood flows for maximal vasodilation and rest by approximately 40% [112].

Our research group has shown that accurate myocardial blood flow estimates can be obtained by MRI methodologies, in comparison to invasive studies employing radioisotope labeled microspheres [113–116]; note that the latter are acknowledged as gold standards for the measurement of blood flow in tissues. MRI perfusion imaging may therefore play a pivotal future role in assessing novel therapeutic approaches for treating coronary artery disease, and automated quantitative analyses of MR perfusion measurements would play an essential role in this task.

Myocardial Scar Size

Myocardial infarct scar sizing and the identification of dysfunctional but potentially viable myocardium are the major prognostic indicators for the recovery of function after a myocardial infarction and have important clinical implications [117–120]. As such, myocardial infarct size measured using delayed ce-MRI has been shown to correlate well with histological measurements both in the acute and chronic settings [35, 121]. Furthermore, ce-MRI offers distinct advantages over other imaging modalities that either rely on the functional recovery of wall motion abnormalities to identify viability [17] or are not able to accurately depict smaller subendocardial infarctions [40].

Because of these advantages, ce-MRI is increasingly being used to quantify scar size in the acute and chronic setting and to predict the recovery of regional myocardial function using measurements of the segmental ‘‘transmural extent of infarction’’ (TEI) [37, 38, 122, 123]. Importantly, the exact measurement of infarct size with ce-MRI is of particular interest because both early revascularization and lytic therapy have been shown to lead to a reduced incidence of transmural infarctions, and also myocardial infarcts tend to be patchy [124, 125].

For the ce-MRI images, pixels containing nonviable myocardium have a signal intensity statistically greater (hyperenhanced) than a baseline sample from a remote normal region. Typically, hyperenhanced pixels have been classified as those with signal intensities greater than the mean + (2–6) standard deviations of a remote normal region [126, 127]. This threshold, whether manually or statistically defined, is highly subjective and highly dependent on the image quality and the noise present. Regions of signal hypoenhancement, associated with microvascular obstruction [33, 122] in the acute infarct case, are typically manually segmented and included as scar. The TEI can also be computed for each segment as the ratio (%) of scar to nonscar pixels (Figure 1.18). Overall scar size is computed by summing the myocardial scar volume in each slice throughout the heart. Finally, infarct extent can be calculated as the scar volume divided by the myocardial volume.

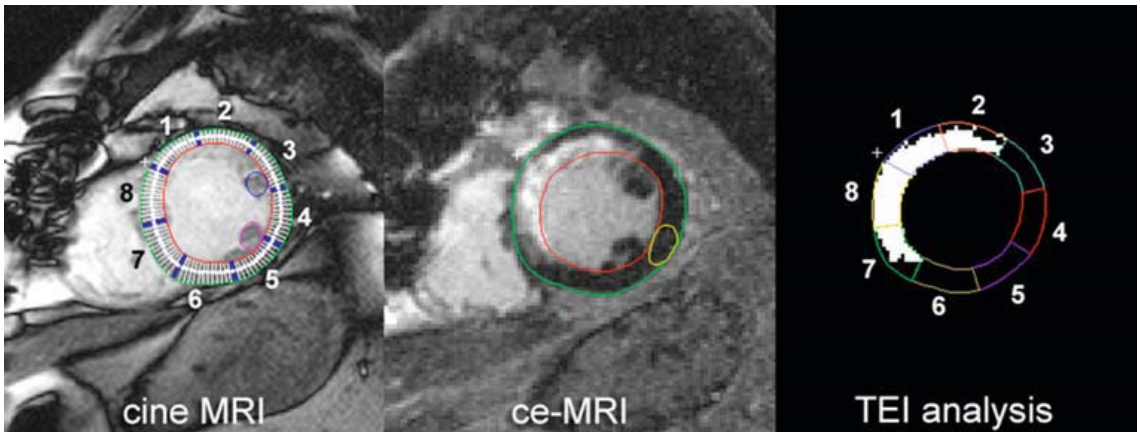

Figure 1.18 Relative correspondence between the cine (left) image showing the 100 chords calculated using the centerline method (grouped into eight segments per slice) and contrast-enhanced MRI (ce-MRI) (middle) showing hyperenhanced scar region with the transmural extent of infarction (TEI) calculated in the eight segments (right).

Conclusions

For the biomedical engineer, cardiac MRI represents an opportunity to study the function of the heart and use these insights to design better biomedical devices. Due to the increasing relevance of cardiac MRI in the clinical arena, it will become even more important to address the challenges inherent in the use of cardiac MRI in patients with implanted devices. It should be noted that numerous topics such as MR coronary angiography and plaque imaging, although of great interest, have been left out of this overview of cardiac MRI.

Chapter 2: Cardiac Fiber Orientation Assessed Using DTMRI: A Review of Current Methodologies and Potential Uses in Cardiac Research[†]

[†] Authors: Michael D. Eggen, MS[1,2], Cory M. Swingen, PhD[3], Paul A. Iaizzo, PhD[2,4] Department of Biomedical Engineering[1], Department of Surgery[2], Department of Medicine[3],Department of Integrative Biology and Physiology [4], University of Minnesota, Minneapolis, Minnesota, 55455

Preface

The beginning of this chapter provides a literature review on the structure of the myocardium and the measurement techniques used to quantify cardiac fiber orientation. Furthermore, the importance of the helical structure of the myocardium is discussed. In the latter half of this chapter, the concepts of diffusion tensor magnetic resonance image are described in detail and a description of the computational tools and methods developed to measure fiber orientation for this thesis work are presented. Lastly, the potential uses for cardiac DTMRI are presented in the context of studying heart failure.

Introduction

There are two primary methods that investigators have used to quantitatively study cardiac fiber architecture and orientation: microscopy and diffusion tensor magnetic resonance imaging (DTMRI). Microscopy methods such as light microscopy of stained myocardium and scanning electron microscopy (SEM) can provide static structural details at the cellular and sub-cellular levels (i.e. location of myocyte nuclei, visualization of intercollated discs between cells, myocyte branching, architecture of collagen, etc.). Although DTMRI cannot probe details at the sub-cellular level, it has been successfully utilized as a non-invasive imaging modality to probe tissue microstructure at different levels of hierarchical organization. Specifically, DTMRI has been validated to provide microstructural details as to fiber orientation in both skeletal muscle and the cardiac myocardium, and also the lamina orientation within the heart [1, 2]. Although light microscopy, SEM, and DTMRI methods all have been used to accurately depict myocardial architecture, DTMRI imaging is preferred to probe local fiber and laminar structural organization, as it is less time consuming per sample area studied (hours compared to months) and is free of dissection artifacts.

Microscopic Study of Cardiac Myofiber Organization

Morphological studies of ventricular myocardium utilizing hematoxylin and eosin (H&E) stained myocardium have revealed that cardiac muscle fibers or myofibers are arranged as counter-wound helices encircling the ventricular cavities where fiber orientation is a function of their transmural location [3-5]. Furthermore, myocardial fibers are predominantly organized in the base-apex direction at the epicardial and

endocardial surfaces and rotate to a circumferential direction in the midwall. This counter wound helical structure is responsible for the twisting motion of the ventricle during contraction [6].

At a lower architectural level, there is a syncytium of myocytes organized into branching laminae (sheets) which are approximately four cells thick and stack roughly from apex to base [4]. A sectioned heart is shown in Figure 2.1 which clearly demonstrates the cleavage planes of the laminae.

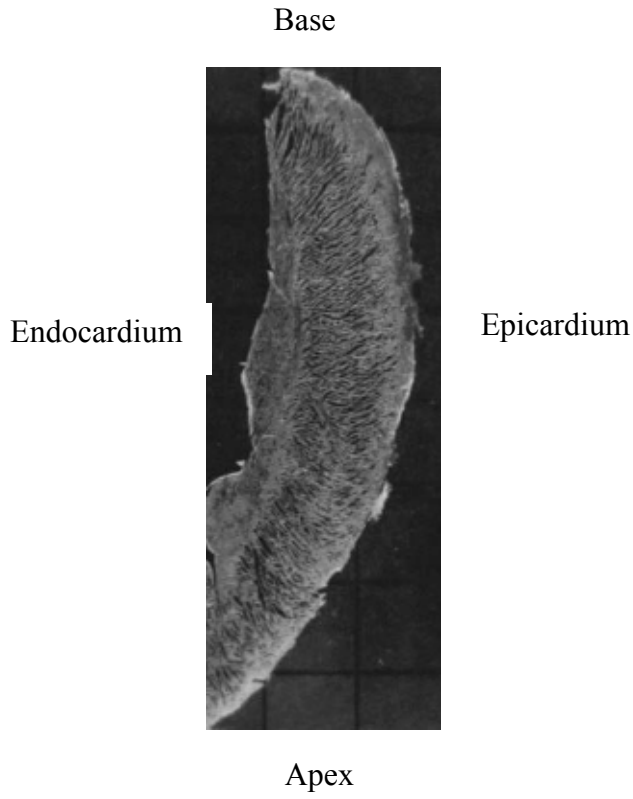

Figure 2.1 Micrograph of a longitudinal-transmural section of a canine left ventricle demonstrating radial alignment of the laminae. (Reprinted, with permission, from: LeGrice, I.J., et al., *Laminar structure of the heart: ventricular myocyte arrangement and connective tissue architecture in the dog.* Am J Physiol, 1995)

Additionally, a network of collagen fibers provides tight coupling of myocytes within the sheet and looser coupling between adjacent sheets. A three dimensional SEM image of a canine left ventricular tissue sample is shown in Figure 2.2 revealing collagen fibers mechanically coupling laminae to one another [4]. A computerized rendition of the three-dimensional hierarchical microstructure of the ventricular myocardium is shown in Figure 2.3 [4].

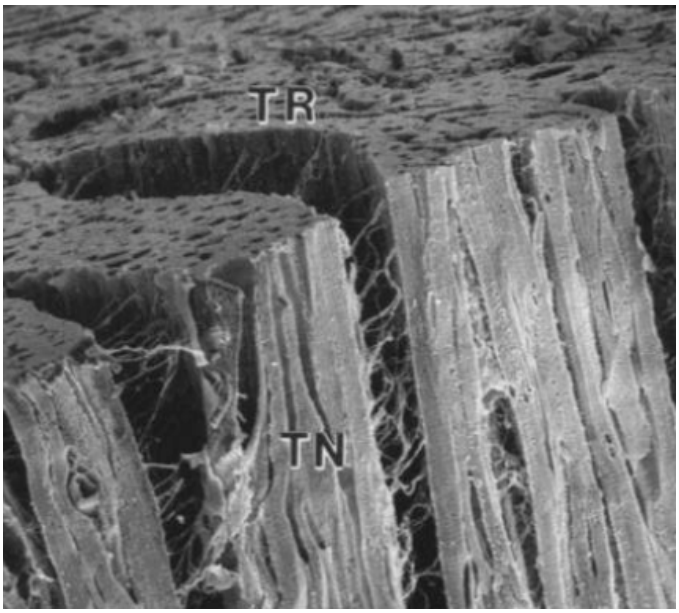

Figure 2.2 Scanning electron micrograph of a left ventricular midwall section showing the collagen network mechanically coupling parallel fibers (Reprinted, with permission, from: LeGrice, I.J., et al., *Laminar structure of the heart: ventricular myocyte arrangement and connective tissue architecture in the dog.* Am J Physiol, 1995)

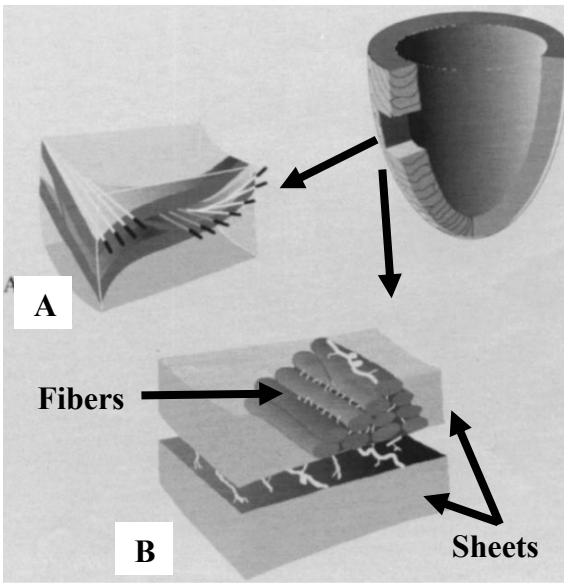

Figure 2.3 Computer rendition of cardiac myocyte structure. (A) Two laminar sheets with fiber orientation depicted. (B) Myocardial structure at the cellular level including the structural collagen matrix. (Reprinted, with permission, from: LeGrice, I.J., et al., *Laminar structure of the heart: ventricular myocyte arrangement and connective tissue architecture in the dog.* Am J Physiol, 1995)

Because there are substantial transmural and regional differences in fiber orientation, one must be careful to denote the region, transmural depth, and coordinate system used when describing the fiber orientation. It is common to reference the fiber orientation relative to a local wall bound coordinate system of the ventricle. The most common wall bound coordinate system, and the system used in this research to describe fiber orientation is depicted in Figure 2.4, where the helix angle is defined as α [5]. For an example, Figure 2.5 depicts fiber inclination angels obtained from histological measurements from four basal sections of a left canine ventricle [5]. In general, the fiber inclination angle in all species of mammals can rotate as much as 180° in the left ventricle from the epicardial to endocardial surface. The fiber angle forms a left handed helix at the epicardial surface with initially negative values of α. There is a gradual

transition in fiber angle transmurally as α increases and approaches 0° midwall (fibers are oriented circumferentially) and continues to increase until the fibers form a right handed helix at the endocardial surface. Specifically, in the human myocardium, the angles covered by the rotation in fiber orientation are normally between 120° and 160° in the anterior left ventricle and close to 180° in the lateral and posterior wall [7].

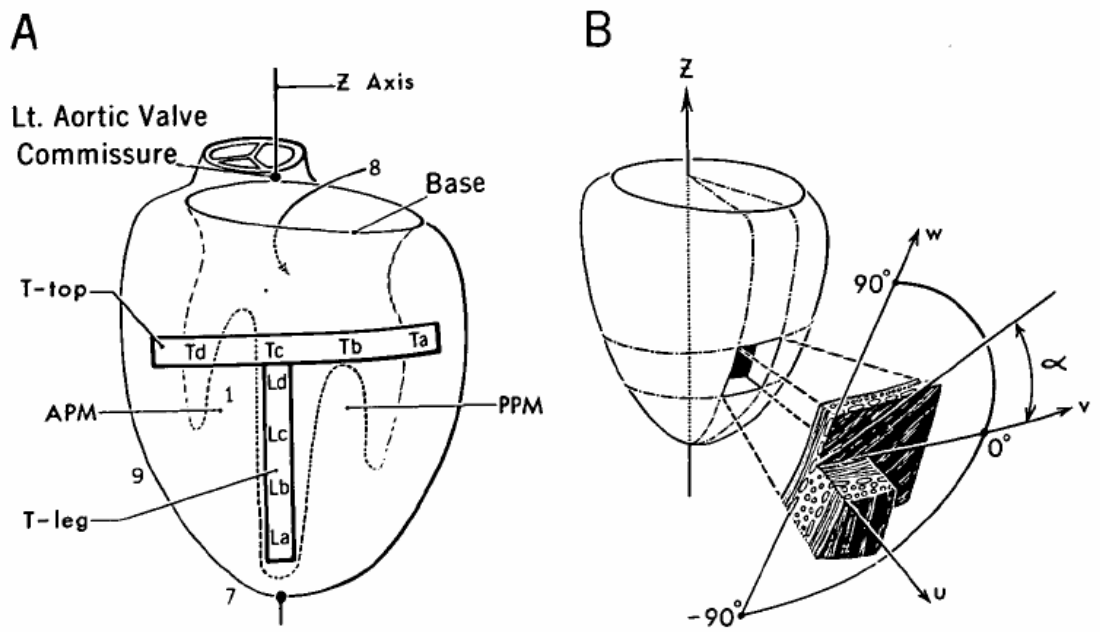

Figure 2.4 Local wall bound coordinate system used in a study of a canine left ventricular free wall.(Reprinted, with permission, from: Streeter, D.D., Jr., et al., *Fiber orientation in the canine left ventricle during diastole and systole.* Circ Res, 1969)

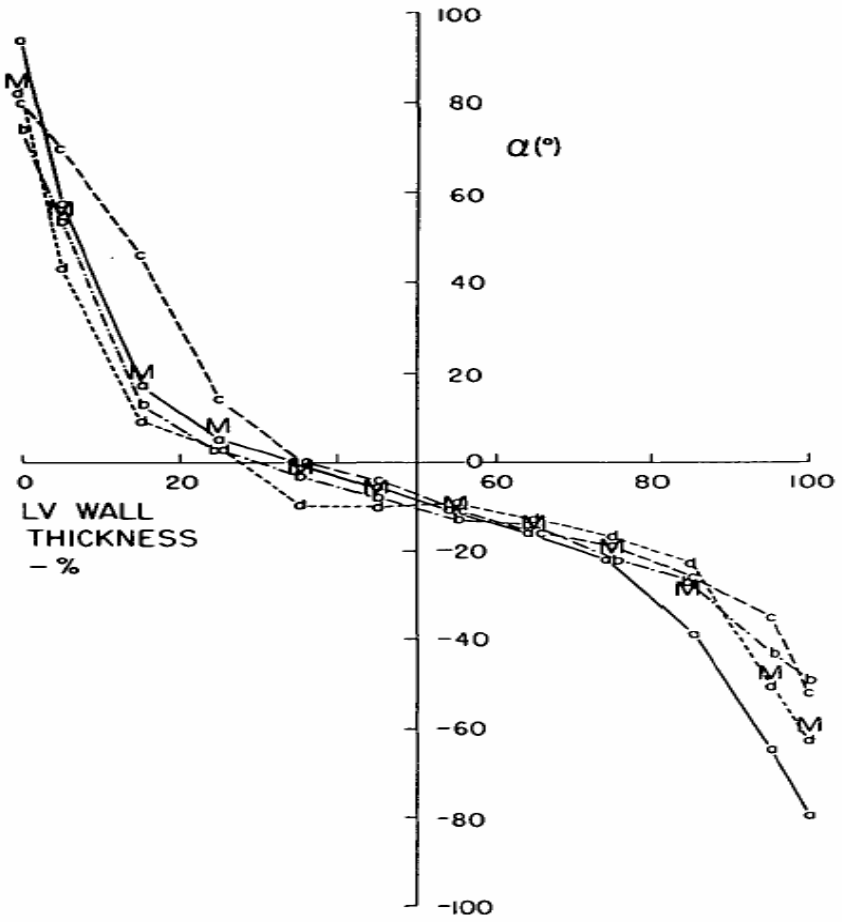

Figure 2.5 Fiber orientation measured in four regions in the left ventricular free wall of a fixed canine heart.(Reprinted, with permission, from: Streeter, D.D., Jr., et al., *Fiber orientation in the canine left ventricle during diastole and systole.* Circ Res, 1969)

The fiber geometry in the right ventricle similarly consists of a counter-wound helical arrangement as observed in the left ventricle, except the transmural rotation in fiber angles is usually less than observed in the left ventricle. Figure 2.6 plots the measured fiber orientations in the right ventricle of a canine heart where the observed transmural fiber angle rotation was approximately 100-120° degrees in all regions measured [8].

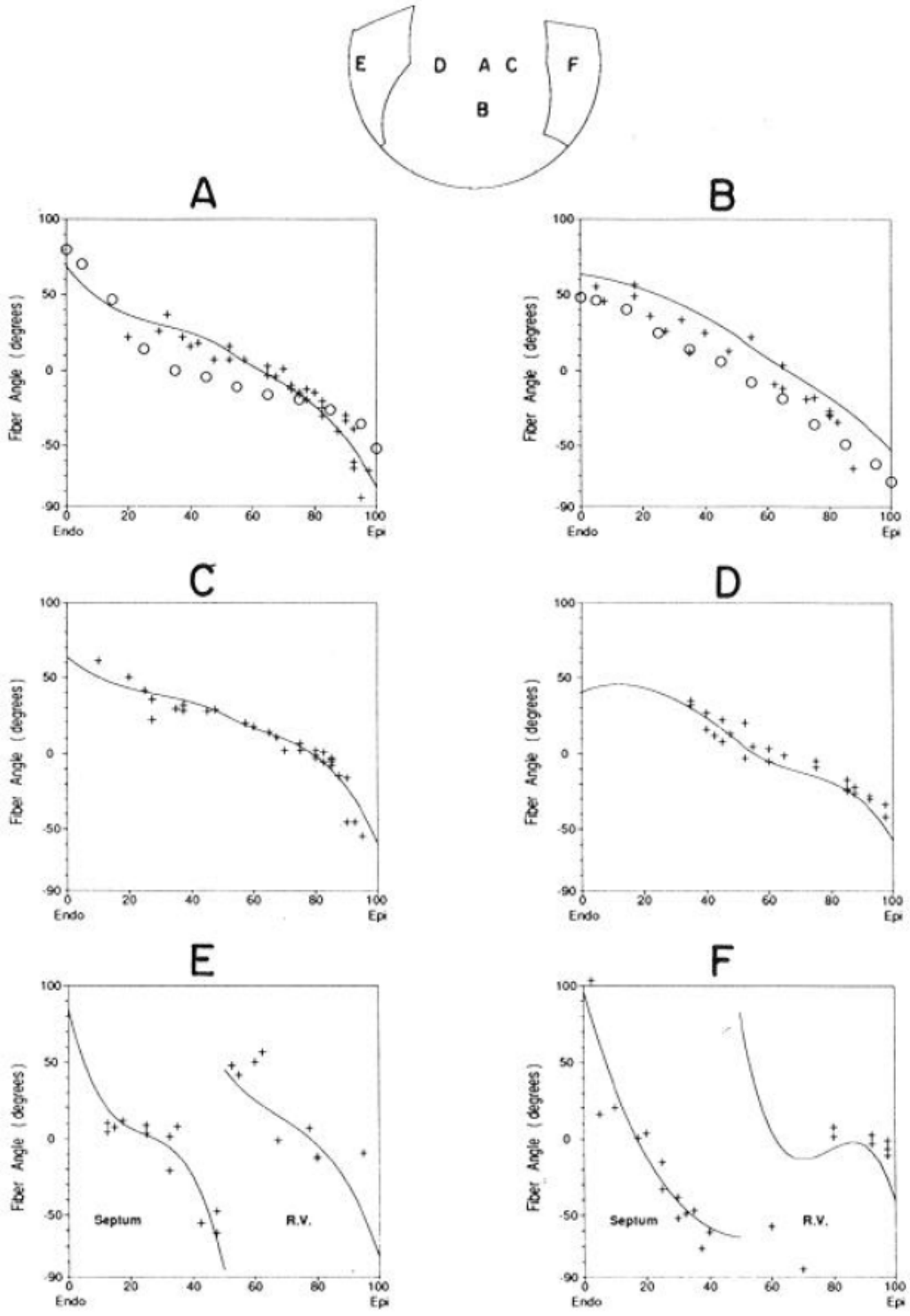

Figure 2.6 Histological fiber orientation data obtained in a canine right ventricle. (Reprinted, with permission, from: Nielsen, P.M., et al., *Mathematical model of geometry and fibrous structure of the heart.* Am J Physiol, 1991)

Importance of the Helical Arrangement of Myofibers

The helical arrangement of cardiac myofibers is responsible for the cell-cell electrical propagation during contraction as well as force production. Cardiac myofibers are arranged as counterwound helices in the ventricles where fiber orientation forms a left handed helix at the epicardium and transitions into a right hand helix at the endocardium. This oblique fiber orientation is important in left ventricular wall deformation and diastolic ventricular filling. Using MRI tissue tagging, Shapiro demonstrated that significant cross fiber shortening resulting from oblique fiber orientation could be responsible for the rearrangement of the endocardial fibers during systole resulting in a large component of radial wall thickening (and thus contributing to stroke volume) [9]. In addition, ventricular twist arising from the helical fiber arrangement can function to store energy in systole resulting in increased ventricular filling during diastole. Ventricular twist in the left ventricle is also associated with greater hemodynamic performance or vigor of contraction [6, 10]. Numerical models have demonstrated that the helical arrangement of cardiac fibers is a mechanism which normalizes fiber strain and workload. In these models, fiber orientations that were predicted to yield homogenous fiber strains correlated with histological findings [11, 12]. In vivo MRI radiofrequency tissue tagging combined with DTMRI has also demonstrated that fiber strains or shortening is uniform throughout the ventricular myocardium [13]. In addition, mathematical models of ventricular function reveal that a helical fiber arrangement optimizes left ventricular ejection fraction over purely circular or circumferential fibers [14]. In fact, mathematical predictions of ejection

fraction are 30% for a heart with purely circumferential fibers versus 60% for one with an oblique pattern [14].

Therefore, the counter-wound helical structure of the myocardium is considered to be responsible for the torsional or wringing motion of the left ventricle and serves three main mechanical functions: (1) equalizing myofiber strain and workload; (2) optimizing the volume of blood ejected during systole (stroke volume); and (3) storing torsional energy in the intracellular and extracellular matrices and, when released, increasing ventricular filling during diastole. Given the importance of cardiac fiber orientation in ventricular function, any remodeling from the endogenous structure would likely be associated with a change in function.

DTMRI and the Measurement of Fiber Orientation

Anisotropic Diffusion in Cardiac Myocytes

The MR measurement of an effective diffusion tensor of water in cardiac tissue (as well as other biological tissues) has been successfully used to quantify myofiber architecture. Because cardiac tissue is anisotropic, the diffusivity or water mobility is known to depend on the tissue orientation and structure [15]. The primary way to characterize diffusion in the cell is through the use of diffusion tensor magnetic resonance imaging (DTMRI). Researchers have shown through parallel ex-vivo DTMRI in formaldehyde fixed hearts and subsequent histological studies that anatomical fiber tract directions are coincident with the principal direction or axis of the diffusion ellipsoid associated with the largest principle diffusivity [2, 3, 16, 17]. In other words, there is quantitative

agreement between principle eigenvector (direction of maximum diffusivity) and the long axis of the cardiac myofibers. [17]. Correlation values of 0.97 between conventional histological fiber orientation measurements and DTMRI data have been demonstrated indicating the ability of this imaging modality to probe tissue microstructure [17].

Since single myofiber lengths are on the order of 100 um, (much larger than the mean free diffusion path between applied diffusion gradients) there are no barriers besides cell organelles and other subcellular structures to prevent water molecules from diffusing parallel to the axis of the myofiber. Thus, the highest diffusivity is measured along the myofiber axis. This concept is illustrated in Figure 2.7.

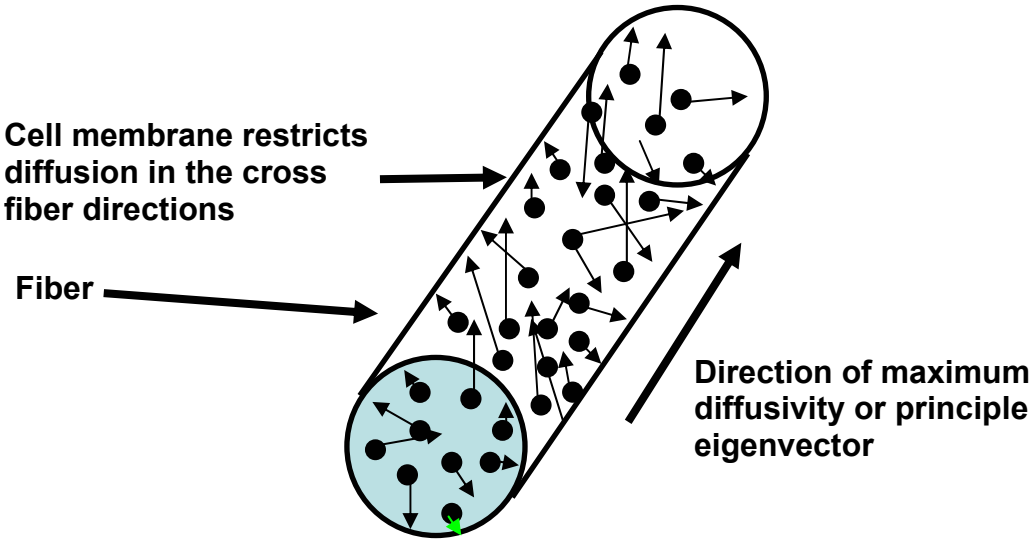

Figure 2.7 Random intracellular diffusion of water occurring between the applied diffusion imaging gradients. Diffusivity is greatest along the long axis of the fiber when the diffusion time during the imaging pulse sequence is chosen such that the mean free path is approximately on the order of the cell diameter and much less than the fiber long axis.

Measurement of Diffusion with MRI

Diffusion weighted MRI probes tissue microstructure by measuring signal attenuation in multiple directions [18]. As discussed, diffusion is restricted in cardiac myofibers such that the greatest diffusion is along the myofiber axis due to microscopic barriers such as the cell membrane, collagen, and laminar sheet borders. In diffusion imaging, magnetic field gradients are applied in a set of predetermined directions, intensities, and durations and subsequently the attenuation of the signal is combined to solve for the diffusion tensor, where greater diffusion results in more signal attenuation. That is, the more the water molecules move between the timing of the applied diffusion gradients, the larger the phase shifts in the magnetic spins of the molecules due to the movement of the molecules in the direction of the applied gradients. This phase shift results in signal attenuation. The diffusion tensor is a second rank tensor which represents the net diffusion in a volume of tissue, or in the case of MRI imaging, a voxel or pixel of an image. The diffusion tensor is related to the MRI signal attenuation as follows:

$$\ln\left(\frac{S_b}{S_0}\right) = -b\bar{q}_i^{\,T} D\bar{q}_i$$

where S_b is the signal of the attenuated image at each voxel, S_0 is the unattenuated image, D is the symmetric 6x6 diffusion tensor, and b is the scalar quantity termed the b-value which describes the diffusion weighting and is a function of the strength of the magnetic field gradients, the shape of the gradients as well as the timing [19]. The

vector $\bar{q}$ is a 3x1 unit vector in the direction of the ith applied gradient referenced to the scanner bore. The diffusion tensor D characterizes the water motion in all directions:

$$D = \begin{bmatrix} D_{xx} & D_{xy} & D_{xz} \\ D_{yx} & D_{yy} & D_{yz} \\ D_{zx} & D_{zy} & D_{zz} \end{bmatrix} \quad (2)$$

In order to solve for the six unique coefficients of the diffusion tensor D, diffusion gradients must be applied in at least six non-collinear directions. Thus, a minimum of seven images must be obtained including the unattenuated image to calculate the diffusion tensor. Once the tensor is known, it can be physically interpreted as a three-axis ellipsoid with each axis being an orthogonal vector (eigenvectors) with a length scaled to its corresponding diffusivity (eigenvalue) in that direction. As already mentioned, for cardiac tissue, the primary eigenvector (direction with the least restricted diffusion) represents the fiber direction, the secondary eigenvector represents the sheet direction, and the tertiary eigenvector (direction with the most restricted diffusion) represents the sheet normal (Figure 2.8).

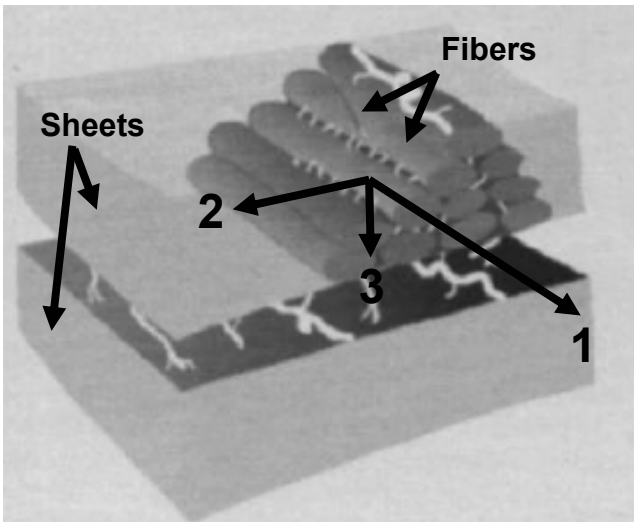

Figure 2.8 Principal eigenvectors of diffusion overlaid on a sketch of the cardiac laminar structure. The primary eigenvector (1), secondary eigenvector (2), and tertiary eigenvector (3) are shown. (Reprinted, with permission, from: LeGrice, I.J., et al., *Laminar structure of the heart: ventricular myocyte arrangement and connective tissue architecture in the dog.* Am J Physiol, 1995)

There are two primary diffusion parameters calculated from the eigenvalues which further describes the diffusion state in the tissue. These parameters are the fractional anisotropy (FA) and the apparent diffusion coefficient (ADC). Fractional anisotropy is a measure of anisotropy (or directionality) of diffusion and is derived from the eigenvalues (E1, E2, E3) as follows:

$$FA = \sqrt{\frac{1}{2}} \frac{\sqrt{(E1 - E2)^2 + (E2 - E3)^2 + (E3 - E1)^2}}{\sqrt{E1^2 + E2^2 + E3^2}}$$

ADC is the mean diffusivity, and is derived from the three eigenvalues of diffusion as follows:

$$ADC = \frac{E1 + E2 + E3}{3}$$

For the FA, values of 0 indicate free or unrestricted diffusion (for example, imaging a glass of water), and as the fraction increases, the diffusion becomes more anisotropic. For example, the FA in cardiac tissue typically ranges from 0.2-0.5. ADC is an overall assessment of the mobility of water in the tissue.

Current Methodologies

Imaging

All diffusion images for this research were acquired using a 3 tesla MRI scanner (Trio; Siemens Medical Systems,U.S.A) that has a maximum gradient amplitude of 40mT/m. The acquisition utilized a Siemens double spin-echo, echo-planar diffusion-weighted sequence which minimized eddy current distortion [20]. A total of six diffusion weighted gradients (b-value=1000 s/mm^2) were applied in 6 non-collinear directions and an additional null weighted image (b-value = 0) was acquired for the estimation of the diffusion tensor. An example of a set of diffusion images in the short-axis plane of a swine heart is shown in Figure 2.9. Furthermore, twenty averages were used to improve the signal to noise ratio for all imaging studies. Other imaging parameters such as the field of view (FOV), time to echo (TE), repetition time (TR), slice thickness, and slice spacing varied based on the cardiac anatomy and such parameters are described in the context of the individual experiments. In general, these parameters were successful in probing local fiber orientation with a 2.0 x 2.0 x 2.0 mm resolution or better.

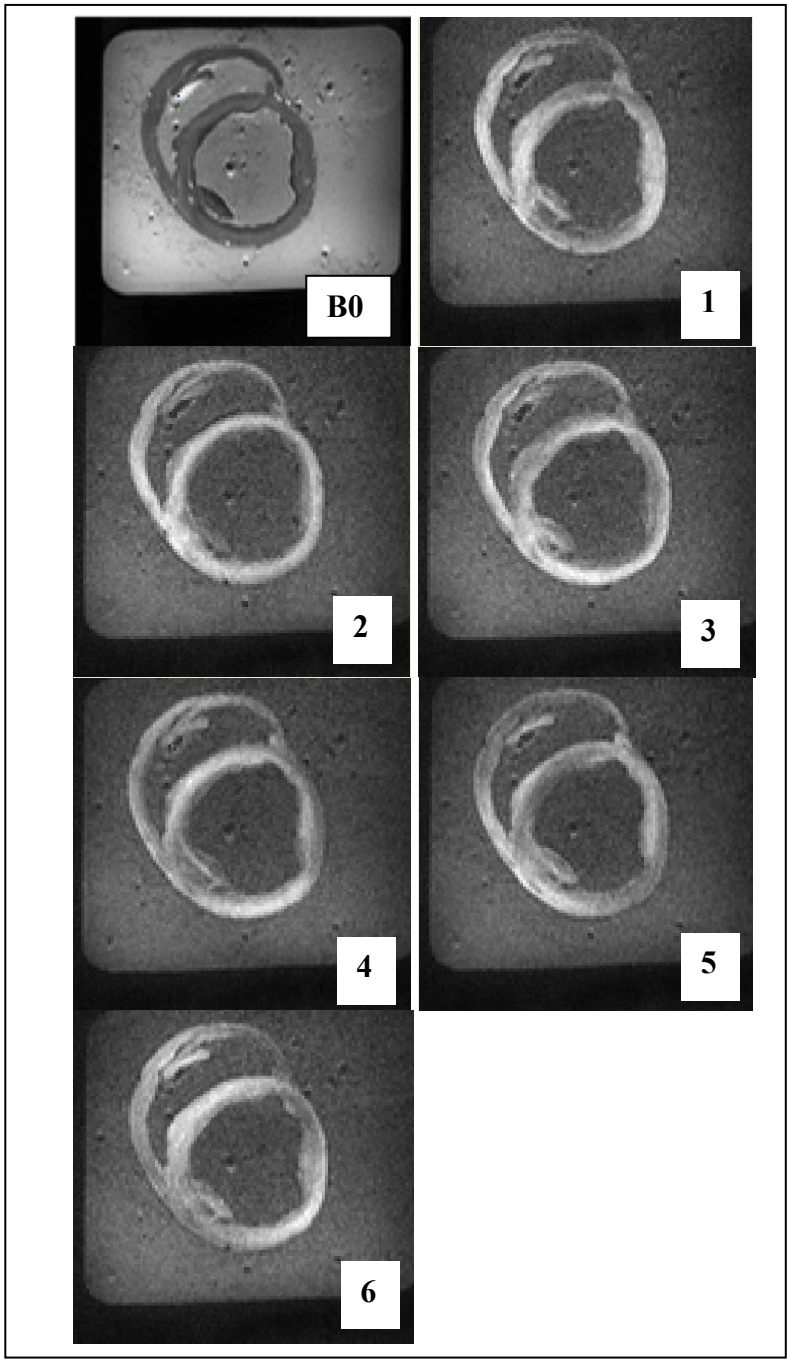

Figure 2.9 Set of diffusion weighted images in the short-axis plane of the heart. B0 represents the null-weighted image (b=0), and images acquired using gradient directions 1-6 are indicated.

In addition, all diffusion weighted images were acquired in the plane of the cardiac short-axis according to the methods reported in the literature [3, 16, 17, 21, 22].

Specimen Preparation

All excised hearts were perfusion fixed in 10% buffered formalin under ~50 mm of pressure for 12-24 hours prior to imaging such that the hearts were preserved an end diastolic shape. Measuring cardiac fiber orientation in an end diastolic shape is appropriate since it has been noted that fiber orientation does not significantly change throughout the cardiac cycle [23]. In addition, the use of formalin for fixation has previously been used in cardiac DTMRI image studies and has been shown not to affect measurements of fiber orientation [16, 24]. Furthermore, the hearts were imaged in an air-free polymer container and embedded in 0.75% agar gel in order to reduce tissue magnetic susceptibility and also to dampen vibration artifacts from the scanner.

Post-processing and Determination of Fiber Orientation

Post-processing of the image data was done by custom software DTITOOL 2009 which was developed using MATLAB version 7.1. The graphical user interface is shown in Figure 2.10. This post-processing tool performs the following tasks:

- Coverts DICOM images from the scanner to cell arrays that can be processed in MATLAB
- Separates and averages mosaic images into single images sorted by b-value and direction

- Allows the user to create a mask through a graphical user interface (GUI) such that calculations will only be made where the myocardium is present, thus reducing computational expense.
- Numerically solves for the diffusion tensors on a pixel by pixel basis using an analytical algorithm described in [25].
- Numerically extracts the eigenvectors and eigenvalues of diffusion on a pixel-wise basis
- Rotates the eigenvectors of diffusion from the patient frame of reference to the image frame of reference
- Calculates and plots the fiber inclination angle using the wall bound coordinate system
- Plots the superimposed fiber inclination angle on the short axis images, and also displays a 3D rendering of fiber orientation
- Exports the diffusion parameters and fiber data to an Excel worksheet

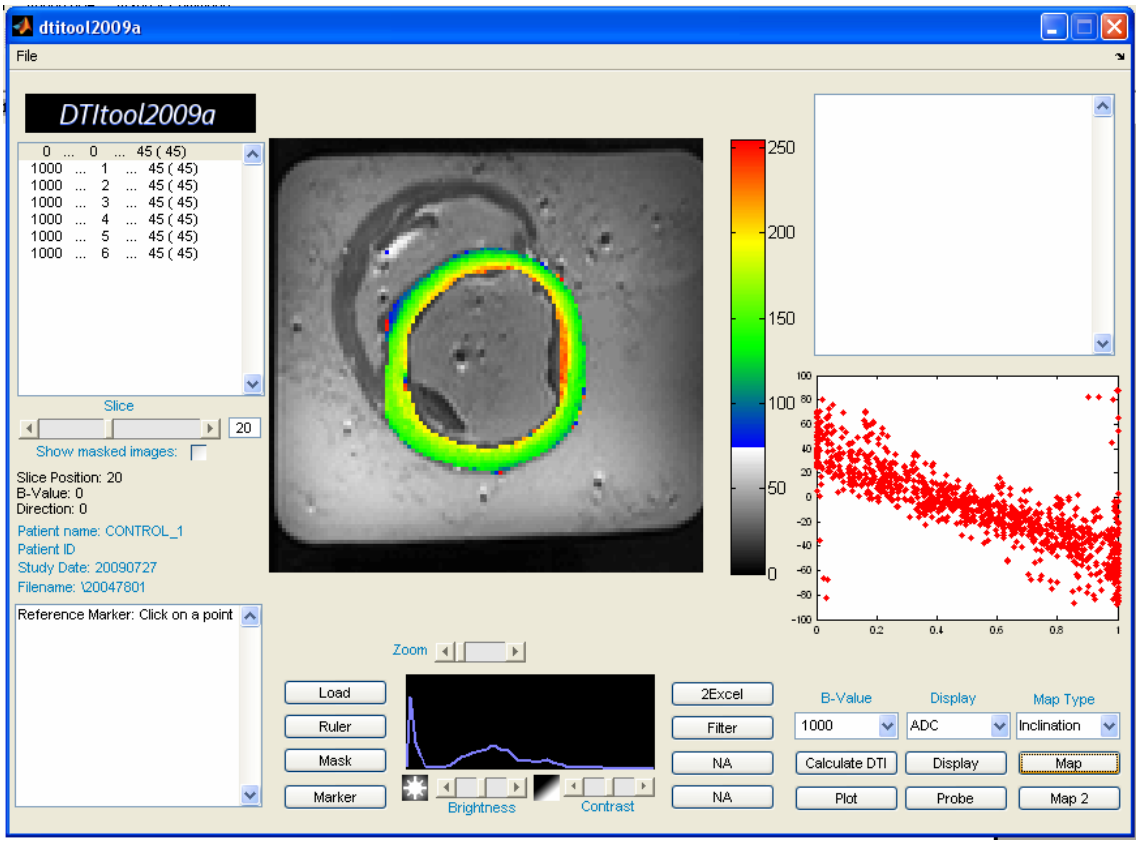

Figure 2.10 DTITOOL2009 graphical user interface.

An example of a 2D plot of the fiber inclination angle and a 3D map of the fiber orientation calculated from the diffusion weighted images in the above example are shown in Figures 2.11-2.13.

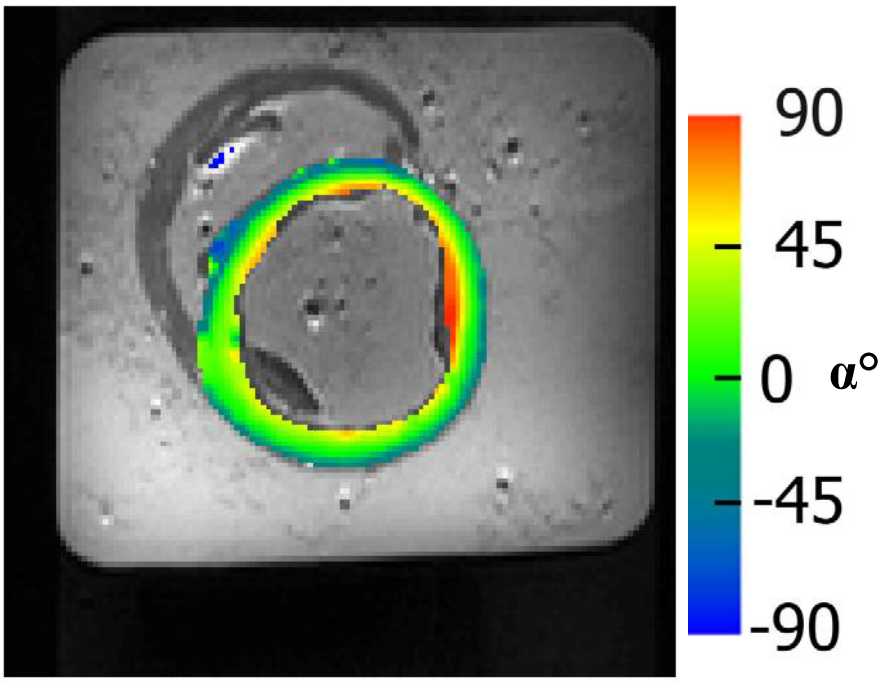

Figure 2.11 2D contour plot of the fiber inclination angle α in the short-axis plane of the left ventricle. The definition of the helix angle α is depicted in Figure 2.4.

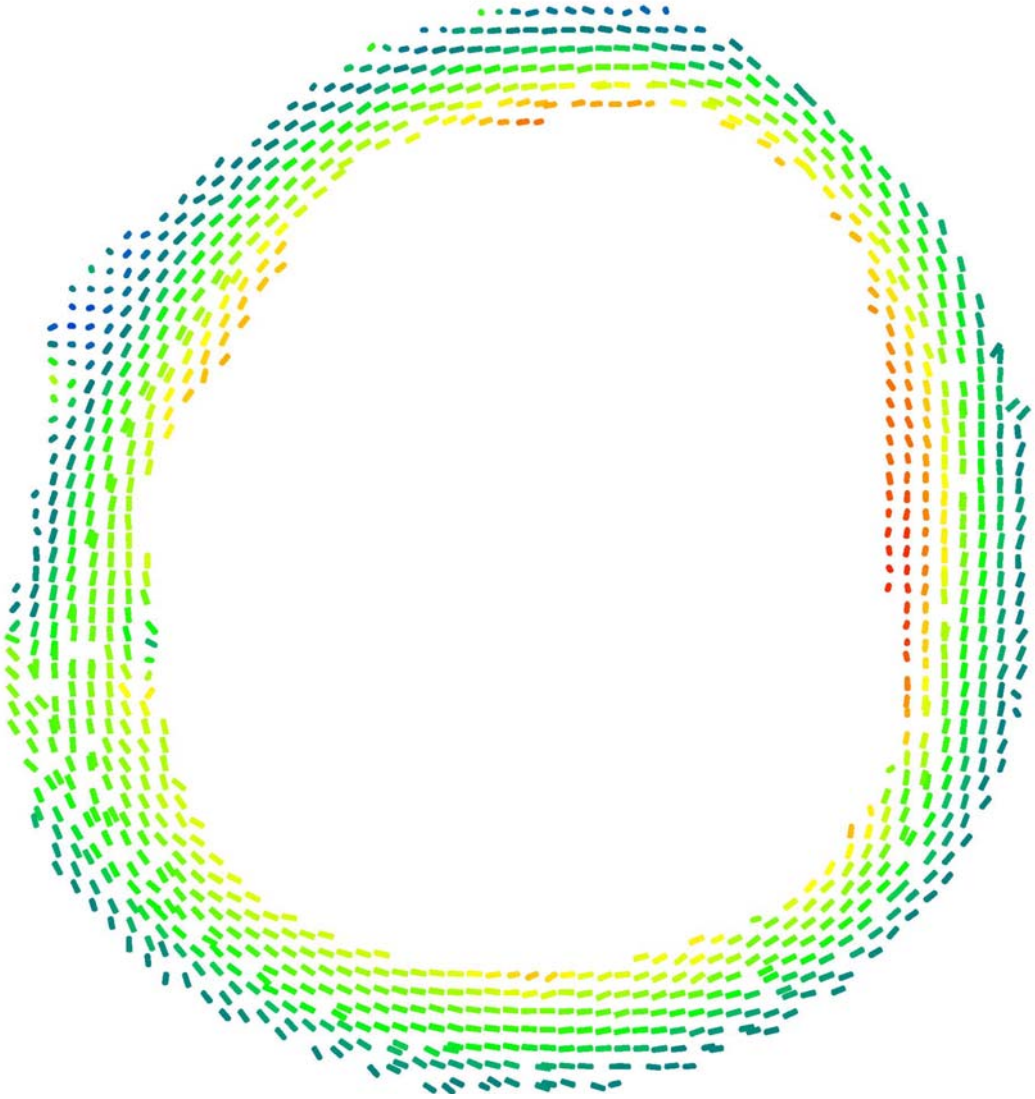

Figure 2.12 3D contour plot of the fiber inclination angle α in the short-axis plane of the left ventricle as viewed from above. This 3D reconstruction is the from the same slice location as in Figure 2.11.

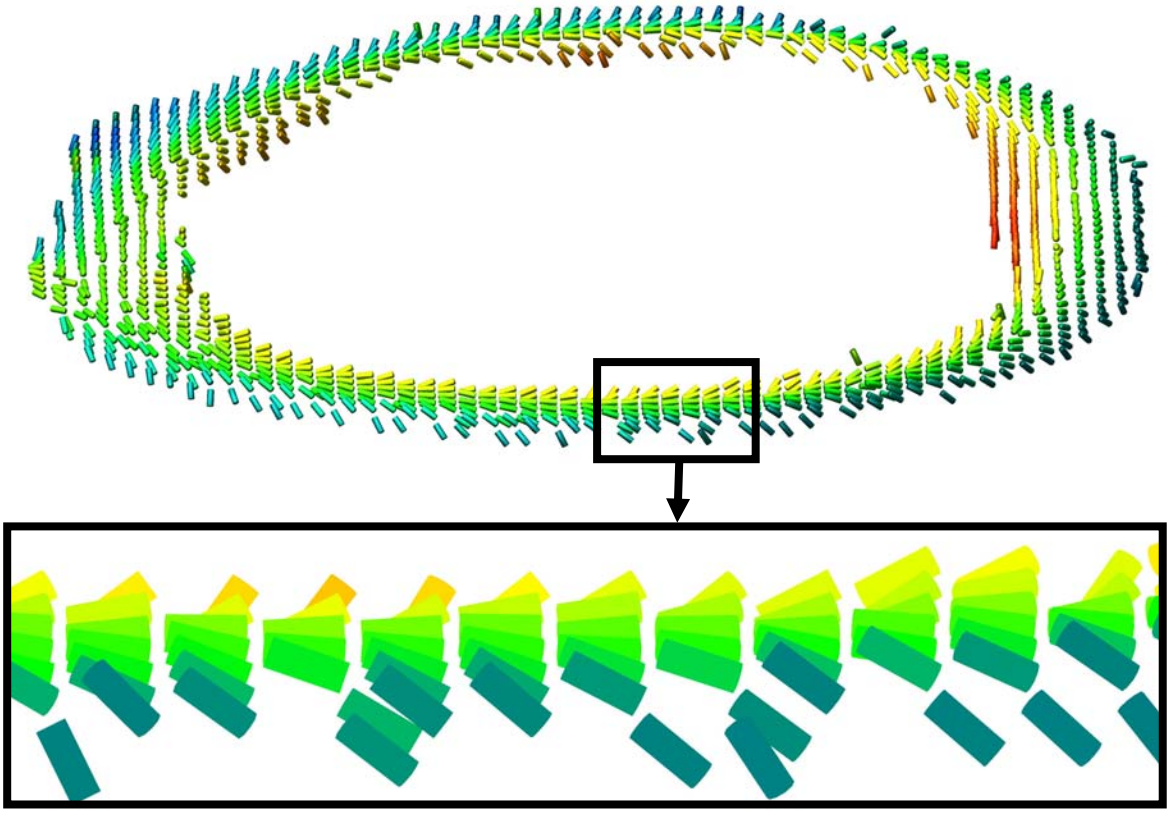

Figure 2.13 3D contour plot of the fiber orientation in the short-axis plane of the left ventricle of a swine heart as viewed from the lateral aspect. The rotation in fiber orientation from a left-handed helix at the epicardium to a right handed helix at the endocardium is clearly demonstrated. This 3D reconstruction is the from the same slice location as in Figure 2.11.

Potential Uses of DTMRI in Quantifying Fiber Orientation in Diseased States

Since the validation of DTMRI imaging in the ability to accurately quantify local fiber orientation, researchers have been using this technique as a means to investigate the arrangement of cardiac myofibers in a diseased state. To date, eight studies have used DTMRI to quantify changes in fiber orientation and cellular structure, where only two

experiments included human hearts [26-33]. These studies quantified changes in fiber structure due to hypertrophy, myocardial infarction, and in the dyssynchronous failing heart. In the disease state of hypertrophy, Tseng et al. noted that the myofibers were disorganized, or in a state of disarray, which lead to the discordination of myocardial contraction [28]. For patients with a myocardial infarction, Wu and colleagues demonstrated using diffusion tensor MRI clinically that the percentage of left hand fibers increases from the remote zone, to the adjacent zone, to the infracted zone [29]. It was also noted that an increasing percentage of left hand fibers in the infracted zone positively correlated with an increase in left ventricular ejection fraction. For the study of the dyssynchronous failing heart, a tachy-pacing dilated cardiomyopathy model in canine was used to cause dilation of the ventricles resulting in impaired pump function [27]. However, the findings indicated that fiber orientation was largely unchanged.

Chapter 3: The Effects of Decomposition on Ex Vivo Diffusion Tensor Magnetic Resonance Imaging of the Human Heart[†]

[†] Authors: Michael D. Eggen, MS[1,2], Paul A. Iaizzo, PhD[2,3] Cory M. Swingen, PhD[4] Department of Biomedical Engineering[1], Department of Surgery[2], Department of Integrative Biology and Physiology [3], Department of Medicine[4], University of Minnesota, Minneapolis, Minnesota, 55455

Preface

More recently, diffusion tensor magnetic resonance imaging (DTMRI) has become the preferred method to measure cardiac myofiber orientation as it is non-destructive, and data acquisition and the reconstruction of fiber geometry can be completed in a matter of hours, as opposed to weeks or months with conventional histology. As such, the major focus of cardiac DTMRI has been the quantification of fiber orientation and the analysis of tissue integrity through the measurement of diffusion parameters (i.e., eigenvalues, apparent diffusion coefficient (ADC), and fractional anisotropy (FA)). Due to the limited resolution that can be obtained *in vivo*, and the long scan times necessary to obtain such measurements, the majority of cardiac DTMRI has focused on animal hearts fixed directly post-mortem. For these reasons, post-mortem imaging of human hearts has become increasingly important for the study of fiber orientation and tissue integrity, especially in the realm of heart failure. However, one caveat in post-mortem imaging of human hearts is that tissue fixation directly post-mortem is difficult; it is common for researchers to obtain hearts from an institution (such as the Anatomy Bequest program at the University of Minnesota) with a 24 hr or greater post-mortem interval. Since one of my research goals is to characterize fiber orientation in failing human hearts, which are commonly obtained with post mortem intervals >24 hrs, the effects of delayed tissue recovery on the diffusion properties of the myocardium must be well understood. Here, we compared the diffusion properties in human hearts fixed directly post-mortem (n=8), with those from hearts recovered with a post-mortem intervals > 1 day. It was discovered that the apparent diffusion coefficient (ADC) increased with an increasing PMI, and the fractional anisotropy decreased with an

increasing postmortem interval. Therefore, since diffusion anisotropy or directionality is the basis for the measurement of fiber orientation using DTMRI, any delay in tissue fixation after death (if not properly preserved using organ transplantation techniques) will therefore compromise the measurement of fiber orientation.

In this research, I was responsible for experimental design (with Dr. Iaizzo), MR imaging of the hearts, data analysis, manuscript preparation, and recovery and perfusion fixation of the hearts (with Dr. Iaizzo). Dr. Cory Swingen was responsible for training me in the use of the 3.0 tesla clinical scanner at the Fairview University Medical Center, and also was responsible for creating the visualization tools in Matlab.

Introduction

More recently, diffusion tensor MRI (DTMRI) has been utilized as a tool to reconstruct the 3D myofiber orientation of the heart in high resolution [1-5]. Cardiac DTMRI is the preferred method to quantitatively study myofiber organization, as the method is noninvasive allowing for *in vivo* measurements, and data acquisition and the reconstruction of fiber geometry can be completed in a matter of hours, as opposed to weeks or months with conventional histology. However, due to long acquisition times, and *in vivo* motion artifacts, the majority of cardiac DTMRI studies have been conducted *ex vivo* in formaldehyde-fixed animal hearts, with few studies of the fixed human heart. Moreover, when using animal tissues, perfusion fixation typically occurs directly postmortem, this is not possible for human tissue, as there is always a delay between death and tissue fixation or a post mortem interval (PMI). As such, when obtaining a heart from a donor with heart failure, the heart and other organs (kidneys, lungs, etc.) typically would not be harvested for transplantation, and an organ procurement team would not be available to recover and preserve the heart for research. Therefore, an approximate PMI of 24 hrs minimum would be inherent when recovering hearts from donors with heart failure, a primary interest in the emerging field of cardiac DTMRI.

It has been previously validated that first eigenvector of diffusion, or maximum direction of diffusivity, coincides with the local fiber orientation in the ventricles [6-8]. It is assumed that the water contained inside and outside the myofiber cannot move freely, but is constrained to move longitudinally along the fiber axis [9]. In addition,

myofibers are arranged in sheets or layers of approximately four cells thick, which are physically separated by cleavage planes [10, 11]. Diffusion is assumed to be smaller in the surface normal direction of the cleavage plane than diffusion inside the plane. Therefore, the secondary and tertiary eigenvectors of diffusion (or radial directions of diffusion) have been suggested to coincide with the local sheet direction and sheet normal respectively [8, 12]. As such, good correlations between histological and DTMRI methods of reconstructing the laminar structure of the myocardium have been shown [8, 13].

The aforementioned assumptions have been successfully used for the DTMRI study of cardiac fiber orientation *in vi*vo or in myocardial tissue fixed directly postmortem. Any decomposition in the myocardium from a delayed recovery of the heart after death compromises the tissue microstructure, which could invalidate the measurement of fiber orientation using DTMRI. To our knowledge, the effect of decomposition on the diffusion properties of the myocardium, and the ability to reconstruct the local fiber orientation within the heart using DTMRI is unknown. In this study, we used DTMRI to compare the diffusion properties of human hearts fixed directly postmortem, with those recovered with varying PMIs > 24 hrs. Furthermore, 2D and 3D reconstructions of fiber orientation using the first eigenvector of diffusion were qualitatively studied to assess the effects of decomposition on the measurement of fiber orientation.

Methods

Heart Procurement and Tissue Fixation

In order to assess the effects of decomposition on the diffusion properties of the myocardium, both freshly excised human hearts, and hearts recovered with varying post mortem intervals (PMI) >24 hours were obtained. The protocol and procedures employed for this research were reviewed and approved by the Human Subjects Committee Internal Review Board at the University of Minnesota. Freshly excised human hearts (n=8), deemed not viable for transplant, were recovered by Life Source Upper Midwest, a nonprofit organ procurement organization, by arresting the heart with cardioplegia and subsequent placement in cold storage. The freshly excised hearts were perfusion fixed within 6 hours after procurement, within the time frame considered viable for transplantation, and therefore represented the "0-day" PMI in the subsequent analysis. Human hearts procured with a PMI >24 hours (n=9) were obtained through the Bequest Anatomy Program at the University of Minnesota, and excised from cadavers stored at 3.7°C and subsequently perfusion fixed, where the PMI was taken as the time between death and the start of perfusion fixation. Perfusion fixation was achieved by cannulation of the pulmonary artery, aorta, superior vena cava, and one pulmonary vein and subsequent pressurization (~50 mmHg) with the continuous flow of 10% buffered formalin for a period of 24-48 hours such that the hearts retained an end-diastolic shape. For imaging, the hearts were placed in a polymer container and submerged in formalin and all air was evacuated to reduce any air-tissue susceptibility artifacts.

Diffusion Tensor Magnetic Resonance Imaging

All diffusion images were acquired on a Siemens 3T MAGNETOM Trio scanner (Siemens, U.S.A.) that had a maximum gradient amplitude of 40 mT/m. An 8-channel phased-array head coil was used for imaging and the bore temperature was 23.7 ± 0.3 °C. The hearts were allowed to equilibrate with the bore temperature prior to scanning. Diffusion weighted images were acquired on the ventricular short axis, with 5 equidistant slices covering the heart from base to apex. The image acquisition utilized a Siemens double spin-echo, echo-planar diffusion-weighted sequence which minimized eddy currents [14]. The following acquisition parameters were used: TE=85 ms; TR=3000 ms; FOV=256 × 256 mm^2; slice thickness = 2 mm; slice spacing = 12 mm; b-value = 1000 s/mm^2; number of diffusion gradient directions = 6; number of averages = 20; matrix size = 128 ×128. A null weighted image (b-value = 0) was also acquired with the six diffusion weighted images for each slice. The acquisition time for each heart was ~7 min.

Data Processing and Fiber Tracking

DTI data and reconstructions of fiber orientation were processed was using an in house analysis tool developed in MATLAB (The MathWorks, Natick, MA) as previously described in Chapter 2. The diffusion tensor for each imaging volume was extracted pixel by pixel after segmentation of the myocardium using the solution developed by Basser and Pierpaoli [15]. From the diffusion tensor, the principal eigenvalues (E1, E2, E3) were further extracted for analysis and the fractional anisotropy (FA) and apparent diffusion coefficient (ADC) were derived from the eigenvalues according to Bammer et

al. [16]. Three regions of interest (ROI) or slices for each heart were selected and analyzed from the base, mid-ventricular, and apical levels. Furthermore, the analysis only included the left ventricle, and the papillary muscles were visually excluded from the analysis.

As such, 3D reconstructions of the local fiber orientation within the slice plane, and 2D contour plots of the fiber inclination angle, or helix angle α were employed to qualitatively assess the effects of decomposition on the measurement of fiber orientation. Specifically, reconstructions of fiber orientation in hearts with PMIs>24 hrs were compared to reconstructions from hearts fixed directly postmortem. For all analyses, fiber orientation was taken as the maximum direction of diffusivity, or the first eigenvector of the diffusion tensor. The cardiac coordinate system used for the analysis of the fiber helix angle is depicted in Figure 3.1. The helix angle was defined as the angle between the local helix projected onto the epicardial tangent plane and the cardiac short-axis plane as described by Streeter et al. [17] and Scollan et al. [8].

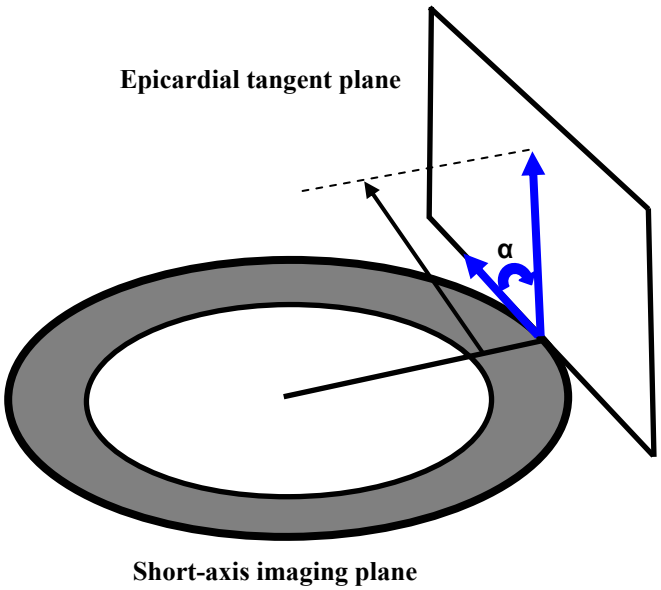

Figure 3.1 Definition of the helix angle α, where a positive angle is shown.

Statistical Analysis and Model Fitting

A two-way analysis of variance (ANOVA) was conducted to assess the effects of time and ROI on the principal eigenvalues, which are used to derive both the FA and ADC (Minitab 15, State College, PA). Subsequently, Bonferroni corrected pairwise comparisons were further used to assess individual differences between regions for each eigenvalue. For all statistical tests, a p-value <0.05 was considered significant. Following ANOVA, nonlinear regression was used to fit predictive exponential models to the time varying diffusion parameters (FA, ADC, E1, E2, E3) (GraphPad Prism, version 3.02, La Jolla, CA). For the FA, the following exponential decay model was used:

$$FA = A + B\exp^{(-C*PMI)}$$

where A, B, and C are constants.

For the remaining diffusion parameters, E1, E2, E3, and ADC, the following concave exponential growth model was fitted:

$$Y = A - B\exp^{(-C*PMI)}$$

where Y is the diffusion parameter of interest and A, B and C are constants. The goodness of fit of the data to the growth and decay models were assessed using the Wald-Wolfowitz test, or runs test for randomness, which examines the probability that sequential data points above or below the fitted curve are random. A p-value <0.05 for the runs test indicates that the sequential data points do not randomly vary about the fitted curve, which would indicate a poor model fit.

Results

Diffusion Parameters

The eigenvalues are plotted vs. the PMI for each ROI in Figures 3.2-3.4. Considering both the effects of PMI and region in a two-way ANOVA, the eigenvalues, E1, E2, and E3 significantly increased as the PMI increased. In addition, there was a significant interaction between the PMI and region for all eigenvalues. As such, for the first eigenvalue of diffusion E1, the mean diffusion in the apex (0.0013309 ± 0.0002381 mm^2/s) was significantly different from the mid-ventricular (0.0013288 ± 0.0002256 mm^2/s) and basal (0.0013313 ± 0.0002084 mm^2/s) regions, where the basal and mid-ventricular regions were not significantly different form one another. For the secondary eigenvalue of diffusion E2, all regions were significantly different from one another where E2 was highest in the apical region (0.0010919 ± 0.0003058 mm^2/s), followed by

the basal region (0.0010852 ± 0.0003025 mm^2/s) and mid-ventricular region (0.0010814 ± 0.0003189 mm^2/s). It followed that there were statistically significant differences between all regions for the tertiary eigenvalue E3, where the diffusivity at the apex, mid-ventricle, and base were 0.0009704 ± 0.0003229 mm^2/s, 0.0009705 ± 0.0003354 mm^2/s, and 0.0009698 ± 0.0003218 respectively.

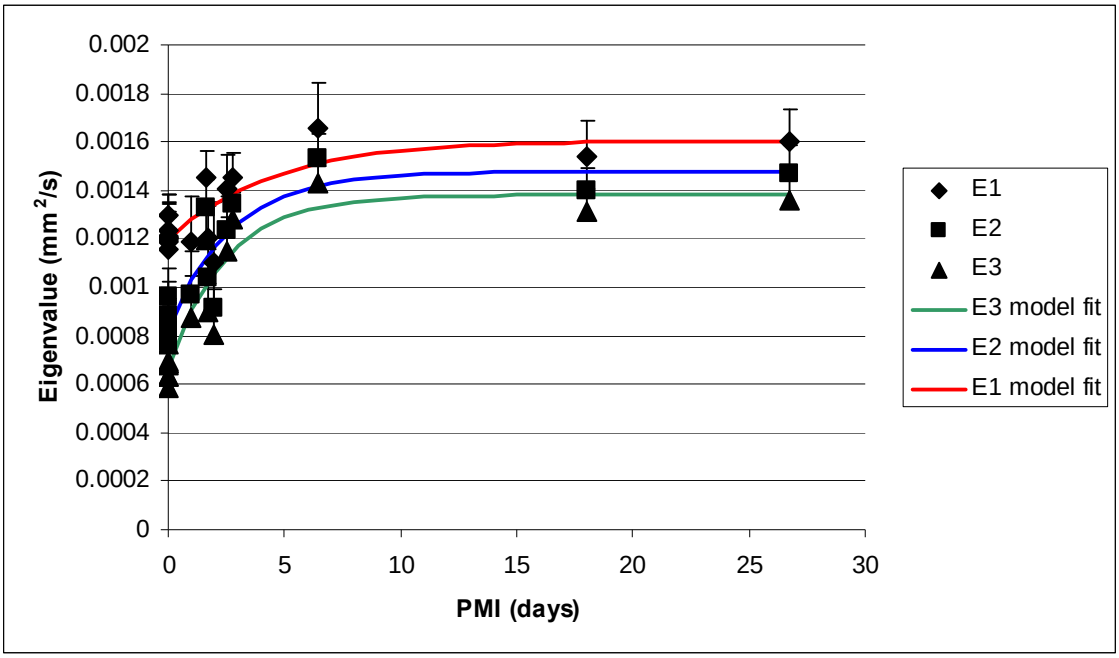

Figure 3.2 Principle eigenvalues plotted vs. PMI for the apical ROI.

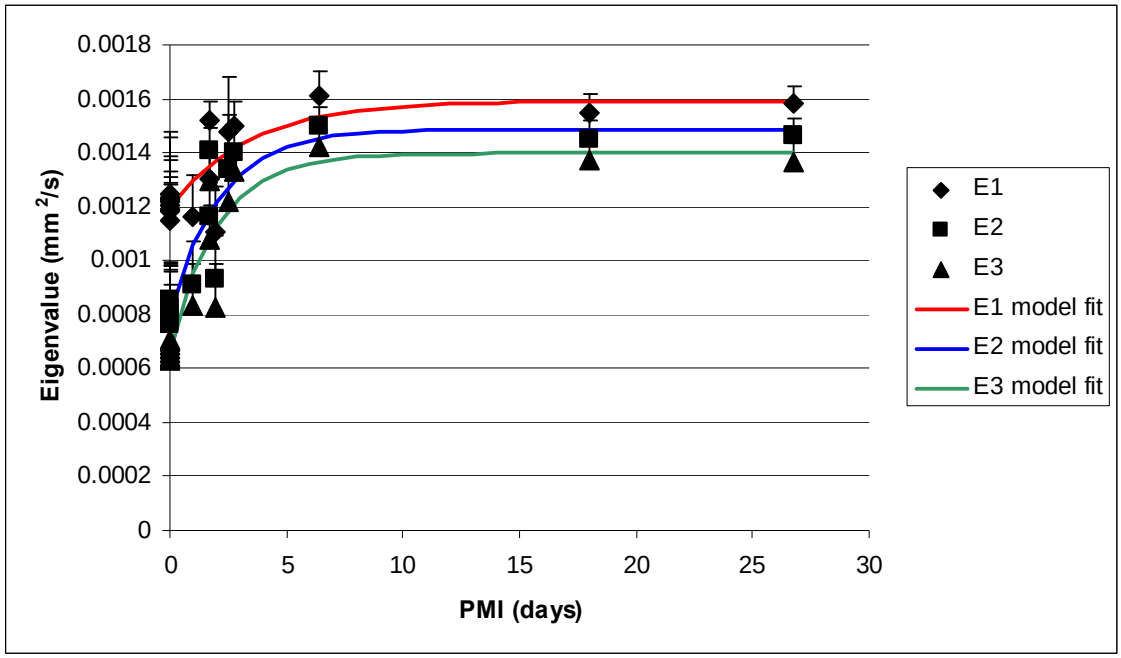

Figure 3.3 Principle eigenvalues plotted vs. PMI for the mid-ventricular ROI.

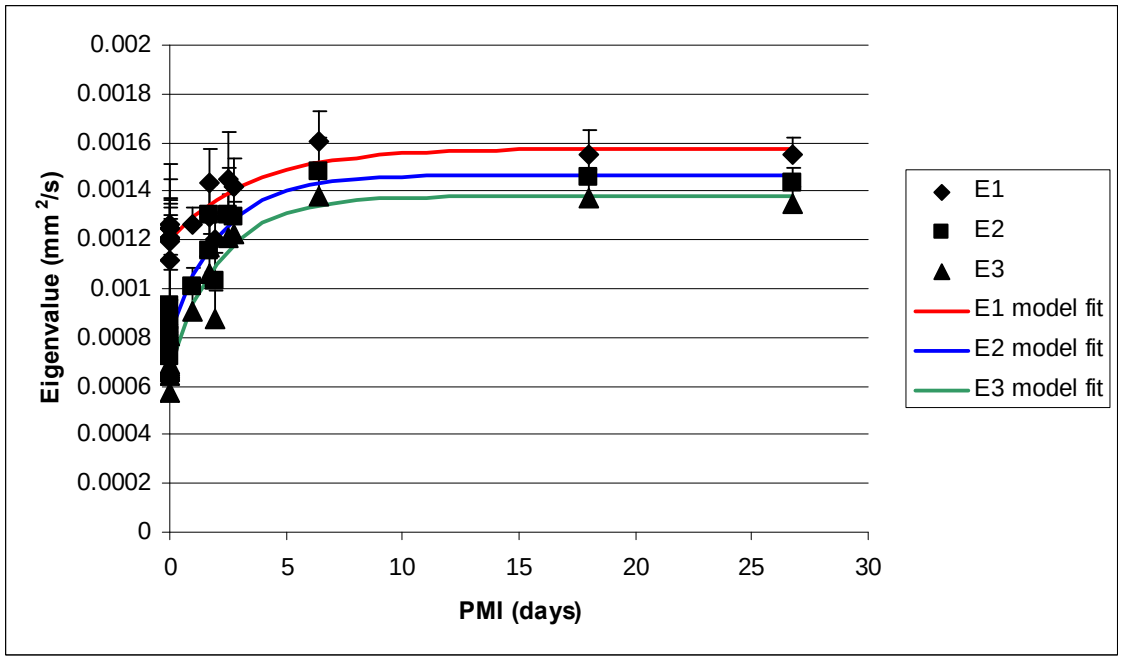

Figure 3.4 Principle eigenvalues plotted vs. PMI for the basal ROI.

Due to the statistically significant regional differences in the eigenvalues, and a significant interaction between the PMI and region, exponential models for the time varying diffusion parameters, E1, E2, E3, ADC, and FA were fitted separately for each ROI. The exponential growth model fit for the eigenvalues for each ROI are shown in Figures 2-4. Likewise, the ADC increased exponentially as the PMI increased as plotted in Figure 3.5-3.7 with and associated model fit. The FA exponentially decreased as the PMI increased as shown in Figures 3.8-3.10 demonstrating the directionality of diffusion decreases in the myocardium as it decomposes. A summary of the coefficients for the model fits for the diffusion parameters are shown in Tables 3.1-3.3. All of model fits passed the runs test for randomness indicating an acceptable model fit (Table 3.4).

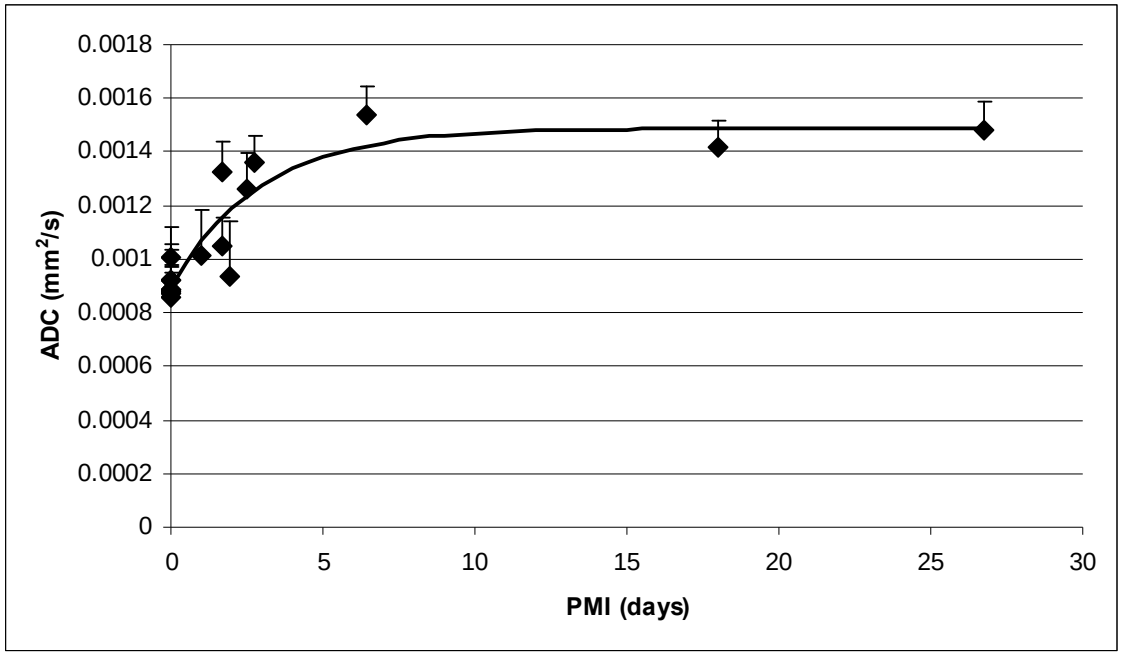

Figure 3.5 ADC plotted vs. PMI for the apical ROI.

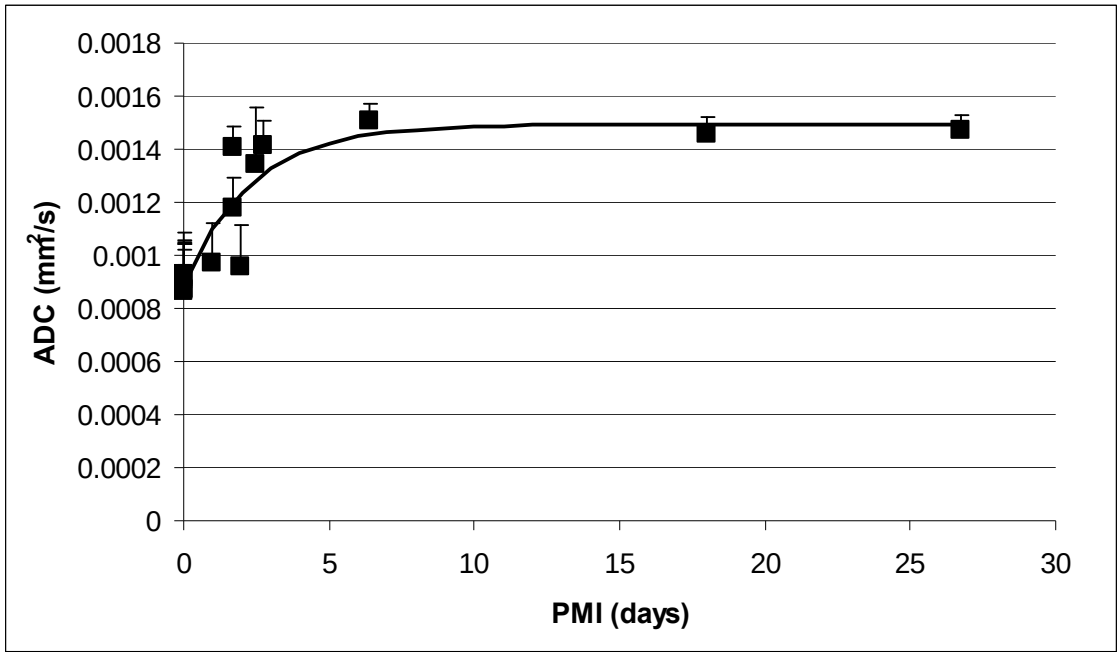

Figure 3.6 ADC plotted vs. PMI for the mid-ventricular ROI.

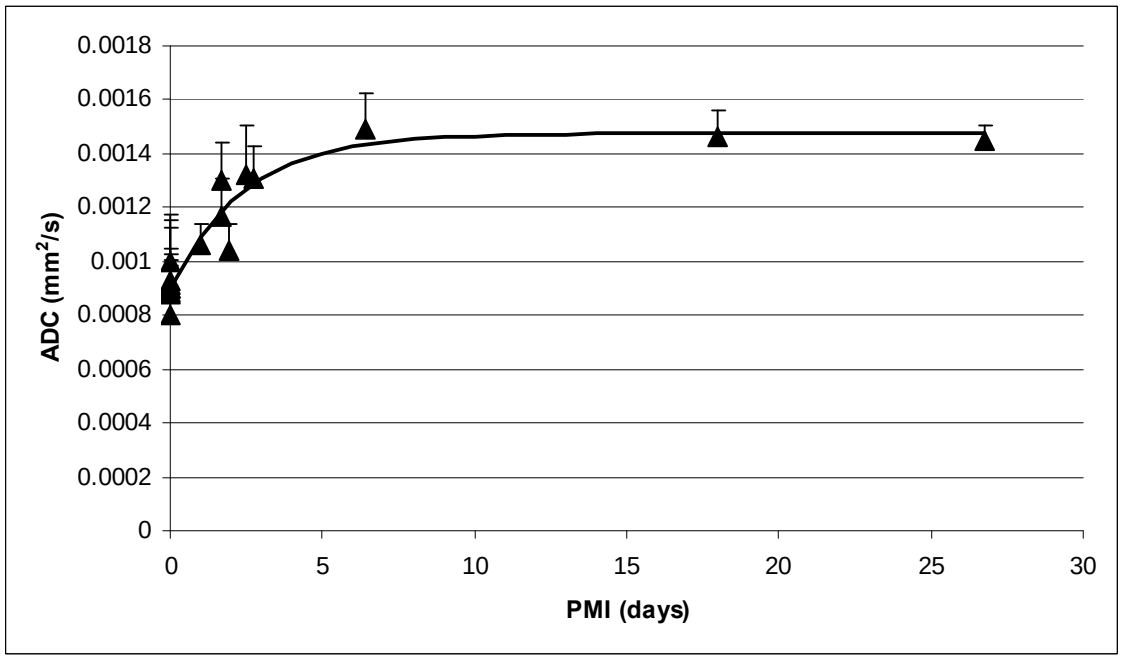

Figure 3.7 ADC plotted vs. PMI for the basal ROI.

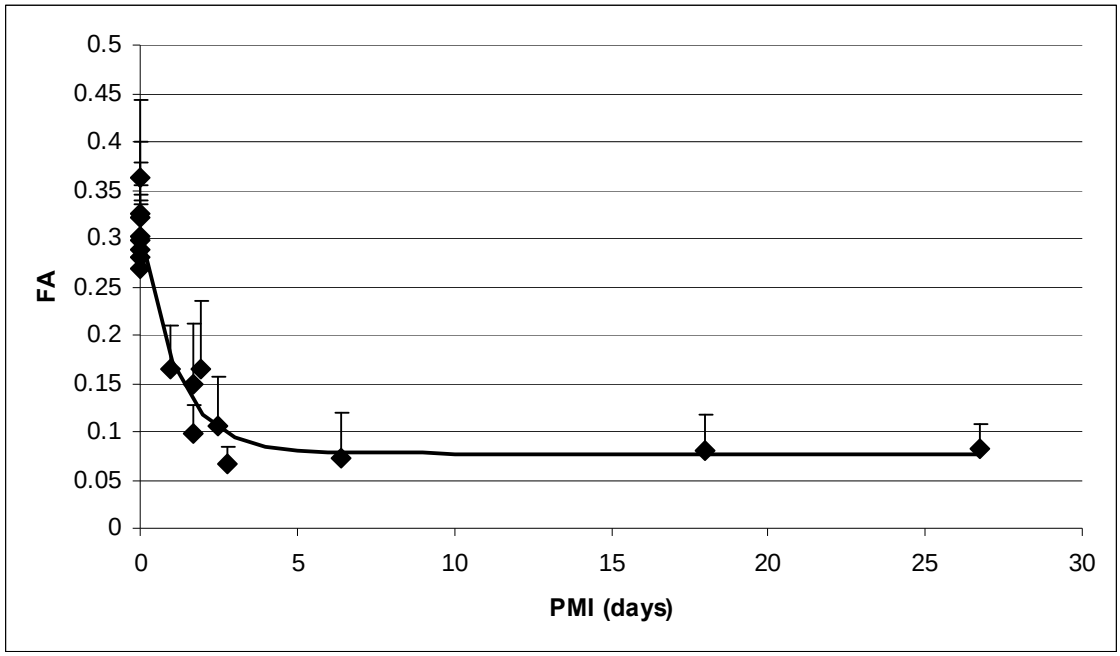

Figure 3.8 FA plotted vs. PMI for the apical ROI.

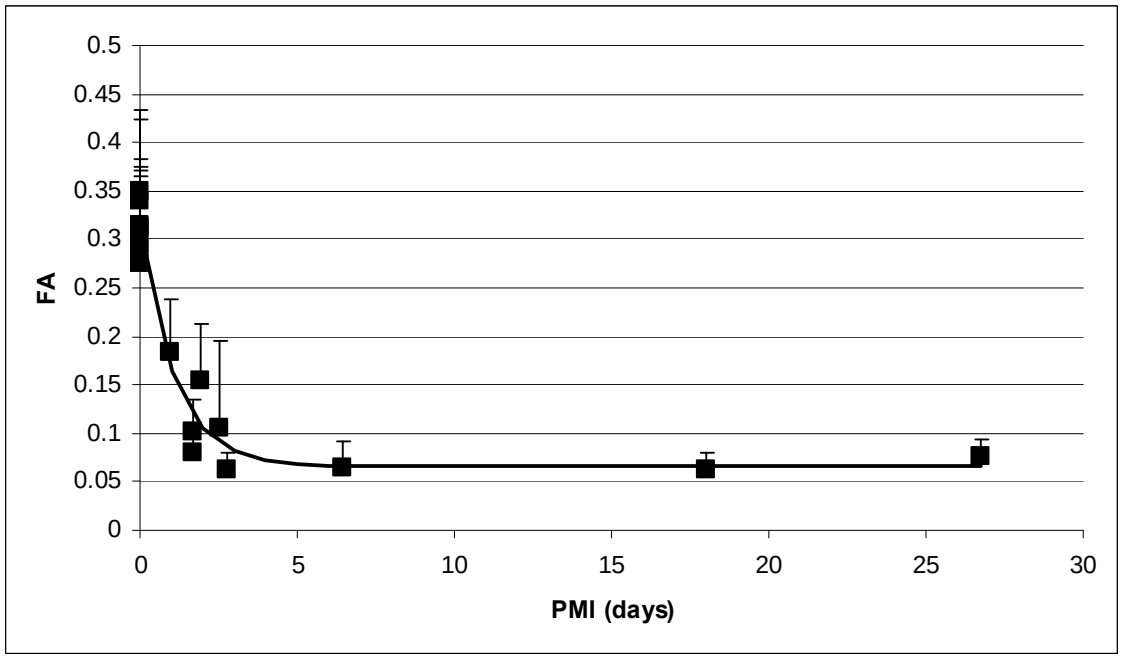

Figure 3.9 FA plotted vs. PMI for the mid-ventricular ROI.

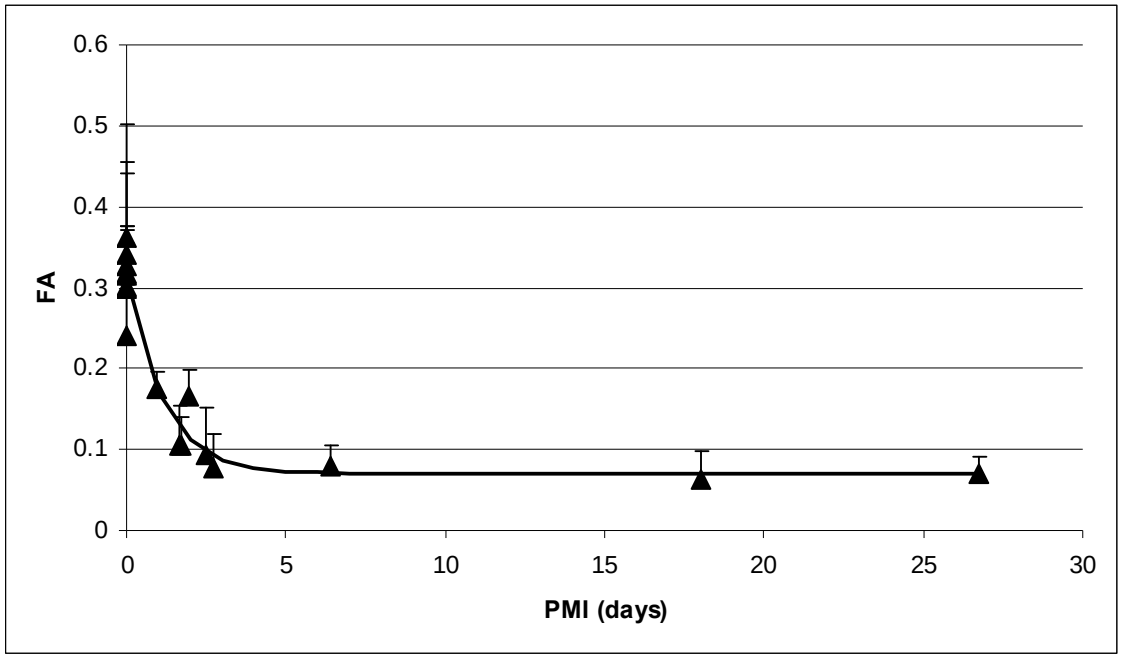

Figure 3.10 FA plotted vs. PMI for the basal ROI.

Table 3.1 Exponential model coefficients as determined by nonlinear regression for the apical ROI. Data are shown ± SEM.

Parameter	A	B	C
E1	0.001606 ± 7.5120e-005	0.0004114 ± 8.0290e-005	0.2250 ± 0.1062
E2	0.001476 ± 7.2710e-005	0.0006538 ± 8.0900e-005	0.3774 ± 0.1084
E3	0.001381 ± 7.0870e-005	0.0007154 ± 7.9190e-005	0.4049 ± 0.1044
ADC	0.001488 ± 6.9770e-005	0.0005925 ± 7.7140e-005	0.3415 ± 0.1031
FA	0.07739 ± 0.01561	0.2281 ± 0.01829	0.8712 0.2085

Table 3.2 Exponential model coefficients as determined by nonlinear regression for the mid-ventricular ROI. Data are shown ± SEM. .

Parameter	A	B	C
E1	0.001592 ± 7.0400e-005	0.0003960 ± 7.7110e-005	0.2970 ± 0.1350
E2	0.001487 ± 7.1320e-005	0.0006867 ± 8.0430e-005	0.4704 ± 0.1303
E3	0.001398 ± 6.9340e-005	0.0007372 ± 7.8480e-005	0.4992 ± 0.1270
ADC	0.001494 ± 6.8660e-005	0.0006069 ± 7.7010e-005	0.4303 ± 0.1277
FA	0.06561 ± 0.01431	0.2460 ± 0.01682	0.9059 ± 0.1895

Table 3.3 Exponential model coefficients as determined by nonlinear regression for the basal ROI. Data are shown ± SEM.

Parameter	A	B	C
E1	0.001576 ± 4.6990e-005	0.0003722 ± 5.1340e-005	0.2877 ± 0.09289
E2	0.001467 ± 4.9300e-005	0.0006508 ± 5.5500e-005	0.4571 ± 0.09185
E3	0.001380 ± 5.2700e-005	0.0007064 ± 5.9350e-005	0.4610 ± 0.09136
ADC	0.001475 ± 4.7570e-005	0.0005764 ± 5.3210e-005	0.4116 ± 0.08856
FA	0.07014 ± 0.01666	0.2430 ± 0.01955	0.8880 ± 0.2159

Table 3.4 Goodness of model fit.

Parameter	p-value (Apex/Mid-ventricle/Base)	R^2 (Apex/Mid-ventricle/Base)
E1	0.70 / 0.94 / 0.16	0.70 / 0.70 / 0.82
E2	0.32 / 0.32 / 0.55	0.85 / 0.87 / 0.93
E3	0.32 / 0.32 / 0.50	0.88 / 0.89 / 0.93
ADC	0.35 / 0.32 / 0.50	0.84 / 0.85 / 0.91
FA	0.32 / 0.069 / 0.84	0.94 / 0.96 / 0.94

Fiber Orientation

In all the hearts analyzed at the 0-day PMI, 3D reconstructions of fiber orientation within the slice plane and 2D contour plots of the fiber inclination angle demonstrated that fiber orientation varied as a function of the transmural depth, where the helix angle was negative at the epicardium and rotated to a positive helix angle at the endocardium, as reported in previous DTMRI and histological studies of human and mammalian hearts [4, 6-8, 12, 18]. Figure 3.11 shows a representative example of a contour plot of the fiber inclination angle obtained in a 0-day PMI fixed heart, where a smooth transition and rotation in the fiber inclination angle from the epicardium to the endocardium is clearly evident. Figure 3.12 shows the 3D fiber orientation reconstructed in the same slice plane as Figure 3.11.

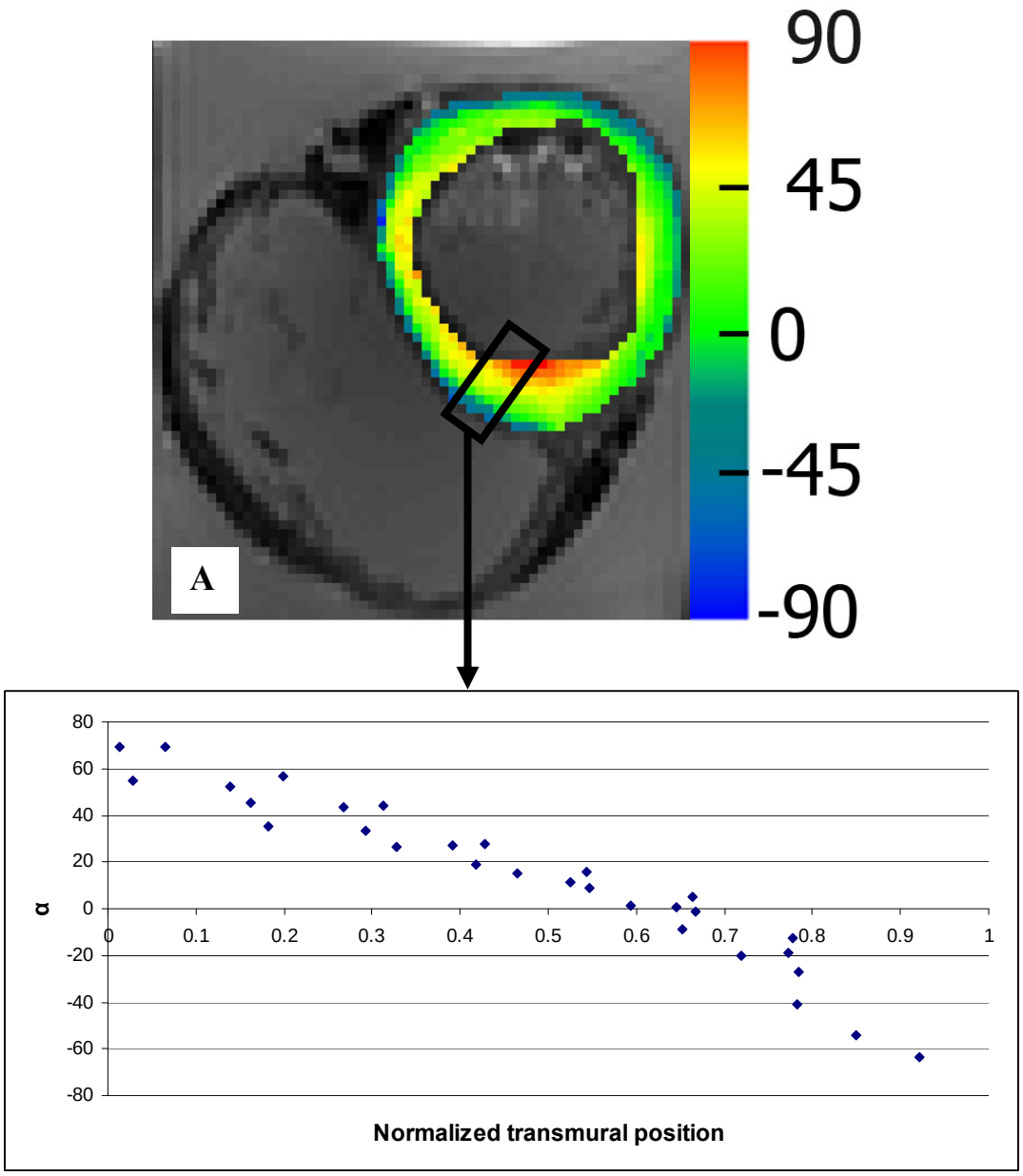

Figure 3.11 (A) 2D contour plot of the fiber inclination angle α in a human heart fixed directly postmortem (PMI=0) (B) Scatter plot of the fiber inclination angle in the indicated region demonstrating the smooth transition in the helix angle over the transmural depth.

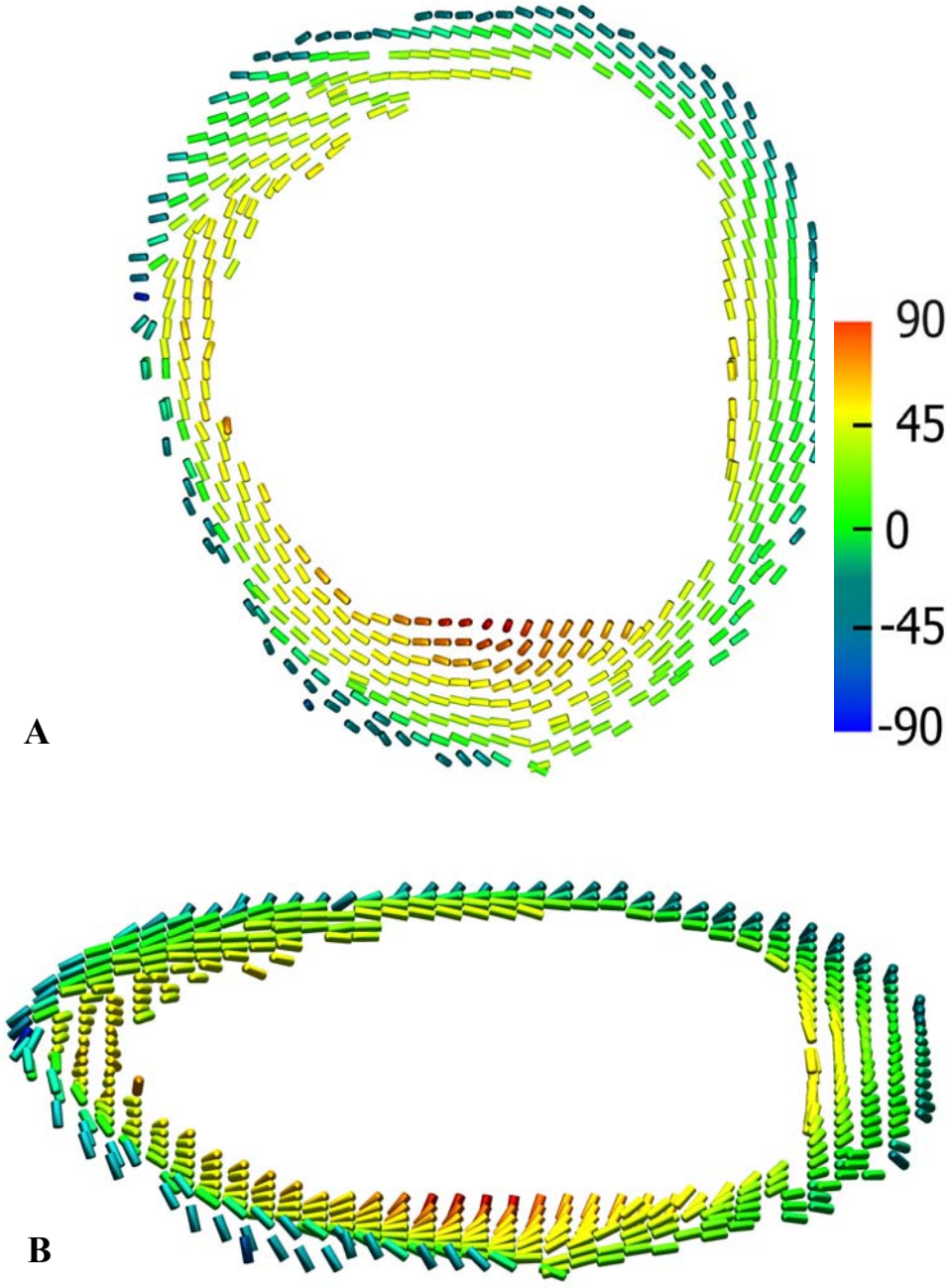

Figure 3.12 3D reconstruction of fiber orientation in a heart fixed directly postmortem (PMI=0) as viewed directly above from the base (A) and at an oblique angle above the short-axis (B). This reconstruction represents the same slice plane as in Figure 10.

After analysis of the reconstructions of fiber orientation in hearts with a PMI>0, it was noted that beginning with the 6-day PMI, the first eigenvector of diffusion did not generate realistic contour plots of fiber orientation, as the transmural variation in α did not necessarily rotate from a negative to a positive angle from the epicardium the endocardium (Figures 3.13-3.14). In addition, there were some instances where fiber orientation was discontinuous and changed rapidly from pixel to pixel, which is not plausible based on current knowledge of the transmural variation in fiber orientation.

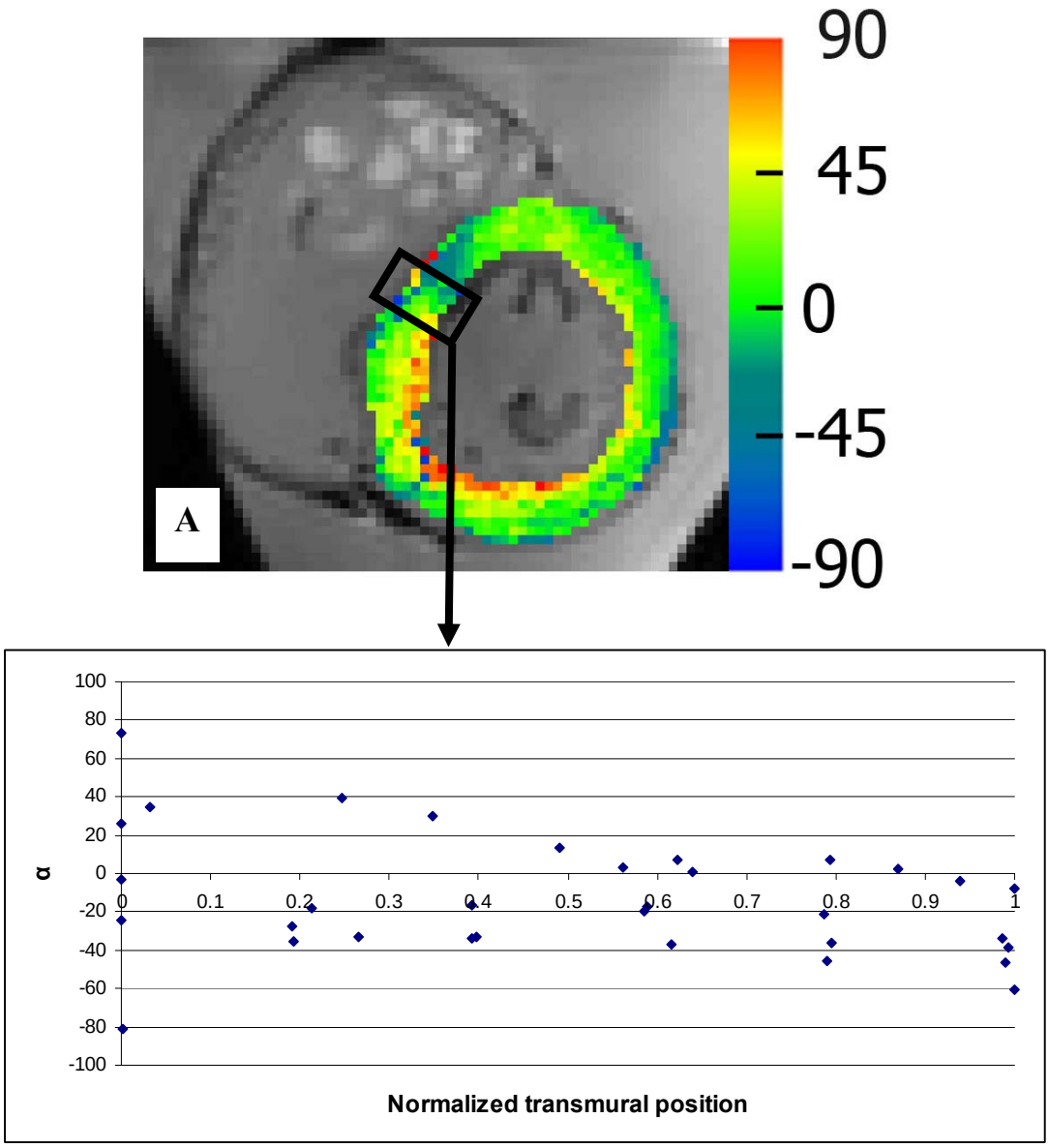

Figure 3.13 (A) 2D contour plot of the fiber inclination angle α in a human heart fixed with a PMI=6.4 days. (B) Scatter plot of the fiber inclination angle in the indicated region, where a smooth transition in the helix angle over the transmural depth was not evident.

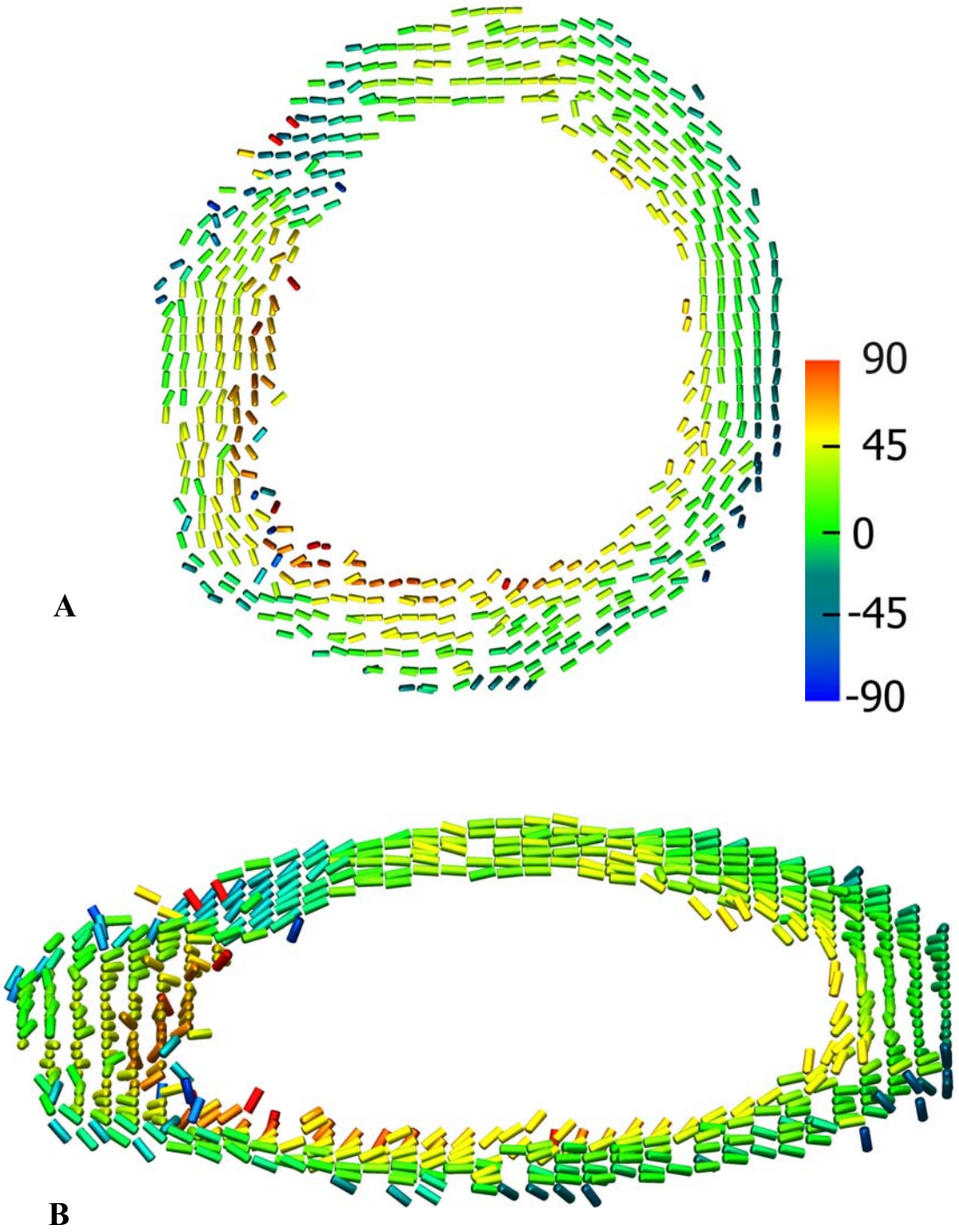

Figure 3.14 3D reconstruction of fiber orientation in a heart fixed with a PMI=6.4 days as viewed directly above from the base (A) and at an oblique angle above the short-axis (B). This reconstruction represents the same slice plane as in Figure 3.13.

Discussion

It is evident that as the PMI increases, diffusion in the myocardium becomes less restricted as indicated by the observed regional increases in the eigenvalues of diffusion, ADC, and associated decreases in FA. Specifically, it was found that the FA decreases exponentially as the PMI increases, and the eigenvalues of diffusion and ADC increase exponentially with an increasing PMI. As such, the diffusion anisotropy or FA at PMI=0 was in good agreement with *in vivo* values [19]. In addition, it is noted that the increases in the secondary and tertiary eigenvalues of diffusion (radial directions of diffusion) were greater than the increases in the primary eigenvalue of diffusion (Figure 3.15). Considering these observations, we hypothesize that increased diffusivity and reduction in directionality are primarily due to the degradation or breakdown of myocyte membranes over time. Furthermore, because diffusion directionality or anisotropy (as primarily measured by FA) is the basis for the measurement of fiber orientation using DTMRI, it is inherent that any delays in tissue fixation after death will compromise the study of fiber orientation (however, not considering hearts properly preserved using cardioplegia and organ transplantation techniques).

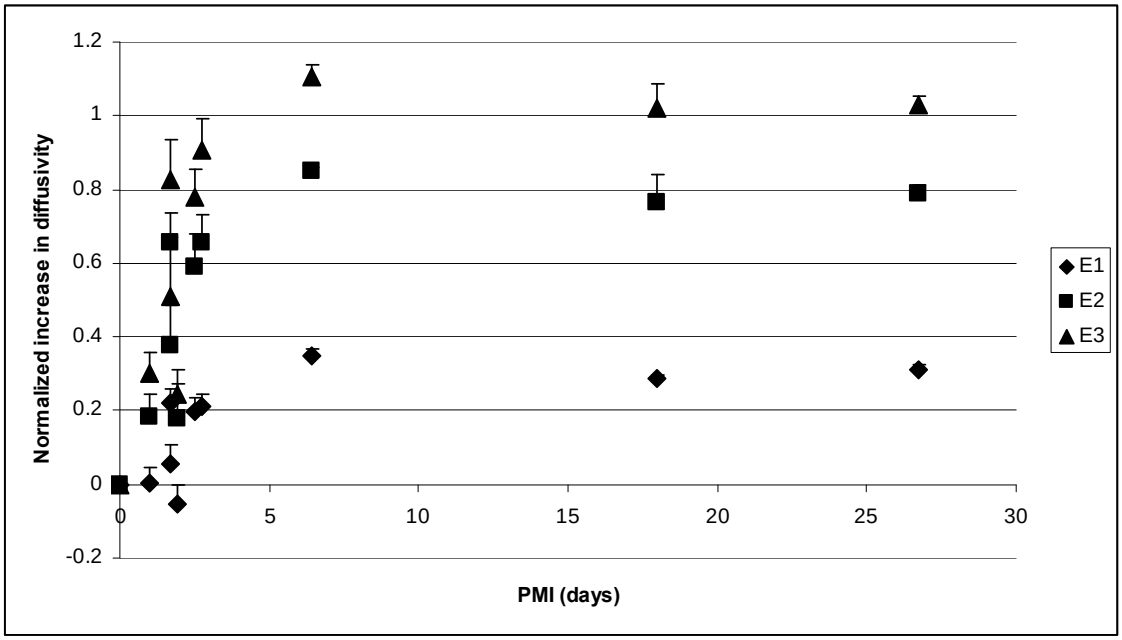

Figure 3.15 Normalized increases in diffusivity for the primary, secondary, and tertiary eigenvalues of diffusion relative to PMI = 0 (all ROIs pooled).

As such, previous investigators have noted a decrease in the FA and an increase in the ADC within infracted regions in the myocardium using DTMRI in both human hearts (*in vivo),* and in animal hearts fixed directly postmortem [1, 3, 19-21]. The results presented here indicate that the ability to determine infracted regions with DTMRI in post-mortem human hearts would be difficult, as the PMI would confound changes in the diffusion parameters due to pathology (ischemia, myocardial infarction) with changes attributed to the decomposition of the myocardium.

Overall, we have qualitatively shown that in hearts with PMIs > 6 days, reconstructions of fiber orientation using DTMRI become unrealistic and demonstrate regional discontinuity across the myocardial wall. Also, in some reconstructions with PMIs > 6

days, fiber orientation did not clearly rotate from the epicardium to the endocardium, contradicting current knowledge of the transmural arrangement of cardiac myocytes.

One limitation in this study is that we could not pinpoint the post-mortem time interval where the analysis of fiber orientation using DTMRI becomes invalid, as we were not able to obtain any hearts with a PMI between 2.75 and 6.4 days. However, considering the fitted exponential models of FA vs. PMI, and that diffusion directionality is the basis for the measurement of fiber orientation, it is estimated that a PMI < 3 days (approximately where the FA begins to increase above the 6-day PMI value) would still allow an accurate DTMRI measurement of fiber orientation.

Conclusions

In this novel dataset, it was found that diffusion becomes less restricted in the myocardium as it decomposes, as indicated by increases in the eigenvalues of diffusion and decrease in FA. Since diffusion anisotropy or directionality is the basis for the measurement of fiber orientation using DTMRI, any delay in tissue fixation after death (if not properly preserved using organ transplantation techniques) will therefore compromise the measurement of fiber orientation. Furthermore, based on the quantitative models of FA, and the qualitative analysis of reconstructions of fiber orientation, we recommend that hearts should be recovered within ~3 days in order to accurately reconstruct fiber orientation using DTMRI.

Chapter 4: A Swine Model of Dilated Cardiomyopathy: Model Development and the Subsequent Assessment of Fiber Orientation Using DTMRI[†]

[†] Authors: Michael D. Eggen, MS[1,2], Michael G. Bateman, MENG[1,2], Christopher D. Rolfes, BA[1,2], Stephen A. Howard, BA[1,2], Cory M. Swingen, PhD[3], Paul A. Iaizzo, PhD[2,4]

Department of Biomedical Engineering[1], Department of Surgery[2], Department of Medicine[3], Department of Physiology[4], University of Minnesota, Minneapolis, MN 55455

Preface

In the disease state of dilated cardiomyopathy, the ventricles enlarge, wall thickness is reduced, and ventricular pump function in severely compromised. The current hypothesis relative to this disease state is that ventricular fiber orientation is compromised during the progressive dilation of the ventricles, thus reducing pump function. However, it is currently unknown whether fiber orientation is altered in this disease state. Here, we investigated ventricular function, shape, anatomy, and fiber orientation in a high rate pacing induced model of dilated cardiomyopathy in swine using various MRI methodologies. After three weeks of high rate pacing, impaired function and ventricular dilation were evident, as the left ventricular volume doubled and the ejection fraction was markedly reduced to 10%. When fiber orientation was assessed *ex vivo* with DTMRI, we found that distribution of fiber inclination angles was largely unchanged. Therefore, pacing induced dilated cardiomyopathy in swine results in symmetrical dilation of the ventricles leaving the endogenous fiber orientation intact. Rearrangement of fiber orientation is unlikely a key contributor to the reduced pump function in this animal model.

For this work, I was responsible for all of the cardiac imaging. I was trained by Dr. Cory Swingen to acquire *in vivo* functional images on a1.5 tesla MRI scanner and also to perform *ex vivo* DTMRI using a 3 tesla unit. All of the images were acquired in the imaging lab located at the Fairview University Medical Center.

Furthermore, I was responsible for sterilizing and programming the pacemakers and leads, preparing the anesthetic regiment (with Dr Mike Loushin, Anesthesiology, Fairview University Medical Center), and perfusion fixation and cannulation of the hearts. Interestingly, I also had to carry a pager and was on call anytime there was a problem with any of the heart failure animals. I was also responsible for experimental design (with Dr. Iaizzo), data analysis, and preparation of this manuscript. The other authors listed in this manuscript were responsible for animal care, transport, and monitoring anesthesia during the imaging studies. Additionally, Dr. Iaizzo performed all surgeries for these experiments. I also have contributed to the initial model development, as described in Appendix A.

Introduction

It is generally agreed that high-rate pacing-induced dilated cardiomyopathy (DCM) in animal models appropriately recreates the heart failure condition as observed in humans. Specifically, in our lab, we have developed a high-rate pacing model of DCM in swine. By pacing swine hearts at a high rate (200 beats per minute) in the right ventricular apex for a 3-4 week period, dramatic changes in both cardiac anatomy and function develop, including: large increases in left ventricular volumes, wall thinning, mitral and tricuspid valve regurgitation, and left ventricular ejection fractions <25%. A draft manuscript describing the details of this animal model is included in Appendix A.

In general, the ventricles in patients with DCM remodel from an elliptical to a more spherical shape [1]. Furthermore, it is believed that fiber orientation in the LV wall changes from an oblique pattern to a more transverse or circumferential pattern [1]**.** This concept is illustrated in Figure 4.1.

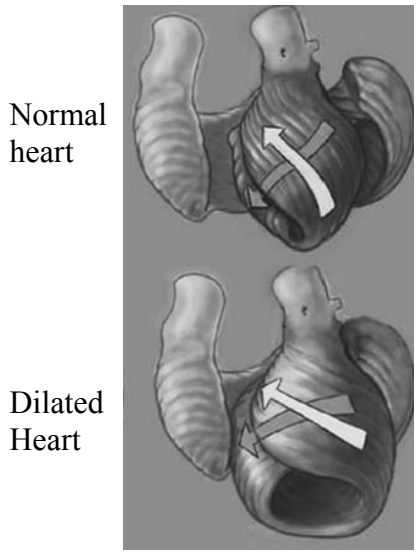

Figure 4.1 Illustration of potential changes in fiber orientation from a normal oblique pattern to a more transverse or circumferential pattern.(Reprinted, with permission, from: Buckberg, G.D., *Form versus disease: optimizing geometry during ventricular restoration.* Eur J Cardiothorac Surg, 2006)

Because oblique fiber orientation in the ventricular walls is considered important for maintaining ejection fraction, and the belief that ventricular dilation results in a transmural fiber orientation change to a more circumferential pattern, it has been hypothesized that such change may be a main cause of ventricular dysfunction in DCM [1]. Furthermore, mathematical predictions of ejection fraction are 30% for a heart with purely circumferential fibers versus 60% for one with an oblique pattern [2]. In addition, some successful surgical restorations for DCM patients such as SAVE (septal anterior ventricular exclusion) are attributed to relative correction of fiber orientation to a more oblique pattern [1, 3]. There have also been some newly developed surgical restoration concepts for DCM centered around restoring oblique fiber orientation [4].

However, it has not been established whether fiber orientation changes in DCM. In one study by Helm et al., fiber orientation was investigated using DTMRI in a dyssynchronous high rate pacing model of DCM [5]. The investigators noted chamber dilation and significant changes in wall thickness, but concluded that fiber orientation was largely the same as compared to healthy hearts removed from age and weight matched dogs. Furthermore, this study was limited, as no functional data was recorded and the extent of heart failure that was exhibited in these animals was largely unknown.

In this study, we investigated whether fiber orientation changes in DCM using DTMRI in a swine model of dilated cardiomyopathy. In addition, cardiac function and anatomy were assessed using MRI. We hypothesized that the fiber orientation in the high rate pacing model of DCM would shift to a more circumferential pattern, in agreement with the current body of literature.

Methods

In brief, high rate pacing from the right ventricular apex for a period of 3 weeks was employed in swine (n=10) to induce dilated cardiomyopathy. Weight matched animals (n=7) were used as controls. A description of the study progression follows.

In the paced group, the animals were sedated and MRI was used to assess cardiac function and anatomy using a 1.5 tesla scanner (as described in the following section) prior to implantation of the pacing system. Sedation was achieved with a constant infusion of midazolam (1.25 mg/kg/hr) and fentanyl (7.5 mcg/kg/hr). After the imaging

session, sedation was continued and the animals were transported back to the laboratory and a pacing system was implanted. Following implantation, the pacemaker was subsequently turned on at a rate of 200 beats per minute and the animal was allowed to recover. After 3 weeks of pacing, the animals were sedated, pacing was terminated, and cardiac function and anatomy were assessed again using MRI. Following this final imaging session, the animals were transported to the lab and the heart was removed via a median sternotomy after being arrested in end-diastole with cold cardioplegia. Following excision, the heart was perfusion fixed according to the methods described in Chapter 3. Further details regarding the implantation of the pacemaker and associated surgical procedures are described in Appendix A.

For the control group, animals were sedated and function and anatomy were assessed using MRI. Following the imaging session, the animals were transported back to the laboratory and the heart was removed using the same procedures as were employed in the paced group. The animals used for the control group were weight matched to the measured weight in the paced group after 3 weeks of pacing.

Additionally, for the paced animals, the body weight was recorded at the time of implantation and after 3 weeks of pacing, and the heart weight was recorded at the time of termination. For the control group, both the heart weight and body weight were recorded on the study day.

In Vivo Functional and Anatomical Assessment Using MRI

For each heart, a set of cines were acquired in 3 standard anatomical planes to assess both cardiac anatomy and function; (1) a four chamber-cine, (2) a two-chamber-cine, and (3) a series 5 consecutive slices in the cardiac short-axis which were equally spanned between the base and the apex. A 1.5 tesla Siemens Avanto scanner was used to acquire all of the images. From these images, stroke volume and ejection fraction were the functional parameters assessed. As such, the following anatomical parameters were assessed: left ventricular mass, end-diastolic volume, end-systolic volume, sphericity index, and the end-diastolic wall thickness. The sphericity index is a measure of how closely the shape of the left ventricle resembles a sphere, and is defined as the ratio between the ventricular short-axis (at the mid-ventricular level) and the long axis [6]. For this parameter, increasing values indicate a more spherical shape. An example calculation of the sphericity index is shown in Figure 4.2. The sphericity index was calculated from the four chamber view in end-diastole for all animals. For a further description of the functional parameters listed and associated methods of calculation, see Chapter 1.

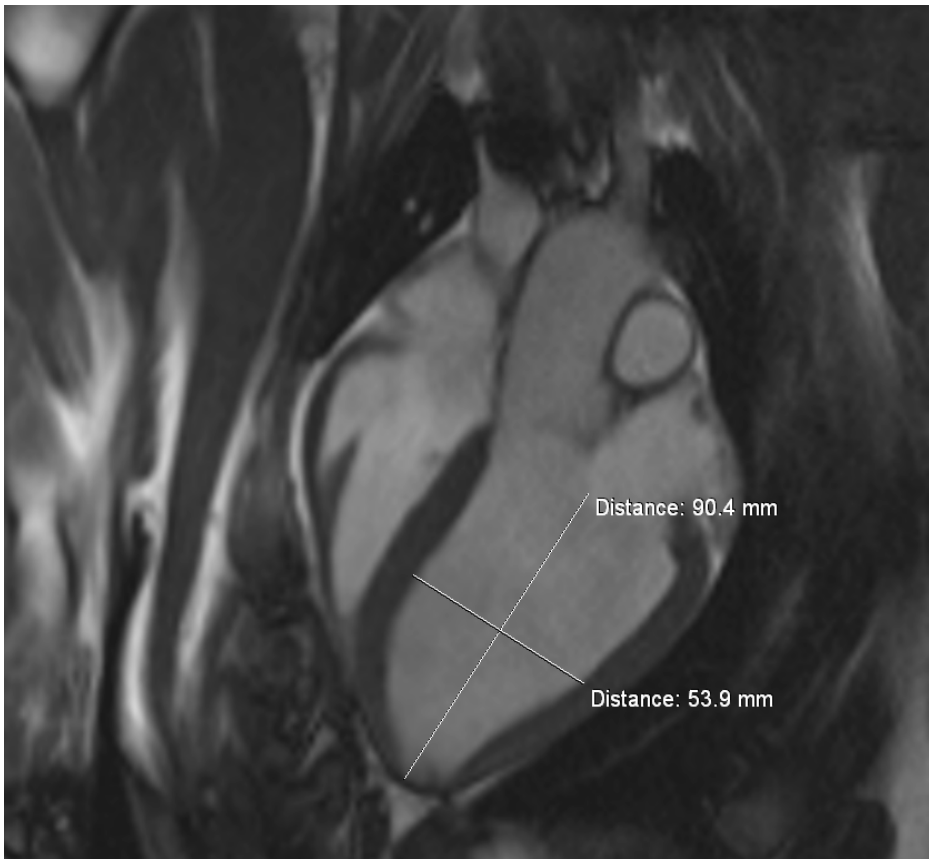

Figure 4.2 Demonstration of the measurement of the sphericity index in a four-chamber view of a control animal. In this example, the sphericity index was 0.60.

Ex Vivo Diffusion Tensor Magnetic Resonance Imaging

DTMRI was used to assess fiber orientation in the left ventricle as described in Chapter 2 and Chapter 3 except with the following changes in acquisition parameters: TE=93 ms; TR=15000 ms; FOV=160 × 160 mm^2; slice thickness = 2 mm; slice spacing = 0 mm. A total of 45-55 slices were acquired to image the entire left ventricular short axis. These changes resulted in a higher resolution (1.25 x 1.25 x 2 mm^3) and also increased the acquisition time for each heart (~37 min). In addition, due to the increased number of slices acquired, the hearts were embedded in 0.75% agar gel and surrounded by

sound proofing material prior to imaging in order eliminate any diffusion artifacts caused by vibration of the scanner bed.

Data Processing and Statistical Analysis

For all anatomical and functional parameters, a one-way analysis of variance was used to compare control, pre-implantation, and post-pacing values. If significant effects were found, individual pairwise comparisons were performed using a bonferroni correction for sample size. Data were considered statistically significance for $p<0.05$.

In order to test the hypothesis that myofibers become arranged in a more circumferential pattern in DCM, the distribution of the primary fiber orientation or inclination angle α was studied in the left ventricle. A total of 15 slices were analyzed spanning 5 regions across the left ventricle from the base to the apex as shown in Figure 4.3, where 3 slices were included in each region. For the analysis, the fibers were first grouped in 15° intervals from -90° to 90° (for a total of 12 groups) in each slice. Then, the percentage of fibers in each interval relative to the total number of fibers in the slice was calculated. Therefore, a histogram consisting of 12 groups for each slice was obtained. For comparison, the fraction of fibers in each bin of the histogram for a given region in the normal hearts was tested against the corresponding region in the failing hearts using a one-way analysis of variance. A p-value <0.05 was considered statistically significant.

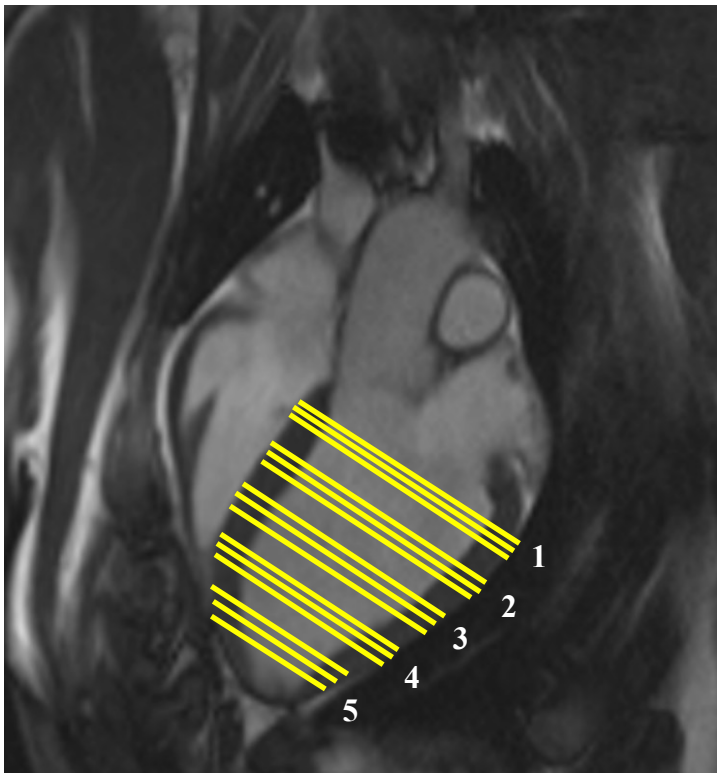

Figure 4.3 Regions and slices used for the measurement of fiber orientation. Each region consisted of 3 slices (yellow).

Results

Cardiac Function and Anatomy Assessed With MRI

Shown in Figure 4.4 and 4.5, are representative images acquired in end-diastole for a normal and high rate paced (failing) heart. Global dilation of both ventricles and dramatic changes in cardiac function were evident. Although not quantified, severe mitral and tricuspid valve regurgitation were noted in all animals in the paced group. Additionally, two of the high rate paced animals died during the final imaging experiment, and these hearts were excluded from the study of fiber orientation because they were unable to be perfusion fixed in end-diastole.

A summary of the measured functional and anatomical parameters is given in Figures 4.6-4.15. There were statistically significant increases in the left ventricular end-diastolic volume, end-systolic volume, left ventricular mass, heart weight, and heart weight to body weight ratio in the high rate paced animals as compared to both the control and the pre-implant values. Furthermore, the stroke volume, ejection fraction, and end-diastolic wall thickness were significantly reduced in the high rate paced animals as compared to both the control and pre-implant groups. These data were consistent with out previous experience using this animal model (Appendix A). Interestingly, the sphericity index did not increase in the high rate pacing group in comparison to the control and pre-implant groups. Also, there were no differences in functional or anatomical parameters between the control and pre-implant groups.

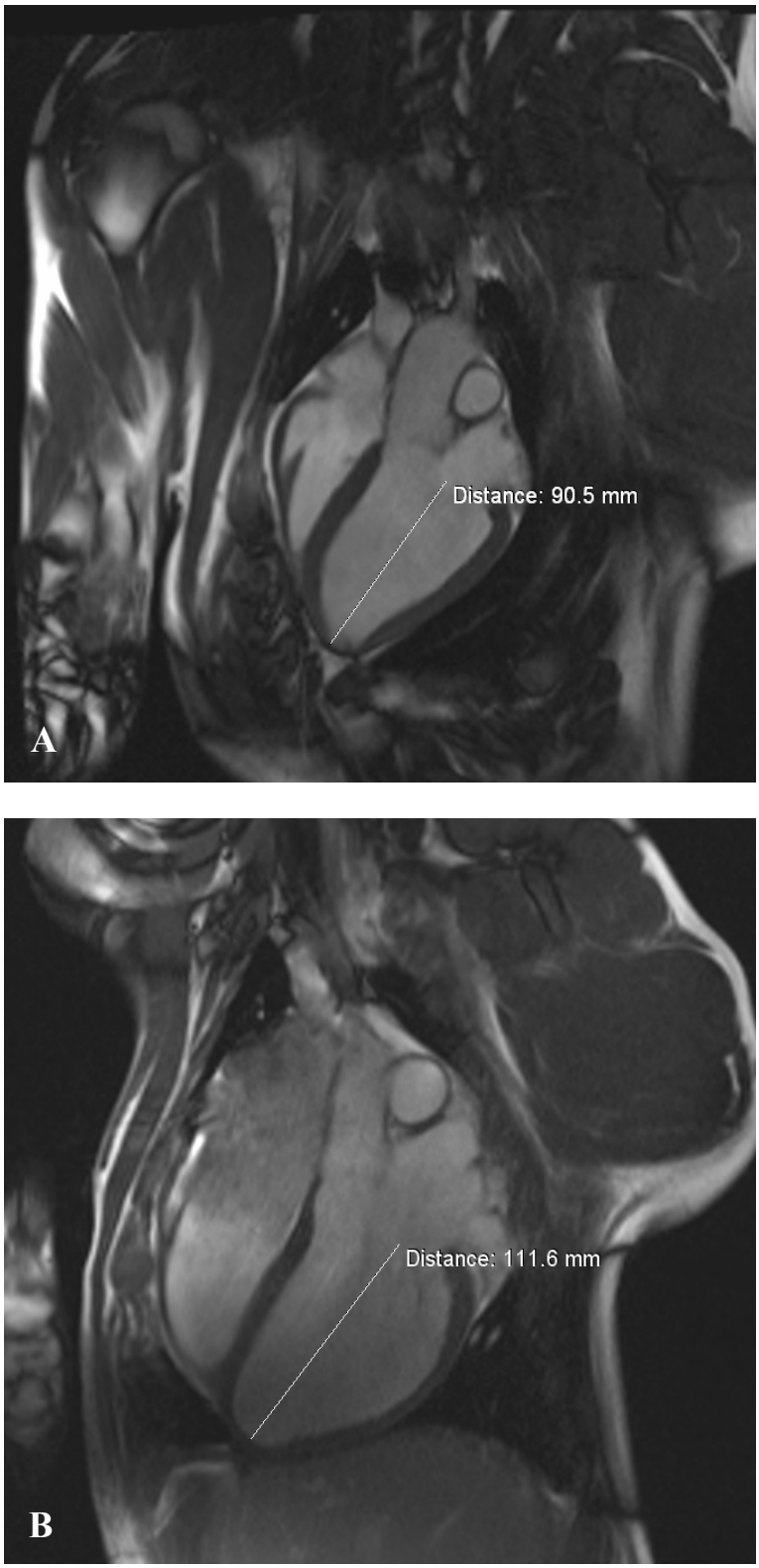

Figure 4.4 Representative four-chamber images from a control heart (A) and a failing heart (B) as assessed in end-diastole

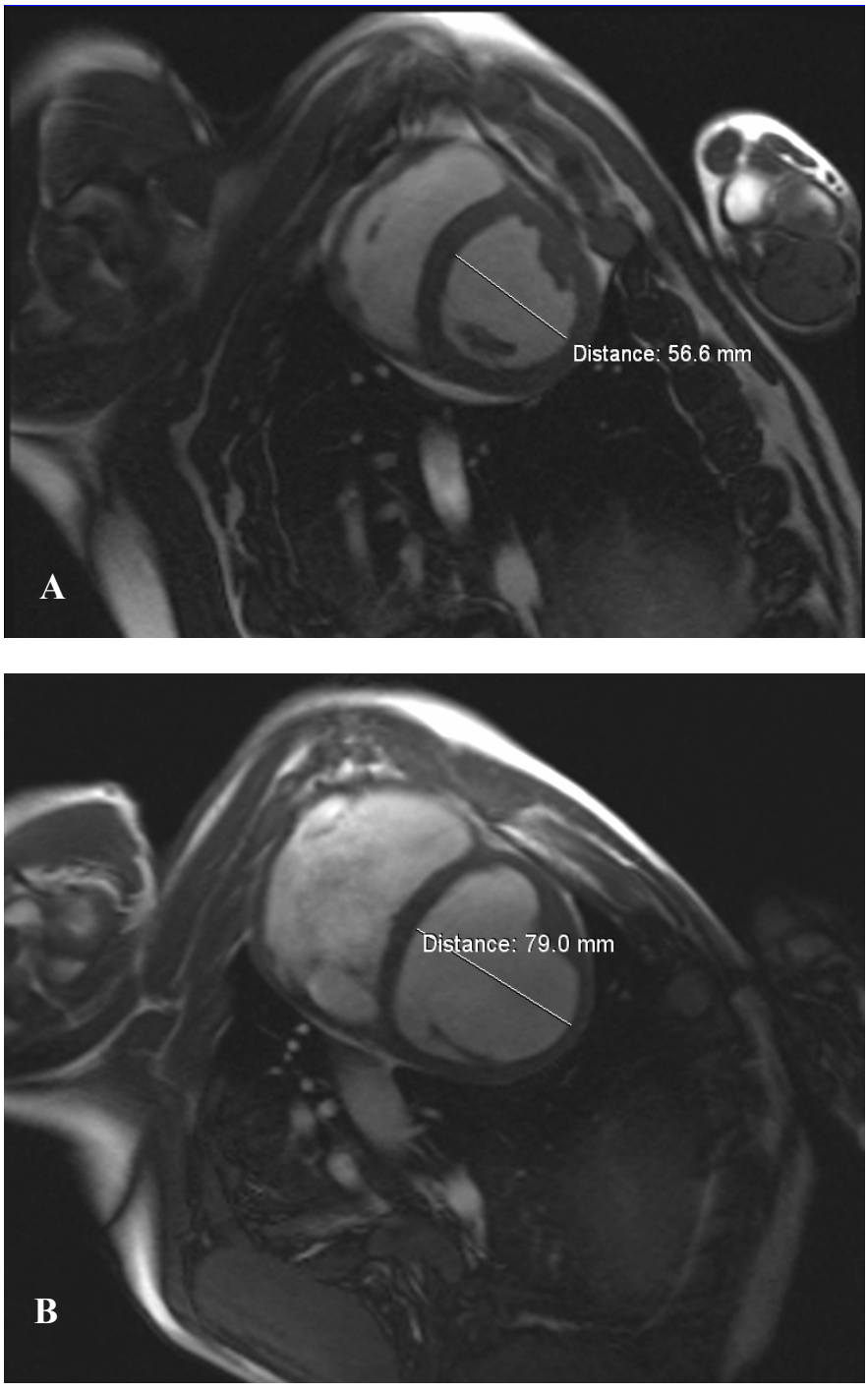

Figure 4.5 Representative short-axis images from a control heart (A) and a failing heart (B) as assessed from the basal location of the left ventricle in end-diastole

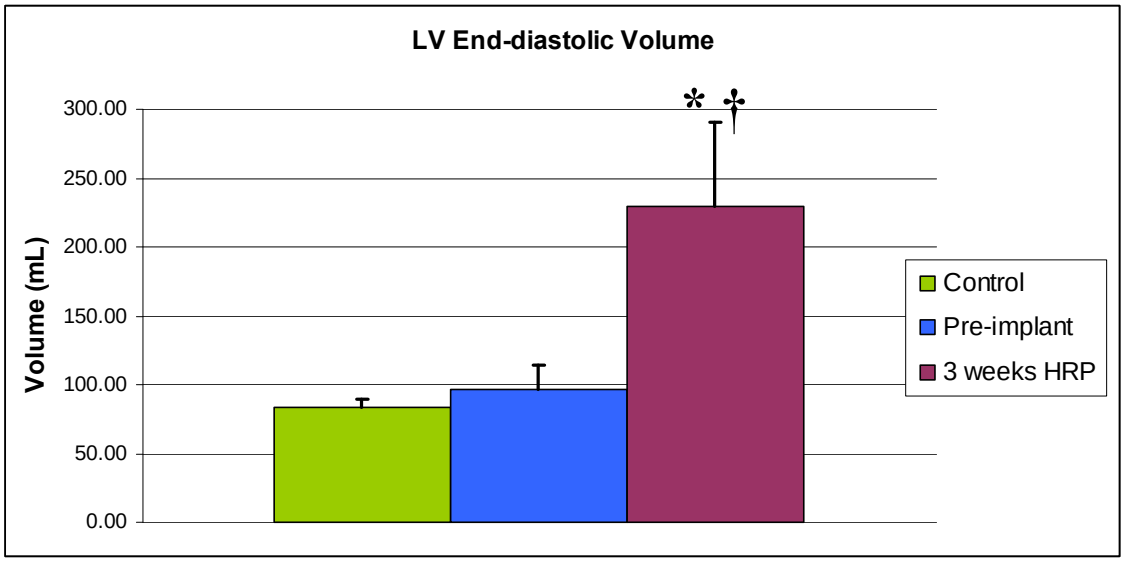

Figure 4.6 Left ventricular end-diastolic volume assessed with MRI. * p<0.05 HRP vs. control, † p<0.05 HRP vs. pre-implant, ‡ p<0.05 pre-implant vs. control

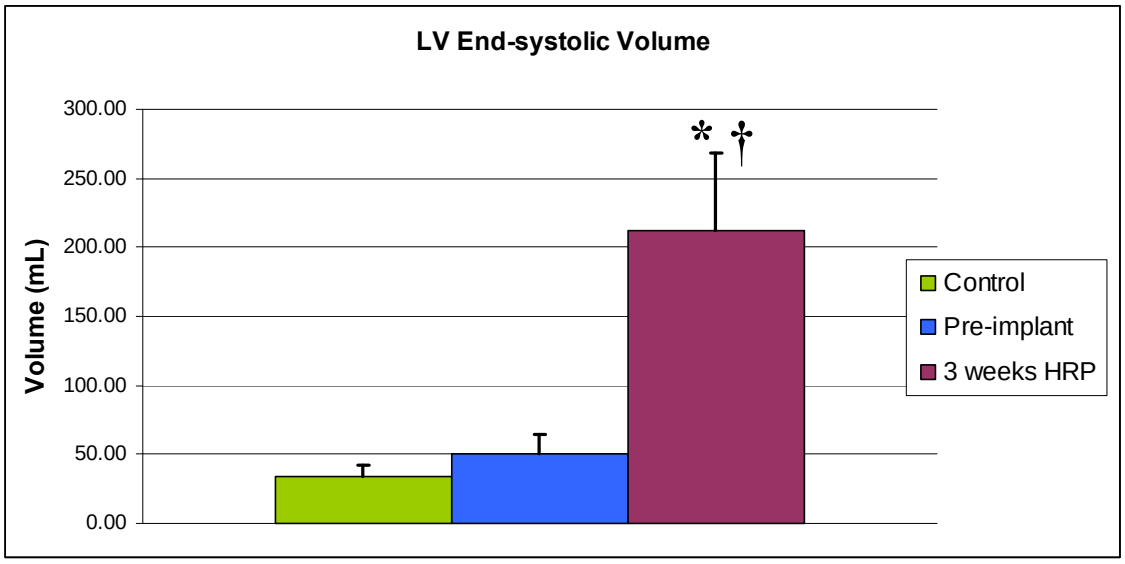

Figure 4.7 Left ventricular end-systolic volume assessed with MRI. * p<0.05 HRP vs. control, † p<0.05 HRP vs. pre-implant, ‡ p<0.05 pre-implant vs. control

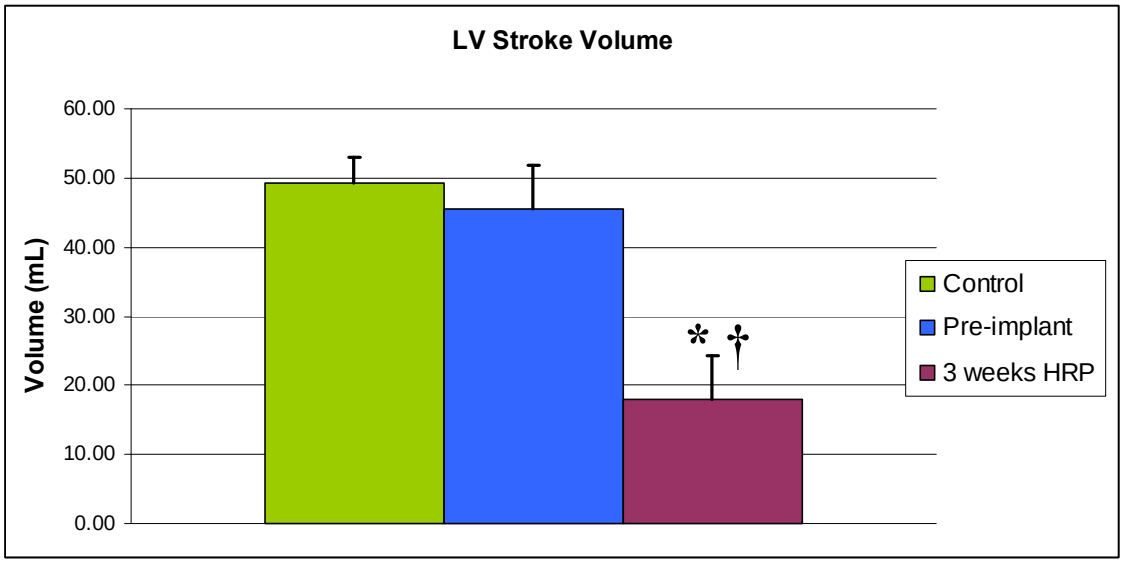

Figure 4.8 Left ventricular stroke volume assessed with MRI. * p<0.05 HRP vs. control, † p<0.05 HRP vs. pre-implant, ‡ p<0.05 pre-implant vs. control

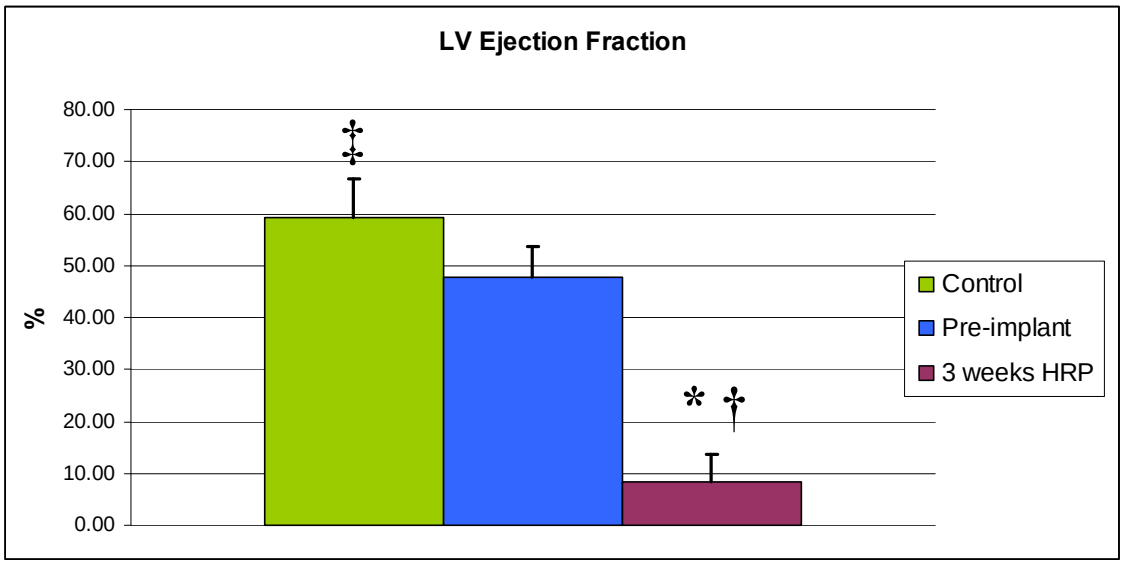

Figure 4.9 Left ventricular ejection fraction assessed with MRI. * p<0.05 HRP vs. control, † p<0.05 HRP vs. pre-implant, ‡ p<0.05 pre-implant vs. control

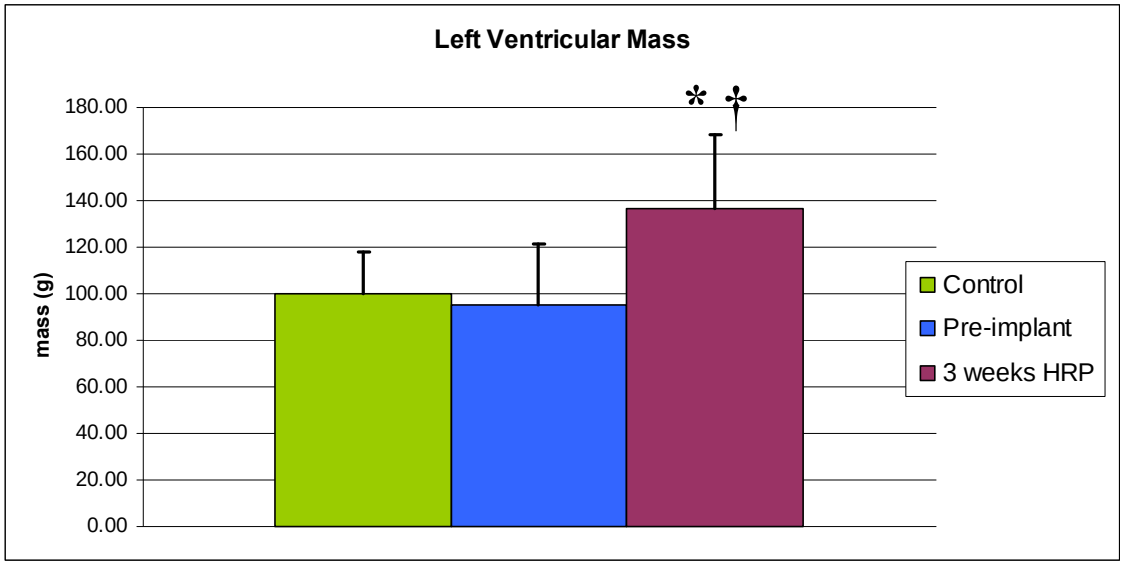

Figure 4.10 Left ventricular mass assessed with MRI. * p<0.05 HRP vs. control, † p<0.05 HRP vs. pre-implant, ‡ p<0.05 pre-implant vs. control

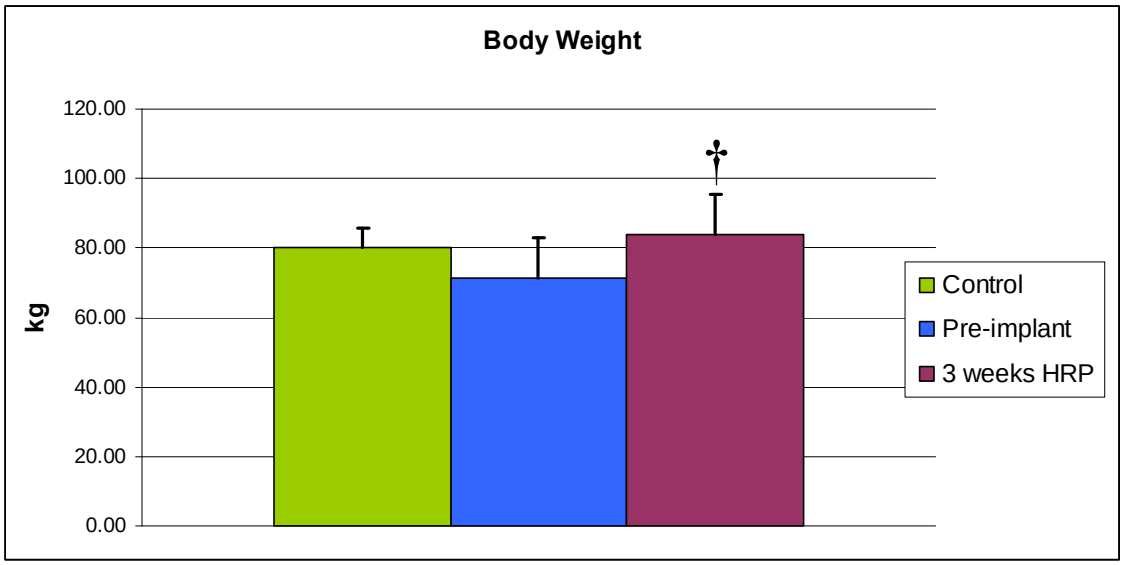

Figure 4.11 Comparison of body weights among the experimental groups.* p<0.05 HRP vs. control, † p<0.05 HRP vs. pre-implant, ‡ p<0.05 pre-implant vs. control

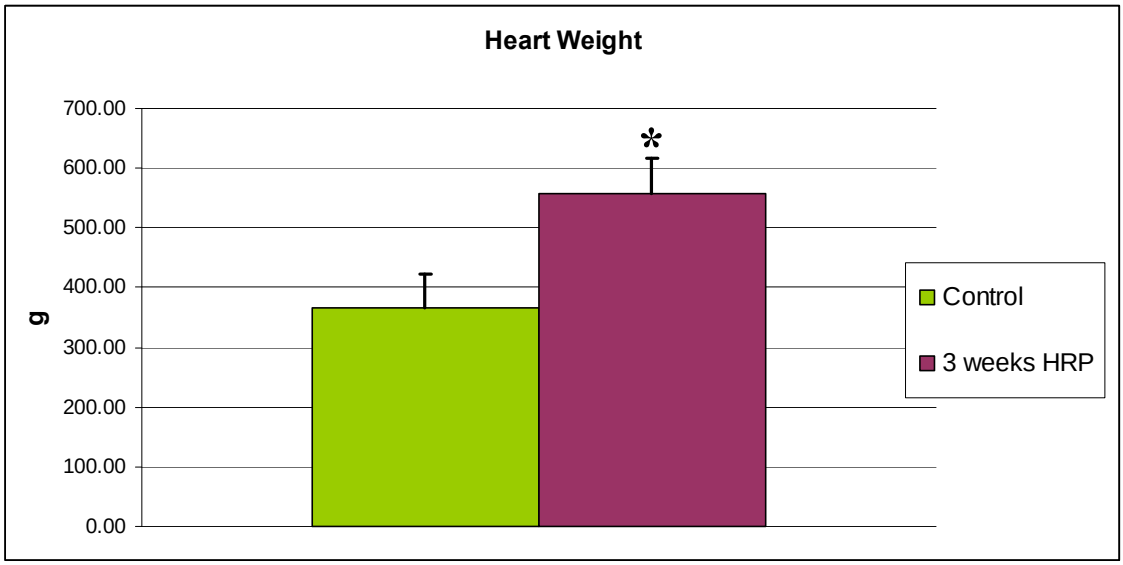

Figure 4.12 Comparison of heart weights among the experimental groups.* p<0.05 HRP vs. control, † p<0.05 HRP vs. pre-implant, ‡ p<0.05 pre-implant vs. control

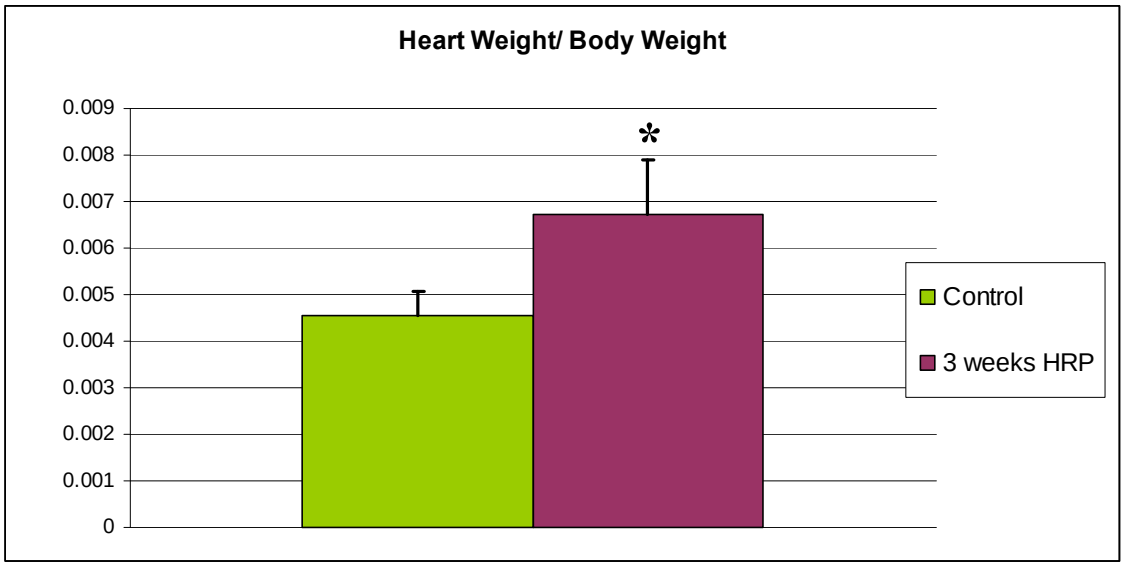

Figure 4.13 Comparison of the heart weight relative to the body weight.* p<0.05 HRP vs. control, † p<0.05 HRP vs. pre-implant, ‡ p<0.05 pre-implant vs. control

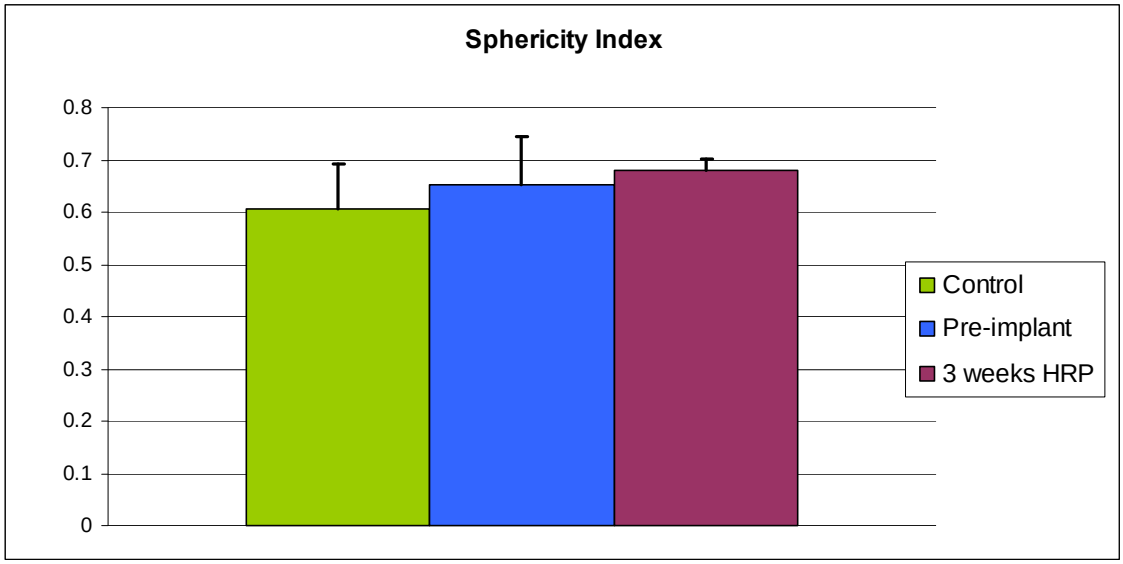

Figure 4.14 Sphericity index assessed with MRI from the four-chamber end-diastolic images. * p<0.05 HRP vs. control, † p<0.05 HRP vs. pre-implant, ‡ p<0.05 pre-implant vs. control

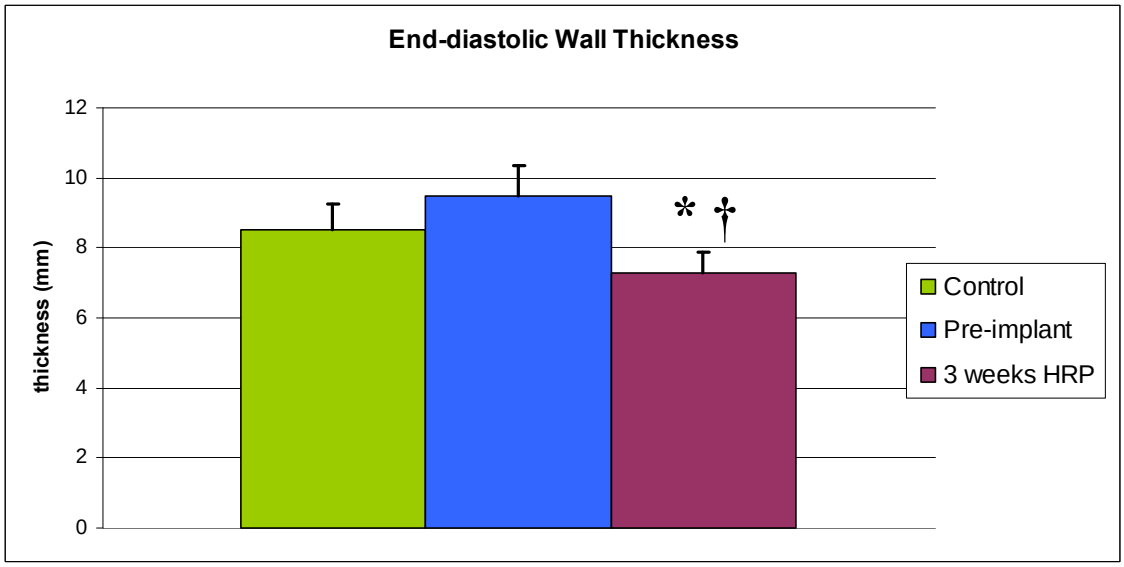

Figure 4.15 Left ventricular wall thickness assessed with MRI from the short-axis end-diastolic images. * p<0.05 HRP vs. control, † p<0.05 HRP vs. pre-implant, ‡ p<0.05 pre-implant vs. control

Fiber Orientation

Distributions of the fiber inclination angle or helix angle α are plotted in Figures 4.16-4.20. In these plots the x axis labels represent the following groupings of helix angles: **1** ($-90 < \alpha < -75$), **2** ($-75 < \alpha < -60$), **3** ($-60 < \alpha < -45$), **4** ($-45 < \alpha < -30$), **5** ($-30 < \alpha < -15$), **6** ($-15 < \alpha < 0$), **7** ($0 < \alpha < 15$), **8** ($15 < \alpha < 30$), **9** ($30 < \alpha < 45$), **10** ($45 < \alpha < 60$), **11** ($60 < \alpha < 75$), and **12** ($75 < \alpha < 90$). Overall, few significant increases in the fraction of circumferential helix angles were found.

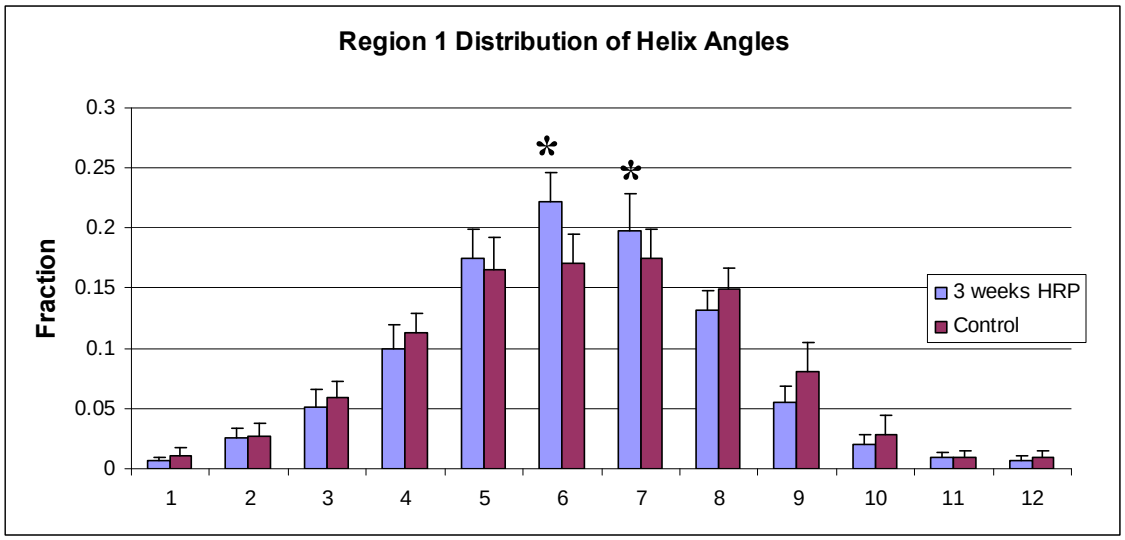

Figure 4.16 Region 1 distribution of α. * $p<0.05$ HRP vs. control

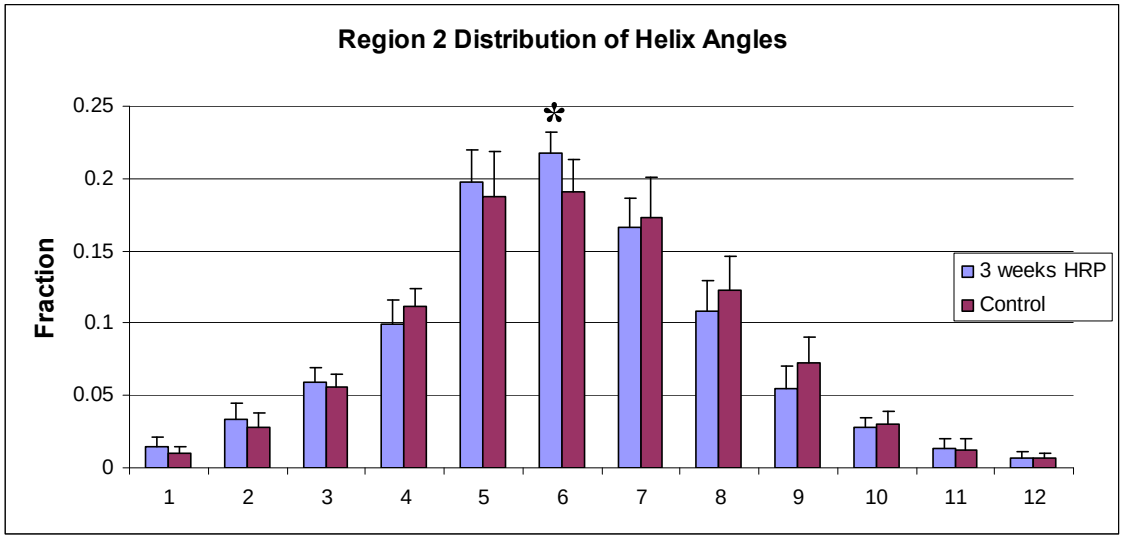

Figure 4.17 Region 2 distribution of α. * $p<0.05$ HRP vs. control

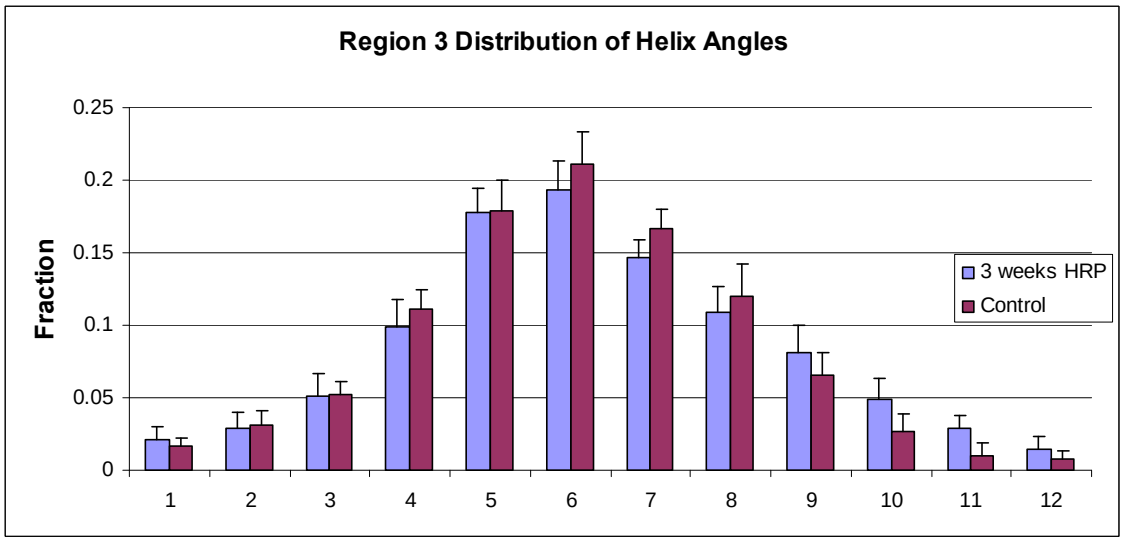

Figure 4.18 Region 3 distribution of α.

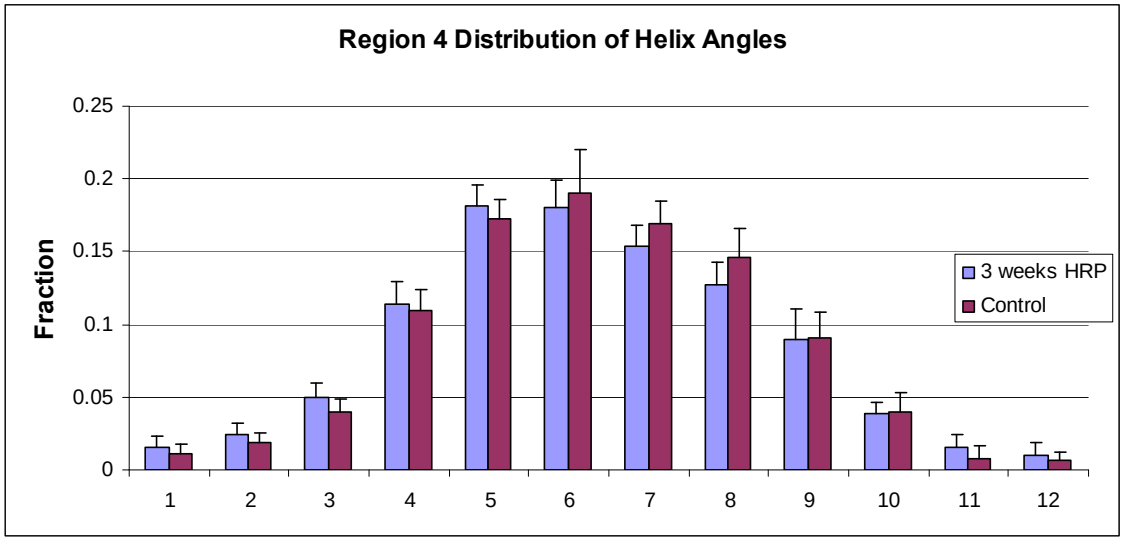

Figure 4.19 Region 4 distribution of α.

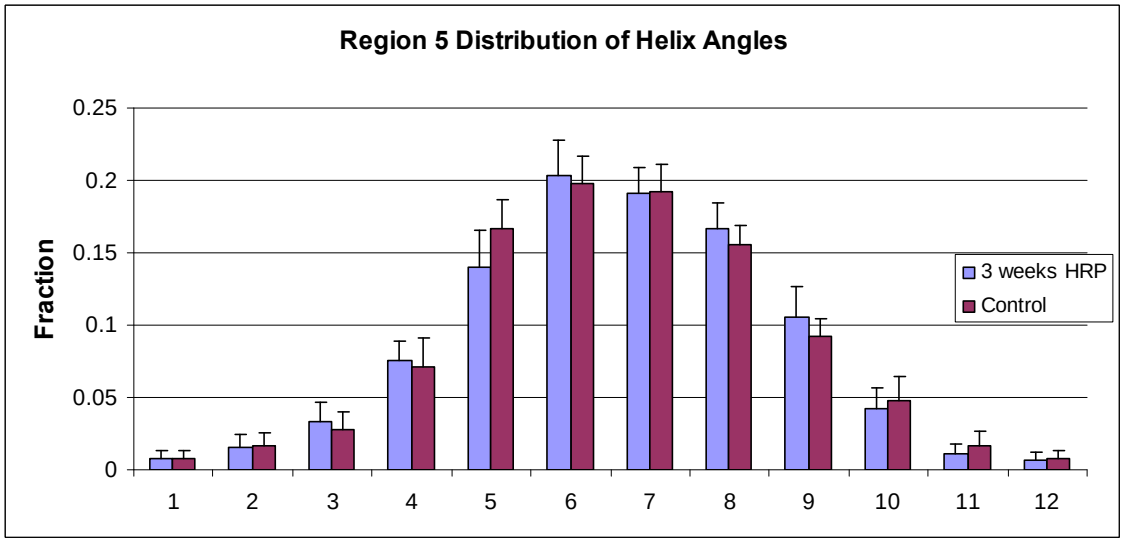

Figure 4.20 Region 5 distribution of α.

Discussion

Using MRI, both dramatic changes in cardiac function and anatomy were found. However, there was no global change in fiber orientation to a more circumferential pattern due to dilation of the left ventricle. Furthermore, there was global wall thinning, biventricular dilation, an increase in mass, but without an associated change in the sphericity index. Therefore, we hypothesize that the heart is dilating proportionally, as evident by the unchanged sphericicty index, which may not alter fiber orientation. This concept is further illustrated in Figures 4.21 and 4.22.

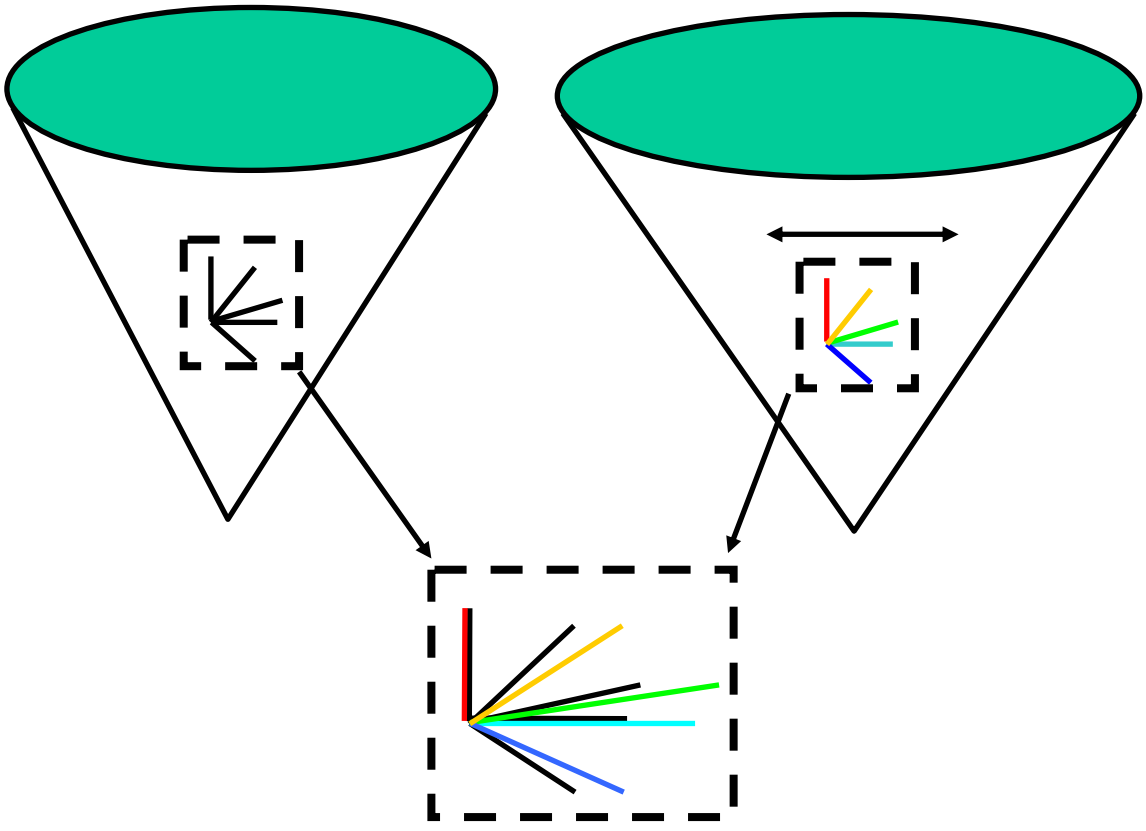

Figure 4.21 Expected change in fiber orientation in a heart only dilating along the short axis only. The sphericity index would increase, and the inclination angles would all be reduced, and therefore the distribution of fiber angles would be more circumferential.

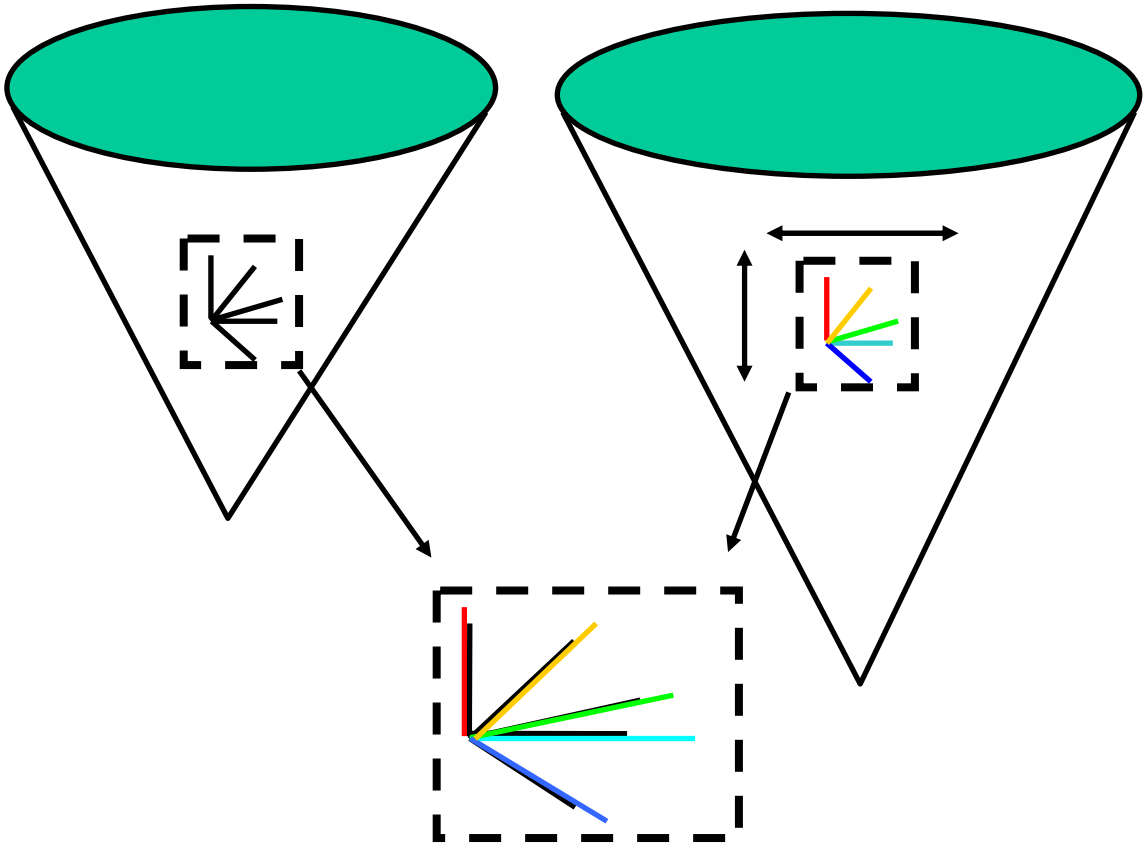

Figure 4.22 Expected change in fiber orientation in a heart dilating while maintaining the same aspect ratio. The sphericity index would remain the same, and the inclination angles would remain constant, and therefore the distribution of fiber angles would be relatively unchanged.

As such, chronic high rate pacing is known a volume overload model of heart failure, where cells elongate, rather than thicken radially. Because of the combination of wall thinning and increase in mass that was observed in this study, we hypothesize that the cardiac myofibers are getting thinner (which would reduce the myocardial wall thickness), but are also increasing in length such that net mass of each cell is greater (which allows dilation of the heart and increases the mass). This concept is supported by histological studies in a chronic canine high rate pacing model of dilated

cardiomyopathy, where it was found that the cells lost lateral aspect (reduction in width) and the Z lines were expanded in the contractile filaments [7].

Overall, rearrangement of fiber orientation is unlikely a key contributor to the reduced pump function in this animal model. Furthermore, in this model, we found that the heart did not become more spherical, as noted in human subjects. Future work in diseased human tissue is necessary to bring further insights into the rearrangement of myofibers in heart failure.

Conclusions

Cardiac functional anatomy and fiber orientation were investigated in a high rate pacing model of dilated cardiomyopathy in swine using MRI. After three weeks of high rate pacing, impaired function and ventricular dilation were evident, as the left ventricular volume doubled and the ejection fraction was markedly reduced to 10%. When fiber orientation was assessed *ex vivo* with DTMRI, we found that distribution of fiber inclination angles was largely unchanged. Therefore, pacing induced dilated cardiomyopathy in swine results in symmetrical dilation of the ventricles leaving the endogenous fiber orientation intact. This symmetrical dilation was evident in the measured sphericity index, which remained unchanged after pacing. Therefore, rearrangement of fiber orientation is unlikely a key contributor to the reduced pump function in this animal model. Future work in diseased human tissue will bring further insights into the rearrangement of myofibers in heart failure.

Chapter 5: Analysis of Fiber Orientation in Normal and Failing Human Hearts Using Diffusion Tensor MRI[†]

[†] Authors: Michael D. Eggen, MS[1,2], Cory M. Swingen, PhD[3], Paul A. Iaizzo, PhD[2,4] Department of Biomedical Engineering[1], Department of Surgery[2], , Department of Medicine[3],Department of Integrative Biology and Physiology [4], University of Minnesota, Minneapolis, Minnesota, 55455

This chapter published in the 2009 IEEE International Society of Biomedical Engineering Conference Proceedings.

Preface

The helical arrangement of cardiac myofibers is responsible for equalizing myofiber strain and maximizing the ejection fraction in a normal heart. In one form of chronic heart failure (CHF) known as dilated cardiomyopathy (DCM), the heart dilates, wall stress is increased, and ventricular pump function is reduced. We investigated whether myofiber orientation is altered in DCM by quantifying fiber orientation in excised human hearts using diffusion tensor MRI. Normal hearts (n=4) and failing hearts (n=4) were imaged in the plane of the cardiac short-axis at the base and mid-ventricular levels. There was a shift in the distribution of fiber inclination angles in the CHF hearts to a more oblique orientation at both the base and mid-ventricular levels. These preliminary results provide information about remodeling of the myocardial architecture in heart failure.

Furthermore, this data was presented and published as a conference paper in the recent IEEE ISBI meeting in Boston (June 2009). In this research, I was responsible for MR imaging of the hearts, data analysis, manuscript preparation, and recovery and perfusion fixation of the hearts (with Dr. Iaizzo). Dr. Cory Swingen was responsible for training me in the use of the 3.0 tesla clinical scanner at the Fairview University Medical Center, and also was responsible for creating the visualization tools in Matlab.

Introduction

Cardiac muscle fibers or myofibers are arranged as counter-wound helices encircling the ventricular cavities where fiber orientation is a function of their transmural location [1-3]. Myofibers are predominantly organized in the base-apex direction at the epicardial and endocardial surfaces and rotate to a circumferential direction in the midwall. This counter-wound helical structure is responsible for the torsional or wringing motion of the left ventricle and serves to equalize myofiber strain and workload, optimize the volume of blood ejected during systole (stroke volume), and store torsional energy in the intracellular and extracellular matrix during systole, and when released, increases ventricular filling during diastole [4-11]. Therefore, fiber orientation is a primary determinant of ventricular pump function.

Diffusion tensor MRI has been utilized to rapidly probe tissue microstructural organization in the brain, skeletal muscle, and cardiac muscle. Scollan and Holmes et al. have validated in formaldehyde-fixed hearts that the primary direction of diffusivity corresponds with the local myofiber orientation in diffusion tensor MRI [12-13]. This imaging technique allows the 3D reconstruction of ventricular fiber orientation in a matter of hours, as compared to months with classical histological methods.

More recently, diffusion tensor MRI has been extended to study cardiac fiber orientation in various pathological states including hypertrophic cardiomyopathy and post myocardial infarction. Tseng et al. determined that regionally disordered fiber orientation or fiber disarray exists in the hypertrophic myocardium [14]. Wu and

colleagues demonstrated using diffusion tensor MRI clinically that the percentage of left hand fibers increases from the remote zone, to the adjacent zone, and the infracted zone in patients with a myocardial infarction. It was also noted that an increasing percentage of left hand fibers in the infracted zone positively correlated with an increase in left ventricular ejection fraction [15]. However, this study did not include a comparison to normal hearts.

In this study, we compare fiber orientation in four normal excised human hearts to four enlarged hearts excised from donors with a history of CHF. To our knowledge, there has not been a characterization of myofiber reorganization in CHF in man.

Methods

Specimen Preparation

Freshly excised human hearts deemed not viable for transplant were obtained from Life Source, a non-profit organ procurement organization. The hearts were placed on ice immediately after excision. After cannulation of the pulmonary artery, aorta, superior vena cava, and one pulmonary vein the hearts were perfusion fixed in 10% buffered formalin for 24-48 hours under pressure such that the hearts retained an end-diastolic shape. As such, all of the hearts were perfusion fixed within 6 hours of excision. Four normal hearts, and four enlarged hearts removed from donors with a history of chronic heart failure were recovered and preserved using these processes. Table 5.1 lists the patient demographics and Figure 5.1 shows an example of an anatomic comparison between a normal and failing heart.

Table 5.1 Patient demographic information*

Heart #	Age (years)	Gender	Body weight (kg)	Heart weight (g)	Disease state
1	36	M	110.2	585.7	Quadriplegic, ventilator dependent, tracheostomy, subdural hematoma
2	53	M	74.7	431.01	No known cardiomyopathies
3	54	M	85.5	598.7	High blood pressure (>10 years),poor circulation, renal failure, diabetes, semilunar valvular regurgitation, intracranial hemorrhage
4	68	F	65.5	351.42	Stroke, high blood pressure for 30 years (medicated with atenolol, cozaar, aspirin)
5	79	F	95	980	Coronary artery disease, triple CABG, atrial fibrillation, CRT pacing system, shingles, arthritis, dilated ventricles
6	69	M	76.2	736.6	CABG, Hypertension, bioprosthetic aortic valve, ascending aortic aneurism, severe mitral valve regurgitation, dilated ventricles
7	61	M	105.9	586	Three stents, myocardial infarction, enlarged heart, intracranial hemorrhage
8	76	F	67	660.8	Coronary artery bypass, angioplasty, chronic heart failure, pacemaker, CAD, CABG, asthma

*Hearts 1-4 were grouped as normal, or free of cardiomyopathies for the comparison to the diseased hearts (5-8)
CABG=coronary artery bypass graft; CRT=cardiac resynchronization therapy, CAD=coronary artery disease

Figure 5.1 Anterior aspect of a perfusion fixed normal heart (left, heart #4) and a failing heart (right, heart #7).

Diffusion Tensor MRI

Diffusion tensor MRI was performed using a Siemens 3.0 Tesla MAGNETOM Trio scanner (Siemens, U.S.A.) that has a maximum gradient amplitude of 40mT/m. Prior to imaging, the hearts were placed in a polymer container and submerged in formalin to reduce any air tissue susceptibility artifacts. An 8-channel head coil was used for imaging and the bore temperature was approximately 25° C.

In order to determine the LV short-axis, first a set of scout images were acquired. A set of localizer images were then used to locate a pseudo LV long axis which spanned through the most apical portion of the LV. Subsequently, the LV long axis was defined by the intersection of two orthogonal planes, each of which were perpendicular to the

pseudo LV long axis and divided the LV into four quadrants spanning from the apex to the base. The cardiac short axis was defined as a plane perpendicular to the LV long axis.

The following acquisition parameters were used: TE=85 ms; TR=3000 ms; FOV=1.6 x 1.6 mm^2; slice thickness = 3mm, slice spacing = 6 mm, number of slices = 10; b-value = 1000 s/mm^2; number of diffusion gradient directions = 6; number of averages = 20; matrix size = 128 x 128. A null weighted image (b-value = 0) was also acquired with the six diffusion weighted images (b-value = 1000 s/mm^2) for each slice. The acquisition utilized a Siemens double spin-echo, echo-planar diffusion-weighted sequence which minimized eddy currents [16]. The acquisition time for each heart was approximately 7 min. Examples of the acquired images are shown in Figure 5.2.

Determination of Fiber Orientation

Three dimensional maps of fiber orientation were constructed using an in house analysis tool developed in MATLAB (The MathWorks, Natick, MA). The diffusion tensor for each imaging volume was calculated on a pixel by pixel basis using the solution developed by Basser and Pierpaoli [17]. After the tensor was determined for each imaging volume, the eigenvectors and eigenvalues were found by solving the eigensystem of the diffusion tensor. Since the diffusion gradients were applied relative to the patient frame of reference, the eigenvectors were rotated from the patient coordinate system into the image coordinate system for analysis of cardiac fiber orientation. Fiber orientation was taken as the maximum direction of diffusivity, or the first eigenvector of the diffusion tensor. The cardiac coordinate system used for the

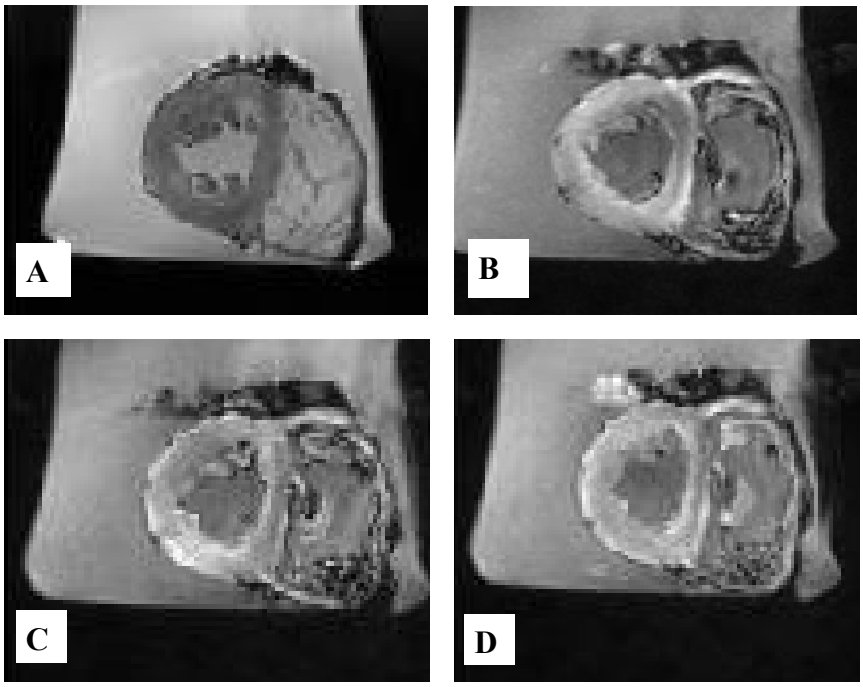

Figure 5.2 Null weighted image of a mid-ventricular slice for a normal heart (A). Diffusion weighted images for three of the six directions (B-D).

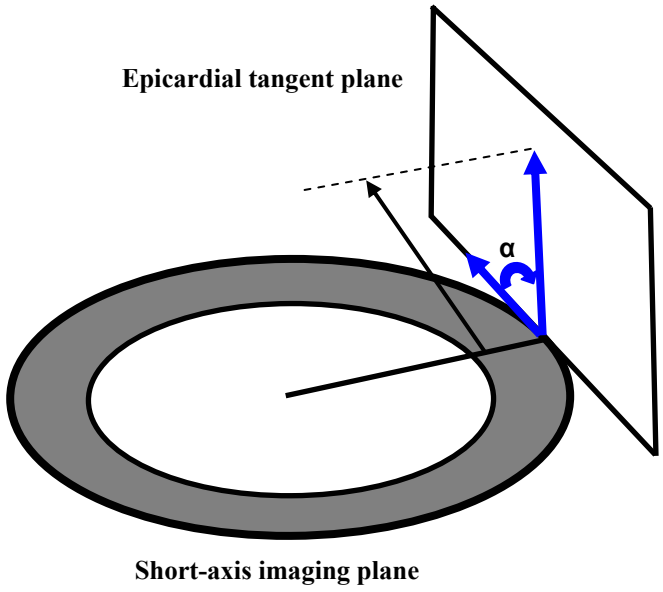

Figure 5.3 Definition of the helix angle α, where a positive angle is shown.

analysis of fiber inclination angles is depicted in Figure 5.3. The fiber inclination angle or helix angle α was defined as the angle between the local helix projected onto the epicardial tangent plane and the cardiac short-axis plane as described by Streeter et al. [3] and Scollan et al. [13]. Two slices for each heart were analyzed, at the base and mid-ventricular level. The analysis only included the left ventricle, and the papillary muscles were excluded from the analysis.

Results

Basal Level

The quantitative distribution of helix angles for the basal and mid-ventricular levels is plotted in Figures 5.4 and 5.5 respectively. A one way analysis of variance (ANOVA) was used to compare the percentage of fibers in the normal and failing hearts grouped in each bin of the histogram. Although there were no statistically significant differences between the normal and failing groups, the helix angles at the basal level of the failing hearts shifted to a more oblique pattern than in the normal hearts. For $\alpha < -40°$, and $\alpha > 40°$, the mean percentage of fibers increased in the failing hearts as compared to the normal group. It followed that the mean percentage of circumferential fibers for $40° > \alpha > -40°$ decreased in the failing hearts. A demonstration of this change in helix angle distribution can be seen in Figures 5 and 6. In a representative normal heart (heart 1, Figure 5.6) there is a smooth transition in helix angle from the epicardium to the endocardium with an overall high percentage of circumferential fibers. In contrast, the contour plot of failing heart 6 (Figure 5.7) demonstrates there is a higher percentage of

longitudinal fibers and regional disarray in the location of the longitudinal fibers, which have penetrated into the midwall.

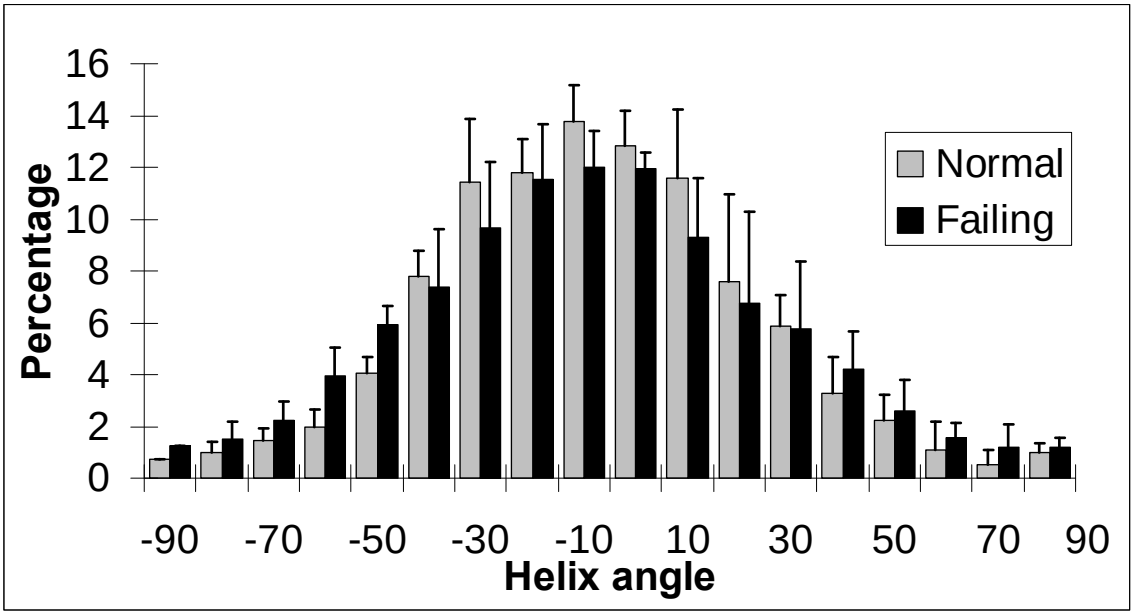

Figure 5.4 Quantitative distribution of fiber orientation at the basal level.

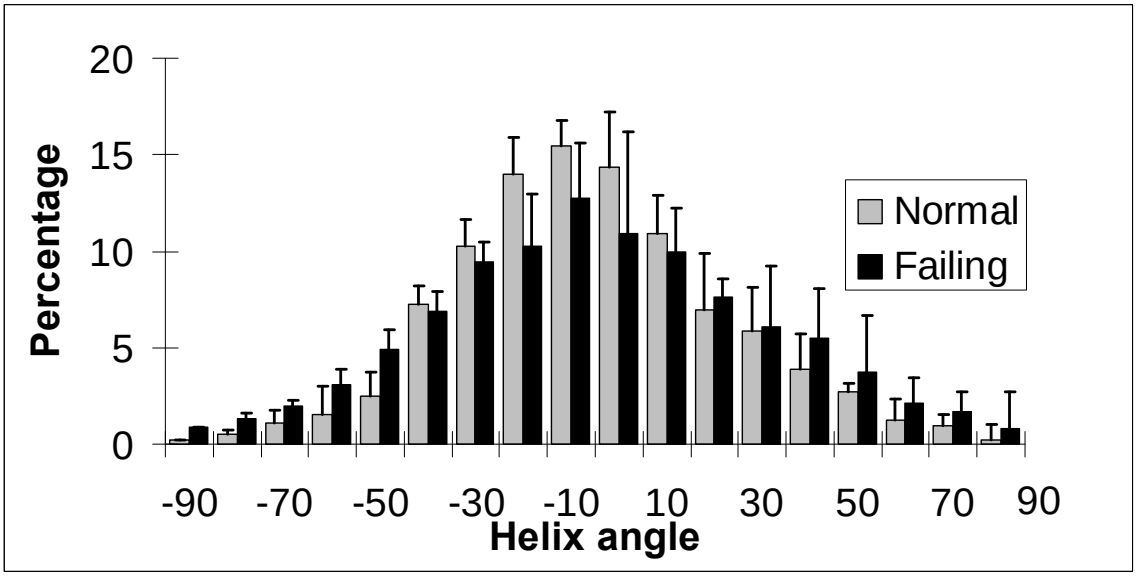

Figure 5.5 Quantitative distribution of fiber orientation at the mid-ventricular level.

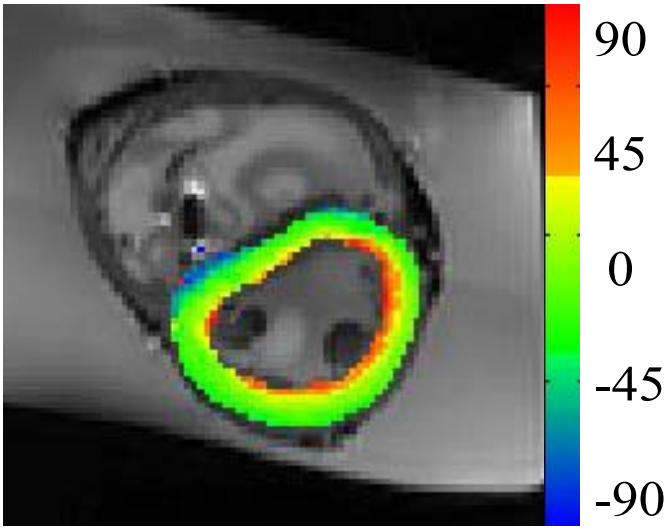

Figure 5.6 Color map of the fiber helix angle in the LV at the basal level of normal heart 1.

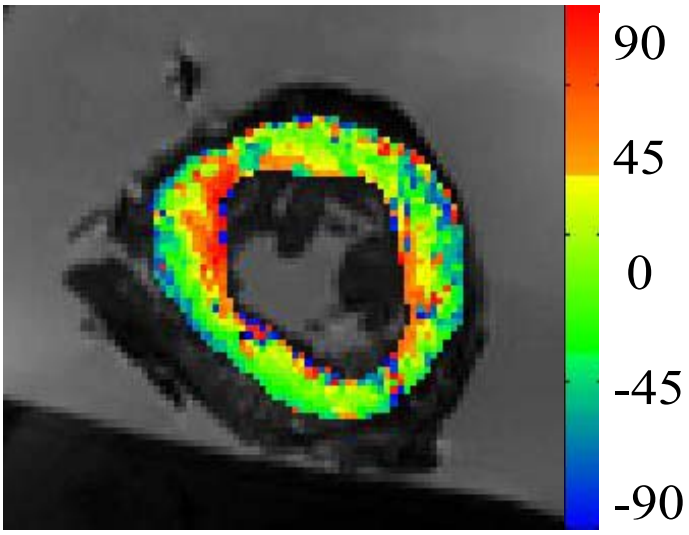

Figure 5.7 Color map of the fiber helix angle in the LV at the basal level of failing heart 6.

Mid-ventricular level

At the mid-ventricular level, there were no statistically significant differences in the helix angles in each grouping of the histogram. Similar to the fiber distribution at the basal level, the fiber orientation in the failing hearts demonstrated a more oblique pattern. For $\alpha < -40°$, and $\alpha > 20°$, the mean percentage of fibers was higher in the failing hearts as compared to the normal group. It also followed that the percentage of circumferential fibers $20° > \alpha > -40°$ decreased in the failing hearts.

Conclusions

In this pilot study, the distribution of fiber helix angles was investigated in normal and failing human hearts using diffusion tensor MRI. It was found that the percentage of longitudinal fibers increased in the failing hearts as compared to the normal hearts, following a decrease in the percentage of circumferential fibers in the failing heats. These results provide information as to the architectural remodeling of the myocardium in heart failure. In future studies, we plan to conduct a regional analysis within each slice with co-registered images and will include a greater number of preserved hearts. As such, other anatomical remodeling parameters (e.g., wall thickness, chamber volume) will also be included in future analyses.

Chapter 6: MRI Assessment of Pacing Induced Ventricular Dyssynchrony in an Isolated Human Heart[†]

[†] Authors: Michael D. Eggen, MS[1,2], Michael G. Bateman, MENG[1,2], Christopher D. Rolfes, BA[1,2], Stephen A. Howard, BA[1,2], Cory M. Swingen, PhD[3], Paul A. Iaizzo, PhD[2,4]

Department of Biomedical Engineering[1], Department of Surgery[2], Department of Medicine[3], Department of Physiology[4], University of Minnesota, Minneapolis, MN 55455

This chapter has been accepted for publication in the Journal of Magnetic Resonance Imaging as a clinical note. Permission has been granted for inclusion of this work in my dissertation.

Preface

When physicians first began to implant cardiac pacing leads and implantable pulse generators, the primary purpose was to save a patient from the morbid effects of bradycardia. Traditionally, cardiac pacing leads have been implanted in the right ventricular apex (RVA) because of the ease of the implantation procedure and relative lead stability. However, more recently this pacing site has been associated with the induction of asynchronous mechanical activation of the ventricles, and more importantly, has been shown to change fiber orientation in the ventricles and induce some degree of heart failure itself. Specifically, investigators have noted myofiber disorganization and alterations in myofiber size after chronic RVA pacing [1-3]. Therefore, it was of great interest to characterize myocardial strain and motion during RVA pacing as part of my thesis project. To date, there have been no studies using MRI to assess ventricular activation in a human heart during pacing, due to the risks involved in cardiac MR imaging with an implanted pacing system.

This study demonstrates the capabilities of MR imaging in the assessment of pacing induced ventricular dyssynchrony, and findings emphasize the need for more physiological cardiac pacing. A human donor heart deemed non-viable for transplantation, was reanimated using an MR compatible, four-chamber working perfusion system. The heart was imaged using a 1.5T MR scanner while being paced from the right ventricular apex (RVA) via an epicardial placed lead. Four-chamber, short-axis, and tagged short-axis cines were acquired in order track wall motion and intramyocardial strain during pacing. The results of this study revealed that the

activation patterns of the left ventricle (LV) during RVA pacing demonstrated intraventricular dyssynchrony; as the left ventricular mechanical activation proceeded from the septum and anterior wall to the lateral wall, with the posterior wall being activated last. As such, the time difference to peak contraction between the septum and lateral wall was ~125 ms. Likewise, interventricular dyssynchrony was demonstrated from the four-chamber cine as the time difference between the peak LV and RV free wall motion was 180 ms. With the ongoing development of MR safe and MR compatible pacing systems, we can expect MRI to be added to the list of imaging modalities used to optimize cardiac resynchronization therapy and/or alternate site pacing.

Furthermore, in order to complete this work, I designed and constructed an MRI compatible, portable, isolated perfusion system for the reanimation of human and animal hearts within an MRI unit. This system was first tested using 2 swine hearts and data and design details were presented in poster format at the 2009 Design of Medical Devices Conference at the University of Minnesota (see Appendix B). Phil Matta, an undergraduate student in biomedical engineering, assisted with the design and prototype testing. In addition, I was awarded $6,000 seed funding for this project from the Institute for Engineering and Medicine in 2006.

For this experiment Cory Swingen was responsible for MR imaging, Paul Iaizzo was responsible for all surgical procedures and reanimation of the heart, and Michael Bateman, Christopher Rolfes, and Stephen Howard were responsible for general

experiment support and troubleshooting equipment during the experiment. I was responsible for constructing and running the apparatus, experimental design, data analysis, and preparation of this manuscript. This novel study has been accepted for publication in the Journal of Magnetic Resonance Imaging as a clinical note with high priority. The supplemental movies will be available online through the Journal of Magnetic Resonance Imaging after publication.

Introduction

The right ventricular apex (RVA) has been the standard site for cardiac pacing lead implantation site for decades; due to both the relative ease of implantation and associated lead stability. More recently, through imaging modalities such as echocardiography, pacing at the RVA has been clinically shown to result in both mechanical dyssynchrony and deleterious ventricular remodeling [4,5]. Nevertheless, it has also been recently considered that cardiac MR (CMR) has several advantages over current echocardiographic methods for the assessment of mechanical dyssynchrony, including: (1) the ability to quantify transmural circumferential strain and myocardial scar burden and distribution, and/or (2) image acquisition is relatively independent of operator skill and thus has fewer technical issues, resulting in more accurate and reproducible results [6]. Furthermore, myocardial tagging has been employed to quantify mechanical dyssynchrony as a MRI predictor of responses to biventricular pacing [7]. However, to date the use of MRI for the assessment of mechanical dyssynchrony during cardiac pacing, is nonexistent: as having an implanted pacing system remains an absolute contraindication for CMR. Here we uniquely made use of MR imaging to visualize and quantify RVA pacing induced interventricular and intraventricular dyssynchrony in an isolated human heart.

Methods

A human donor heart, deemed not viable for transplant, was reanimated using a custom built, MR safe and compatible, four-chamber working perfusion system adapted from previously described Visible Heart methodologies [8, 9] (See Appendix B for further

design details). After cannulation of the superior vena cava, aorta, pulmonary artery, and left pulmonary vein, the heart was perfused with a clear, Krebs-Henseleit buffer solution which was used as a blood substitute. All CMR images were acquired with a 1.5T Siemens Avanto scanner (Siemens, Erlangen, Germany). For the pacing study, a temporary bipolar pacing lead (6495 STREAMLINE, Medtronic, Inc.) was epicardially placed at the RVA and activated using a pacing system analyzer (5311, Medtronic, Inc.); thus used to control the heart rate and stimulus amplitude (Figure 6.1A).

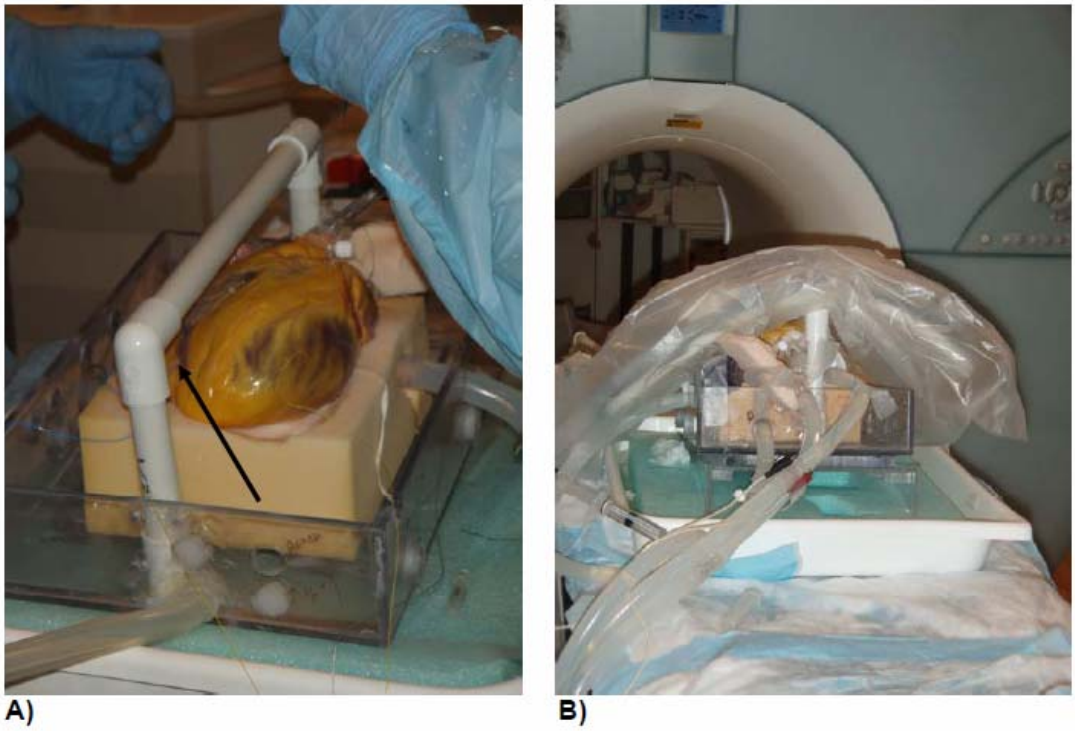

Figure 6.1 (A) The human heart is shown with the location of the temporary pacing lead indicated (*arrow*). (B) Placement of the heart and receiver coil on the patient bed prior to imaging.

Following defibrillation, and the elicitation of a native sinus rhythm, the heart was paced at a rate of 80 beats/minute and three surface electrodes were placed on the

ventricles for image gating. Subsequently, a flexible phased-array receiver coil was placed over the heart and the patient bed was positioned such that the heart was located at the isocenter of the magnet (Figure 6.1B). Four-chamber, short-axis, and tagged short-axis cines were acquired for the tracking of wall motion and intramyocardial strain in order to quantify and visualize pacing induced dyssynchrony. A retro-gated steady state free precession (True-FISP) cine imaging sequence was used with the following parameters: TR/TE = 3.41 ms/ 1.18 ms, slice thickness = 6 mm, pixel spacing = 1.4 × 1.4 mm^2, number of phases = 25, FOV = 360 mm × 292 mm, flip angle = 67°. A fast gradient-echo (FLASH) sequence was used for tagged cine imaging: TR/TE = 4.49 ms/ 2.32 ms effective, slice thickness = 8 mm, pixel spacing = 0.94 × 0.94 mm^2, number of phases = 20, tag separation = 6 mm, field of view = 240 × 240 mm, flip angle = 10°. Analysis of the cine images was performed using the MASS software system (Medis, Leiden, The Netherlands) to segment the RV and LV endocardial border and compute the regional wall motion throughout all cardiac phases. In order to quantify interventricular dyssynchrony, wall motion, was measured in the four-chamber cine at each time point as the average displacement of 50 equally distributed points along the RV and LV endocardium toward the central long-axis of each ventricle (Figure 6.2). A harmonic phase analysis software package, HARP (Diagnosoft, Maryland, USA), was employed to calculate intramyocardial circumferential strain and map the sequence of contraction of the LV [10].

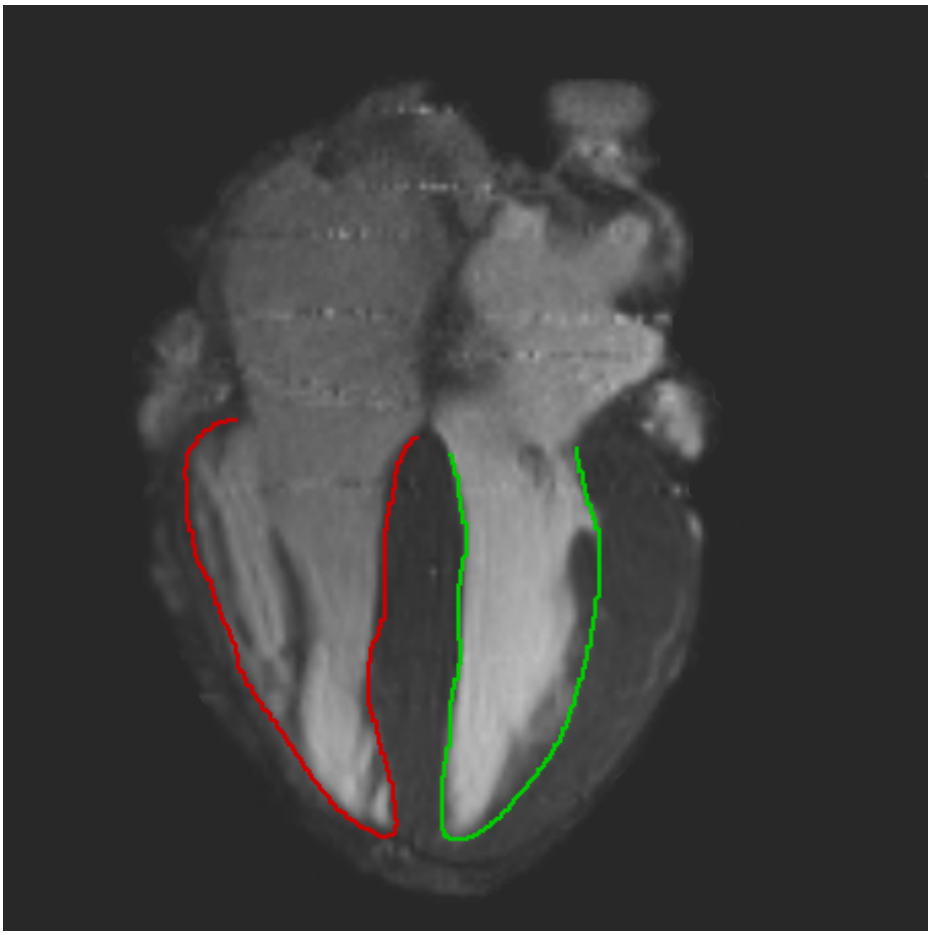

Figure 6.2 Long-axis cine image used to measure endocardial excursion of the LV (green) and RV (red).

Results

A color map of circumferential strain in the left ventricular (LV) short-axis at the papillary level during RVA pacing is shown in Figure 6.3. The activation pattern of the LV during RVA pacing demonstrated pacing induced intraventricular dyssynchrony; as the mechanical activation proceeded from the septum and anterior wall (Figure 6.3, probe locations 4 and 1 respectively) to the LV lateral wall (probe 2) with the posterior

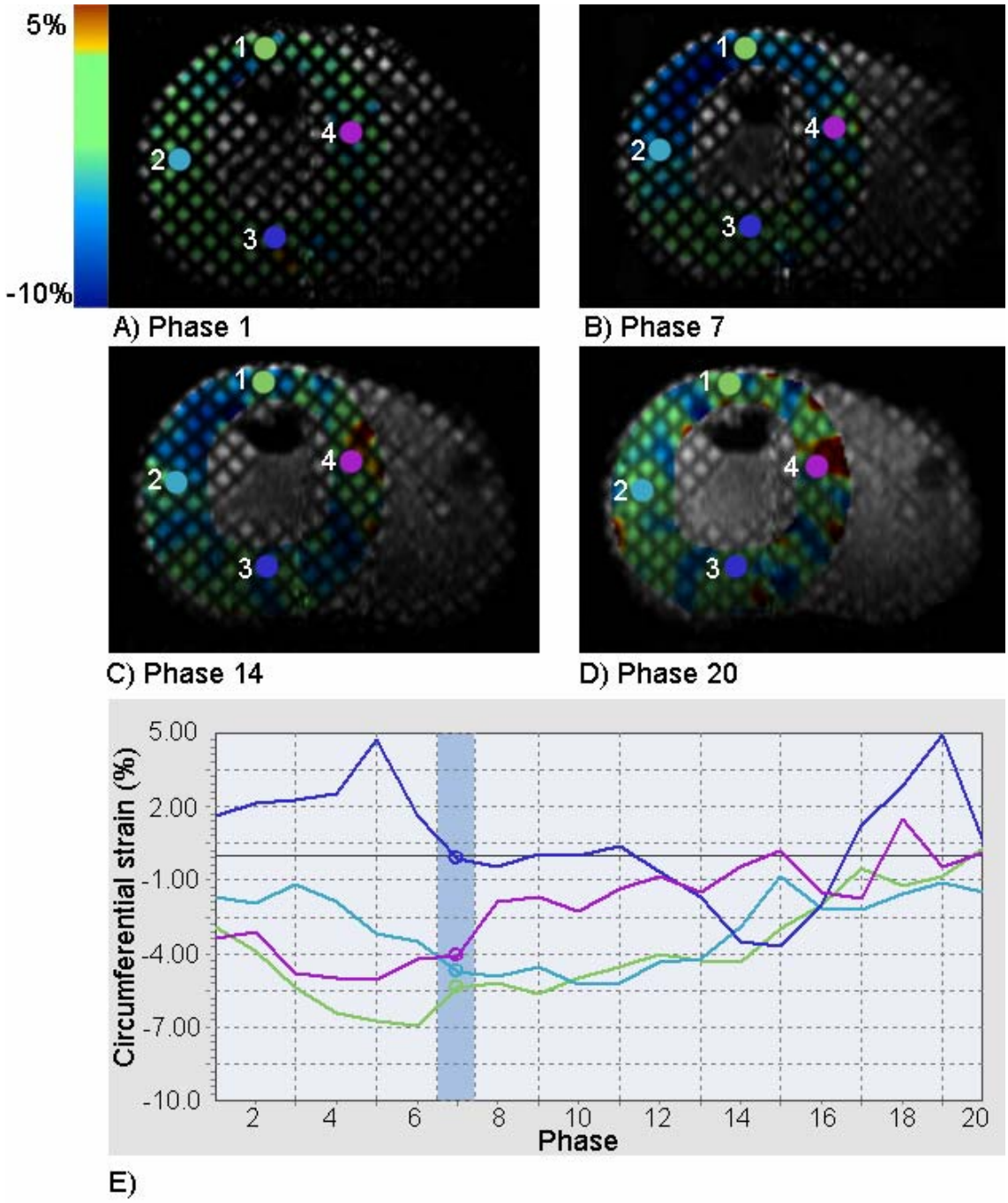

Figure 6.3 Circumferential strain superimposed on the LV short-axis at beginning-systole (A), mid-systole (B), end-systole (C), and end-diastole (D). The circumferential strain values are plotted throughout the cardiac cycle (E) for the given probe locations (1-4) indicated in the short-axis images, where the phase at mid-systole is highlighted (Phase 7).

wall (probe 3) being activated the last. Furthermore, the septum, anterior wall, and lateral wall were relaxing as the posterior wall was contracting (Figure 6.3, Phase 14), where the time difference to peak contraction between the septum and lateral wall was approximately 125 ms. Figure 6.3 can also be viewed as a cine in Data Supplemental Movie 1. Pacing induced dyssynchrony can also be visualized in the short-axis cine without tagging (Data Supplemental Movie 2), where pre-excitation of the RV, and LV asynchronous mechanical activation can easily be discerned. Interventricular dyssynchrony was evident from the analysis of RV and LV wall motion plotted in Figure 6.4, as the RV free wall attained maximal displacement approximately 180 ms before the LV free wall. The four-chamber cine used to calculate wall motion can be viewed in real-time in Data Supplemental Movie 3, where interventricular dyssynchrony or pre-excitation of the RV is clearly demonstrated.

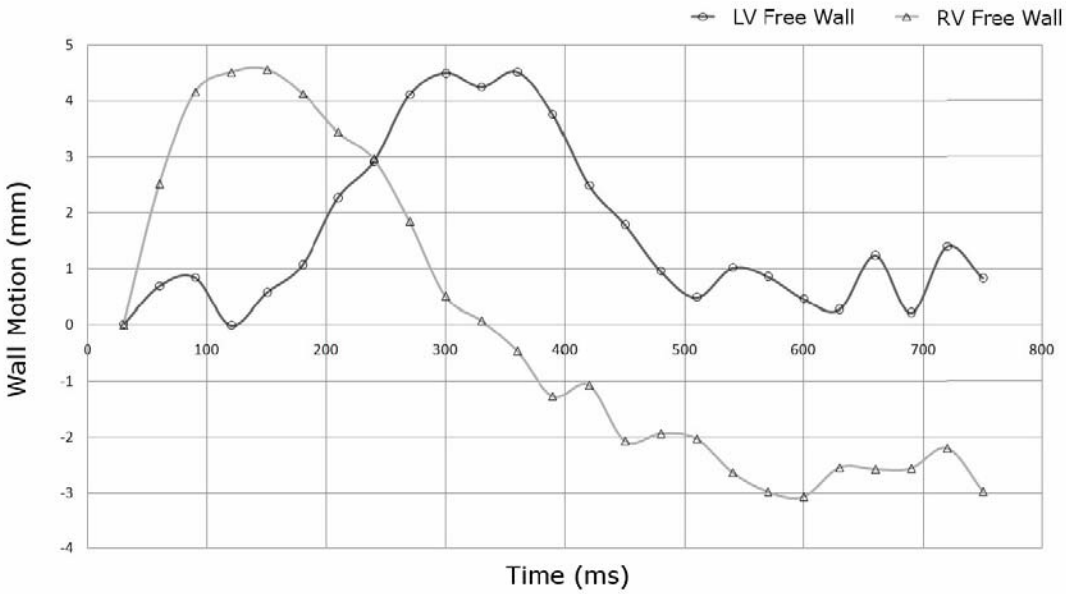

Figure 6.4 Average endocardial excursion of the RV and LV measured from the four-chamber long-axis cine.

Discussion

To our knowledge, this is the first demonstration of pacing induced dyssynchrony in an isolated human heart using MRI. This unique characterization of RVA pacing induced dyssynchrony further emphasizes the need for clinical approaches to induce more physiological pacing, and also demonstrates the capabilities of MRI in the assessment of pacing induced ventricular dyssynchrony. With the ongoing development of MR safe and MR compatible pacing systems, and the ability of MRI to quantify regional circumferential strain, MRI will likely be used as a clinical tool to accurately characterize the effects of cardiac resynchronization therapies, alternate site lead placements, and/or the optimization of any such pacing therapies.

Thesis Summary

The objective of this thesis was to characterize cardiac structural and functional remodeling in heart failure using MRI methodologies. Specifically, DTMRI was employed to quantify the fiber structure of the myocardium in normal and failing human and swine hearts.

In order to achieve these goals, first the computational tools and diffusion imaging methodologies were developed using the clinical 3 tesla MRI scanner located in the University Fairview Medical Center. With the methods developed, we were able to reconstruct cardiac fiber orientation in high resolution. Another important aspect of the developed methods was the study of the relative effects of decomposition on the diffusion properties of the myocardium. More specifically, by recovering human hearts at varying post-mortem intervals, we were able to determine that in order to properly track fiber orientation using DTMRI, all human hearts must be recovered and perfusion fixed within 3 days. This obtained knowledge was then used to set the subsequent collection intervals for all ex vivo human heart MRI research.

Following the development of the imaging tools, a high rate pacing model of dilated cardiomyopathy in swine was studied using both physiological and imaging assessments. For example, in these studies, MRI was used to characterize *in vivo* function, and fiber orientation was investigated *ex vivo* using DTMRI. In this model, severe contractile dysfunction was found, resulting in a 30% mortality rate. Although

there was severe dilation of the ventricles, we found that fiber orientation in this swine model of dilated cardiomyopathy was largely unchanged.

Furthermore, cardiac myocyte fiber orientations were investigated in both a set of healthy (n=4) and failing (n=4) human hearts. We found that the fiber orientation relative to normal hearts shifted to a more oblique angle with disease, and in some cases the myofibers were in a significant state of disarray. It should be note the both due to the rareness of obtaining fresh hearts for this research and the interest in clinically obtaining such information, this investigation is ongoing.

Lastly, to our knowledge for the first time ever, the mechanical activation of the myocardium was studied in a paced, isolated human heart using MRI, as pacing from the right ventricular apex is known result in deleterious fiber reorganization. Both intraventricular and interventricular dyssynchrony were quantified, and this novel study was the first published quantification of pacing induced dyssynchrony in a functional isolated human heart using MRI.

In conclusion, various MRI methodologies were used to investigate the structural and functional remodeling that occurs with the progression of heart failure, and these investigations have provided important and novel insights as to the myocardial structural and functional changes that can occur during the onset of such disease.

References

Chapter 1 References

1. Pettigrew, R.I. Dynamic cardiac MR imaging. Techniques and applications. Radiol Clin North Am 1989;27(6):1183-203.
2. Bloomgarden, D.C., Z.A. Fayad, V.A. Ferrari, B. Chin, M.G. Sutton, and L. Axel. Global cardiac function using fast breath-hold MRI: validation of new acquisition and analysis techniques. Magn Reson Med 1997;37(5):683-92.
3. Sakuma, H., N. Fujita, T.K. Foo, et al. Evaluation of left ventricular volume and mass with breath-hold cine MR imaging. Radiology 1993;188(2):377-80.
4. Anand, I.S., V.G. Florea, S.D. Solomon, M.A. Konstam, and J.E. Udelson. Noninvasive assessment of left ventricular remodeling: concepts, techniques, and implications for clinical trials. J Card Fail 2002;8(6 Suppl):S452-64.
5. Atkinson, D.J. and R.R. Edelman. Cineangiography of the heart in a single breath hold with a segmented turboFLASH sequence. Radiology 1991;178(2):357-60.
6. Bluemke, D.A., J.L. Boxerman, E. Atalar, and E.R. McVeigh. Segmented K-space cine breath-hold cardiovascular MR imaging: Part 1. Principles and technique. AJR Am J Roentgenol 1997;169(2):395-400.
7. Bluemke, D.A., J.L. Boxerman, T. Mosher, and J.A. Lima. Segmented K-space cine breath-hold cardiovascular MR imaging: Part 2. Evaluation of aortic vasculopathy. AJR Am J Roentgenol 1997;169(2):401-7.
8. Chien, D. and R.R. Edelman. Ultrafast imaging using gradient echoes. Magn Reson Q 1991;7(1):31-56.
9. Oppelt, A., R. Graumann, H. Barfuss, H. Fischer, W. Hartl, and W. Schajor. FISP: a new fast MRI sequence. Electromedica (Engl.Ed.) 1986;54:15-18.
10. Zur, Y., M.L. Wood, and L.J. Neuringer. Motion-insensitive, steady-state free precession imaging. Magn Reson Med 1990;16(3):444-59.
11. Pereles, F.S., V. Kapoor, J.C. Carr, et al. Usefulness of segmented trueFISP cardiac pulse sequence in evaluation of congenital and acquired adult cardiac abnormalities. AJR Am J Roentgenol 2001;177(5):1155-60.
12. Plein, S., T.N. Bloomer, J.P. Ridgway, T.R. Jones, G.J. Bainbridge, and M.U. Sivananthan. Steady-state free precession magnetic resonance imaging of the heart: comparison with segmented k-space gradient-echo imaging. J Magn Reson Imaging 2001;14(3):230-6.
13. Francois, C.J., D.S. Fieno, S.M. Shors, and J.P. Finn. Left ventricular mass: manual and automatic segmentation of true FISP and FLASH cine MR images in dogs and pigs. Radiology 2004;230(2):389-95.
14. Shors, S.M., C.W. Fung, C.J. Francois, J.P. Finn, and D.S. Fieno. Accurate quantification of right ventricular mass at MR imaging by using cine true fast imaging with steady-state precession: study in dogs. Radiology 2004;230(2):383-8.

15. Yang, X., E. Atalar, D. Li, et al. Magnetic resonance imaging permits in vivo monitoring of catheter-based vascular gene delivery. Circulation 2001;104(14):1588-90.
16. Weiger, M., K.P. Pruessmann, and P. Boesiger. Cardiac real-time imaging using SENSE. SENSitivity Encoding scheme. Magn Reson Med 2000;43(2):177-84.
17. Penicka, M., J. Bartunek, W. Wijns, et al. Tissue doppler imaging predicts recovery of left ventricular function after recanalization of an occluded coronary artery. J Am Coll Cardiol 2004;43(1):85-91.
18. Sanz, G., A. Castaner, A. Betriu, et al. Determinants of prognosis in survivors of myocardial infarction: a prospective clinical angiographic study. N Engl J Med 1982;306(18):1065-70.
19. Weiss, J.L., P.N. Marino, and E.P. Shapiro. Myocardial infarct expansion: recognition, significance and pathology. Am J Cardiol 1991;68(14):35D-40D.
20. Lieberman, A.N., J.L. Weiss, B.I. Jugdutt, et al. Two-dimensional echocardiography and infarct size: relationship of regional wall motion and thickening to the extent of myocardial infarction in the dog. Circulation 1981;63(4):739-46.
21. Sasayama, S., D. Franklin, J. Ross, Jr., W.S. Kemper, and D. McKown. Dynamic changes in left ventricular wall thickness and their use in analyzing cardiac function in the conscious dog. Am J Cardiol 1976;38(7):870-9.
22. Azhari, H., J.L. Weiss, W.J. Rogers, C.O. Siu, and E.P. Shapiro. A noninvasive comparative study of myocardial strains in ischemic canine hearts using tagged MRI in 3-D. Am J Physiol 1995;268(5 Pt 2):H1918-26.
23. Gotte, M.J., A.C. van Rossum, J.W.R. Twisk, J.P.A. Kuijer, J.T. Marcus, and C.A. Visser. Quantification of regional contractile function after infarction: strain analysis superior to wall thickening analysis in discriminating infarct from remote myocardium. J Am Coll Cardiol 2001;37(3):808-17.
24. Rickers, C., R. Gallegos, R.T. Seethamraju, et al. Applications of magnetic resonance imaging for cardiac stem cell therapy. J Interv Cardiol 2004;17(1):37-46.
25. Axel, L., R.C. Goncalves, and D. Bloomgarden. Regional heart wall motion: two-dimensional analysis and functional imaging with MR imaging. Radiology 1992;183(3):745-50.
26. Clark, N.R., N. Reichek, P. Bergey, et al. Circumferential myocardial shortening in the normal human left ventricle. Assessment by magnetic resonance imaging using spatial modulation of magnetization. Circulation 1991;84(1):67-74.
27. McVeigh, E.R. MRI of myocardial function: motion tracking techniques. Magn Reson Imaging 1996;14(2):137-50.
28. McVeigh, E.R. and E. Atalar. Cardiac tagging with breath-hold cine MRI. Magn Reson Med 1992;28(2):318-27.
29. McVeigh, E.R. and E.A. Zerhouni. Noninvasive measurement of transmural gradients in myocardial strain with MR imaging. Radiology 1991;180(3):677-83.

30. Koenig, S.H., M. Spiller, R.D. Brown, 3rd, and G.L. Wolf. Relaxation of water protons in the intra- and extracellular regions of blood containing Gd(DTPA). Magn Reson Med 1986;3(5):791-5.
31. Strich, G., P.L. Hagan, K.H. Gerber, and R.A. Slutsky. Tissue distribution and magnetic resonance spin lattice relaxation effects of gadolinium-DTPA. Radiology 1985;154(3):723-6.
32. Braunwald, E., Heart disease: A textbook of cardiovascular medicine. 1997, Philadelphia, PA: W.B. Saunders Company.
33. Lima, J.A., R.M. Judd, A. Bazille, S.P. Schulman, E. Atalar, and E.A. Zerhouni. Regional heterogeneity of human myocardial infarcts demonstrated by contrast-enhanced MRI. Potential mechanisms. Circulation 1995;92(5):1117-25.
34. Tsekos, N.V., Y. Zhang, H. Merkle, et al. Fast anatomical imaging of the heart and assessment of myocardial perfusion with arrhythmia insensitive magnetization preparation. Magn Reson Med 1995;34(4):530-6.
35. Kim, R.J., D.S. Fieno, T.B. Parrish, et al. Relationship of MRI delayed contrast enhancement to irreversible injury, infarct age, and contractile function. Circulation 1999;100(19):1992-2002.
36. Simonetti, O.P., R.J. Kim, D.S. Fieno, et al. An improved MR imaging technique for the visualization of myocardial infarction. Radiology 2001;218(1):215-23.
37. Bello, D., D.J. Shah, G.M. Farah, et al. Gadolinium cardiovascular magnetic resonance predicts reversible myocardial dysfunction and remodeling in patients with heart failure undergoing beta-blocker therapy. Circulation 2003;108(16):1945-53.
38. Kim, R.J., E. Wu, A. Rafael, et al. The use of contrast-enhanced magnetic resonance imaging to identify reversible myocardial dysfunction. N Engl J Med 2000;343(20):1445-53.
39. Klein, C., S.G. Nekolla, F.M. Bengel, et al. Assessment of myocardial viability with contrast-enhanced magnetic resonance imaging: comparison with positron emission tomography. Circulation 2002;105(2):162-7.
40. Wagner, A., H. Mahrholdt, T.A. Holly, et al. Contrast-enhanced MRI and routine single photon emission computed tomography (SPECT) perfusion imaging for detection of subendocardial myocardial infarcts: an imaging study. Lancet 2003;361(9355):374-9.
41. Lekx, K.S., F.S. Prato, J. Sykes, and G. Wisenberg. The partition coefficient of Gd-DTPA reflects maintained tissue viability in a canine model of chronic significant coronary stenosis. J Cardiovasc Magn Reson 2004;6(1):33-42.
42. Tong, C.Y., F.S. Prato, G. Wisenberg, et al. Measurement of the extraction efficiency and distribution volume for Gd-DTPA in normal and diseased canine myocardium. Magn Reson Med 1993;30(3):337-46.
43. Wendland, M.F., M. Saeed, J. Bremerich, H. Arheden, and C.B. Higgins. Thallium-like test for myocardial viability with MnDPDP-enhanced MRI. Acad Radiol 2002;9 Suppl 1:S82-3.

44. Kim, R.J., R.M. Judd, E.L. Chen, D.S. Fieno, T.B. Parrish, and J.A. Lima. Relationship of elevated 23Na magnetic resonance image intensity to infarct size after acute reperfused myocardial infarction. Circulation 1999;100(2):185-92.
45. Duprez, D.A., C. Swingen, R. Sih, T. Lefebvre, D.R. Kaiser, and M. Jerosch-Herold. Heterogeneous remodelling of the ascending and descending aorta with age. J Hum Hypertens 2007;21(8):689-91.
46. Hsu, E.W., A.L. Muzikant, S.A. Matulevicius, R.C. Penland, and C.S. Henriquez. Magnetic resonance myocardial fiber-orientation mapping with direct histological correlation. Am J Physiol 1998;274(5 Pt 2):H1627-34.
47. LeGrice, I.J., B.H. Smaill, L.Z. Chai, S.G. Edgar, J.B. Gavin, and P.J. Hunter. Laminar structure of the heart: ventricular myocyte arrangement and connective tissue architecture in the dog. Am J Physiol 1995;269(2 Pt 2):H571-82.
48. Streeter, D.D., Jr., H.M. Spotnitz, D.P. Patel, J. Ross, Jr., and E.H. Sonnenblick. Fiber orientation in the canine left ventricle during diastole and systole. Circ Res 1969;24(3):339-47.
49. Ingels, N.B., Jr. Myocardial fiber architecture and left ventricular function. Technol Health Care 1997;5(1-2):45-52.
50. Rijcken, J., P.H. Bovendeerd, A.J. Schoofs, D.H. van Campen, and T. Arts. Optimization of cardiac fiber orientation for homogeneous fiber strain at beginning of ejection. J Biomech 1997;30(10):1041-9.
51. Rijcken, J., P.H. Bovendeerd, A.J. Schoofs, D.H. van Campen, and T. Arts. Optimization of cardiac fiber orientation for homogeneous fiber strain during ejection. Ann Biomed Eng 1999;27(3):289-97.
52. Sallin, E.A. Fiber orientation and ejection fraction in the human left ventricle. Biophys J 1969;9(7):954-64.
53. Tomioka, H., O.J. Liakopoulos, G.D. Buckberg, N. Hristov, Z. Tan, and G. Trummer. The effect of ventricular sequential contraction on helical heart during pacing: high septal pacing versus biventricular pacing. European Journal of Cardio-Thoracic Surgery 2006;29(Supplement 1):S198-S206.
54. Tseng, W.Y., T.G. Reese, R.M. Weisskoff, T.J. Brady, and V.J. Wedeen. Myocardial fiber shortening in humans: initial results of MR imaging. Radiology 2000;216(1):128-39.
55. Van Der Toorn, A., P. Barenbrug, G. Snoep, et al. Transmural gradients of cardiac myofiber shortening in aortic valve stenosis patients using MRI tagging. Am J Physiol Heart Circ Physiol 2002;283(4):H1609-15.
56. Shapiro, E.P. and F.E. Rademakers. Importance of oblique fiber orientation for left ventricular wall deformation. Technol Health Care 1997;5(1-2):21-8.
57. Tseng, W.Y., V.J. Wedeen, T.G. Reese, R.N. Smith, and E.F. Halpern. Diffusion tensor MRI of myocardial fibers and sheets: correspondence with visible cut-face texture. J Magn Reson Imaging 2003;17(1):31-42.
58. Helm, P.A., H.J. Tseng, L. Younes, E.R. McVeigh, and R.L. Winslow. Ex vivo 3D diffusion tensor imaging and quantification of cardiac laminar structure. Magn Reson Med 2005;54(4):850-9.

59. Scollan, D.F., A. Holmes, J. Zhang, and R.L. Winslow. Reconstruction of cardiac ventricular geometry and fiber orientation using magnetic resonance imaging. Ann Biomed Eng 2000;28(8):934-44.
60. Geerts, L., P. Bovendeerd, K. Nicolay, and T. Arts. Characterization of the normal cardiac myofiber field in goat measured with MR-diffusion tensor imaging. Am J Physiol Heart Circ Physiol 2002;283(1):H139-45.
61. Basser, P.J., J. Mattiello, and D. LeBihan. Estimation of the effective self-diffusion tensor from the NMR spin echo. J Magn Reson B 1994;103(3):247-54.
62. Garrido, L., V.J. Wedeen, K.K. Kwong, U.M. Spencer, and H.L. Kantor. Anisotropy of water diffusion in the myocardium of the rat. Circ Res 1994;74(5):789-93.
63. Holmes, A.A., D.F. Scollan, and R.L. Winslow. Direct histological validation of diffusion tensor MRI in formaldehyde-fixed myocardium. Magn Reson Med 2000;44(1):157-61.
64. Scollan, D.F., A. Holmes, R. Winslow, and J. Forder. Histological validation of myocardial microstructure obtained from diffusion tensor magnetic resonance imaging. Am J Physiol 1998;275(6 Pt 2):H2308-18.
65. Helm, P., M.F. Beg, M.I. Miller, and R.L. Winslow. Measuring and mapping cardiac fiber and laminar architecture using diffusion tensor MR imaging. Ann N Y Acad Sci 2005;1047:296-307.
66. Dou, J., W.Y. Tseng, T.G. Reese, and V.J. Wedeen. Combined diffusion and strain MRI reveals structure and function of human myocardial laminar sheets in vivo. Magn Reson Med 2003;50(1):107-13.
67. Reese, T.G., R.M. Weisskoff, R.N. Smith, B.R. Rosen, R.E. Dinsmore, and V.J. Wedeen. Imaging myocardial fiber architecture in vivo with magnetic resonance. Magn Reson Med 1995;34(6):786-91.
68. Rohmer, D., A. Sitek, and G.T. Gullberg. Reconstruction and visualization of fiber and laminar structure in the normal human heart from ex vivo diffusion tensor magnetic resonance imaging (DTMRI) data. Invest Radiol 2007;42(11):777-89.
69. Tseng, W.Y., J. Dou, T.G. Reese, and V.J. Wedeen. Imaging myocardial fiber disarray and intramural strain hypokinesis in hypertrophic cardiomyopathy with MRI. J Magn Reson Imaging 2006;23(1):1-8.
70. Chen, J., S.K. Song, W. Liu, et al. Remodeling of cardiac fiber structure after infarction in rats quantified with diffusion tensor MRI. Am J Physiol Heart Circ Physiol 2003;285(3):H946-54.
71. Wu, M.T., W.Y. Tseng, M.Y. Su, et al. Diffusion tensor magnetic resonance imaging mapping the fiber architecture remodeling in human myocardium after infarction: correlation with viability and wall motion. Circulation 2006;114(10):1036-45.
72. Lardo, A.C. Real-time magnetic resonance imaging: diagnostic and interventional applications. Pediatr Cardiol 2000;21(1):80-98.
73. Kerr, A.B., J.M. Pauly, B.S. Hu, et al. Real-time interactive MRI on a conventional scanner. Magn Reson Med 1997;38(3):355-67.

74. Serfaty, J.M., X. Yang, T.K. Foo, A. Kumar, A. Derbyshire, and E. Atalar. MRI-guided coronary catheterization and PTCA: A feasibility study on a dog model. Magn Reson Med 2003;49(2):258-63.
75. Lardo, A.C., E.R. McVeigh, P. Jumrussirikul, et al. Visualization and temporal/spatial characterization of cardiac radiofrequency ablation lesions using magnetic resonance imaging. Circulation 2000;102(6):698-705.
76. Atalar, E., P.A. Bottomley, O. Ocali, et al. High resolution intravascular MRI and MRS by using a catheter receiver coil. Magn Reson Med 1996;36(4):596-605.
77. Moore, P. MRI-guided congenital cardiac catheterization and intervention: the future? Catheter Cardiovasc Interv 2005;66(1):1-8.
78. McVeigh, E.R., M.A. Guttman, R.J. Lederman, et al. Real-time interactive MRI-guided cardiac surgery: aortic valve replacement using a direct apical approach. Magn Reson Med 2006;56(5):958-64.
79. Nazarian, S., A. Roguin, M.M. Zviman, et al. Clinical utility and safety of a protocol for noncardiac and cardiac magnetic resonance imaging of patients with permanent pacemakers and implantable-cardioverter defibrillators at 1.5 tesla. Circulation 2006;114(12):1277-84.
80. Roka, A., T. Simor, H. Vago, C. Minorics, G. Acsady, and B. Merkely. Magnetic resonance imaging-based biventricular pacemaker upgrade. Pacing Clin Electrophysiol 2004;27(7):1011-3.
81. Sommer, T., C. Vahlhaus, G. Lauck, et al. MR imaging and cardiac pacemakers: in-vitro evaluation and in-vivo studies in 51 patients at 0.5 T. Radiology 2000;215(3):869-79.
82. Achenbach, S., W. Moshage, B. Diem, T. Bieberle, V. Schibgilla, and K. Bachmann. Effects of magnetic resonance imaging on cardiac pacemakers and electrodes. Am Heart J 1997;134(3):467-73.
83. Nitz, W.R., A. Oppelt, W. Renz, C. Manke, M. Lenhart, and J. Link. On the heating of linear conductive structures as guide wires and catheters in interventional MRI. J Magn Reson Imaging 2001;13(1):105-14.
84. Yeung, C.J., R.C. Susil, and E. Atalar. RF safety of wires in interventional MRI: using a safety index. Magn Reson Med 2002;47(1):187-93.
85. Houlind, K., O. Eschen, E.M. Pedersen, T. Jensen, J.M. Hasenkam, and P.K. Paulsen. Magnetic resonance imaging of blood velocity distribution around St. Jude medical aortic valves in patients. J Heart Valve Dis 1996;5(5):511-7.
86. Walker, P.G., E.M. Pedersen, S. Oyre, et al. Magnetic resonance velocity imaging: a new method for prosthetic heart valve study. J Heart Valve Dis 1995;4(3):296-307.
87. Botnar, R., E. Nagel, M.B. Scheidegger, E.M. Pedersen, O. Hess, and P. Boesiger. Assessment of prosthetic aortic valve performance by magnetic resonance velocity imaging. Magma 2000;10(1):18-26.
88. Wyman, B.T., W.C. Hunter, F.W. Prinzen, O.P. Faris, and E.R. McVeigh. Effects of single- and biventricular pacing on temporal and spatial dynamics of ventricular contraction. Am J Physiol Heart Circ Physiol 2002;282(1):H372-9.

89. van der Geest, R.J., A. de Roos, E.E. van der Wall, and J.H. Reiber. Quantitative analysis of cardiovascular MR images. Int J Card Imaging 1997;13(3):247-58.
90. van der Geest, R.J., B.P. Lelieveldt, and J.H. Reiber. Quantification of global and regional ventricular function in cardiac magnetic resonance imaging. Top Magn Reson Imaging 2000;11(6):348-58.
91. van der Geest, R.J. and J.H. Reiber. Quantification in cardiac MRI. J Magn Reson Imaging 1999;10(5):602-8.
92. Young, A.A., B.R. Cowan, S.F. Thrupp, W.J. Hedley, and L.J. Dell'Italia. Left ventricular mass and volume: fast calculation with guide-point modeling on MR images. Radiology 2000;216(2):597-602.
93. Swingen, C.M., R.T. Seethamraju, and M. Jerosch-Herold. Feedback-assisted three-dimensional reconstruction of the left ventricle with MRI. J Magn Reson Imaging 2003;17(5):528-37.
94. Swingen, C., X. Wang, and M. Jerosch-Herold. Evaluation of myocardial volume heterogeneity during end-diastole and end-systole using cine MRI. J Cardiovasc Magn Reson 2004;6(4):829-35.
95. Baer, F.M., E. Voth, C.A. Schneider, P. Theissen, H. Schicha, and U. Sechtem. Comparison of low-dose dobutamine-gradient-echo magnetic resonance imaging and positron emission tomography with [18F]fluorodeoxyglucose in patients with chronic coronary artery disease. A functional and morphological approach to the detection of residual myocardial viability. Circulation 1995;91(4):1006-15.
96. Baer, F.M., E. Voth, K. LaRosee, et al. Comparison of dobutamine transesophageal echocardiography and dobutamine magnetic resonance imaging for detection of residual myocardial viability. Am J Cardiol 1996;78(4):415-9.
97. Nagel, E., H.B. Lehmkuhl, W. Bocksch, et al. Noninvasive diagnosis of ischemia-induced wall motion abnormalities with the use of high-dose dobutamine stress MRI: comparison with dobutamine stress echocardiography. Circulation 1999;99(6):763-70.
98. Matheijssen, N.A., A. de Roos, J. Doornbos, J.H. Reiber, G.J. Waldman, and E.E. van der Wall. Left ventricular wall motion analysis in patients with acute myocardial infarction using magnetic resonance imaging. Magn Reson Imaging 1993;11(4):485-92.
99. Holman, E.R., H.W. Vliegen, R.J. van der Geest, et al. Quantitative analysis of regional left ventricular function after myocardial infarction in the pig assessed with cine magnetic resonance imaging. Magn Reson Med 1995;34(2):161-9.
100. Nagel, E. and E. Fleck. Functional MRI in ischemic heart disease based on detection of contraction abnormalities. J Magn Reson Imaging 1999;10(3):411-7.
101. Sheehan, F.H., E.L. Bolson, H.T. Dodge, D.G. Mathey, J. Schofer, and H.W. Woo. Advantages and applications of the centerline method for characterizing regional ventricular function. Circulation 1986;74(2):293-305.
102. Osman, N.F., W.S. Kerwin, E.R. McVeigh, and J.L. Prince. Cardiac motion tracking using CINE harmonic phase (HARP) magnetic resonance imaging. Magn Reson Med 1999;42(6):1048-60.

103. Osman, N.F., E.R. McVeigh, and J.L. Prince. Imaging heart motion using harmonic phase MRI. IEEE Trans Med Imaging 2000;19(3):186-202.
104. Osman, N.F. and J.L. Prince. Visualizing myocardial function using HARP MRI. Phys Med Biol 2000;45(6):1665-82.
105. Kraitchman, D., S. Sampath, J.A. Derbyshire, A.W. Heldman, J.L. Prince, and N.F. Osman. Detetecting the Onset of Ischemia Using Real-Time HARP. Proceedings of the International Society of Magnetic Resonance in Medicine 2001.
106. Cerqueira, M.D., N.J. Weissman, V. Dilsizian, et al. Standardized myocardial segmentation and nomenclature for tomographic imaging of the heart: a statement for healthcare professionals from the Cardiac Imaging Committee of the Council on Clinical Cardiology of the American Heart Association. Circulation 2002;105(4):539-42.
107. Thompson, H.K., Jr., C.F. Starmer, R.E. Whalen, and H.D. McIntosh. Indicator Transit Time Considered as a Gamma Variate. Circ Res 1964;14:502-15.
108. Al-Saadi, N., E. Nagel, M. Gross, et al. Noninvasive detection of myocardial ischemia from perfusion reserve based on cardiovascular magnetic resonance. Circulation 2000;101(12):1379-83.
109. Al-Saadi, N., E. Nagel, M. Gross, et al. Improvement of myocardial perfusion reserve early after coronary intervention: assessment with cardiac magnetic resonance imaging. J Am Coll Cardiol 2000;36(5):1557-64.
110. Panting, J.R., P.D. Gatehouse, G.Z. Yang, et al. Abnormal subendocardial perfusion in cardiac syndrome X detected by cardiovascular magnetic resonance imaging. N Engl J Med 2002;346(25):1948-53.
111. Schwitter, J., D. Nanz, S. Kneifel, et al. Assessment of myocardial perfusion in coronary artery disease by magnetic resonance: a comparison with positron emission tomography and coronary angiography. Circulation 2001;103(18):2230-5.
112. Ibrahim, T., S.G. Nekolla, K. Schreiber, et al. Assessment of coronary flow reserve: comparison between contrast-enhanced magnetic resonance imaging and positron emission tomography. J Am Coll Cardiol 2002;39(5):864-70.
113. Jerosch-Herold, M., X. Hu, N.S. Murthy, C. Rickers, and A.E. Stillman. Magnetic resonance imaging of myocardial contrast enhancement with MS-325 and its relation to myocardial blood flow and the perfusion reserve. J Magn Reson Imaging 2003;18(5):544-54.
114. Jerosch-Herold, M., R.T. Seethamraju, C.M. Swingen, N.M. Wilke, and A.E. Stillman. Analysis of myocardial perfusion MRI. J Magn Reson Imaging 2004;19(6):758-70.
115. Jerosch-Herold, M., C. Swingen, and R.T. Seethamraju. Myocardial blood flow quantification with MRI by model-independent deconvolution. Med Phys 2002;29(5):886-97.
116. Jerosch-Herold, M., N. Wilke, Y. Wang, et al. Direct comparison of an intravascular and an extracellular contrast agent for quantification of myocardial perfusion. Cardiac MRI Group. Int J Card Imaging 1999;15(6):453-64.

117. Baer, F.M., P. Theissen, C.A. Schneider, et al. MRI assessment of myocardial viability: comparison with other imaging techniques. Rays 1999;24(1):96-108.
118. Haas, F., C.J. Haehnel, W. Picker, et al. Preoperative positron emission tomographic viability assessment and perioperative and postoperative risk in patients with advanced ischemic heart disease. J Am Coll Cardiol 1997;30(7):1693-700.
119. Lee, K.S., T.H. Marwick, S.A. Cook, et al. Prognosis of patients with left ventricular dysfunction, with and without viable myocardium after myocardial infarction. Relative efficacy of medical therapy and revascularization. Circulation 1994;90(6):2687-94.
120. Pagley, P.R., G.A. Beller, D.D. Watson, L.W. Gimple, and M. Ragosta. Improved outcome after coronary bypass surgery in patients with ischemic cardiomyopathy and residual myocardial viability. Circulation 1997;96(3):793-800.
121. Fieno, D.S., R.J. Kim, E.L. Chen, J.W. Lomasney, F.J. Klocke, and R.M. Judd. Contrast-enhanced magnetic resonance imaging of myocardium at risk: distinction between reversible and irreversible injury throughout infarct healing. J Am Coll Cardiol 2000;36(6):1985-91.
122. Beek, A.M., H.P. Kuhl, O. Bondarenko, et al. Delayed contrast-enhanced magnetic resonance imaging for the prediction of regional functional improvement after acute myocardial infarction. J Am Coll Cardiol 2003;42(5):895-901.
123. Mahrholdt, H., A. Wagner, M. Parker, et al. Relationship of contractile function to transmural extent of infarction in patients with chronic coronary artery disease. J Am Coll Cardiol 2003;42(3):505-12.
124. Marino, P., L. Zanolla, and P. Zardini. Effect of streptokinase on left ventricular modeling and function after myocardial infarction: the GISSI (Gruppo Italiano per lo Studio della Streptochinasi nell'Infarto Miocardico) Trial. J Am Coll Cardiol 1989;14(5):1149-58.
125. Sheehan, F.H., R. Doerr, W.G. Schmidt, et al. Early recovery of left ventricular function after thrombolytic therapy for acute myocardial infarction: an important determinant of survival. J Am Coll Cardiol 1988;12(2):289-300.
126. Gerber, B.L., J. Garot, D.A. Bluemke, K.C. Wu, and J.A. Lima. Accuracy of contrast-enhanced magnetic resonance imaging in predicting improvement of regional myocardial function in patients after acute myocardial infarction. Circulation 2002;106(9):1083-9.
127. Kolipaka, A., G.P. Chatzimavroudis, R.D. White, T.P. O'Donnell, and R.M. Setser. Segmentation of non-viable myocardium in delayed enhancement magnetic resonance images. Int J Cardiovasc Imaging 2005;21(2-3):303-11.

Chapter 2 References

1. Basser, P.J., *Inferring microstructural features and the physiological state of tissues from diffusion-weighted images.* NMR Biomed, 1995. 8(7-8): p. 333-44.
2. Tseng, W.Y., et al., *Diffusion tensor MRI of myocardial fibers and sheets: correspondence with visible cut-face texture.* J Magn Reson Imaging, 2003. 17(1): p. 31-42.
3. Hsu, E.W., et al., *Magnetic resonance myocardial fiber-orientation mapping with direct histological correlation.* Am J Physiol, 1998. 274(5 Pt 2): p. H1627-34.
4. LeGrice, I.J., et al., *Laminar structure of the heart: ventricular myocyte arrangement and connective tissue architecture in the dog.* Am J Physiol, 1995. 269(2 Pt 2): p. H571-82.
5. Streeter, D.D., Jr., et al., *Fiber orientation in the canine left ventricle during diastole and systole.* Circ Res, 1969. 24(3): p. 339-47.
6. Tomioka, H., et al., *The effect of ventricular sequential contraction on helical heart during pacing: high septal pacing versus biventricular pacing.* Eur J Cardiothorac Surg, 2006. 29 Suppl 1: p. S198-206.
7. Fox, C.C. and G.M. Hutchins, *The architecture of the human ventricular myocardium.* Johns Hopkins Med J, 1972. 130(5): p. 289-99.
8. Nielsen, P.M., et al., *Mathematical model of geometry and fibrous structure of the heart.* Am J Physiol, 1991. 260(4 Pt 2): p. H1365-78.
9. Dou, J., et al., *Combined diffusion and strain MRI reveals structure and function of human myocardial laminar sheets in vivo.* Magn Reson Med, 2003. 50(1): p. 107-13.
10. Ingels, N.B., Jr., *Myocardial fiber architecture and left ventricular function.* Technol Health Care, 1997. 5(1-2): p. 45-52.
11. Rijcken, J., et al., *Optimization of cardiac fiber orientation for homogeneous fiber strain at beginning of ejection.* J Biomech, 1997. 30(10): p. 1041-9.
12. Rijcken, J., et al., *Optimization of cardiac fiber orientation for homogeneous fiber strain during ejection.* Ann Biomed Eng, 1999. 27(3): p. 289-97.
13. Tseng, W.Y., et al., *Myocardial fiber shortening in humans: initial results of MR imaging.* Radiology, 2000. 216(1): p. 128-39.
14. Sallin, E.A., *Fiber orientation and ejection fraction in the human left ventricle.* Biophys J, 1969. 9(7): p. 954-64.
15. Forder, J.R., et al., *MR imaging measurement of compartmental water diffusion in perfused heart slices.* Am J Physiol Heart Circ Physiol, 2001. 281(3): p. H1280-5.
16. Holmes, A.A., D.F. Scollan, and R.L. Winslow, *Direct histological validation of diffusion tensor MRI in formaldehyde-fixed myocardium.* Magn Reson Med, 2000. 44(1): p. 157-61.
17. Scollan, D.F., et al., *Histological validation of myocardial microstructure obtained from diffusion tensor magnetic resonance imaging.* Am J Physiol, 1998. 275(6 Pt 2): p. H2308-18.

18. Basser, P.J. and D.K. Jones, *Diffusion-tensor MRI: theory, experimental design and data analysis - a technical review.* NMR Biomed, 2002. 15(7-8): p. 456-67.
19. Gaige, T.A., et al., *Three dimensional myoarchitecture of the human tongue determined in vivo by diffusion tensor imaging with tractography.* J Magn Reson Imaging, 2007. 26(3): p. 654-61.
20. Reese, T.G., et al., *Reduction of eddy-current-induced distortion in diffusion MRI using a twice-refocused spin echo.* Magn Reson Med, 2003. 49(1): p. 177-82.
21. Helm, P., et al., *Measuring and mapping cardiac fiber and laminar architecture using diffusion tensor MR imaging.* Ann N Y Acad Sci, 2005. 1047: p. 296-307.
22. Rohmer, D., A. Sitek, and G.T. Gullberg, *Reconstruction and visualization of fiber and laminar structure in the normal human heart from ex vivo diffusion tensor magnetic resonance imaging (DTMRI) data.* Invest Radiol, 2007. 42(11): p. 777-89.
23. Chen, J., et al., *Regional ventricular wall thickening reflects changes in cardiac fiber and sheet structure during contraction: quantification with diffusion tensor MRI.* Am J Physiol Heart Circ Physiol, 2005. 289(5): p. H1898-907.
24. Scollan, D.F., et al., *Reconstruction of cardiac ventricular geometry and fiber orientation using magnetic resonance imaging.* Ann Biomed Eng, 2000. 28(8): p. 934-44.
25. Basser, P.J. and C. Pierpaoli, *A simplified method to measure the diffusion tensor from seven MR images.* Magn Reson Med, 1998. 39(6): p. 928-34.
26. Chen, J., et al., *Remodeling of cardiac fiber structure after infarction in rats quantified with diffusion tensor MRI.* Am J Physiol Heart Circ Physiol, 2003. 285(3): p. H946-54.
27. Helm, P.A., et al., *Evidence of structural remodeling in the dyssynchronous failing heart.* Circ Res, 2006. 98(1): p. 125-32.
28. Tseng, W.Y., et al., *Imaging myocardial fiber disarray and intramural strain hypokinesis in hypertrophic cardiomyopathy with MRI.* J Magn Reson Imaging, 2006. 23(1): p. 1-8.
29. Wu, M.T., et al., *Diffusion tensor magnetic resonance imaging mapping the fiber architecture remodeling in human myocardium after infarction: correlation with viability and wall motion.* Circulation, 2006. 114(10): p. 1036-45.
30. Wu, Y., et al., *MR study of the effect of infarct size and location on left ventricular functional and microstructural alterations in porcine models.* J Magn Reson Imaging, 2009. 29(2): p. 305-12.
31. Wu, Y., H.F. Tse, and E.X. Wu, *Diffusion tensor MRI study of myocardium structural remodeling after infarction in porcine model.* Conf Proc IEEE Eng Med Biol Soc, 2006. 1: p. 1069-72.
32. Wu, E.X., et al., *MR diffusion tensor imaging study of postinfarct myocardium structural remodeling in a porcine model.* Magn Reson Med, 2007. 58(4): p. 687-95.

33. J.C., et al., *Helical myofiber orientation after myocardial infarction and ventricular surgical restoration in sheep.* J Thorac Cardiovasc Surg, 2005. 129(2): p. 382-90.

Chapter 3 References

1. Chen, J., et al., *Remodeling of cardiac fiber structure after infarction in rats quantified with diffusion tensor MRI.* Am J Physiol Heart Circ Physiol, 2003. 285(3): p. H946-54.
2. Helm, P., et al., *Measuring and mapping cardiac fiber and laminar architecture using diffusion tensor MR imaging.* Ann N Y Acad Sci, 2005. 1047: p. 296-307.
3. Wu, Y., et al., *MR study of the effect of infarct size and location on left ventricular functional and microstructural alterations in porcine models.* J Magn Reson Imaging, 2009. 29(2): p. 305-12.
4. Rohmer, D., A. Sitek, and G.T. Gullberg, *Reconstruction and visualization of fiber and laminar structure in the normal human heart from ex vivo diffusion tensor magnetic resonance imaging (DTMRI) data.* Invest Radiol, 2007. 42(11): p. 777-89.
5. Geerts, L., et al., *Characterization of the normal cardiac myofiber field in goat measured with MR-diffusion tensor imaging.* Am J Physiol Heart Circ Physiol, 2002. 283(1): p. H139-45.
6. Holmes, A.A., D.F. Scollan, and R.L. Winslow, *Direct histological validation of diffusion tensor MRI in formaldehyde-fixed myocardium.* Magn Reson Med, 2000. 44(1): p. 157-61.
7. Hsu, E.W., et al., *Magnetic resonance myocardial fiber-orientation mapping with direct histological correlation.* Am J Physiol, 1998. 274(5 Pt 2): p. H1627-34.
8. Scollan, D.F., et al., *Histological validation of myocardial microstructure obtained from diffusion tensor magnetic resonance imaging.* Am J Physiol, 1998. 275(6 Pt 2): p. H2308-18.
9. Le Bihan, D., et al., *Diffusion tensor imaging: concepts and applications.* J Magn Reson Imaging, 2001. 13(4): p. 534-46.
10. Costa, K.D., et al., *Laminar fiber architecture and three-dimensional systolic mechanics in canine ventricular myocardium.* Am J Physiol, 1999. 276(2 Pt 2): p. H595-607.
11. LeGrice, I.J., et al., *Laminar structure of the heart: ventricular myocyte arrangement and connective tissue architecture in the dog.* Am J Physiol, 1995. 269(2 Pt 2): p. H571-82.
12. Scollan, D.F., et al., *Reconstruction of cardiac ventricular geometry and fiber orientation using magnetic resonance imaging.* Ann Biomed Eng, 2000. 28(8): p. 934-44.
13. Tseng, W.Y., et al., *Diffusion tensor MRI of myocardial fibers and sheets: correspondence with visible cut-face texture.* J Magn Reson Imaging, 2003. 17(1): p. 31-42.

14. Reese, T.G., et al., *Reduction of eddy-current-induced distortion in diffusion MRI using a twice-refocused spin echo.* Magn Reson Med, 2003. 49(1): p. 177-82.
15. Basser, P.J. and C. Pierpaoli, *A simplified method to measure the diffusion tensor from seven MR images.* Magn Reson Med, 1998. 39(6): p. 928-34.
16. Bammer, R., et al., *New methods in diffusion-weighted and diffusion tensor imaging.* Magn Reson Imaging Clin N Am, 2009. 17(2): p. 175-204.
17. Streeter, D.D., Jr., et al., *Fiber orientation in the canine left ventricle during diastole and systole.* Circ Res, 1969. 24(3): p. 339-47.
18. Theofilogiannakos, E.K., et al., *The clockwise rotation of myocardial fiber orientation from epicardial to endocardial surface in left ventricular free wall in a post-mortem human heart.* Stud Health Technol Inform, 2009. 142: p. 386-8.
19. Wu, M.T., et al., *Diffusion tensor magnetic resonance imaging mapping the fiber architecture remodeling in human myocardium after infarction: correlation with viability and wall motion.* Circulation, 2006. 114(10): p. 1036-45.
20. Wu, Y., H.F. Tse, and E.X. Wu, *Diffusion tensor MRI study of myocardium structural remodeling after infarction in porcine model.* Conf Proc IEEE Eng Med Biol Soc, 2006. **1**: p. 1069-72.
21. Wu, E.X., et al., *MR diffusion tensor imaging study of postinfarct myocardium structural remodeling in a porcine model.* Magn Reson Med, 2007. 58(4): p. 687-95.

Chapter 4 References

1. Buckberg, G.D., *Form versus disease: optimizing geometry during ventricular restoration.* Eur J Cardiothorac Surg, 2006. 29 Suppl 1: p. S238-44.
2. Sallin, E.A., *Fiber orientation and ejection fraction in the human left ventricle.* Biophys J, 1969. 9(7): p. 954-64.
3. Isomura, T., et al., *Septal anterior ventricular exclusion operation (Pacopexy) for ischemic dilated cardiomyopathy: treat form not disease.* Eur J Cardiothorac Surg, 2006. 29 Suppl 1: p. S245-50.
4. Cirillo M, A.G., *Rewind the heart: A novel technique to reset heart fibers' orientation in surgery for ischemic cardiomyopathy.* Med Hypotheses 2007. doi:10.1016/j.mehy.2007.07.047.
5. Helm, P.A., et al., *Evidence of structural remodeling in the dyssynchronous failing heart.* Circ Res, 2006. 98(1): p. 125-32.
6. Di Donato, M., et al., *Left ventricular geometry in normal and post-anterior myocardial infarction patients: sphericity index and `new' conicity index comparisons.* European Journal of Cardio-Thoracic Surgery, 2006. 29(Supplement 1): p. S225-S230.
7. Komamura, K., et al., *Exhaustion of Frank-Starling mechanism in conscious dogs with heart failure.* Am J Physiol, 1993. 265(4 Pt 2): p. H1119-31

Chapter 5 References

1. Hsu, E.W., A.L. Muzikant, S.A. Matulevicius, R.C. Penland, and C.S. Henriquez. Magnetic resonance myocardial fiber-orientation mapping with direct histological correlation. Am J Physiol 1998;274(5 Pt 2):H1627-34.
2. LeGrice, I.J., B.H. Smaill, L.Z. Chai, S.G. Edgar, J.B. Gavin, and P.J. Hunter. Laminar structure of the heart: ventricular myocyte arrangement and connective tissue architecture in the dog. Am J Physiol 1995;269(2 Pt 2):H571-82.
3. Streeter, D.D., Jr., H.M. Spotnitz, D.P. Patel, J. Ross, Jr., and E.H. Sonnenblick. Fiber orientation in the canine left ventricle during diastole and systole. Circ Res 1969;24(3):339-47.
4. Ingels, N.B., Jr. Myocardial fiber architecture and left ventricular function. Technol Health Care 1997;5(1-2):45-52.
5. Rijcken, J., P.H. Bovendeerd, A.J. Schoofs, D.H. van Campen, and T. Arts. Optimization of cardiac fiber orientation for homogeneous fiber strain at beginning of ejection. J Biomech 1997;30(10):1041-9.
6. Rijcken, J., P.H. Bovendeerd, A.J. Schoofs, D.H. van Campen, and T. Arts. Optimization of cardiac fiber orientation for homogeneous fiber strain during ejection. Ann Biomed Eng 1999;27(3):289-97.
7. Sallin, E.A. Fiber orientation and ejection fraction in the human left ventricle. Biophys J 1969;9(7):954-64.
8. Tomioka, H., O.J. Liakopoulos, G.D. Buckberg, N. Hristov, Z. Tan, and G. Trummer. The effect of ventricular sequential contraction on helical heart during pacing: high septal pacing versus biventricular pacing. European Journal of Cardio-Thoracic Surgery 2006;29(Supplement 1):S198-S206.
9. Tseng, W.Y., T.G. Reese, R.M. Weisskoff, T.J. Brady, and V.J. Wedeen. Myocardial fiber shortening in humans: initial results of MR imaging. Radiology 2000;216(1):128-39.
10. Van Der Toorn, A., P. Barenbrug, G. Snoep, et al. Transmural gradients of cardiac myofiber shortening in aortic valve stenosis patients using MRI tagging. Am J Physiol Heart Circ Physiol 2002;283(4):H1609-15.
11. Shapiro, E.P. and F.E. Rademakers. Importance of oblique fiber orientation for left ventricular wall deformation. Technol Health Care 1997;5(1-2):21-8.
12. Holmes, A.A., D.F. Scollan, and R.L. Winslow, Direct histological validation of diffusion tensor MRI in formaldehyde-fixed myocardium. Magn Reson Med, 2000. 44(1): p. 157-61.
13. Scollan, D.F., et al., Histological validation of myocardial microstructure obtained from diffusion tensor magnetic resonance imaging. Am J Physiol, 1998. 275(6 Pt 2): p. H2308-18.
14. Tseng, W.Y., et al., Imaging myocardial fiber disarray and intramural strain hypokinesis in hypertrophic cardiomyopathy with MRI. J Magn Reson Imaging, 2006. 23(1): p. 1-8.
15. Wu, M.T., et al., Diffusion tensor magnetic resonance imaging mapping the fiber architecture remodeling in human myocardium after infarction: correlation with viability and wall motion. Circulation, 2006. 114(10): p. 1036-45.

16. Reese, T.G., O. Heid, R.M. Weisskoff, and V.J. Wedeen. Reduction of eddy-current-induced distortion in diffusion MRI using a twice-refocused spin echo. Magn Reson Med 2003;49(1):177-82.
17. Basser, P.J. and C. Pierpaoli. A simplified method to measure the diffusion tensor from seven MR images. Magn Reson Med 1998;39(6):928-34.

Chapter 6 References

1. Adomian, G.E. and J. Beazell, *Myofibrillar disarray produced in normal hearts by chronic electrical pacing.* Am Heart J, 1986. 112(1): p. 79-83.
2. Karpawich, P.P., et al., *Developmental sequelae of fixed-rate ventricular pacing in the immature canine heart: an electrophysiologic, hemodynamic, and histopathologic evaluation.* Am Heart J, 1990**.** 119(5): p. 1077-83.
3. Karpawich, P.P., R. Rabah, and J.E. Haas, *Altered cardiac histology following apical right ventricular pacing in patients with congenital atrioventricular block.* Pacing Clin Electrophysiol, 1999. 22(9): p. 1372-7.
4. Tops LF, Schalij MJ, Holman ER, van Erven L, van der Wall EE, Bax JJ. Right ventricular pacing can induce ventricular dyssynchrony in patients with atrial fibrillation after atrioventricular node ablation. J Am Coll Cardiol 2006:48(8):1642-8.
5. Thambo JB, Bordachar P, Garrigue S, et al. Detrimental ventricular remodeling in patients with congenital complete heart block and chronic right ventricular apical pacing. Circulation 2004:110(25):3766-72.
6. Helm RH, Lardo AC. Cardiac magnetic resonance assessment of mechanical dyssynchrony. Current opinion in cardiology 2008:23(5):440-446.
7. Russel IK, Zwanenburg JJ, Germans T, et al. Mechanical dyssynchrony or myocardial shortening as MRI predictor of response to biventricular pacing? J Magn Reson Imaging 2007;26(6):1452-1460.
8. Eggen M, Swingen C, Matta P, et al. Design of a Novel Perfusion System to Perform MR Imaging of an Isolated Beating Heart. J. Med. Devices 2009:3(2):027536.
9. Hill AJ, Laske TG, Coles JA Jr., et al. In vitro studies of human hearts. Ann Thorac Surg. 2005:79:168 –177.
10. Osman, NF and Prince JL. Visualizing myocardial function using HARP MRI. Phys Med Biol 2000:45(6):1665-82.

Appendix A: Induction of Dilated Cardiomyopathy in Swine by Chronic High-rate Ventricular Pacing: Structural, Electrical, and Hemodynamic Characterization[†]

[†] Authors: Michael W. Kimmel, PhD[1,2,4], Michael D. Eggen, MS[1,2], Jason L. Quill, PhD[1,2], Xiaohuan Li, MD[2], Eric S. Richardson, PhD[1,2], William J. Gallagher, BA[2], Kenneth K. Liao, MD[2], Paul A. Iaizzo, PhD[1,2,3]

Departments of [1]Biomedical Engineering, [2]Surgery, and [3]Integrative Biology and Physiology, University of Minnesota (Minneapolis, MN)

[4]Medtronic, Inc. (Minneapolis, MN)

Preface

In animal models, chronic high-rate pacing has been shown to induce physiologic and anatomic changes that are clinically relevant to heart failure in humans. This study was performed to better characterize a high-rate pacing-induced dilated cardiomyopathy model in swine using multimodal analysis.

Swine (n=9) were anesthetized and implanted with a pacing lead in the apex of the right ventricle and pacemaker for delivery of high-rate pacing (200 bpm) for four weeks. At study termination, hemodynamics, echocardiography, and noncontact mapping were utilized to assess the electrical and mechanical function of the hearts. Post-termination, hearts were perfusion fixed for anatomic assessment and compared against controls. Compared to controls, minLVP and dP/dt_{min} were significantly increased ($p<0.05$), while maxLVP and dP/dt_{max} were significantly decreased ($p<0.05$) in the high-rate pacing group. Total activation duration significantly decreased ($p<0.05$) and QRSd tended to increase (p=ns) following high-rate pacing. Heart weight, heart weight/body weight, and total left-heart volume increased significantly ($p<0.05$), while echo-derived ejection fraction decreased significantly ($p<0.05$) within each animal.

High-rate pacing induced well characterized and significant anatomic, physiologic, and electrical cardiac changes that will allow continued research into therapies for heart failure with dilated cardiomyopathy and their underlying mechanisms of action.

Introduction

Heart failure (HF) affects over 22 million people worldwide and more than 5 million individuals in the U.S. alone each year, and causes or contributes to over 300,000 deaths [1,2]. It is generally agreed that high-rate pacing-induced cardiomyopathy in animal models appropriately recreates the HF condition as observed in humans [1-3]. The canine model has been the primary large mammalian model of pacing-induced HF, with porcine and ovine models also utilized [1-5].

In the setting of HF, neurohormonal, cellular, and overall structural changes lead to cardiac electrical and mechanical dysfunction, ultimately worsening pump function. Separately, researchers have shown chronic high-rate pacing (HRP) to induce a range of physiologic and anatomic alterations, including changes in: 1) gross anatomy [1,2]; 2) hemodynamics [6,9-10; 3] electrophysiology [1-3]; 4) myocyte/cellular structure; 5) fiber reorganization/disarray; 6) metabolic parameters [4, 5]; and 7) neurohormonal disruption [6-9]. Each of these factors is certainly of interest by itself, but the ability to concurrently measure multiple parameters within the same individual subject is of great value. To our knowledge, a comprehensive analysis of the structural, hemodynamic, and electrical effects of HRP-induced dilated cardiomyopathy (DCM) in the same cohort of animals has not been described to date.

Given the established relevance of the cellular, anatomic, hemodynamic, and neurohormonal changes induced by prolonged exposure to HRP, selecting the appropriate animal model is likewise key; the porcine model has been used successfully

to approximate the human clinical DCM condition [10]. The overall anatomy, especially the coronary artery anatomy, as well as the electrophysiological similarities between swine and humans make the swine model attractive for use in translational research [11-13]. Further, research has shown that HF-relevant hemodynamic endpoints have been reached after one week of HRP in swine, while canine require a longer treatment period, sometimes up to eight weeks [7, 10, 14]. With the above considerations in mind, as well as our laboratory's extensive experience using swine in cardiac research, the current study was performed to utilize multiple methodologies to provide a detailed characterization of a swine model of chronic HRP-induced DCM.

Methods

This research protocol was reviewed and approved by the University of Minnesota Institutional Animal Care and Use Committee, and was designed to ensure the humane treatment of all animals as indicated by the "Guide for the Care and Use of Laboratory Animals" (NIH).

High-Rate Pacing Protocol

The overall study progression is depicted in Figure A.1. Briefly, induction of DCM with HRP was accomplished over the course of four weeks, with weekly animal check-up examinations during HRP administration. Pre-HRP and post-HRP exams were carried out to evaluate the associated pacing-induced changes. A variety of methodologies were used to characterize the model and to assess cardiac function. A more detailed description of the procedure follows.

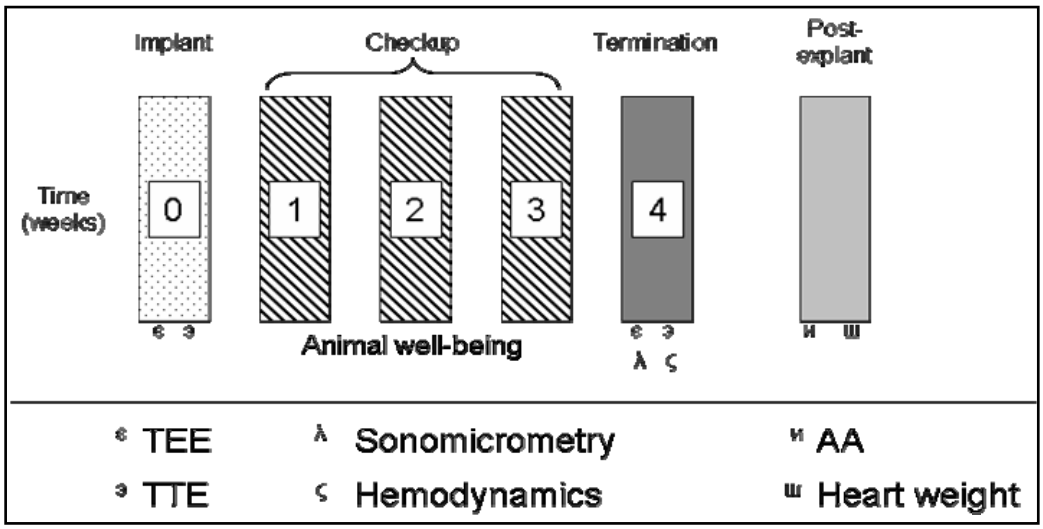

Figure A.1 Schematic overview of the experimental protocol, beginning with device implantation at week 0, termination at week 4, and weekly animal check-ups in between. At termination, transesophageal echo and transthoracic echo were performed along with hemodynamic and cardiac mechanic measurements. Following explantation, the heart was weighed and post perfusion fixed anatomical assessments were made.

Device Implantation

Yorkshire-cross swine (n=9, 73.4 ± 9.2 kg) were anesthetized to a surgical plane and prepped for surgery using aseptic techniques. A minimal incision was made exposing the right external jugular vein for implantation of a bipolar pacing lead (CapsureFix Novus 5076, Medtronic, Inc., Minneapolis, MN) in the right ventricular apex (RVA) using fluoroscopy. Typical RVA lead location as recorded with MRI post-study is shown in Figure A.2. The lead was fixated and pacing threshold and impedance were verified to be acceptable (< 2 V, < 500 Ω,). A modified implantable pulse generator (Kappa 700-series, Medtronic, Inc.) was implanted subcutaneously via a lateral incision on the neck and surgically closed.

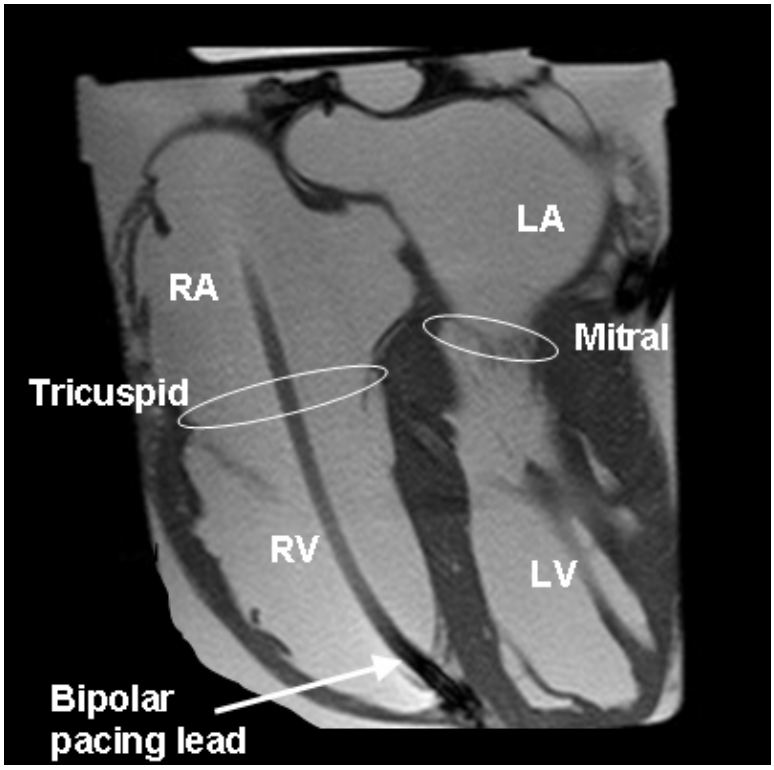

Figure A.2 High-rate pacing (HRP) lead location within the right ventricular apex as recorded using MRI in a perfusion fixed HRP heart. Labeled right heart landmarks include the right atrium (RA), tricuspid valve, and right ventricle (RV); left-heart landmarks include the left atrium (LA), mitral valve, and left ventricle (LV).

Following successful lead placement and implantable pulse generator implantation, cardiac ultrasound was used to record baseline images (see *Echocardiography* section). Swine were allowed to recover to the point of extubation, and permanent HRP was initiated at 200 bpm (2-3 V, 0.5 ms). Buprenorphine (0.01 mg/kg) along with cefazolin (1g in 5cc @ 1cc/min) were administered near the end of the procedure, and animals were subsequently monitored during recovery for stress and discomfort.

Study Termination

Following four weeks of HRP, the animals were again anesthetized with telazol and intubated for administration of isoflurane. Cardiac functional and structural conditions were examined using multiple methodologies. Closed-chest echocardiographic assessment was performed as described below (see *Echocardiography* section). Following baseline data acquisition, the chest was opened and the pericardium was removed to allow access to the epicardial surface. Intracardiac access was provided by introducers placed within the right and left external jugular veins, as well as the right common carotid artery. Each animal was instrumented to allow data collection for use in model assessment as described below.

Model Assessment and Characterization

Echocardiography

At implant and termination, transthoracic and transesophageal cardiac ultrasound (Acuson Cypress, Siemens Medical, Malvern, PA) assessments were performed with HRP off. Long-axis two- and four-chamber left ventricular (LV) apical images were recorded in 2D mode. Short-axis views of the LV were also taken in 2D and M-mode. Ejection fraction (EF) was determined using the CypressViewer software (Acuson Cypress) to delineate and compare end-systolic and end-diastolic LV dimensions from short-axis M-mode images taken at the papillary level.

Echocardiographic images were also analyzed to calculate LV volume, mass, sphericity index, and wall thickness. Left ventricular volume was calculated at end-diastole (LV

EDV) and end-systole (LV ESV) using the biplane ellipsoid method. Mean wall thickness was calculated using epicardial and endocardial areas from a short-axis view.

For purposes of calculating LV mass, L was subdivided into two segments: a papillary-to-base length (d) and a papillary-to-apex length (a). These lengths, along with endocardial radius (b) and mean wall thickness (t), were used to calculate LV mass using equation 1 (19).

$$LVmass = 1.05\pi\left\{(b+t)^2\left[\frac{2}{3}(a+t)+d-\frac{d^3}{3(a+t)^2}\right]-b^2\left[\frac{2}{3}a+d-\frac{d^3}{3a^2}\right]\right\}$$

Equation 1: LV mass calculation

Sphericity index was defined as the ratio of LV EDV to that of a theoretical sphere with a diameter equal to L. An SI of 1 corresponds to a perfect sphere.

Hemodynamic and Cardiac Mechanic Evaluation

Separate Millar Mikro-Tip® pressure catheters (5 French (Fr), MPR 500, Millar, Houston, TX) were inserted into each ventricle to allow for continuous assessment of right and left ventricular pressures (RVP, LVP) via the external jugular veins and the common carotid artery, respectively. During open-chest experimentation, 4-6 piezoelectric sonomicrometry crystals (SonoMetrics, London, ON, Canada) were implanted into the mid-myocardium as shown in Figure A.3 at the base, apex, and anterior and posterior walls of the LV for continuous measurement of volumetric data [15-17], as determined by the two-axis ellipsoid model [18].

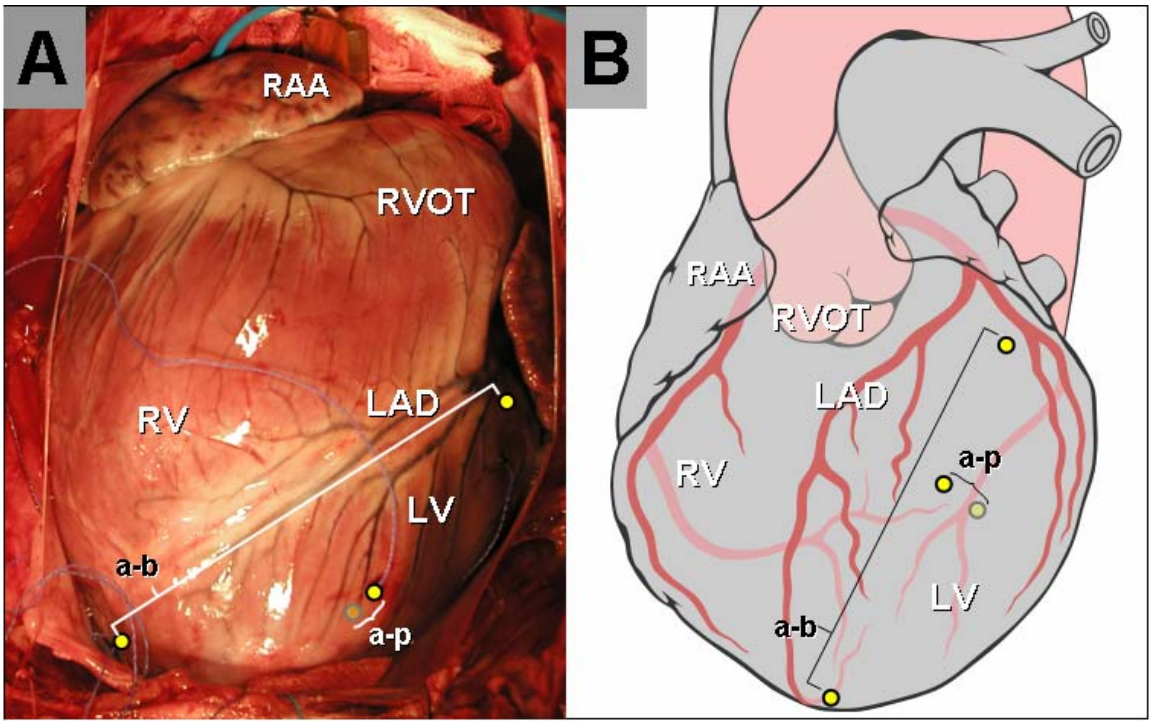

Figure A.3 Anatomical (A) and schematic (B) depiction of sonomicrometry crystal locations (yellow dots) as seen from the epicardial surface. The right and left ventricles (RV, LV), right atrial appendage (RAA), right ventricular outflow tract (RVOT), and left anterior descending coronary artery (LAD) have been labeled for reference. Crystals were implanted mid-myocardially. The apex-base (a-b) and anterior-posterior (a-p) dimensions were used to calculate left ventricular volume utilizing a two-axis ellipsoid model. Schematic B is modified from CC Patrick J. Lynch and C. Carl Jaffe, Yale University, 2006.

Endocardial Mapping

Using methods similar to those previously published, LV endocardial electrical activation was recorded at termination with HRP on and off using a noncontact mapping system (EnSite 3000, St. Jude Medical, St. Paul, MN)[19-26]. Briefly, a 9 Fr multielectrode array was inserted into the LV via the left coronary artery, and a 7 Fr steerable electrophysiology catheter (Conductr MC 6022, Medtronic, Inc.) was advanced via the left carotid artery under fluoroscopic guidance.

Noncontact mapping was used to analyze LV electrical activation patterns, total LV endocardial activation duration (TAD), local activation duration, and endocardial breakout. The breakout location was identified as the site on the LV endocardium where depolarization first appeared, or the instant when the time-derivative of the virtual unipolar electrogram (dV/dt) was maximally negative (maximum negative slope) at the breakout location [21, 27-31]. The TAD was defined as the interval from endocardial breakout to the latest observed LV electrical activation (based on virtual unipolar electrogram recordings).

Anatomic Examination

After termination of animals, excised hearts were formalin fixed with continuous flow under pressure, such that the specimens retained a fixed, end-diastolic shape. Fixed hearts from the chronic high-rate study (n=9) were compared to those from control animals of similar size (n=5, 60-80kg). Weight, total right-side volume, total left-side volume, and sulcus circumference were measured in each heart. Body weights from HRP and control animals were compared directly and were also used to calculate heart weight-to-body weight ratios for further comparison between HRP and controls.

To determine right-side volume measurements, the left side was clamped off at the aorta and the pulmonary vein and the heart were submerged in water to fill the right side. After removing the air from the chamber, the heart was removed and drained into a graduated cylinder. A similar process was used on the left side to obtain left-side

volume measurements. For sulcus circumference measurements, a string was placed around the heart along the atrioventricular sulcus, removed, and then measured with a ruler.

Statistical Analysis

Analysis of variance (ANOVA) was performed to determine the effects of HRP on the measured parameters. When significance was indicated by ANOVA, Fisher's least squares *post hoc* test was performed, with a p-value < 0.05 considered significant. Data are reported as the mean ± standard error. When possible, animals served as their own control. When instrumentation and data acquisition were not possible at implant, values were used from previous swine experimentation using animals of similar weight and age.

Results

At termination, 3 of 9 animals died before completion of data collection, two upon administration of anesthesia and one after the echo exam. Two animals exhibited extreme lethargic behavior attributed to HRP treatment. Qualitative observations of systemic dysfunction included: visually dilated hearts, enlarged/discolored livers, abdominal ascites (5-10 L), lung congestion, hypotension, decreased gastric motility, and general malaise.

For fixated hearts, animals were unable to serve as their own controls, so information was used from an internal database generated from previous experimentation. The

database included perfusion fixed hearts, as well as hemodynamic and electrophysiologic data from animals of age and body weight similar to those in the present study.

Echocardiography

Figure A.4 shows a reference schematic and a series of images taken from a single subject over the course of the DCM induction protocol. There is noticeable ventricular wall thinning present already after one week of HRP. As shown in Table A.1D, EF decreased significantly over the course of the pacing protocol, from an average initial value of 68.10 ± 3.71% to a final (failing) EF of 26.72 ± 5.14% ($p<0.01$). End-diastolic volume and ESV both increased significantly, with EDV beginning at 44.76 ± 6.46 mL and ending at 120.46 ± 14.79 mL ($p<0.01$), and ESV increased from 14.11 ± 2.45 mL to 86.27 ± 11.02 mL ($p<0.01$) after high-rate pacing. Stroke volume was maintained, with pre-HRP values of 30.65 ± 4.87 mL and post-HRP values of 34.16 ± 8.30 mL ($p=0.72$). Sphericity index increased due to HRP (pre-HRP: 0.74 ± 0.07 versus post-HRP: 0.95 ± 0.06, $p=0.06$), but did not reach significance. Additionally, LV mass increased following four weeks of HRP, from protocol initiation (85.71 ± 6.99 g) to study termination (130.65 ± 19.21 g, $p<0.05$).

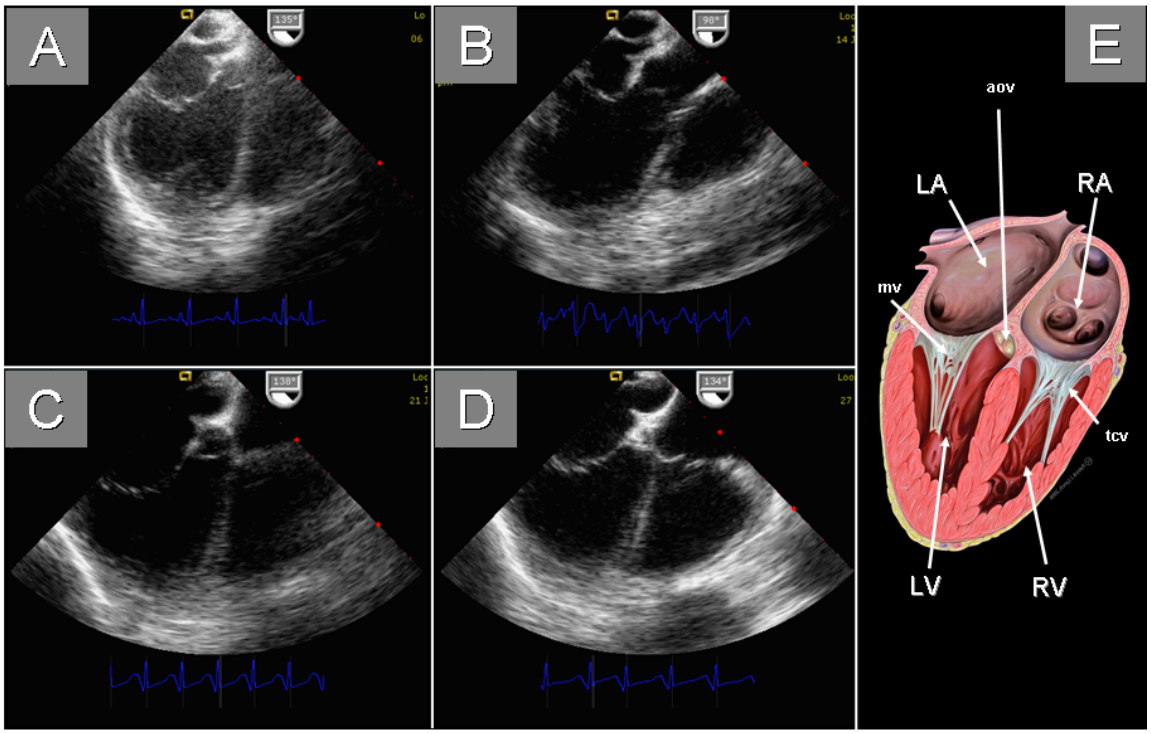

Figure A.4 Four-chamber long-axis transesophageal echocardiographic images taken over the course of high-rate pacing (HRP) of the right ventricular apex (200 bpm). Images were recorded with pacing off as well as (A) at implantation, (B) after 1 week of HRP, (C) after 2 weeks of HRP, and (D) after 3 weeks of HRP. A reference four-chamber schematic is included to provide correct landmark identification (E). Major chambers are labeled for reference, including the left atrium (LA), left ventricle (LV), right atrium (RA), and right ventricle (RV); visible valves, including the mitral valve (mv), aortic valve (aov), and tricuspid valve (tcv) are also labeled. Schematic E is modified from CC Patrick J. Lynch and C. Carl Jaffe, Yale University, 2006.

Hemodynamics and Cardiac Mechanics

Table A.1A shows a summary of the hemodynamic results of HRP-induced DCM as measured at termination. Following four weeks of HRP, minimum LV pressure (LVP) increased significantly compared to controls as measured both with HRP on and off (*control*: 4.9 ± 0.6 mmHg; *HRP on*: 23.2 ± 1.1 mmHg; *HRP off*: 19.5 ± 3.2 mmHg, $p<0.05$). Compared to controls, maxLVP was unchanged with HRP off, however with HRP on, maxLVP was significantly lower (76.8 ± 3.6 mmHg versus 89.3 ± 1.5 mmHg).

Maximum rate of LVP increase (dP/dt_{max}) was significantly lower with HRP on and off when compared to controls (*control*: 1349 ± 48 mmHg/sec; *HRP on*: 619 ± 68 mmHg/sec; *HRP off*: 628 ± 28 mmHg/sec, $p<0.05$). Likewise, the maximum rate of LVP decrease ($-dP/dt_{max}$) was significantly impaired with HRP on and off compared to controls (*control*: -1654 ± 73 mmHg/sec; *HRP on*: -738 ± 81 mmHg/sec; *HRP off*: -806 ± 18 mmHg/sec, $p<0.05$). End-systolic pressure was unchanged with HRP off, however, end-diastolic LVP was significantly higher compared to controls (*control*: 12.2 ± 2.3 mmHg versus *HRP off*: 21.3 ± 4.3 mmHg, $p<0.05$).

Figure A.5 shows an example of a pressure-volume loop series from within the same animal, including acute progression from unpaced to HRP. With HRP on, a characteristic shift towards decreased pressure generation and stroke volume is apparent.

Table A.1 Comparison of parameters between control and high-rate paced animals

		n	Control	n	Failure		
A	*Hemodynamics*				HRP off		HRP on
	maxLVP (mmHg)	32	89.3 ± 1.5	6	90.0 ± 1.1		76.8 ± 3.6 *#
	minLVP (mmHg)		4.9 ± 0.6		19.5 ± 3.2 *		23.2 ± 1.1 *
	dP/dt_{max}		1349 ± 48		628 ± 28 *		619 ± 68 *
	dP/dt_{min}		-1654 ± 73		-806 ± 18 *		-738 ± 81 *
	ES LVP	11	81.5 ± 2.4	6	80.0 ± 3.1		
	ED LVP		12.2 ± 2.3		21.3 ± 4.3 *		
B	*Electrophysiology*	6		4		5	
	QRSd (ms)		56.3 ± 1.6		62.9 ± 3.2 *		95.6 ± 2.7 *
	TAD (ms)		62.7 ± 2.6		27.9 ± 1.2 *		47.6 ± 2.9 *
C	*Body and Heart Weight*	66		9			
	BW (kg)		86.3 ± 1.4		Pre-HRP: 73.5 ± 3.1 # Post-HRP: 85.9 ± 4.9		
	HW (kg)		0.46 ± 0.006		0.53 ± 0.024 *		
	HW/BW		0.0054 ± 0.0001		0.0062 ± 0.0003 *		
D	*Echocardiography*			9	Pre-HRP		Post-HRP
	LV EDV (mL)				44.8 ± 6.5		120.5 ± 14.8#
	LV ESV (mL)				14.1 ± 2.5		86.3 ± 11.0#
	LV SV (mL)				30.7 ± 4.9		34.2 ± 8.3
	LV EF (%)				68.1 ± 3.7		26.7 ± 5.1#
	LV mass (g)				85.7 ± 7.0		130.7 ± 19.2#
	LV SI ()				0.7 ± 0.1		1.0 ± 0.1
	Note: Echo data from 2 animals were taken after 3 weeks of pacing						

Hemodynamic (A), electrophysiologic (B), and anatomic (C, D) data as recorded for control and high-rate paced (HRP) animals. Where available, HRP data are provided with pacing turned off (HRP off) and on (HRP on). Data are presented ± SE (*p<0.05 versus control, #p<0.05 versus pre-/post-HRP). BW=body weight, ED LVP=end-diastolic left ventricular pressure, ES LVP=end-systolic left ventricular pressure, HW=heart weight, LV EDV=left ventricular end-diastolic volume, LV EF=left ventricular ejection fraction, LV ESV=left ventricular end-systolic volume, LVP=left ventricular pressure, LV SI=left ventricular sphericity index, LV SV=left ventricular stroke volume, TAD=total activation duration.

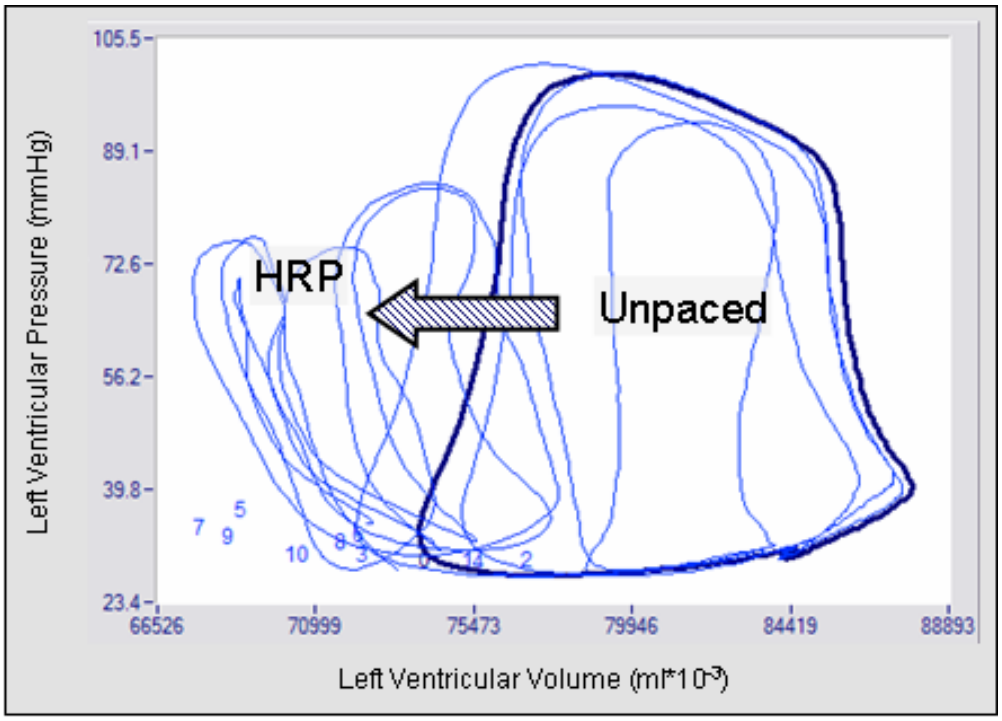

Figure A.5 Pressure-volume loops as recorded during transition from unpaced to high-rate pacing (HRP) in a swine. It can be seen that both pressure and volume decreased upon initiation of HRP; stroke volume also decreased.

Endocardial Mapping

Left ventricular endocardial activation in normal (non-HRP) swine hearts is initiated in the basal to mid-septal region, which results in a single depolarization wavefront radiating across the inferior portion of the LV, and then continuing up the lateral wall. The posterior-basal region of the lateral wall is the latest to be activated.

Following four weeks of HRP at 200 bpm, there were noticeable alterations in the endocardial electrical activation progression. Figure A.6 shows sample activation patterns from a healthy heart and a HRP heart. The colors in the figure correspond to voltage as measured by a unipolar electrode, with white designating the region of greatest depolarization (negative potential) and purple indicating tissue that has not yet depolarized. The movement of the depolarization wavefront across the endocardium as shown in Figure A.6A normally progresses from basal septum, down the septum to the apex, then up around to the lateral wall, terminating high on the lateral LV. Comparatively, the activation patterns following four weeks of HRP can be seen with the pacing turned on (Fig. A.6B) and off (Fig. A.6C).

Electrophysiology data is provided in Table A.1B. Compared to control data, QRSd was significantly longer both with HRP on and off (*control*: 56.3 ± 1.6 ms; *HRP on*: 95.6 ± 2.7 ms; *HRP off*: 62.9 ± 3.2ms, $p<0.05$). Total activation duration was likewise significantly shorter in the HRP group (both on and off) when compared to controls (*control*: 62.7 ± 2.6 ms; *HRP on*: 47.6 ± 2.9 ms; *HRP off*: 27.9 ± 1.2 ms, $p<0.05$).

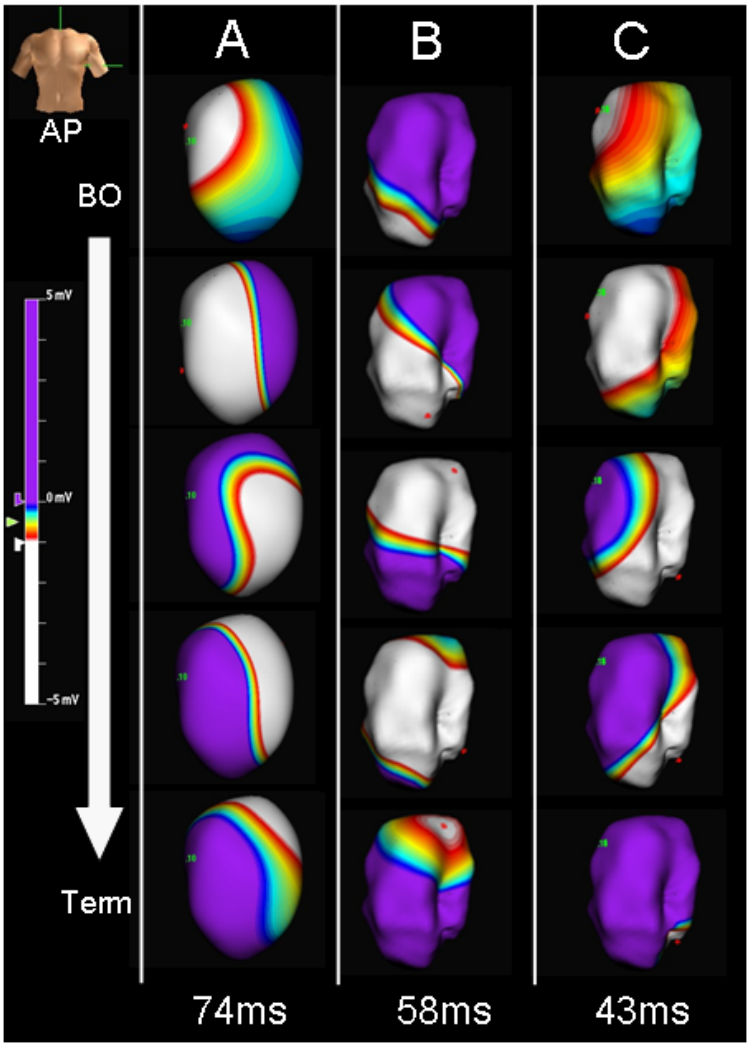

Figure A.6 Electrical activation progression depicted using isopotential electrical maps of the approximate left ventricular (LV) endocardial geometry, as recorded using noncontact mapping. All maps are oriented spatially in the anterior-posterior view as indicated by the torso, and oriented temporally top to bottom from breakout (BO) to termination (Term). Progression in the normal heart (A) began high on the LV septum, progressed downward towards the apex, swept across the apex and up the lateral wall, terminating postero-laterally; this process was completed in 74 ms as indicated. Notable electrical disruption was observed following a 4-week high-rate pacing (HRP) protocol for dilated cardiomyopathy induction. With HRP turned on (B), activation was initiated low on the LV septum, progressed radially upward across the anterior and posterior surfaces, and terminated high on the lateral wall. This progression was completed in 58 ms, quicker than the normal heart. With HRP turned off (C), BO was located high on the LV septum, where the activation wavefront quickly radiated laterally downward across both anterior and posterior surfaces, terminating laterally at the LV apex. This progression occurred over 43 ms, noticeably shorter than both HRP on and normal hearts.

Anatomic Examination

As outlined in Table A.1C, there was no significant difference in animal body weights between non-HRP and HRP animals prior to initiation of pacing. Heart weights from the control group averaged 0.46 ± 0.01 kg, while those following HRP averaged 0.53 ± 0.02 kg ($p<0.05$). In the control group, average heart weight/body weight was 0.0054 ± 0.0005, which was significantly increased in HRP animals to 0.0062 ± 0.0009 ($p<0.05$). Figure A.7 provides a qualitative comparison between the HRP and non-HRP groups, including right lateral (7A), anterior (7B), and left lateral (7C) views of the heart. Left-side volume significantly increased from 89 ± 16 ml (control) to 207 ± 24 ml (HRP)($p<0.01$) . Likewise, right-side volume significantly increased from 134 ± 14 ml (control) to 239 ± 30 ml (HRP)($p<0.05$). Sulcus circumference was not significantly larger ($p<0.01$) for the HRP animals compared to controls.

Discussion

Previously published work has demonstrated the utility of the chronically high-rate paced HF model, however, going back to the earliest description of the model, the majority of research has been performed using canine models [32, 33]. High-rate pacing disturbs not only mechanical performance, but also disrupts myocardial perfusion resulting in the heart being overworked and undernourished. Given the established similarities in the coronary blood supply between swine and humans, the swine heart was predicted to react to metabolic insult more similarly to the human heart than the canine heart. Swine hearts are also more similar to human hearts regarding arrhythmia potential.

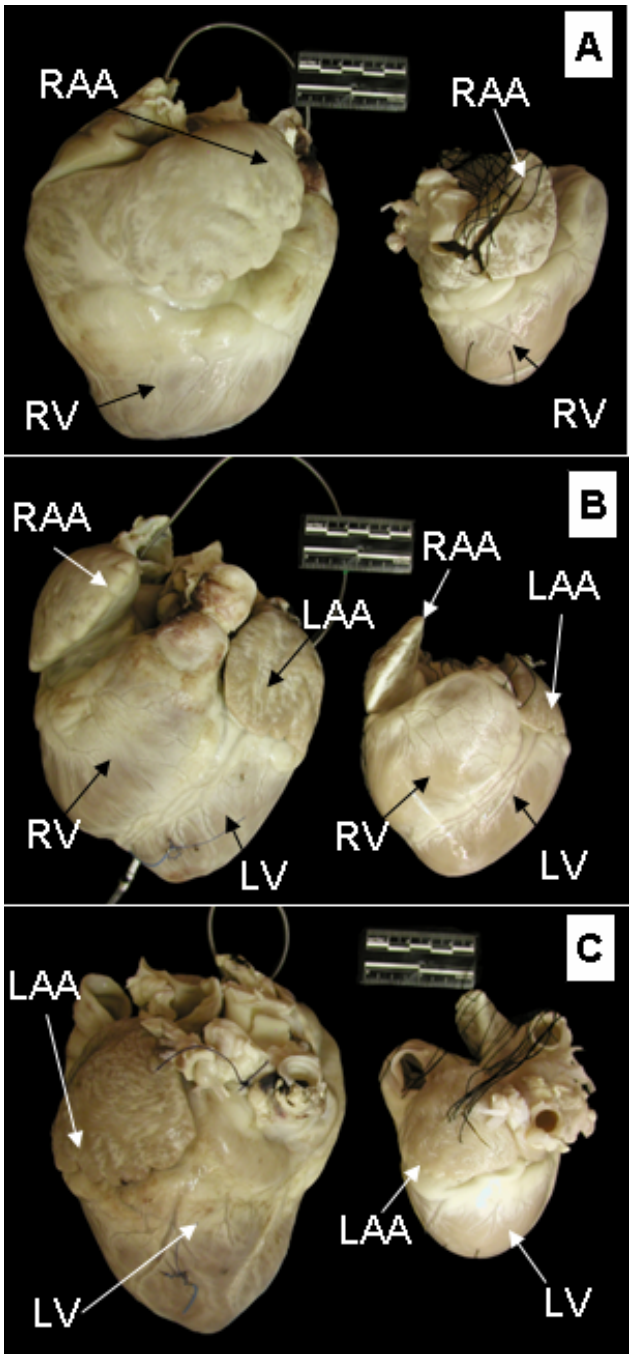

Figure A.7 A direct comparison of exemplar control and high-rate failure perfusion fixed swine hearts. The control (non-paced) heart is shown on the right, and the heart from a swine subjected to high-rate pacing at 200 bpm for four weeks is shown on the left. The hearts are shown from the (A) right-lateral, (B) anterior-posterior, and (C) left-lateral views. The right atrial appendage (RAA), right ventricle (RV), left atrial appendage (LAA), and left ventricle (LV) are labeled for reference.

Published studies utilizing HRP models in dogs, sheep, and to a lesser extent, swine, indicate that remodeling (dilatation) occurs within a week of overdrive pacing. Other observed pathophysiologic changes include elevated levels of circulating neurohormones (BNP, epinephrine), decreased cardiac output, altered expression of certain membrane channel proteins, as well as myocyte morphologic and fiber orientation changes [34]. In DCM, ejection fraction decreases, however stroke volume may be preserved. Additionally, while chamber volume increases, it does so without a proportional muscle mass gain, increasing the volume/mass ratio.

Echocardiography

Analyses determined that stroke volume was maintained following the HRP protocol, while EDV, ESV, stroke volume, EF, sphericity index, and LV mass all significantly increased over the course of the study. This is in agreement with what is currently known about DCM in humans, where the volume overload maintains the stroke volume even as the heart continues to remodel.

Hemodynamics and Cardiac Mechanics

There was no significant change in maxLVP with HRP off following the 4-week induction period. Also, there was correspondingly no difference in end-systolic LVP. Diastolic measures, such as minLVP and $-dP/dt_{max}$, were significantly impaired in the HRP group, even with the pacing turned off. In general, systolic dysfunction associated with HF is observed after diastolic impairment has already occurred. With this in mind,

the results of the present study are in line with clinical observations. That maxLVP was preserved but dP/dt_{max} was significantly decreased following HRP indicates that the heart's contractility was hindered, however, maxLVP was augmented by the increased diastolic pressures and shift in chamber volume.

Endocardial Mapping

Chronic RVA pacing at 200 bpm was found to disrupt normal electrical activity, specifically LV endocardial activation sequence, QRSd, and TAD as described earlier. As shown in Figure A.6, not only was the activation pattern disrupted, but the duration was consistently altered. While QRSd was slightly increased, TAD in the HRP animals (with HRP off) was markedly decreased compared to normal. From figure A.6C, activation started at what would be considered a normal breakout point. From there it raced downward across both the anterior and posterior surfaces to a termination point low on the lateral wall near the apex. Further, during unpaced periods, multiple sequential spontaneous beats were observed to exhibit breakout and activation patterns mimicking HRP from the RVA. In effect, it appears that some kind of substrate modification occurred, creating a modified conduction pathway.

Anatomic Examination: Body and Heart Weight

While on average, animals continued to gain weight while undergoing the HRP protocol, the average gain was less than expected given the animals' unlimited access to food. Assuming a growth rate of about 1 kg/day, it would have been expected that the animals would weigh at or above 100 kg at termination, rather than about 86 kg in the

current study [35]. In fact, several animals actually lost or maintained weight over the duration of the HRP protocol.

Anatomic Examination: Atrial Appendage Alterations

While there was no significant difference in weight, sulcus circumference, or left atrial appendage short axis compared to control hearts used in this section, the atrial measures taken from HRP hearts were significantly larger than control hearts in all other measurements. Minimized enlargement in the sulcus circumference could possibly be due to the fibrous nature of the cardiac skeleton. Also, the left atrial appendage short axis was the smallest measurement made, so lack of significant difference could be due to our measurement capabilities.

Limitations

While anatomic and physiologic changes associated with HRP have been correlated with DCM in the human population, due to the comparatively short period over which the condition is induced, it is generally assumed that the specific pathophysiology is not exactly the same as clinically occurring DCM [14]. Upon cessation of HRP, an initial rapid (~hours) improvement of hemodynamic parameters followed by a gradual (~days) increase has been shown by others. Similarly, neurohormonal disturbances improve initially, and gradually reach pre-failure levels [7, 36]. It has been reported in humans that upon correction of supraventricular tachycardia, EF values recover initially within days and continue to improve gradually over several months [37]. Other studies have shown restoration of normal function over the course of several weeks [38]. By

immediately carrying out any experimentation using this model, the effects of any "recovery" are considered to be minimized.

Conclusions

Previous animal research has used using high-rate atrial or ventricular pacing to induce and/or study anatomic, neurohormonal, and hemodynamic alterations associated with rate-induced ventricular dysfunction. By combining advanced endocardial electrical mapping with traditional hemodynamic and echocardiographic imaging, the current study demonstrated that RVA pacing at 200 bpm for four weeks in swine causes a condition analogous to DCM in humans. Further, by utilizing an animal model which is considered to approximate human anatomy and physiology, along with a wide range of measurement/characterization methodologies, we feel that insight has been gained into the condition of tachycardia-induced DCM.

This model and the measurement methodology described here should aid continued research into the understanding of therapies and their underlying mechanisms of action, as associated with DCM. Studies of gross cardiac anatomical changes, valvular structural disorders, and even variations in arrhythmogenicity of cardiac substrate are all relevant using this model. Further, given the observed electrical and structural changes, this model is well suited to investigations of relative effects of pacing lead placements and implications for therapy.

References

1. Kaab, S., et al., *Ionic mechanism of action potential prolongation in ventricular myocytes from dogs with pacing-induced heart failure.* Circ Res, 1996. 78(2): p. 262-73.
2. Lacroix, D., et al., *Repolarization abnormalities and their arrhythmogenic consequences in porcine tachycardia-induced cardiomyopathy.* Cardiovasc Res, 2002. 54(1): p. 42-50.
3. Power, J.M., et al., *Effects of left atrial dilatation on the endocardial atrial defibrillation threshold: a study in an ovine model of pacing induced dilated cardiomyopathy.* Pacing Clin Electrophysiol, 1998. 21(8): p. 1595-600.
4. Montgomery, C., N. Hamilton, and C.D. Ianuzzo, *Energy status of the rapidly paced canine myocardium in congestive heart failure.* J Appl Physiol, 1992. 73(6): p. 2363-7.
5. Wilson, J.R., et al., *Experimental congestive heart failure produced by rapid ventricular pacing in the dog: cardiac effects.* Circulation, 1987. 75(4): p. 857-67.
6. Redfield, M.M., et al., *Cardiorenal and neurohumoral function in a canine model of early left ventricular dysfunction.* Circulation, 1993. 87(6): p. 2016-22.
7. Travill, C.M., et al., *Haemodynamic and neurohumoral response in heart failure produced by rapid ventricular pacing.* Cardiovasc Res, 1992. 26(8): p. 783-90.
8. Nikolaidis, L.A., et al., *Mechanisms whereby rapid RV pacing causes LV dysfunction: perfusion-contraction matching and NO.* Am J Physiol Heart Circ Physiol, 2001. 281(6): p. H2270-81.
9. Rademaker, M.T., et al., *Natriuretic peptide responses to acute and chronic ventricular pacing in sheep.* Am J Physiol, 1996. 270(2 Pt 2): p. H594-602.
10. Chow, E., J.C. Woodard, and D.J. Farrar, *Rapid ventricular pacing in pigs: an experimental model of congestive heart failure.* Am J Physiol, 1990. 258(5 Pt 2): p. H1603-5.
11. Bowman, T.A. and H.C. Hughes, *Swine as an in vivo model for electrophysiologic evaluation of cardiac pacing parameters.* Pacing Clin Electrophysiol, 1984. **7**(2): p. 187-94.
12. Weaver, M.E., et al., *A quantitative study of the anatomy and distribution of coronary arteries in swine in comparison with other animals and man.* Cardiovasc Res, 1986. 20(12): p. 907-17.
13. Dondelinger, R.F., et al., *Relevant radiological anatomy of the pig as a training model in interventional radiology.* Eur Radiol, 1998. 8(7): p. 1254-73.
14. Armstrong, P.W., et al., *Rapid ventricular pacing in the dog: pathophysiologic studies of heart failure.* Circulation, 1986. 74(5): p. 1075-84.
15. Badke, F.R., P. Boinay, and J.W. Covell, *Effects of ventricular pacing on regional left ventricular performance in the dog.* Am J Physiol, 1980. 238(6): p. H858-67.
16. Hoit, B.D., et al., *Determination of left atrial volume using sonomicrometry: a cast validation study.* Am J Physiol, 1993. 264(3 Pt 2): p. H1011-6.

17. Urheim, S., et al., *Myocardial strain by Doppler echocardiography. Validation of a new method to quantify regional myocardial function.* Circulation, 2000. 102(10): p. 1158-64.
18. Little, W.C., G.L. Freeman, and R.A. O'Rourke, *Simultaneous determination of left ventricular end-systolic pressure-volume and pressure-dimension relationships in closed-chest dogs.* Circulation, 1985. 71(6): p. 1301-8.
19. Fung, J.W., et al., *Effect of Left Ventricular Endocardial Activation Pattern on Echocardiographic and Clinical Response to Cardiac Resynchronization Therapy.* Heart, 2007.
20. Fung, J.W., et al., *Variable left ventricular activation pattern in patients with heart failure and left bundle branch block.* Heart, 2004. 90(1): p. 17-9.
21. Kroll, M., et al., *Origin of electrical activation within the right atrial and left ventricular walls: differentiation by electrogram characteristics using the noncontact mapping system.* Pacing Clin Electrophysiol, 2003. 26(10): p. 1970-8.
22. Laske, T.G., et al., *Excitation of the intrinsic conduction system through his and interventricular septal pacing.* Pacing Clin Electrophysiol, 2006. 29(4): p. 397-405.
23. Schilling, R.J., N.S. Peters, and D.W. Davies, *Feasibility of a noncontact catheter for endocardial mapping of human ventricular tachycardia.* Circulation, 1999. 99(19): p. 2543-52.
24. Schilling, R.J., N.S. Peters, and D.W. Davies, *Mapping and ablation of ventricular tachycardia with the aid of a non-contact mapping system.* Heart, 1999. 81(6): p. 570-5.
25. Schilling, R.J., N.S. Peters, and D.W. Davies, *Simultaneous endocardial mapping in the human left ventricle using a noncontact catheter: comparison of contact and reconstructed electrograms during sinus rhythm.* Circulation, 1998. 98(9): p. 887-98.
26. Skadsberg, N.D., J.A. Coles, and P.A. Iaizzo, *Electrophysiologic Assessment of Right Ventricular Cardiac Pacing Sites Employing Non-Contact Electrical Mapping.* International Journal of Bioelectromagnetism, 2005. **7**(1): p. 325-328.
27. Anderson, K.P., et al., *Criteria for local myocardial electrical activation: effects of electrogram characteristics.* IEEE Trans Biomed Eng, 1993. 40(2): p. 169-81.
28. Kimber, S., et al., *A comparison of unipolar and bipolar electrodes during cardiac mapping studies.* Pacing Clin Electrophysiol, 1996. 19(8): p. 1196-204.
29. Paul, T., et al., *Epicardial mapping: how to measure local activation?* Pacing Clin Electrophysiol, 1990. 13(3): p. 285-92.
30. Potse, M., et al., *Properties of unipolar electrograms recorded with a multielectrode basket catheter.* J Electrocardiol, 2004. 37(1): p. 1-10.
31. Weiss, C., et al., *Electroanatomical Mapping (CARTO) of ectopic atrial tachycardia: impact of bipolar and unipolar local electrogram annotation for localization the focal origin.* J Interv Card Electrophysiol, 2001. 5(1): p. 101-7.
32. Whipple, G.H., et al., *Reversible congestive heart failure due to chronic rapid stimulation of the normal heart.* Proc New Engl Cardiovasc Soc, 1962. 20: p. 39-40.

33. Hasenfuss, G., *Animal models of human cardiovascular disease, heart failure and hypertrophy.* Cardiovasc Res, 1998. 39(1): p. 60-76.
34. Helm, P.A., et al., *Evidence of structural remodeling in the dyssynchronous failing heart.* Circ Res, 2006. 98(1): p. 125-32.
35. Hoberg, M., et al. *Tri-State Swine Nutrition Guide; Bulletin 869-98; Genetics*. [Web page] 1998 [cited 2007 12/12]; Tri-State Swine Nutrition Guide]. Available from: http://ohioline.osu.edu/b869/b869_30.html.
36. Zupan, I., et al., *Tachycardia induced cardiomyopathy in dogs; relation between chronic supraventricular and chronic ventricular tachycardia.* Int J Cardiol, 1996. 56(1): p. 75-81.
37. Packer, D.L., et al., *Tachycardia-induced cardiomyopathy: a reversible form of left ventricular dysfunction.* Am J Cardiol, 1986. 57(8): p. 563-70.
38. Van Gelder, I.C., et al., *Time course of hemodynamic changes and improvement of exercise tolerance after cardioversion of chronic atrial fibrillation unassociated with cardiac valve disease.* Am J Cardiol, 1993. 72(7): p. 560-6.

Appendix B: Design of a Novel Perfusion System to Perform MR Imaging of an Isolated Beating Heart[†]

[†] Authors: Michael D. Eggen, MS[1,2], Cory M. Swingen, PhD[3], Phil Matta[1], Michael G. Bateman, MENG[1,2], Christopher D. Rolfes, BA[1,2], Jason Quill, PhD[1,2], Eric Richardson, PhD[1,2], Stephen A. Howard, BA[1,2], , Paul A. Iaizzo, PhD[2,4]

Department of Biomedical Engineering[1], Department of Surgery[2], Department of Medicine[3], Department of Physiology[4], University of Minnesota, Minneapolis, MN 55455

This abstract has been published in the ASME Journal of Medical Devices, 2009:3(2):027536. Permission has been granted for inclusion of this work in my dissertation.

Background

Isolated mammalian hearts have been used to study cardiac physiology, pharmacology, and biomedical devices in order to separate myocardial characteristics from the milieu of the intact animal and to allow for increased control over experimental conditions. Considering these benefits and that MRI is the "gold" standard for measuring myocardial function, it was considered desirable to have a system which would allow simultaneous MR imaging of an isolated beating heart. Here we describe a unique portable system, which enables physiologic perfusion of an isolated heart during simultaneous MR imaging.

Methods

A two unit system was designed to physiologically support a large mammalian isolated heart during MR imaging where a modified Krebs-Henseleit perfusate was used as a blood substitute. The first unit (Fig B.1), which resides in an adjacent support room next to the scanner, contains all electronically powered equipment and components (with ferromagnetic materials) which cannot operate safely near the magnet, including (1) a thermal module and custom tube in tube heat exchanger warming the perfusate to 38°C; (2) a carbogen tank (95%O_2 5%CO_2) and hollow fiber oxygenator; and (3) two centrifugal blood pumps which circulates and pressurizes the left and right atrial filling chambers. The second unit (Fig B.2), which resides next to the magnet and is free of ferromagnetic materials, receives warmed, oxygenated perfusate from the first unit via PVC tubing. The isolated hearts were connected to the second unit via four cannulae

sutured to the great vessels. A support system (Fig B.3) placed inside the scanner on the patient bed secured the hearts and cannulae in the correct anatomical position.

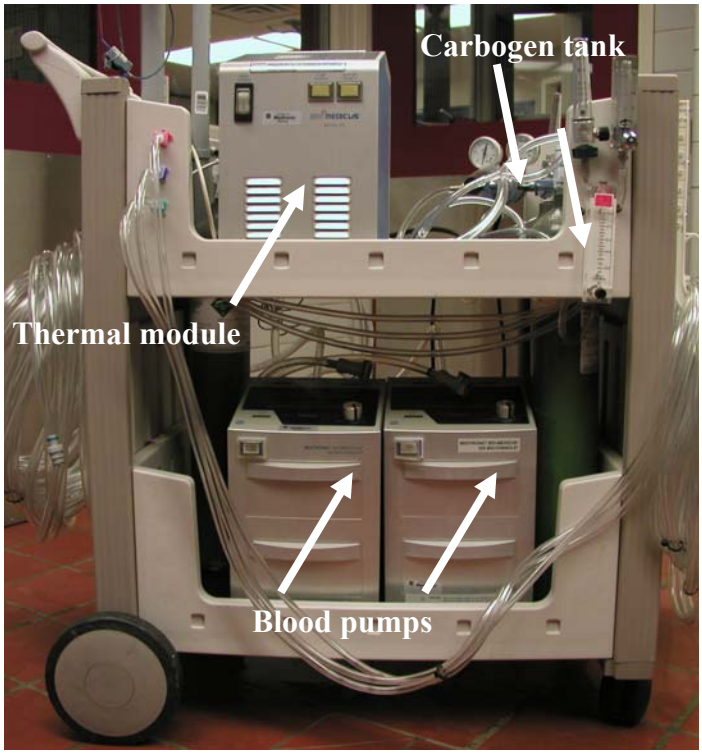

Figure B.1 Functional unit containing all electronically powered equipment and components.

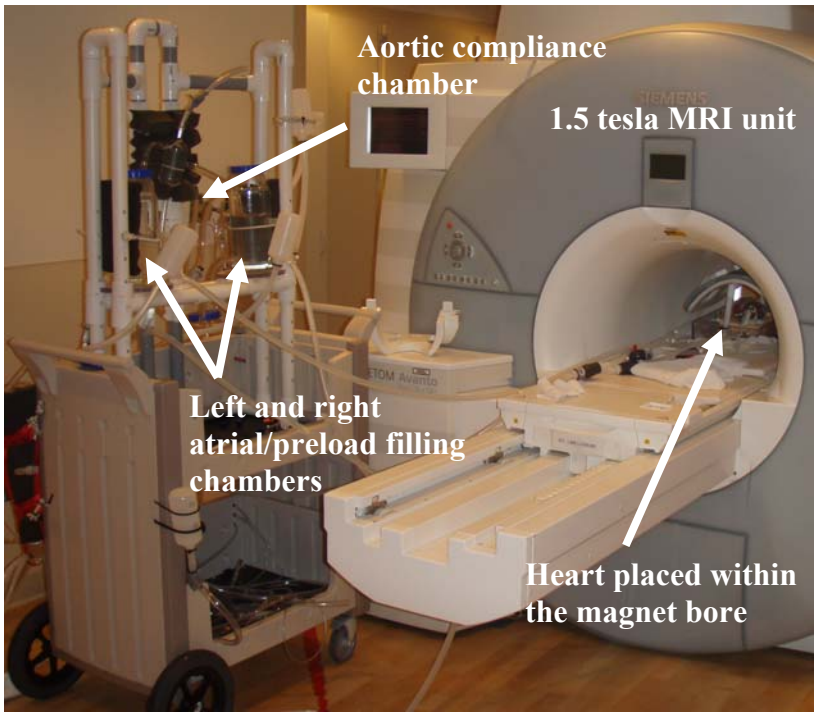

Figure B.2 Circulation unit responsible for maintaining physiological pressures which resides next to the MRI scanner.

Figure B.3 Heart support system which secures the heart in the correct anatomical position.

Results

To date, this system was tested in a 1.5 T Siemens scanner using swine hearts (n=2). The hearts were arrested with St. Thomas cardioplegia and removed via a medial sternotomy. After cannulation of the great vessels, reperfusion, and defibrillation, four-chamber and tagged short-axis cine loops were acquired using standard ECG gating. Tagged short-axis images (i.e. Fig B.4 with transmural LV circumferential strain superimposed in end-systole, green=negative, red=positive) obtained at the base, mid-ventricle, and apex were used to measure the following functional parameters for one heart: LV end-diastolic volume=38.84 ml, LV end-systolic volume=23.23 ml, LV stroke volume=15.6 ml, LV ejection fraction=40.18%, and peak LV circumferential strain=16%.

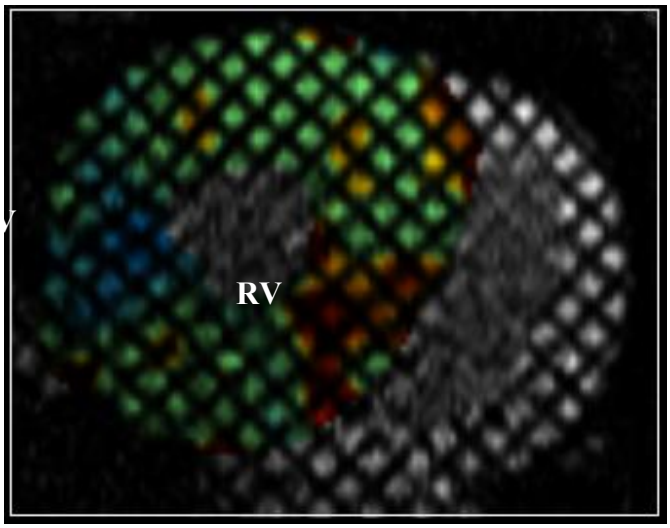

Figure B.4 Circumferential stain map in a mid-ventricular slice during systole (green=negative, red=positive).

Conclusions

The feasibility of MR imaging an isolated, four-chamber working large mammalian heart was demonstrated using a custom designed and built portable MRI compatible perfusion system. This system will be useful in studying in vitro cardiac function (including human hearts) and developing MRI safe biomedical devices and MRI guided therapies in a controlled setting.